

UNIVERSITY OF KWAZULU-NATAL (HOWARD COLLEGE)

MASTERS THESIS

**A Fluorescent Image Segmentation Model Based
on Improved Discrete Active Contours**

Author:
Ryan NAIDOO

Supervisor:
Dr. Jules-Raymond TAPAMO

*A thesis submitted in fulfillment of the requirements
for the degree of Master of Science in Engineering*

in the

Department of Electrical, Electronic and Computer Engineering
School of Engineering

November 12, 2016

Declaration of Authorship

I, Ryan NAIDOO, declare that this thesis titled, "A Fluorescent Image Segmentation Model Based on Improved Discrete Active Contours" and the work presented in it are my own. I confirm that:

- This work was done wholly or mainly while in candidature for a research degree at this University.
- Where any part of this thesis has previously been submitted for a degree or any other qualification at this University or any other institution, this has been clearly stated.
- Where I have consulted the published work of others, this is always clearly attributed.
- Where I have quoted from the work of others, the source is always given. With the exception of such quotations, this thesis is entirely my own work.
- I have acknowledged all main sources of help.
- Where the thesis is based on work done by myself jointly with others, I have made clear exactly what was done by others and what I have contributed myself.

Signed:

Date:

"If any of you is deficient in wisdom, let him ask of the giving God [Who gives] to everyone liberally and ungrudgingly, without reproaching or faultfinding, and it will be given him."

James 1.5 AMPC

UNIVERSITY OF KWAZULU-NATAL (HOWARD COLLEGE)

Abstract

Faculty of Engineering
School of Engineering

Master of Science in Engineering

A Fluorescent Image Segmentation Model Based on Improved Discrete Active Contours

by Ryan NAIDOO

For multiple fields, from biosciences and pharmaceutical drug development to semiconductor and geology research and beyond, fluorescence microscopy has been established as an essential tool which allows for the visualisation of the diminutive organisms and objects that escape visibility with the naked eye. The consequent insight into this world has allowed us to view the world from an indispensably unique perspective which has since played in vital role in enriching the livelihood of mankind.

Fluorescence microscopy isn't the sole player in this venture. It shares the limelight with another important and just as critical field, and that is image segmentation. However, the course between fluorescence images and extracting a meaningful segmentation is laden with barriers and hurdles such as noise, extreme low contrast, non-uniform illumination, etc. The aim of this research is to better understand fluorescence image properties and use this information to enhance and develop domain-specific segmentation methods, using discrete combinatorial techniques, for extracting meaningful results.

We design a pre-processing scheme which attempts to "undo" the adverse effects inherent in the image procurement stage. Specifically, we tackle noise removal, boundary completion and enhancement and contrast enhancement. We also modify the Chan-Vese segmentation scheme such by defining a weighting process and parameter relations. We then use the information from an initial unsupervised segmentation to estimate the correct parameter settings for segmentation on the image of interest specifically. We compare this scheme with other well-known parameter estimation schemes and parameter settings.

The results exhibit a significant boost in segmentation correctness and consistency. It is also supersedes previous schemes in terms of being applicable over a wider range of images. It also boasts a greater sense of generalisation since the parameters can be tuned for other images properties inherent in other domains.

The methods and techniques presented herein will greatly improve the results and stability of higher level decision making as well as removing the need to manually fine-tune segmentation results.

Acknowledgements

The acknowledgments and the people to thank go here, don't forget to include your project advisor...

Contents

Declaration of Authorship	i
Abstract	iii
Acknowledgements	iv
List of Figures	vii
List of Tables	xi
List of Abbreviations	xiii
1 Fluorescence Microscopy	1
1.1 Physics of Fluorescence	1
1.2 Specimen Labelling	2
1.3 The Epifluorescence Microscope and Image Acquisition	4
1.4 Image Processing	6
1.4.1 Preprocessing	6
1.4.2 Segmentation	9
1.5 Object Measurement and Analysis	10
2 Mathematical Background	13
2.1 Labelling Problems	14
2.2 Maximum A Posteriori Estimation for Discrete Models	14
2.2.1 Markov Random Fields	15
2.2.2 MAP-MRF Estimation as Energy Minimisation	17
2.3 Introduction to Graph Cuts	19
2.3.1 Network Theory and the Min-cut Problem	19
2.3.2 Image Segmentation Graph Structure	23
2.3.3 Submodular Functions	23
2.4 Graph Cut Algorithms for Energy Minimisation	25
2.4.1 Ford-Fulkerson	25
2.4.2 Dinic/Edmonds-Karp	25
2.4.3 Push-Relabel	26
2.4.4 Move Making Algorithms	30
3 Pre-Processing and Post-Processing Scheme for Fluorescence Microscopy Images	32
3.1 Preprocessing Scheme	32
3.1.1 Denoising	32
3.1.2 Separation under Intensity	34
3.1.3 Channel Mixing	38
3.1.4 Intra-Region Smoothing and Edge Completion and Enhancement	39
3.2 Experimental Results	40
3.3 Discussion	40

4 Parameter Estimation for ACWE Chan-Vese Segmentation	48
4.1 Graph Cut Model for Chan-Vese Segmentation	48
4.2 Modified Weighting and Parameter Estimation	50
4.2.1 Graph Weighting	51
4.2.2 Analysis of Weighting System and Parameter Relationships	52
4.2.3 Tuning Parameters for Fluorescence Microscopy	56
4.3 Experimental Results	72
4.4 Discussion	107
A Introduction to Graph Theory	109
B Cell Images Dataset	112
B.1 Sample Set	112
B.2 Test Set	112
Bibliography	117

List of Figures

1.1	(a) Simplified fluorescence process. (b) The Jabłoński diagram depicting the electronics states from photon absorption to photo emission.	2
1.2	Normalised Excitation and Emmision Spectra of the Alexa Fluor 532 fluophore. The emmission maximum is at 553nm which is a more yellow-green than excitation maximum at 5534nm. Data obtained from ThermoFisher Scientific [13].	3
	https://www.thermofisher.com/us/en/home/life-science/cell-analysis/labeling-chemistry/fluorescence-spectraviewer.html	
1.3	(a) FISH (Fluorescent 'in-situ' Hybridization) in mouse chromosomes using a BAC clone labeled with Spectrum Orange. The picture shows two metaphases and one interphase with two signals in each exemplifying a homozygous mouse for a transgenic clone. Image Source: "All About the Human Genome Project" Genetic and Genomic Image and Illustration Database. (b) p53 Binding Protein 1 (53BP1) was detected in perfusion fixed frozen sections of rat kidney using Goat Anti-Human 53BP1 Antigen Affinity-purified Polyclonal Antibody (Catalog # AF1877) at 15 µg/mL overnight at 4°C. Tissue was stained using the NorthernLights™557-conjugated Anti-Goat IgG Secondary Antibody (red; Catalog # NL001) and counterstained with DAPI (blue). Specific staining was localized to nuclei of epithelial cells in convoluted tubules. Image Source: R&D Systems' IHC image database.	4
	https://unlockinglifescode.org/media/images/	
	https://www.rndsystems.com/resources/ihc-images/53bp1	
1.4	The schematic of the epifluorescence microscope.	5
1.5	The effect of nonuniform illumination on segmentation. (a) Original image. Image source: The Cell Image Library [30]. (b) Nonuniformly illuminated image. The Vignette effect. (c) K-means clustering using the Euclidean distance metric and 2 clusters. The blue curve is from the original, the red curve is from the nonuniformly illuminated image. Notice that less of the object is recognised towards the edges.	6
	http://www.cellimagelibrary.org/images/2173	
1.6	The effect of photobleaching. Image Source: Molecular Expressions [32]. (a) Original image at $t = 0s$. (b) Image after $t = 10s$. (c) Image after $t = 20s$	7
1.7	The image formation process. Image source: [34]	8
1.8	The effect of noise on segmentation. (a) Original image. (b) Poisson noise corrupted image. (c) ACWE Chan-Vese segmentated output. The red curve is from the original, the green curve is from the Poisson noise corrupted image. Notice that there are more artifacts and the segmented output is less accurate especially towards the bottom left from the green curve.	9
2.1	Common lattice structure for 2D and 3D image data. (a) Simplest connection of neighbouring pixels for 2D images. Each non-edge pixel is connected to 4 pixels. This is 4-connectedness. (b) Simplest connection of neighbouring voxels for 3D images. Each non-edge voxel is connected to 6 voxels. This is 6-connectedness.	16
2.2	4-connected random field Y over the sites \mathcal{P}	16
2.3	Caption. (a) Caption. (b) Caption.	17
2.4	Network N with no flow. The in-degree and out-degree for the source, s , and the sink, t , are shown next to the corresponding node.	20

2.5	Network N with flow. The flow out of the source node, s , is equal to the flow into the sink node, t . For all other nodes, the flow-in is equal to the flow-out. This is the conservation of flow principle. This is only part of the network. The remaining part is the residual graph which shows the amount of reverse flow is available on an edge.	20
2.6	Network N with with a valid cut C . The nodes within the red region are reachable from the source and the nodes within the blue region are able to reach the sink. The cut set, C , is show in the orange filled block.	21
2.7	Network N with with a invalid cut C . The cut does not partition source node s and sink node t into distinct sets.	21
2.8	Network N with with a invalid cut C . The cut partition partitions the graph into more than two sets and the cut intersects the edges <i>ab</i> and <i>ad</i> twice.	22
2.9	Network N with maximum flow. There is no way to push more flow out of the source into the sink without breaking the rules for the conservation of flow.	22
2.10	Network N with minimal cut C . The sum of the capacity of all the edges in the cut set is the minimum of all possible valid cuts on the network N .	23
2.11	Overall process of the graph cut image segmentation process. (a) Image with object and background seeds. (b) Graph representation of the energy function to be minimised over the image. The n-links are represented by black arrows, the t-links from the source are shown in red, and the t-links to the sink are shown in blue. (c) Minimised energy function by cut C . The light red, light blue and grey edges are those that belong to the cut set C . (d) Segmentation mask after label assignment. In this case, all nodes that are still attached to the source, their corresponding pixel label is shown in white, similarly, nodes that are connected to the sink have their corresponding pixel labels shown in black.	24
3.1	Segmentation Scheme.	33
3.2	Proxy image generation.	33
3.3	Feature data set.	34
3.4	Plot of remapping function.	36
3.5	Amplification function control points and curve.	37
3.6	Original images with direct conversion to grayscale.	40
3.7	Removed noisy channels with corresponding grayscale images.	41
3.8	Original channel, TV denoised and remapped.	43
3.9	Mixed.	44
3.10	Final proxy after CED-ORI Filtering.	44
3.11	Segmentation results.	45
3.12	Running time vs Image size	47
4.1	(a) Cauchy-Crofton length approximation. (b) 8-connected neighbourhood system.	49
4.2	CAPTION MISSING HERE.	51
4.3	CAPTION MISSING HERE.	52
4.4	Fully connected single node.	52
4.5	Data energy functions plot.	54
4.6	Relationship between α and p_e .	55
4.7	Image 1 from sample set Figure B.1 initial masks.	58
4.8	Segmented output for various combination of α and λ_1 for Image 1 in the sample set.	58
4.9	Image 2 from sample set Figure B.1 initial masks.	59
4.10	Segmented output for various combination of α and λ_1 for Image 2 in the sample set.	59
4.11	Image 3 from sample set Figure B.1 initial masks.	60
4.12	Segmented output for various combination of α and λ_1 for Image 3 in the sample set.	60
4.13	Image 4 from sample set Figure B.1 initial masks.	61
4.14	Segmented output for various combination of α and λ_1 for Image 4 in the sample set.	61

4.15 Image 5 from sample set Figure B.1 initial masks.	62
4.16 Segmented output for various combination of α and λ_1 for Image 5 in the sample set.	62
4.17 Image 6 from sample set Figure B.1 initial masks.	63
4.18 Segmented output for various combination of α and λ_1 for Image 6 in the sample set.	63
4.19 p_e as a fraction of the distance between c_0 and c_1 .	64
4.20 h as a fraction of the distance between c_0 and c_1 .	65
4.21 Image 1 from test set Appendix B initial masks.	75
4.22 Image 1 from test set Appendix B segmentation results.	75
4.23 Image 2 from test set Appendix B initial masks.	76
4.24 Image 2 from test set Appendix B segmentation results.	76
4.25 Image 3 from test set Appendix B initial masks.	77
4.26 Image 3 from test set Appendix B segmentation results.	77
4.27 Image 4 from test set Appendix B initial masks.	78
4.28 Image 4 from test set Appendix B segmentation results.	78
4.29 Image 5 from test set Appendix B initial masks.	79
4.30 Image 5 from test set Appendix B segmentation results.	79
4.31 Image 6 from test set Appendix B initial masks.	80
4.32 Image 6 from test set Appendix B segmentation results.	80
4.33 Image 7 from test set Appendix B initial masks.	81
4.34 Image 7 from test set Appendix B segmentation results.	81
4.35 Image 8 from test set Appendix B initial masks.	82
4.36 Image 8 from test set Appendix B segmentation results.	82
4.37 Image 9 from test set Appendix B initial masks.	83
4.38 Image 9 from test set Appendix B segmentation results.	83
4.39 Image 10 from test set Appendix B initial masks.	84
4.40 Image 10 from test set Appendix B segmentation results.	84
4.41 Image 11 from test set Appendix B initial masks.	85
4.42 Image 11 from test set Appendix B segmentation results.	85
4.43 Image 12 from test set Appendix B initial masks.	86
4.44 Image 12 from test set Appendix B segmentation results.	86
4.45 Image 13 from test set Appendix B initial masks.	87
4.46 Image 13 from test set Appendix B segmentation results.	87
4.47 Image 14 from test set Appendix B initial masks.	88
4.48 Image 14 from test set Appendix B segmentation results.	88
4.49 Image 15 from test set Appendix B initial masks.	89
4.50 Image 15 from test set Appendix B segmentation results.	89
4.51 Image 16 from test set Appendix B initial masks.	90
4.52 Image 16 from test set Appendix B segmentation results.	90
4.53 Image 17 from test set Appendix B initial masks.	91
4.54 Image 17 from test set Appendix B segmentation results.	91
4.55 Image 18 from test set Appendix B initial masks.	92
4.56 Image 18 from test set Appendix B segmentation results.	92
4.57 Image 19 from test set Appendix B initial masks.	93
4.58 Image 19 from test set Appendix B segmentation results.	93
4.59 Image 20 from test set Appendix B initial masks.	94
4.60 Image 20 from test set Appendix B segmentation results.	94
4.61 Image 21 from test set Appendix B initial masks.	95
4.62 Image 21 from test set Appendix B segmentation results.	95
4.63 Image 22 from test set Appendix B initial masks.	96
4.64 Image 22 from test set Appendix B segmentation results.	96
4.65 Image 23 from test set Appendix B initial masks.	97

4.66	Image 23 from test set Appendix B segmentation results.	97
4.67	Image 24 from test set Appendix B initial masks.	98
4.68	Image 24 from test set Appendix B segmentation results.	98
4.69	Image 25 from test set Appendix B initial masks.	99
4.70	Image 25 from test set Appendix B segmentation results.	99
4.71	Precision vs Recall over test set.	108
4.72	Accuracy over test set.	108
A.1	Undirected weighted graph G . The degree of each node is shown next to the corresponding node. The graph is simple. The red box shows the vertex set, V_G , and edge set, E_G , and their corresponding norm.	109
A.2	Directed weighted graph (Digraph) D . The in-degree and out-degree is shown next to each node. The graph is simple and not balanced. The red box shows the vertex set, V_D , and edge set, E_D , and their corresponding norm.	110
A.3	Undirected weighted graph H is a subgraph of G in Figure XX, $\mathbf{H} \subseteq \mathbf{G}$. Directed weighted graph I is a subgraph of D in Figure XX, $\mathbf{I} \subseteq \mathbf{D}$. The degree of each node is shown next to the corresponding node. The red box shows the vertex set, the edge set and their corresponding norms.	111
A.4	Cliques of the undirected weighted graph G . The maximal cliques are shown by the hyperedges that encompass the nodes of that clique.	111
B.1	Sample set.	112
B.2	Uneven Illumination	113
B.3	High cell density	113
B.4	Multi-modal (non-bi-modal)	114
B.5	Hazy/Glowing Edges	115
B.6	Thin Tentacles	115
B.7	Bright Spots and Speckles	116

List of Tables

2.1	The impact of the number of cites and labels on the solution space	14
3.1	Classification Statistics[A - Original gray scale image, B - CED-ORI only, C - Anisotropic TV denoising only, D - Proposed Preprocessing Scheme]	42
3.2	Channel Mixing Weights	42
3.3	Running Time Results	46
4.1	Initial means and standard deviations for all images in the sample set for Otsu, K-means and EMGMM clustering.	64
4.2	Results from manual tuning.	65
4.3	Average of final means for good segmentations.	68
4.4	Dilation after Otsu binarization.	68
4.5	Dilation after K-means clustering.	69
4.6	Dilation after EM-GMM clustering.	70
4.7	Parameter Settings and Segmentation Results.	100
4.8	Segmentation Efficiency.	103
4.9	Overall Segmentation Efficiency.	107

List of Algorithms

1	Ford-Fulkerson Max-flow	26
2	Min-cut from Max-flow	26
3	Edmonds-Karp Max-flow	26
4	Push Operation	28
5	Relabel Operation	29
6	Discharge Operation	29
7	Push-Relabel Maxflow Algorithm	30

List of Abbreviations

ACWE	Active Contours Without Edges
AOD	Average Optical Density
BCC	Boundary Chain Code
BFS	Breadth First Search
BP	Belief Propagation
CCD	Charge-Coupled Device
CED	Coherence Enhancing Diffusion
CLSM	Confocal Laser Scanning Microscopy
CRF	Conditional Random Field
DCC	Differential Chain Code
DFS	Depth First Search
DNA	Deoxyribonucleic Acid
DP	Dynamic Programming
DT	Delaunay Triangulation
EGFP	Enhanced Green Fluorescent Protein
EM	Expectation Maximisation
FCS	Fluorescence Correlation Spectroscopy
FIFO	First-In First-Out
FISH	Fluorescence in-situ Hybridisation
FLIM	Fluorescence Lifetime Imaging Microscopy
FRAP	Fluorescence Recovery After Photobleaching
FRET	Fluorescence Resonance Energy Transfer
GA	Genetic Algorithm
GCBLS	Graph Cut Based Level Set
GFP	Green Fluorescent Protein
GLCM	Gray Level Co-occurrence Matrix
GMM	Guassian Mixture Modelling
GRF	Gibbs Random Field
HLF	Highest Level First
ICC	Immunocytochemistry
ICF	Immunocytofluorescence
ICM	Iterated Conditional Modes
IHC	Immunohistochemistry
IHF	Immunohistofluorescence
IOD	Integrated Optical Density
Laser	Light Amplification by Stimulated Emission of Radiation
LBP	Loopy Belief Propagation
LED	Light Emitting Diode
LoG	Laplacian of Gaussian
MAP	Maximum A Posteriori
MCC	Matthews Correlation Coefficient
MIS	Medical Image Segmentation
MLP	Multi-Layered Perceptron
MRF	Markov Random Field

MST	Minimum Spanning Tree
NA	Numerical Aperture
ORI	Optimised Rotational Invariance
OTF	Optical Transfer Function
PSF	Point Spread Function
RF	Random Field
RNA	Ribonucleic Acid
SNR	Signal-to-Noise Ratio
TV	Total Variation
UV	Ultraviolet

For/Dedicated to/To my...

Chapter 1

Fluorescence Microscopy

Fluorescence microscopy has become an essential tool in diverse fields, such as petrology, semiconductors, etc, and has especially been established as a choice imaging technique in cellular and molecular biology for visualisation of cells and tissues [1–5]. In this thesis we confine our attention to its use in cellular biology.

Certain substances emit radiation when irradiated with a higher intensity light, such as ultraviolet (UV), blue or green, which is off a longer wavelength than that of the exciting light, this is known as *Stokes' Law*. This phenomenon is known as *photoluminescence* [6–9]. There are two types of photoluminescence. If emission persists at an appreciable level after the exciting light is turned off, then we call this *phosphorescence*. If emission persist only so long as the exciting light is on, then we call this *fluorescence* [6, 10].

The first observance and publishing of fluorescence is credited to Sir John Frederick William Herschel around 1852. In 1852, Sir John George Stokes published a 100 page treatise about this luminescent phenomenon and coined the term *fluorescence*, over Herschel's *dispersive reflection*, when he observed that the mineral *fluorite* emitted red light when irradiated by ultraviolet (UV) light [2, 11].

In the remainder of this chapter we present the underlying principles of fluorescence, how specimens are fluorescently marked, the optical principles of microscope design, image acquisition, image processing and common analysis in cellular biology. We only go so far in depth as to present a rudimentary understanding of fluorescence microscopy as is necessary for the comprehension of this thesis.

1.1 Physics of Fluorescence

Fluorescence microscopy is a cross-disciplinary field. It is encouraged, if not necessary, to have a photophysical understanding of the principles of fluorescence, for biologists and computer scientists. The knowledge of the "under the hood" mechanics of fluorescence empower computer scientists to make informed and directed research in terms of image processing. The aim here is to present an elementary introduction into the physics of fluorescence.

The overall principle of fluorescence can be explained in three steps [12] as illustrated in 1.1(a): (1) Energy is absorbed by an atom upon collision with a photon. (2) The atom becomes excited and an electron jumps to a higher energy level. (3) Shortly after jumping to the higher energy level the electron returns to the ground state and emits a photon.

Excitation and emission One of the best ways to visualise the fluorescing process is using a Jabłoński diagram. A detailed Jabłoński diagram is shown in 1.1(b). When a photon collides with an atom, all its energy is transferred to the atom. The energy of the photon is inversely related to it's wavelength, $E = h \frac{c}{\lambda}$, where h is Planck's constant and c and λ are the speed and wavelength of light in a vacuum respectively. This increase in energy moves an electron from the ground state S_0 to a higher level energy state. Depending on the energy of the photon and the number of photons absorbed by the photon the electron can move to different energy levels e.g. S_1, S_2, etc . This process happens almost immediately in the order of femtoseconds(10^{-15}s). Before moving to the lowest next higher energy

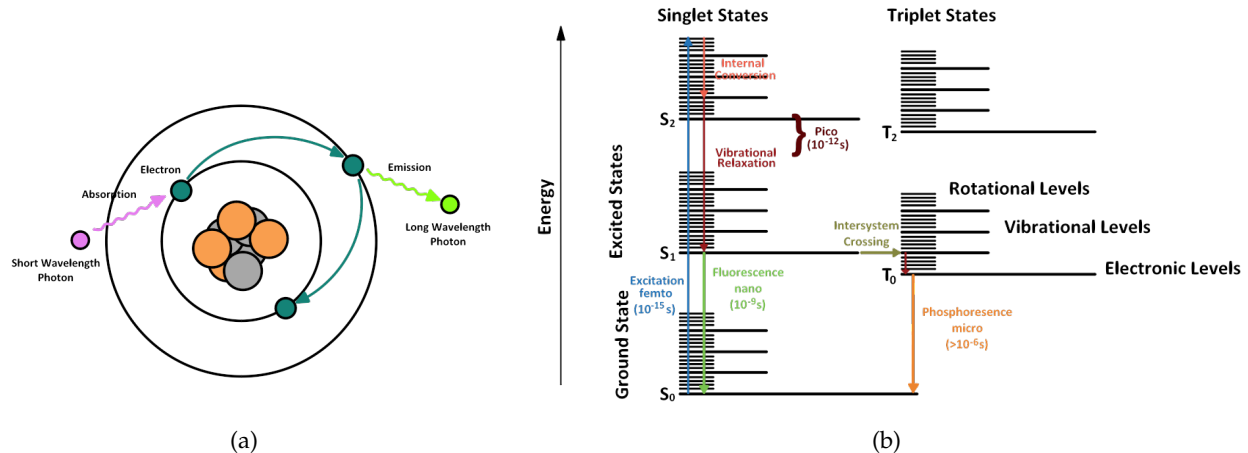


FIGURE 1.1: (a) Simplified fluorescence process. (b) The Jabłoński diagram depicting the electronics states from photon absorption to photo emission.

level (S_1), some energy is lost due to internal conversion and vibrational relaxation. When the electron spontaneously decays from S_1 to S_0 it emits a photon of longer wavelength than the absorption photon. This happens few nanoseconds (10^{-9} s) after excitation.

The difference in wavelength of the emission photon and excitation photon is known as the *Stokes' Shift* or *Stokes' Law*. The larger the Stokes' Shift the easier it is to separate the emission light from the excitation light [1]. The emission curve is often a mirror image and shifted to longer wavelengths than the excitation curve as illustrated in Figure 1.2.

Fluorophores Substances that exhibit the fluorescent property are called fluorophores, also known as *fluorochromes* or *fluorescent dyes*. Early investigations showed that many substance naturally possess fluorescent properties, such as minerals, crystals, resins, crude drugs, butter, chlorophyll, vitamins, etc [1]. This is known as *autofluorescence*. Substances that do not fluoresce must be *stained* such that it can be observed through a fluorescent microscope, more on this later.

Intersystem crossing If the electron spin as the electron transfer between energy states is preserved then the energy states are known as *singlet states*. It is also possible for the electron to reverse its spin. This is very unlikely and is known as *forbidden transition* in Quantum mechanics. When this happens the electron is said to be in a *triplet state*, see 1.1(b). The only way for the electron to reach the ground state is to again undergo another forbidden transition which is unlikely. When this does eventually happen the electron may emit a photon and this phenomenon is known as *phosphorescence*. This process takes much longer, in the order of microseconds (10^{-6} s).

1.2 Specimen Labelling

Many of the components of interest, such as cell nuclei, cytoplasm, genes, chromosomes, proteins, do not possess a high degree of, if not any, autofluorescence. In this scenario, these components can be marked with a fluorescent dye [14], also known as a fluorophore or fluorochrome, a substance that can bind to a specific target whose excitation and emission spectra are well known. This is known as staining [2, 3, 11]. Once the specimen is stained it can be indirectly observed using a fluorescence microscope.

The most prevalent staining techniques are fluorescence in-situ hybridisation (FISH) and immunostaining [2, 4, 15, 16].

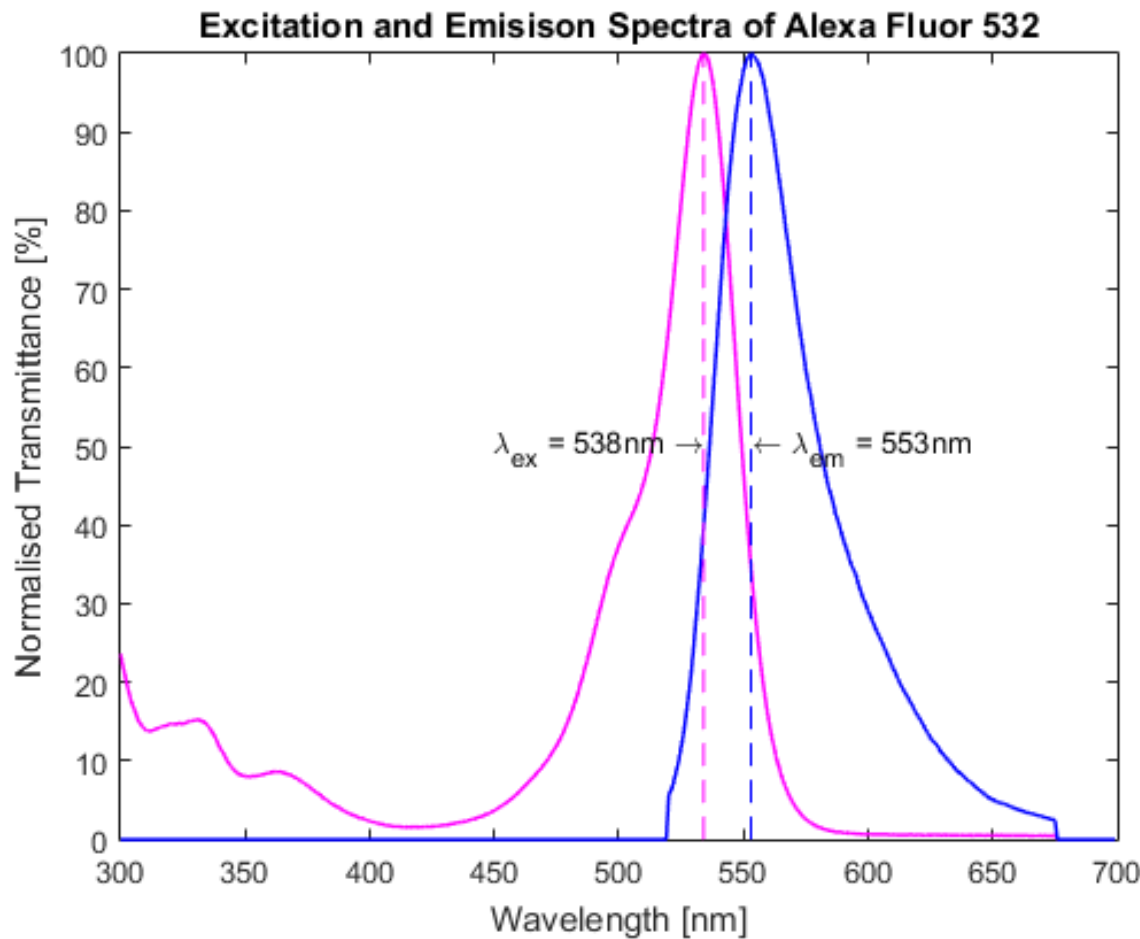


FIGURE 1.2: Normalised Excitation and Emission Spectra of the Alexa Fluor 532 fluorophore. The emission maximum is at 553nm which is a more yellow-green than excitation maximum at 5534nm . Data obtained from ThermoFisher Scientific [13].

FISH staining FISH is a molecular cytogenetic technique that uses fluorophores that bind to selected regions in nucleic acids [2, 4]. FISH is the most frequently used staining technique used primarily for visualisation and localisation of nucleic acid sequences, chromosomes, cytoplasm or organelles which contain those acids [3]. This makes FISH highly attractive for finding specific features in DNA and RNA used in genetic diagnosis and research, medicine and species identification [4, 17]. Figure 1.3(a) is a capture of mouse chromosomes using the FISH staining technique.

Immunostaining Immunofluorescence is the detection method where an antibody is used to detect an antigen in a tissue or a cell using fluorescence. Fluorophores are usually conjugated onto antibodies, which are proteins that are designed to bind to specific antigens, target proteins, on a cell [18]. The two types of immunofluorescent detection are immunocytofluorescence (ICF) and immunohistofluorescence (IHF). It must not be confused with immunocytochemistry (ICC) and immunohistochemistry (IHC). *Immuno* refers to the immunological technique, i.e. the binding of antibodies to antigens. *Cyto* refers to cells, i.e. cells without the extracellular membrane. *Histo* refers to tissue i.e. cells with the extracellular membrane. *Chemistry* refers to the chemical method of detection, e.g. a change in colour. *Fluorescence* detection by emission of light [19]. Figure 1.3(b) shows the detection of the p53 Binding Protein 1 in perfusion fixed frozen sections of rat kidney.

Live-cell staining The previously discussed staining techniques are not suitable to observe living cells. The fluorescent dyes used are phototoxic and cause cells to die. The circumvent this problem an

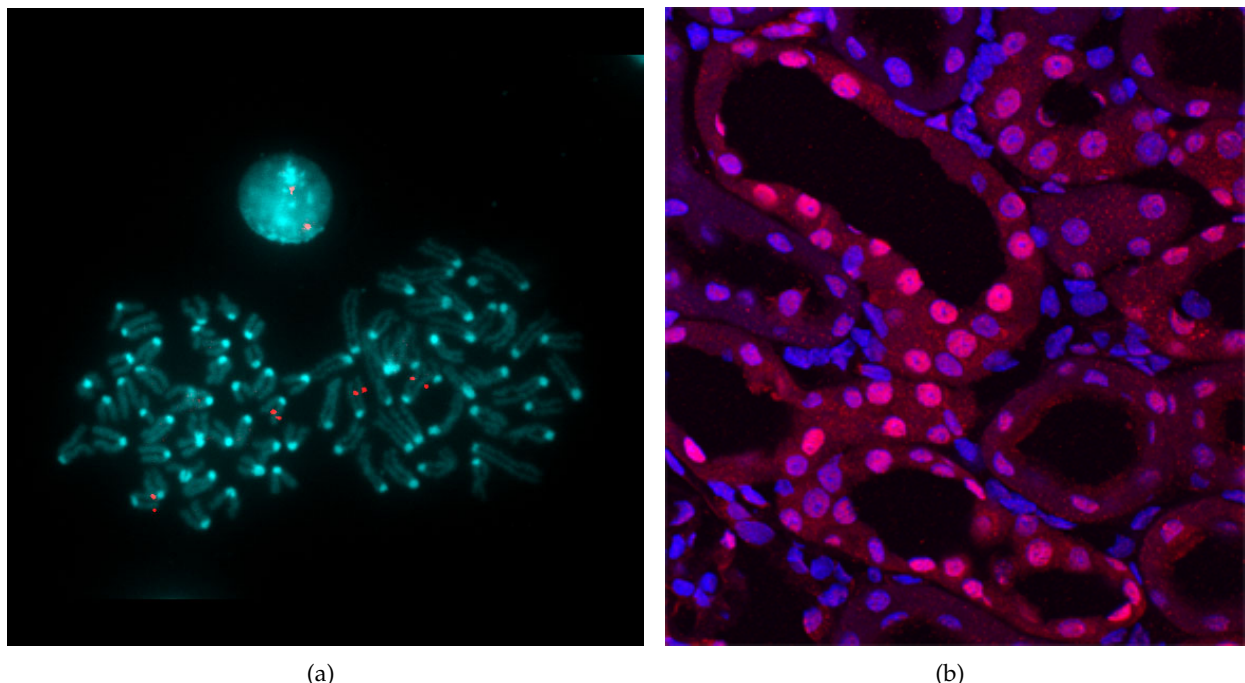


FIGURE 1.3: (a) FISH (Fluorescent 'in-situ' Hybridization) in mouse chromosomes using a BAC clone labeled with Spectrum Orange. The picture shows two metaphases and one interphase with two signals in each exemplifying a homozygous mouse for a transgenic clone. Image Source: "All About the Human Genome Project" Genetic and Genomic Image and Illustration Database. (b) p53 Binding Protein 1 (53BP1) was detected in perfusion fixed frozen sections of rat kidney using Goat Anti-Human 53BP1 Antigen Affinity-purified Polyclonal Antibody (Catalog # AF1877) at 15 µg/mL overnight at 4°C. Tissue was stained using the NorthernLights™557-conjugated Anti-Goat IgG Secondary Antibody (red; Catalog # NL001) and counter-stained with DAPI (blue). Specific staining was localized to nuclei of epithelial cells in convoluted tubules. Image Source: R&D Systems' IHC image database.

elegant solution has been devised. Instead of staining, the cells are modified to produce a fluorescent substance in the target structures. Derivatives of the *green fluorescent protein* (GFP), isolated from the *Aequorea victoria* jellyfish [4, 14, 20], are used as it generates a strong photon emission and is non-toxic to living cells [2, 3, 11].

1.3 The Epifluorescence Microscope and Image Acquisition

A fluorescence microscope is an optical microscope that is designed specifically to exploit the principle of fluorescence to allow for the observation of fluorescently labelled specimens [3, 4, 8, 11, 21]. There are many types of fluorescent microscopes available but the favoured type among many biologists and geneticists is the epifluorescent microscope [9, 22]. The schematic of the epifluorescent microscope is illustrated in Figure 1.4.

Light source The light source is typically a high-luminance light source e.g. Mercury or Xenon arc lamps, LEDs, lasers, etc [2, 3, 22–24]. The primary criterion for choosing a light source is that its characteristic peaks must coincide with the excitation spectrum of the fluorophores being used [1, 4, 20]. Wavelength coverage spans from near infra-red to UV. Mercury and Xenon arc lamps are expensive, an inexpensive and lightweight alternative is bright LEDs [4, 6, 11, 23].

Excitation filter The incoming light from the light source is typically multispectral [10]. The excitation filter is a wavelength selection filter which is placed in the path of the incoming light and filters

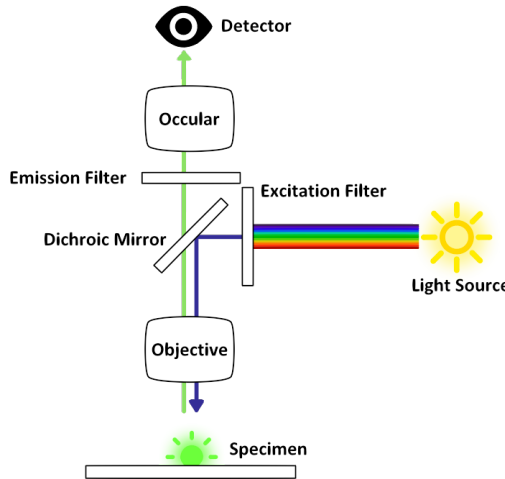


FIGURE 1.4: The schematic of the epifluorescence microscope.

through only those wavelengths in the absorption spectrum of the fluorescent dye [1–4, 11, 18, 20, 24].

Dichroic mirror Also known as a *dichroic beam splitter*. This is placed at a 45° angle and reflects the short-wavelength light filtered through the excitation filter at a 90° angle towards the specimen [1–3, 18] and allows the long-wavelength light from the fluorescing specimen to pass through to the detector [6, 20], thus serving as a separation filter between the absorption and emission light [4, 11].

Objective The incoming light reflected off the dichroic mirror passes through the objective lens before reaching the specimen [1–3, 20]. Emission light from the fluorescing specimen is gathered in the objective lens and passed through to the dichroic mirror.

Specimen The specimen is irradiated by the incoming light from the objective and emits long-wavelength light in all directions. The specimen is stained with a fluorophore whose absorption and emission curves are well known. This is important since the light source and the interference filters are chosen using the peaks of these curves.

Emission filter Also known as a *barrier filter* [1, 6, 20]. The light coming from the specimen contains multiple wavelengths and the dichroic mirror is used to filter out the shorter wavelength light. The emission filter is further used to filter out the wavelengths that correspond to the emission wavelengths of the fluorophore [2, 3, 10, 18, 24].

Detector The detector is used to capture the emission light and can further digitize the image. The detector is usually a photodetector such as a CCD (charge-coupled device) camera or a photomultiplier tube [1–3, 20, 25]. It is vital that an appropriate detector be chosen as this has direct impact on image quality [4].

The type of fluorescence image data that needs to be captured is application dependant and this impacts the decision on which type of microscope to use. The *widefield*, or conventional, microscope produces 2D image data. 3D image data cannot be captured directly. Instead, a series of 2D images are captured to form a 2D stack. The 3D image is then constructed in software. In this scenario, the most common choice of microscope is the *confocal laser scanning microscope* (CLSM). This microscope system is expensive and acquisition is slower. An economical alternative is the *confocal spinning disk microscope*. To detect single molecules, the favoured technique is *total internal reflection fluorescence* (TIRF) which can be achieved by a modification of the epifluorescence microscope.

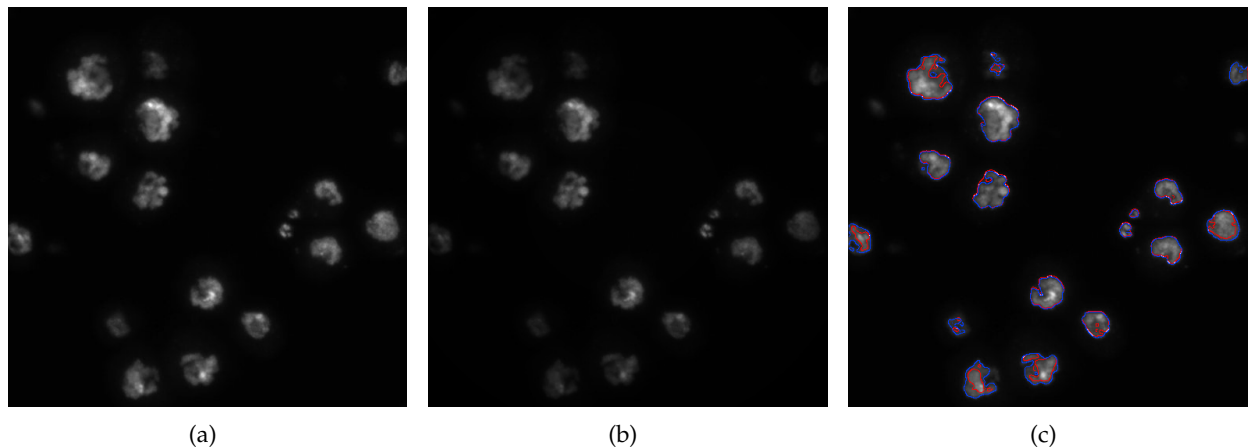


FIGURE 1.5: The effect of nonuniform illumination on segmentation. (a) Original image. Image source: The Cell Image Library [30]. (b) Nonuniformly illuminated image. The Vignette effect. (c) K-means clustering using the Euclidean distance metric and 2 clusters. The blue curve is from the original, the red curve is from the nonuniformly illuminated image. Notice that less of the object is recognised towards the edges.

1.4 Image Processing

Due to the physical nature of the fluorescence and image acquisition process, there are many factors that can degrade image quality. There are measures that can be taken to largely mitigate some problems but they can never be completely abated. The presence of these factors directly affect segmentation accuracy and subsequently higher level analysis. Therefore, images are processed prior to segmentation to suppress the artefacts and reconstruct the original data [2] or better yet enhance it. Chapter 3 takes a step in this vain. Here we present some of the commonly occurring factors that reduce image quality and the methods used to mitigate them, and some of the techniques employed for segmentation.

1.4.1 Preprocessing

Nonuniform illumination There are many factors that could contribute to nonuniform illumination. The specimen layer will not be uniformly lit if the arc lamp is not properly focussed on the black aperture. To prevent this from happening, a liquid light guide-based light source, which provide even illumination may be used [20]. If the light brightness diminished towards the edges of the image then this is known as the *Vignette effect*. Common techniques to suppress this distortion is *background correction*, also known as *flat-field correction*, *background flattening* or *shading correction* [2, 4, 25]. Other causes of nonuniform illumination are inhomogenous detector sensitivity, autofluorescence, dirt particles in the optical system or nonspecific sample staining. An example of the Vignette effect is illustrated in 1.5(b). Computational schemes to eliminate nonuniform illumination have been well researched, although recently it hasn't received too much attention [26–29].

Fading The reduction of emission intensity is called *fading*, of which there are two types: *quenching* and *bleaching*.

Quenching is a reversible loss of fluorescence owing to a variety of nonradiative energy-loss mechanisms such as collisions with nearby acceptor molecules, a phenomenon known as *resonance energy transfer*. This phenomenon is useful in studying molecular interactions below the lateral resolution of the light microscope through a technique called *fluorescence resonance energy transfer* (FRET) [1, 2, 20].

Bleaching refers to all processes that cause a fluorescent signal to fade permanently [20]. From the fluorescence process presented in Section 1.1, one may assume that, under the proper conditions,

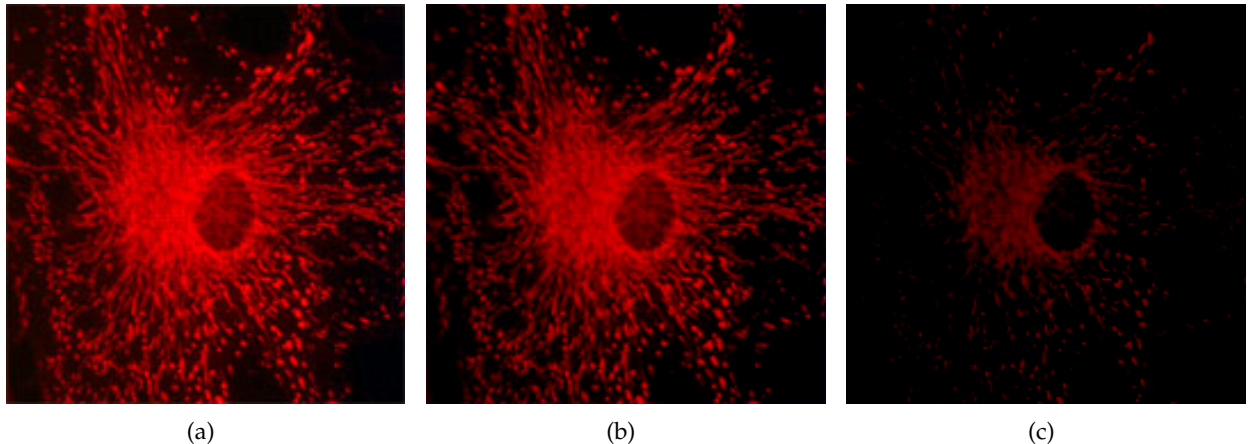


FIGURE 1.6: The effect of photobleaching. Image Source: Molecular Expressions [32]. **(a)** Original image at $t = 0\text{s}$. **(b)** Image after $t = 10\text{s}$. **(c)** Image after $t = 20\text{s}$.

a fluorochrome has the ability to fluoresce indefinitely. However, this is not the case. There is a limit number of cycles before permanent bleaching [20]. Figure 1.6 illustrates the effect of photobleaching. *Photobleaching* is the most prominent form of bleaching. It is due the interaction of the fluorophore with an oxygen molecule. This can move the oxygen molecule to an excited singlet state, which then becomes a reactive molecule. When in this state, the oxygen molecule can participate in many chemically destructive reaction with organic molecules causing *phototoxicity* [2]. Photobleaching is used to study diffusion and motion through a technique called *fluorescence recovery after photobleaching* (FRAP) [9, 20].

Photobleaching cannot be avoided but it can be pushed back. The aim in the measures to avoid photobleaching is to take a longer time to reach *reciprocity failure* [9]. This is done by shortening exposure times and using less intensive excitation light. This, however, yields low contrast images. These images with low signal-to-noise [25] ratio (SNR) are more difficult to segment hence contrast enhancement must be performed on the images prior to segmentation [31].

Image distortion The major contributing factors to image distortion are: The *point spread function* (PSF) and noise [8]. Image formation can be approximated by

$$O = n(s \otimes h), \quad (1.1)$$

where O is the formed image, n is the noise function, s is the exact image and h is the specific PSF of the optical system. We discuss the PSF first. The observed image isn't an exact representation of the real object. Optical systems have an inherent property called the point spread function which is the systems optical response to a point light source [2]. The final image is dependant on the spatial position of a point, numerical aperture (NA) and furthermore differs for various emission wavelengths [3, 33]. The final image is a superposition of all points in the illuminated volume where the contribution of each is described by the PSF.

Theoretically the exact image can be obtained by deconvolution of the observed image with the PSF. However, there are secondary factors that prevent this. Deconvolution seeks to reconstruct the original image given the PSF and certain assumptions about noise [33]. This is an *ill-posed problem* as little is known about the specific PSF or the noise model. Additionally, if the image is corrupted by too much of noise, deconvolution might still produce unsatisfactory results. The PSF is generally experimentally determined or theoretically modelled, and so the true PSF is never attained. Hence, the original image can never be attained by deconvolving with an approximated PSF. The image formation and restoration process is illustrated in Figure 1.7.

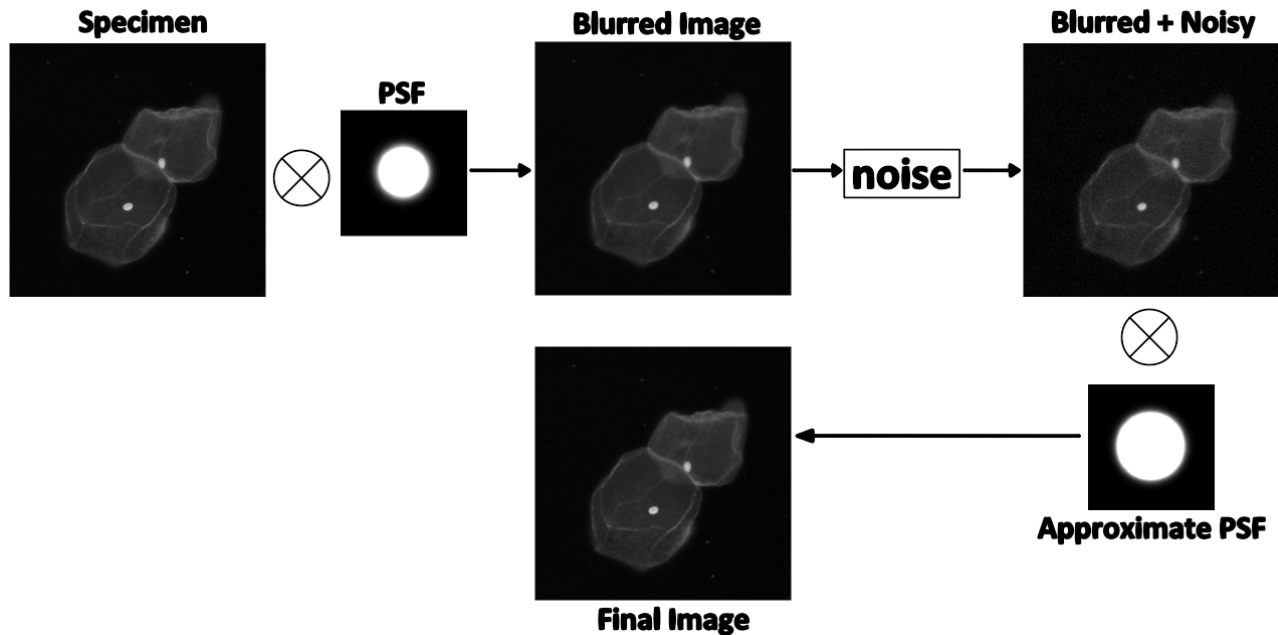


FIGURE 1.7: The image formation process. Image source: [34]

Deconvolution has received a lot of attention in the past with very creative approaches [35–39]. Fluorescence microscopy deconvolution is still a very active field of research. Bayesian methods have become popular in fluorescence microscopy image deconvolution, however noise in low SNR imaging conditions still poses a challenge [40]. Recent trends in 3D deconvolution in widefield microscopy use blind depth-invariant of the PSF [41]. Most PSF deconvolution systems naively assume depth-invariance however, the PSF changes significantly along the optical axis. There are also deconvolution methods that can preserve detail and possibly enhance image quality in diffraction-limited/superresolution imaging modalities [42].

Noise As previously stated, fluorescence imaging is a low light, low contrast and low SNR imaging technique to counter the effects of bleaching. For these reasons, noise becomes prominent. The three types of noise recorded by a camera are *dark noise*, *read noise* and *photon noise* [2, 3, 5, 11].

The electrons in a CCD or film are always in motion due to thermal energy. Dark current is due to the extraneous electrons which enter into the signal. This signal carries a statistical fluctuation known as dark noise. Dark current effects can be reduced by ground image subtraction or cooling the CCD. If there is a significant amount of dark noise then the background won't be as black as it should be. For this reason it is common to mistake dark noise for low-level autofluorescence [11, 43].

Read noise is a result of the conversion process from charge build-up to a voltage and then digitisation.

Photon noise, also known as *shot noise*, is the signal dependant statical variation of the counting of photons incident on the CCD or film. This is a naturally occurring phenomenon and cannot be reduced by camera design or system optimisation [43].

In low-light imaging techniques, such as is common in fluorescence imaging, the dominant form of noise is photon noise. Photon noise and dark noise are Poisson distributed [2, 43, 44]. Noise in low-light images used to be modelled using the Gaussian distribution but was found to be a poor description of the noise. The Poisson distribution provides a more physically accurate model especially in photon-limited recording [8]. We study denoising in Section 3.1.1. The effect of noise on segmentation accuracy is illustrated in Figure 1.8.

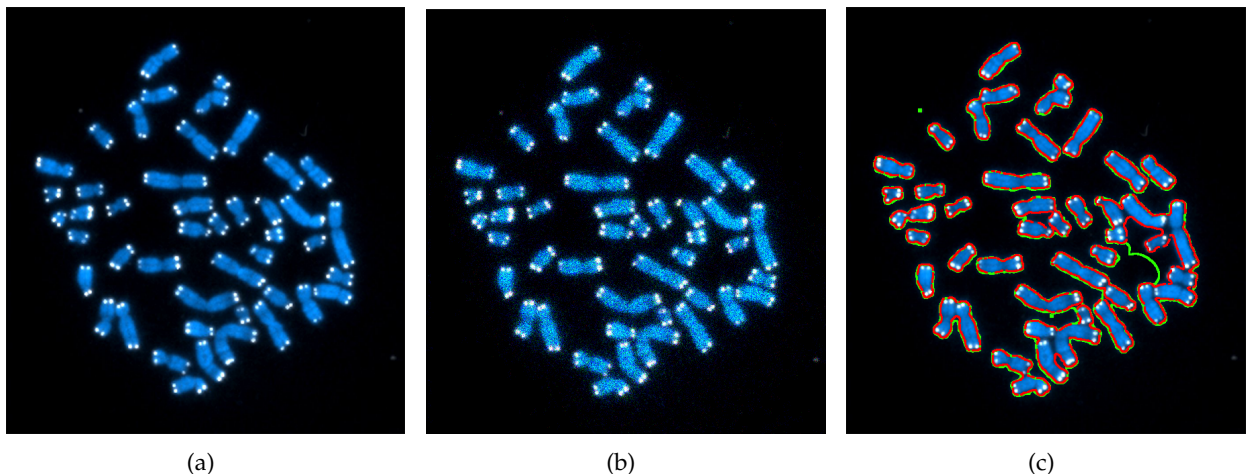


FIGURE 1.8: The effect of noise on segmentation. (a) Original image. (b) Poisson noise corrupted image. (c) ACWE Chan-Vese segmented output. The red curve is from the original, the green curve is from the Poisson noise corrupted image. Notice that there are more artifacts and the segmented output is less accurate especially towards the bottom left from the green curve.

1.4.2 Segmentation

The primary aim of using fluorescence microscopy imaging is to make diagnoses and to study molecular behaviour and interaction. This means that biologists, geneticists and other professionals alike, not only have a superabundance of microscopic imaging techniques at their disposal, but also have an immense amount of image data to analyse since the outburst of image acquisition technology. The abundance, diversity, dimensionality and complexity of fluorescence image data obviates manual image processing as this isn't tractable, by any means, in terms of time or quality [43, 45]. Consequently, the task has fallen to computers to perform these tasks and has now become of essential in advancing these fields [46, 47]. The crux of image analysis lies on the accuracy of image segmentation and has become the principle focus in many studies [48].

Anton van Leeuwenhoek, a Dutch draper and scientist, is credited with the invention of the first real compound microscope in the late 17th century. However, it wasn't until the mid-1950s that computers became involved when systems were developed to automate the classification of smears of exfoliated cells. These systems used simple thresholding rules on 1D scanning of microscopic lines [49]. In the 1960s, automated systems were developed to count leukocytes on 2D image data based on their colour and morphological measurements [50]. In the 1980s the invention of the confocal microscope made it possible to study cells in 3D but it wasn't until the 1990s that computer became powerful enough to process 3D image data or complex 2D images [51]. The trends of increased computing power has made possible the use of more sophisticated cell analysis techniques as well as the ability to use more computationally demanding segmentation methods. The literature on cell segmentation and analysis has experienced exponential growth in the last couple of decades. Many studies comparing segmentation algorithms for cells have been published [52–54]. We review some of the common techniques used in fluorescence microscopy image segmentation.

Intensity thresholding Intensity thresholding assumes a non-overlapping intensity levels between the objects and the background. It is still one of the most common thresholding methods for cell segmentation [55–57]. Locally adaptive thresholding techniques are used when illumination varies across the image. Automated threshold segmentation techniques are usually based on global or local intensity using the histogram [48]. Thresholding produces suboptimal results due to the naïve assumption of mutually exclusive intensity levels.

Morphological segmentation This method uses non-linear mathematical morphological operators like erosion, dilation, opening, closing, etc with geometrical and topological properties to segment the image [56, 58–61]. Generally, this method is used as a post-processing step to polish up coarse segmentation or a pre-processing step to suppress certain image structures [48].

Region accumulation This method starts with selected points, called seeds. The idea is to iteratively add points neighboring previously labelled pixels based on some conformity measure, usually intensity. The most common implementation is called *region growing*. Most cases assume an image model similar to that of thresholding and suffers the same segmented results problems. Another approach is called the *watershed method* which converts the image into an open 3D shape and "fills the shape with water". The different regions are separated by those "filled with water" and those that aren't. A common problem with this method is oversegmentation and usually requires post-processing methods, like *region merging*, to get a meaningful result [48, 62, 63].

Edge-based segmentation There are basically two types of edge-based segmentation: *gradient based methods* and *Laplacian based methods*.

Gradient methods are based on the assumption that there is a rapid intensity gradient between the object and the background. Edges are detected by searching for the maximum and minimum in the first derivative, e.g. Prewitt, Roberts and Sobel operators.

Laplacian methods search for zero-crossings in the second derivative, e.g. Marr-Hildreth, Laplacian of Gaussian (LoG), Canny edge detection.

These algorithms are very fast to compute but the drawback is when closed curves are desired [48], which is a common criterion in biological and molecular segmentation. A solution to this is to use snakes or active shape models.

Energy minimisation The most recent segmentation methods are based on energy minimisation. Most current state-of-the-art techniques fall under this category. This is due to their flexibility and robustness [2]. This group encompasses two main subgroups: *deformable models* and *discrete combinatorial optimisation*.

The aim of deformable model techniques is to fit a deformable model, either a curve or a surface, to the image data. They may be formulated either explicitly, as a parametric contour (2D) or a surface, e.g. snakes [64] or active contours [65–67], or implicitly as a zero-level of a function with one dimension higher than that of the image data, e.g. as a level set [68]. This technique widely used in fluorescence image segmentation [69–74].

The aim discrete combinatorial optimisation is to search a finite countable solution space for the optimal solution. Optimality is defined with respect to some energy function, which embeds one or more criteria, which is to be minimised. The most common implementation exploits the graph cut framework. Graph cut segmentation has recently gained a lot of popularity and momentum in medical image segmentation (MIS) [75–82].

Other miscellaneous techniques The techniques presented are just a select few in a plethora segmentation techniques that have been used in microscopy image segmentation. A few other common techniques are unsupervised clustering segmentation using the k-means [83–85], Otsu binarization [86], dynamic programming [87, 88], Voronoi diagrams [89, 90], gradient flow tracking [91], etc. This is just a few more. Instead of cell segmentation converging to a robust, flexible and unified solution, the number of available options is steadily increasing [45]. There probably exists as many individual unique solutions for cell segmentation as there are problems.

1.5 Object Measurement and Analysis

The aim in fluorescence image analysis is to measure specific properties of interest which enable higher level decision making. Typically, these properties are quantitative measures. In this section we

review some of the important quantitative measurements in digital image analysis. It is important to note that for some of the properties of interest, the accuracy of the measurements depend heavily on the accuracy on the segmentation. The properties of interest are application dependent, one might require just the object morphology of structure and hence properties like perimeter, area, shape, intensity, colour, etc are of significance. Alternatively, if one requires the colocalisation of cells, then distance discriminants, such as Euclidean distance, Manhattan distance, Chessboard distance, etc, are of significance [2, 92].

Object measures can be loosely classified into four categories: geometric measures, histogram-based measures, intensity based measures and temporal measures. One can also argue a fifth category statistical classifiers although this is generally used in higher level analysis.

Size measures Perimeter, area and volume are common measures to describe the size of objects. Area and volume are suitable measures to describe the general size of an object. The perimeter of an object is distinctly useful in discriminating its shape complexity. Complex and irregular shapes need a larger perimeter to enclose its area.

Pose measures This measure defines an object's location and orientation. The centroid is used as an object's locale and its orientation is the measure of the angle subtended by its major axis.

Shape measures Shape features are used to distinguish objects from one another. These measures are generally translationally, rotationally and scale invariant and can be used independent of, or in conjunction with, the size measures. Commonly assessed shape parameters are thinness ratio to describe the regularity of an object, rectangularity, circularity, Euler number, moments, central moments, object dispersion, rotationally invariant moments, Zernike moments and elongation.

Shape descriptors Shape descriptors provide a more wholesome way of describing an object's shape than compared to the single parameter shape measures. Differential chain codes, and its two most common descriptors boundary chain code (BCC) and differential chain code (DCC), are used to represent the distance around an object. Fourier descriptors is another object distance measure that exploits the periodicity of BCC. There are also graph representations of which the two most common are minimum spanning tree (MST) [93, 94] and Delaunay triangulation (DT) [95, 96].

Distance measures There are many ways to compute the separation between objects. The most commonly assessed distance measures are Euclidean distance, Manhattan distance (also known as the City-block distance or absolute value metric), which is a more computationally efficient approximation of Euclidean distance, and the Chessboard distance (also known as the maximum value metric) [97, 98].

Intensity measures Images are segmented generally into regions with low intra-region intensity distribution and high inter-region intensity distribution [56, 99]. Common intensity measures are integrated optical density (IOD) [100, 101], which is simply the sum of all the gray levels that compose the object, its a reflection of the object's "mass" or "weight", average optical density (AOD), is the IOD divided by the object's area, and contrast.

Histogram measures These measures provide a measure of an object's intensity distribution. Common histogram-based measures are mean, standard deviation, skew, entropy and energy [102, 103].

Texture measures In image analysis texture refers to the spatial arrangement of gray level values [104] and hence a texture feature quantifies some characteristic of the intensity variation within an object. Common texture measures are statistical texture measures, gray-level co-occurrence matrix (GLCM) [105, 106] and power spectrum features [107, 108].

Ratiometric measures Some fluorescent dye respond to the changes in Calcium and Hydrogen ion concentration by changing its spectral properties of the fluorescent emission bands. In this case, a ratio of the intensity can be used to calculate concentration of calcium or pH value [11].

Temporal measures Considering the time domain, many interesting properties can be observed. Commonly computed properties of interest are motility [109–111], like velocity and acceleration, rate of growth, rate of change of colour, etc.

These measures are used in higher decision making processes such as the evaluation of a hypothesis to detect the presence of a certain disease. They are also used to aid in the understanding of biological mechanisms, events and interactions [2].

Chapter 2

Mathematical Background

Image segmentation falls under the mathematical classification as being an *ill-posed inverse problem* [112, 113]. It is an inverse problem since we require a model from the observation, this simply means given the results, what are the causes. In image segmentation this translates to, given a 2D matrix of intensity values, which pixels belong to the object and which belong to the background. Image segmentation is also an ill-posed problem since there is a lack of uniqueness or stability of a solution [114], which are two of the three requirements for a solution to be *well-posed*, the other being existence. Image segmentation is an ill-posed because immense amount of information is suppressed in the acquisition process [115–117]. Many tasks in vision are inherently or can be reformulated as ill-posed inverse problems e.g. scene reconstruction, stereo matching, image restoration, image deconvolution, etc. Computer vision is used heavily in industry, medicine and life science fields included, hence there is a need for robust, environment-resistant approach. The *optimisation approach* is an elegant way to obtain a solution. In computer vision, a problem can be posed as an optimisation problem as follows: We are given a coarse, discrete and noisy, approximation of the visual data, d , we aim to infer some hidden quantities x , labels, depth, probable pixel intensity, etc, based on it. We then have to design an *objective function*, also known as an *energy function* or *cost function*,

$$E : (x, d) \rightarrow \mathbb{R}, \quad (2.1)$$

which has to be optimised such that the optimisation of the function provides a solution to the problem. $E(x, d)$ assigns an energy or a cost to each combination (x, d) of the input and hidden quantities. E provides a measure of goodness to how well the candidate solution x fits the expectation given the data d . In optimisation of this function we seek a minimum energy,

$$x^* = \arg \min_x E(x, d), \quad (2.2)$$

which has roots in Statistical Physics where lower energies correspond to more stable solutions. This gives us a general idea of how we should assign energies to solutions; better a solution, the lower an energy we should assign to it. In this case, a huge number of inference problems in vision can be solved by minimising the associated energy. A solution is only as good as the energy model and the optimisation technique. Once a precise energy and minimising algorithm are found, the problem is essentially solved [118].

Early attempts in computer vision would solve problems like these using iteration or relaxation methods [119, 120]. In these attempts the problems are solved in a Calculus of variations framework, this is still a popular approach to optimisation in vision since Poggio *et al.* [112] proposed an integrated framework to regularisation theory for vision [121]. Many important advancements in computer vision are proposals for a better energy, a better algorithm or both [118, 122–125]. In this thesis we focus on discrete energy optimisation using graph cuts for image segmentation.

Image segmentation falls under a broader category of problems known as *labelling problems*. The aim is to find the best label, foreground/object or background, for each pixel. In Section 2.1 we briefly discuss labelling problems and its formulation as an energy minimisation problem.

2.1 Labelling Problems

Among the many computer vision problems, image segmentation is the most easy to understand labelling problem. A labelling problem is simply assigning, to an observation, a label that most accurately explains it. An observation can be anything that we wish to classify e.g. pixels, features, salient points, depth measurement, etc. A label is a description of that observation. There are two types of labels: *semantic labelling* (person, car, tree, sky, face, eye, etc) or *pixel-wise labelling* (texture, shape, colour, background/object, etc) [118, 126].

To formulate a labelling problem we need a set of *cites*, intuitively known as observations, and a set of *labels*, a set of explanations. The goal is to find the best explanation given the observations. In computer vision, the observations, can be features, image segments, etc. However, they will typically represent pixels in an image with some natural structure or ordering. Let

$$\mathcal{P} = \{1, 2, \dots, n\}$$

be the set of n cites and

$$\mathcal{L} = \{l_1, l_2, \dots, l_k\}$$

be the set of k labels. A discrete labelling is a map $f : \mathcal{P} \rightarrow \mathcal{L}$ that assigns each discrete variable f_p one value from \mathcal{L} and $f = \{f_p\}_{p \in \mathcal{P}}$ which is known as a *configuration*. We are interested in binary segmentation, also known as *binarization*, which implies we have two explanations in our label set, $k = 2$. The labels of interest are the *background* and the *object*. Although the solution space is finite, it is very large and grows exponentially as the image size increases or as the number of labels increases. The number of possible configurations is given by $|\mathcal{L}|^{|\mathcal{P}|}$. Table 2.1 shows the largeness of the solution space even for very small images and a few labels. In practice, the image sizes used in Table 2.1 is too small, hence finding a solution is not easy. Most often, settling for an approximate solution is "good enough".

TABLE 2.1: The impact of the number of cites and labels on the solution space

Image (\mathcal{P})	Number of cites ($ \mathcal{P} $)	Number of labels ($ \mathcal{L} $)	Number of configurations $ \mathcal{L} ^{ \mathcal{P} }$
64×64	$2^{12} = 4096$	2	$2^{2^{12}} = 2^{4096} = n$
128×128	$2^{14} = 16384$	2	$2^{2^{14}} = 2^{16384} = n^4$
64×64	$2^{12} = 4096$	3	$3^{2^{12}} = 3^{4096} \approx n^{1.585}$

2.2 Maximum A Posteriori Estimation for Discrete Models

As previously mentioned, image segmentation is can be viewed as a labelling problem. The problem is the huge search space in which the solution exists, or possibly more than one. We need a metric that is able to appropriately weight a configuration f . *Random Fields* are able to provide a structured and yet flexible probabilistic framework for labelling problems. *Markov Random Fields* (MRFs) and *Conditional Random Fields* (CRFs) are mostly used in vision tasks. We focus on the discrete image representation provided by MRFs in which we can embed the properties of a desired segmentation solution. MRFs are pivotal in designing, weighting and structuring graphs, so we give a brief introduction into the concepts needed to understand the probabilistic make-up for graph cut image segmentation.

2.2.1 Markov Random Fields

A *random field* (RF) is a stochastic process where each random variable is indexed by a spatial variable [127, 128]. A random field model can be intuitively represented as an undirected graph $\mathcal{G}(\mathcal{V}_{RF}, \mathcal{E}_{RF})$ where $\mathcal{V}_{RF} = \{1, \dots, n\}$ is the set of sites which correspond to a random variable for each pixel in \mathcal{P} , \mathcal{E}_{RF} is the set of undirected edges which links the random variables. In vision, random variables which correspond to neighbouring or nearby pixels are linked. These links model interdependency and in images, nearby pixels exhibit a high degree of spatial correlation (similarity) [129]. Common connectivity arrangements in 2D images are 4- and 8-connectivity. Similarly, higher dimensional data can be represented using graph. For 3D images, common connectivity arrangements are 6- and 26-connectivity. Connectedness is illustrated in Figure 2.1 for 4-connectivity for 2D image data and 6-connectivity for 3D image data. In this thesis we are concerned with 2D images only. Two sites, p and q , are neighbours if edge $(p, q) \cup (q, p) \in \mathcal{E}_{RF}$. The set of neighbours of p are denoted \mathcal{N}_p . The RF associated with \mathcal{P} is denoted as $\mathbf{Y} = \{Y_p : p \in \mathcal{P}\}$, where each Y_p can be assigned one of k labels from \mathcal{L} . A 4-connected RF is illustrated in Figure 2.2. A *clique* c is a fully connected subgraph; it is defined as $\forall p, q \in c, p \in \mathcal{N}_q$ and $q \in \mathcal{N}_p$. In a clique, each site is connected to all other sites.

The joint event $\{Y_1 = y_1, \dots, Y_n = y_n\}$ where $y_p \in \mathcal{L}$ is called a *realisation* or *configuration* for the random field \mathbf{Y} . For readability we simplify the joint event notation to $\mathbf{Y} = \mathbf{y}$ where $\mathbf{y} = \{y_p : p \in \mathcal{P}\}$. The image segmentation problem is now in the form of an inference problem where the image \mathbf{x} is the observation of a hidden random field \mathbf{Y} and the solution is given by the *maximum a posteriori* (MAP), i.e. the solution is given by

$$\mathbf{y}^* = \arg \max_{\mathbf{y} \in \mathcal{Y}} \Pr(\mathbf{y} | \mathbf{x}), \quad (2.3)$$

where \mathcal{Y} denotes the set of all possible labellings. \mathbf{Y} is said to be a *Markov random field* (MRF) if:

$$\Pr(\mathbf{Y} = \mathbf{y}) > 0 \quad \forall \mathbf{y} \in \mathbf{Y}, \quad (\textit{Positivity}), \quad (2.4)$$

$$\Pr(Y_p = y_p | x_{\mathcal{P} \setminus \{p\}}) = \Pr(Y_p = y_p | y_{\mathcal{N}_p}) \quad \forall p \in \mathcal{P}, \quad (\textit{Markovianity}), \quad (2.5)$$

The positivity property constrains all configurations to have non-zero probability and is needed to ensure that the joint probability can be uniquely determined by the local conditional probabilities [130]. The Markovianity property states that a site is conditionally independent of all other sites given its neighbours.

MRFs are one of the most popular probabilistic modelling tools and was introduced to the computer vision community by Geman and Geman [131] and Besag [132]. MRFs allow us to model local contextual constraints, such as spatial interactions between pixels. According to Baye's rule, the posterior probability relation is:

$$\Pr(\mathbf{y} | \mathbf{x}) \propto \Pr(\mathbf{x} | \mathbf{y}) \Pr(\mathbf{y}), \quad (2.6)$$

$\Pr(\mathbf{x} | \mathbf{y})$ encapsulates the dependency of the labels on the observation, it is the likelihood of observing \mathbf{x} given \mathbf{y} . $\Pr(\mathbf{y})$ is the probability of that specific labelling among all labellings \mathcal{Y} . The joint distribution can be specified as a *Gibbs Random Field* (GRF) [133, 134]:

$$\Pr(x | y) = \frac{1}{Z} \prod_{c \in \mathcal{C}} \exp(-\Psi_c(\mathbf{x}_c)), \quad (2.7)$$

where \mathcal{C} is the set of cliques. 2.3(a) shows a simple MRF construction. This MRF contains cliques of order one and two, i.e. $\mathcal{C} = \{1, 2, \dots, 9, \{1, 2\}, \{1, 4\}, \dots, \{8, 9\}\}$. 2.3(b) shows a more densely connected MRF where there are cliques of order one, two and three, i.e. $\mathcal{C} = \{1, 2, \dots, 9, \{1, 2\}, \{1, 4\}, \{1, 5\}, \dots, \{5, 9\}\}$. However, cliques of orders higher than two are ignored for computational reasons. In Equation 2.7 the term $\Psi_c(\mathbf{x}_c)$ is known as a *potential function* for the clique c , where $\mathbf{x}_c = \{x_i, i \in c\}$. The constant

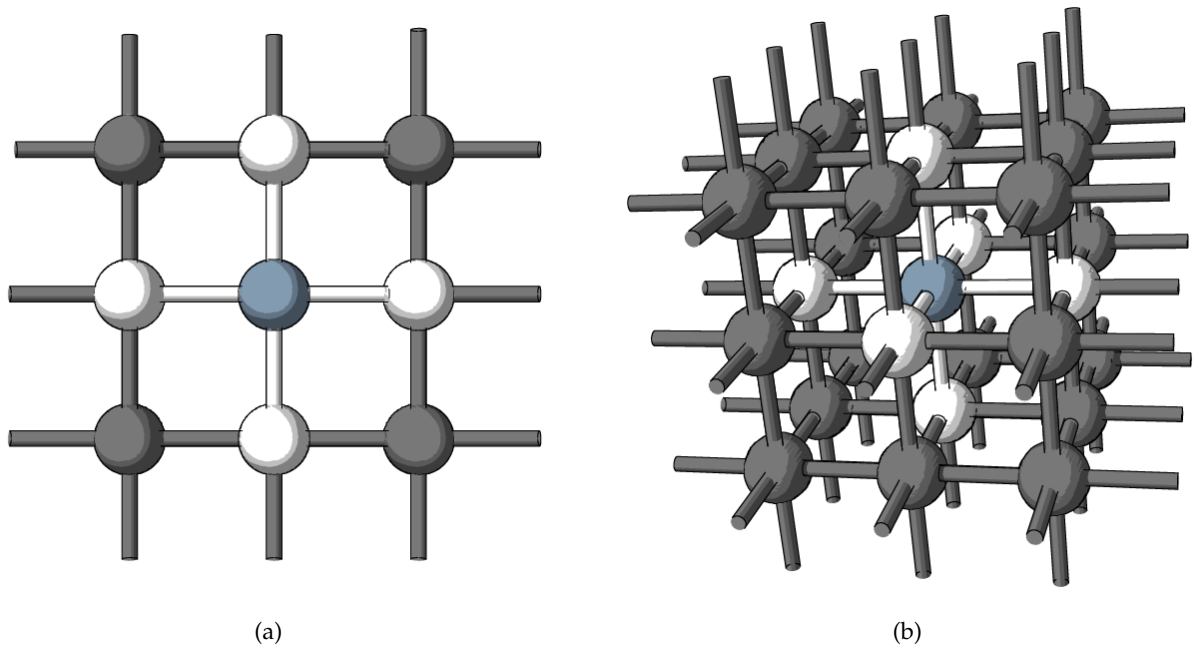


FIGURE 2.1: Common lattice structure for 2D and 3D image data. **(a)** Simplest connection of neighbouring pixels for 2D images. Each non-edge pixel is connected to 4 pixels. This is 4-connectedness. **(b)** Simplest connection of neighbouring voxels for 3D images. Each non-edge voxel is connected to 6 voxels. This is 6-connectedness.

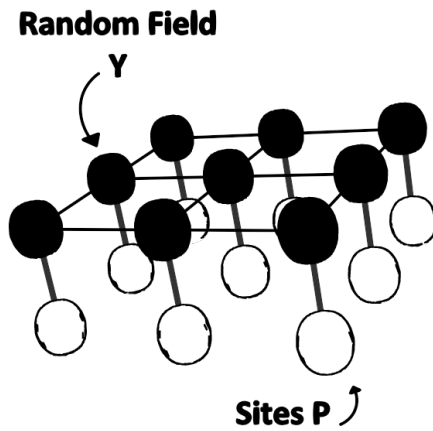


FIGURE 2.2: 4-connected random field \mathbf{Y} over the sites \mathcal{P} .

Z is called the *partition function* and ensures that the sum of all probabilities is one. After expanding Equation 2.7 for a maximum clique order of two, the conditional distribution of a pairwise MRF is:

$$\Pr(x|y) = \frac{1}{Z} \prod_{i \in \mathcal{V}} \exp(-\Psi_i(x_i)) \prod_{(i,j) \in \mathcal{E}} \exp(-\Psi_{ij}(x_i, x_j)), \quad (2.8)$$

where $\mathcal{V} = \{1, 2, \dots, n\}$ and \mathcal{E} is the set of pairwise edges, Ψ_i is the unary potential function, for first order cliques, and Ψ_{ij} is the pairwise potential function, for second order cliques.

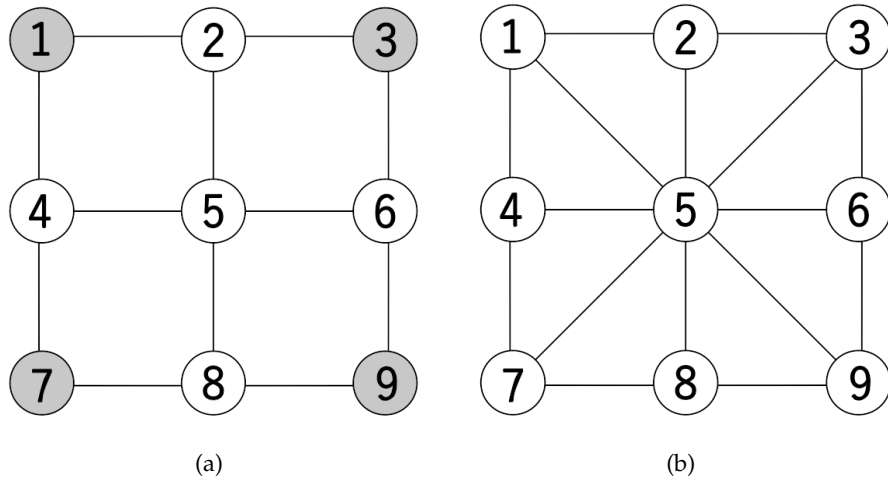


FIGURE 2.3: Caption. (a) Caption. (b) Caption.

2.2.2 MAP-MRF Estimation as Energy Minimisation

The equivalence of MRFs and GRFs, proven by Hammersley-Clifford theorem, means that maximising Equation 2.3 is equivalent to minimising Equation 2.2 [135]:

$$\mathbf{y}^* = \arg \max_{\mathbf{y} \in \mathcal{Y}} \Pr(\mathbf{y} | \mathbf{x}) = \arg \min_{\mathbf{y} \in \mathcal{Y}} E(\mathbf{y}, \mathbf{x}); \quad (2.9)$$

the most probable labelling yields the lowest energy. Obtaining the optimal labelling from Equation 2.9 does not guarantee that the segmented output will be good. The design of a good energy function, that captures all constraints and priors, is not easy. However, optimisation is harder still.

From Equation 2.7, if we take the negative log we get:

$$-\log(\Pr(x|y)) = \log(Z) + \sum_{i \in \mathcal{V}} \Psi(x_i) + \sum_{(i,j) \in \mathcal{E}} \Psi_{i,j}(x_i, x_j), \quad (2.10)$$

the constant Z is not needed as it does not affect the final labelling. In this form, the equation is a sum of potentials, i.e. a sum of energies. The first term encodes the data constraints, E_{data} , and the second term encodes the prior constraints, E_{prior} . In addition, there is a factor that controls the relative importance between the data and the prior, λ . The general form of the energy equation is:

$$E(f) = E_{data}(f) + \lambda E_{prior}(f), \quad (2.11)$$

where f is a particular labelling. The factor λ encodes our belief in the prior i.e. the larger λ is, the more we believe in the prior information. The data energy takes on the following form:

$$E_{data}(f) = \sum_{i \in \mathcal{V}} \Psi(x_i) = \sum_{p \in \mathcal{P}} D_p(f_p). \quad (2.12)$$

D_p measures the level of agreement between the label f_p and the pixel p . A common approximation is to assume independency observations, and this makes designing D_p relatively straightforward. The only restriction is $D_p(f_p) \in \mathbb{R}^+$. The prior energy takes on the following form:

$$E_{prior}(f) = \sum_{(i,j) \in \mathcal{E}} \Psi_{i,j}(x_i, x_j) = \sum_{\{p,q\} \in \mathcal{N}} V_{\{p,q\}}(f_p, f_q). \quad (2.13)$$

$V_{\{p,q\}}(f_p, f_q)$ is known as the *neighbourhood interaction function*. The aim of this function is to encourage neighbouring random variables to take on the same label, i.e. it penalises neighbouring pixels p and q if they have different labels. The form of $V_{\{p,q\}}(f_p, f_q)$ is application dependant and is more tricky to design. In image segmentation, the most common prior is that of smoothness, i.e intra-object pixel intensities are assumed to be the same or vary gradually within some range, it is at edges or boundaries where this assumption is violated. The general form in Equation 2.11 can be rewritten as:

$$E(f) = \sum_{p \in \mathcal{P}} D_p(f_p) + \lambda \sum_{\{p,q\} \in \mathcal{N}} V_{\{p,q\}}(f_p, f_q). \quad (2.14)$$

When we say MAP-MRF estimation we generally mean energy minimisation. Energy minimisation is a non-trivial task given the intractability of the search in the solution space. Energy minimisation can be categorised into *global energy minimisation* and *local energy minimisation*. We briefly discuss some of the energy minimisation techniques.

Iterated Conditional Modes (ICM) This is a deterministic method that converges to a local minimum [136]. It is a greedy technique that was introduced into vision by Besag [132, 137]. The algorithm iteratively chooses the label that results in the largest decrease in energy at each site until convergence. It is extremely sensitive to initialisation as the dimensionality of the space increases with non-convex energies.

Simulated Annealing This is a stochastic optimisation method that simulates the annealing of a material. It is one of the only general-purpose energy minimisation methods. It was developed and published independently by Černý [138] and Kirkpatrick *et al.* [139] and was introduced into computer vision by Geman and Geman [131]. The algorithm is initialised with a random labelling. Each pixel is then visited and a local random change is made. If the change results in a lower energy then it is accepted, else the change is accepted based on a probability parameter, i.e. the temperature. With certain cooling schedules the global minimum can be obtained however, this is horrendously slow in practise so sub-optimal schedules are used instead [131].

Genetic Algorithms (GAs) GAs have been successfully employed in energy minimisation for image segmentation [140–144]. GAs work by performing simultaneous local searches that optimise the energy function via a random walk in the search space. The algorithm terminates by choosing the search that found the lowest energy for the energy functional. Their drawback is their inability to guarantee a global optimum [145].

Gradient Descent Explicit differentiation under the Euler-Lagrange equations can be used to obtain a solution [145]. Each modified energy functional must be accompanied by derivation of obtaining a minimum [64, 65, 146, 147]. With an artificial time step, this algorithm deforms a shape, using the gradient descent process, which is equated to the set of Euler-Lagrange equations. When the deformable models come to rest the equations are satisfied. There are two common drawbacks with this method: Firstly, image noise can severely hinder the gradient descent process and this could lead to instability of the deformation process. Secondly, increasing the number of dependant variables increases the complexity of the search space and time to converge to an optimal solution as there are more derivatives to calculate [145].

Loopy Belief Propagation (LBP) The belief propagation algorithm was initially designed to be used on acyclic graphs where it able to obtain a global minimum [148]. However, the same algorithm has been successfully applied on cyclic graphs firstly for error-correcting code problems [149] and then later on in vision [150]. Convergence is not guaranteed as the algorithm might get stuck alternating between two labels [148].

Graph Cuts Graph cuts have become an indispensable tool in computer vision. For a restrictive class of energy functions, *submodular functions*, it is able to obtain a global minimum [151–154]. For non-submodular energy functions it is able to find approximate solutions with strong local optimality [122, 155–157]. Greig *et al.* was the first to use graph cuts in vision to find an exact solution to a certain energy function for the binary image restoration problem [158]. However, it did receive much attention and remained buried for almost ten years primarily because of the disinterest in binary image restoration and that, at the time, its optimisation was notoriously slow which made it an unappealing technique when compared to stochastic optimisation methods, like simulated annealing, which was popular at the time. In the last two decades graph cut optimisation has been a major focus as a key tool in optimisation since Roy and Cox [159] used it to solve more interesting problems in multi-camera stereo. Shortly after, Boykov *et al.* generalised the method for determining the MAP estimate of MRFs [160]. Graph cut optimisation is the technique of focus in this thesis.

2.3 Introduction to Graph Cuts

Graph cuts is a combinatorial optimisation method which can be used to minimise energies of the form presented in Equation 2.14. The aim of graph cuts is to partition a graph into mutual exclusive subgraphs by removing the edges whose sum of capacities is a minimum. We are interested with cutting the graph into two subgraphs. Graph cut algorithms existed long before their use was employed in vision, this is primarily due to the lack of computational power available at the time. Fortunately, computational power is no more as rare a resource as it was previously and this has paved a way into exploiting the power of graph data structures. As a result, this has also lead to vision-specific graph-cut algorithms. There are primarily three types of graph-cut algorithms: *Augmenting Path Algorithms*, such as Ford-Fulkerson algorithm [161], Dinic algorithm [162], Edmond-Karps algorithm [163] etc, *Preflow-Push Algorithms*, also known as *Push-Relabel* [164], and *Move-Making Algorithms* such as the α - β Swap [122], α -Expansion [122], etc.

2.3.1 Network Theory and the Min-cut Problem

In this section we briefly cover the foundation aspects to understanding graph cuts. We cover *Flow networks*, a branch of Graph Theory also known as *Transportation networks*, and introduce the *Min-cut problem*. For a solid understanding in Graph Theory and Flow Networks see [165–168]. A brief introduction is given in Appendix A.

Network A network $\mathbf{N} = (V, E)$ is a directed graph with a source node s , a sink node t and a strictly positive capacity on every edge. That is, for each edge $e \in E$, the capacity, $c(\cdot)$, obeys $c(e) \in \mathbb{R}^+$. The **source node** only has out-going edges, $d_{in}(s) = 0$ and $d_{out}(s) \geq 0$. The **sink node** only has incoming edges, $d_{in} \geq 0$ and $d_{out} = 0$. An example of a network is illustrated in Figure 2.4.

Flow A flow $f : V^2 \rightarrow \mathbb{R}^+$ is associated with each edge $e = (u, v)$ such that:

1. for each edge $e \in E$ we have $0 \leq f(e) \leq c(e)$. That is, the flow is positive and cannot exceed the capacity of the edge.
2. for each intermediate node $v \in V \setminus \{s, t\}$ the in- and out-flow of that node $\sum_{u \in V^-(v)} f(u, v) = \sum_{u \in V^+(v)} f(v, u)$.

The **total flow** F of a network is then what leaves the source s or reaches the sink t :

$$F(\mathbf{N}) := \sum_{u \in V} f(s, u) - \sum_{u \in V} f(u, s) = \sum_{u \in V} f(u, t) - \sum_{u \in V} f(t, u) \quad (2.15)$$

An example of a network with non-zero flow is illustrated in Figure 2.5.

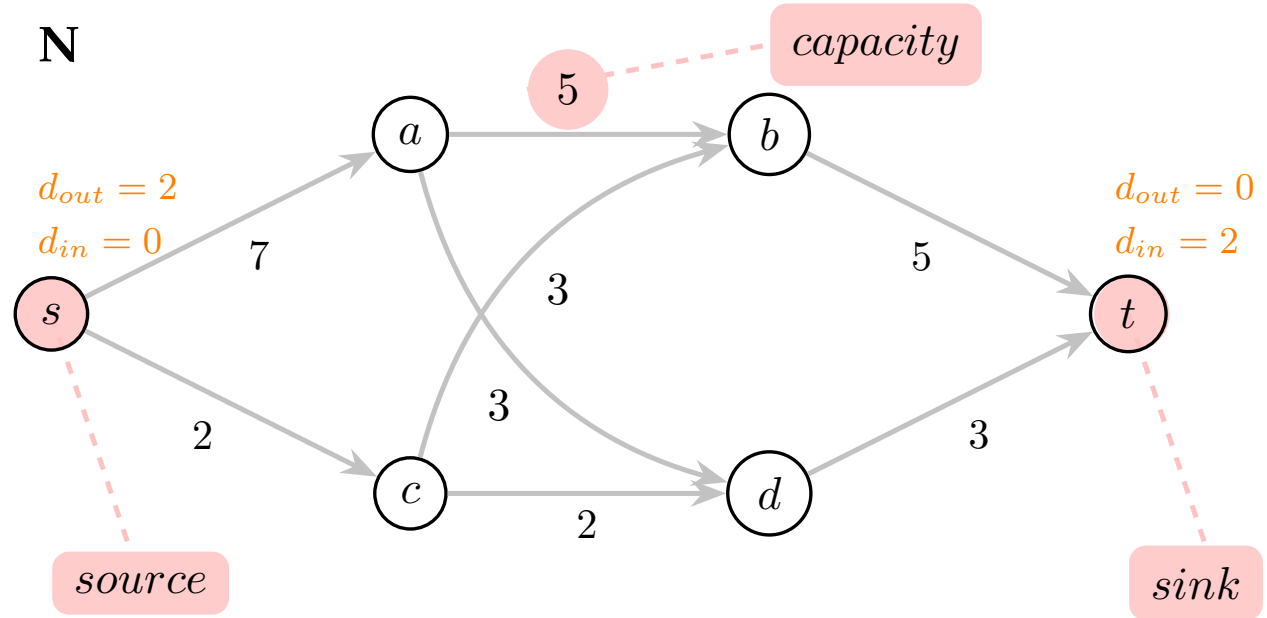


FIGURE 2.4: Network \mathbf{N} with no flow. The in-degree and out-degree for the source, s , and the sink, t , are shown next to the corresponding node.

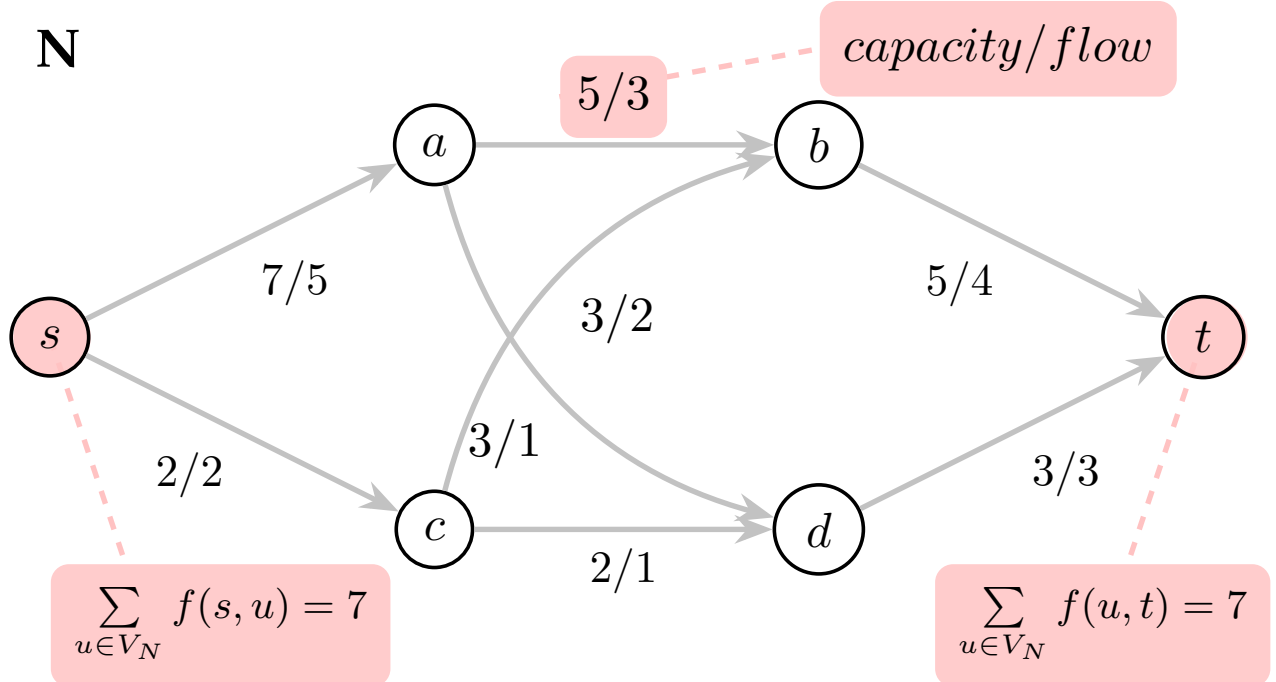
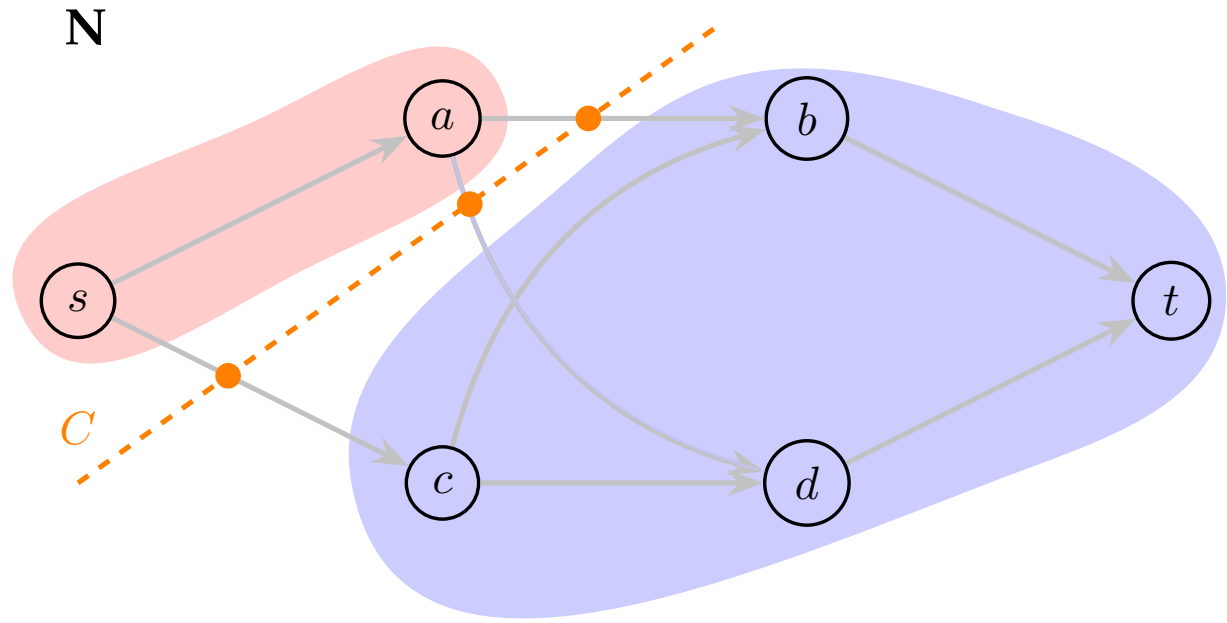


FIGURE 2.5: Network \mathbf{N} with flow. The flow out of the source node, s , is equal to the flow into the sink node, t . For all other nodes, the flow-in is equal to the flow-out. This is the conservation of flow principle. This is only part of the network. The remaining part is the residual graph which shows the amount of reverse flow is available on an edge.

Cut A cut of a network $\mathbf{N} = (V, E)$ is a partitioning of the vertex set $V = P \cup \bar{P}$ into two disjoint sets P containing the source node s and \bar{P} containing the sink node t . $P \cap \bar{P} = \emptyset$. The **cost** of a cut is the sum of the capacity of the edges $(u, v) \in V$ where $u \in P$ and $v \in \bar{P}$:

$$\kappa(P, \bar{P}) = \sum_{u \in P; v \in \bar{P}} c(u, v) \quad (2.16)$$

A network with a valid cut is illustrated in Figure 2.6. Invalid cuts are shown for the same network in Figure 2.7 and Figure 2.8.



$$S = \{s, a\}, \quad T = \{t, b, c, d\}, \quad C = \{(sc), (ab), (ad)\}$$

FIGURE 2.6: Network \mathbf{N} with a valid cut \mathbf{C} . The nodes within the red region are reachable from the source and the nodes within the blue region are able to reach the sink. The cut set, \mathbf{C} , is shown in the orange filled block.

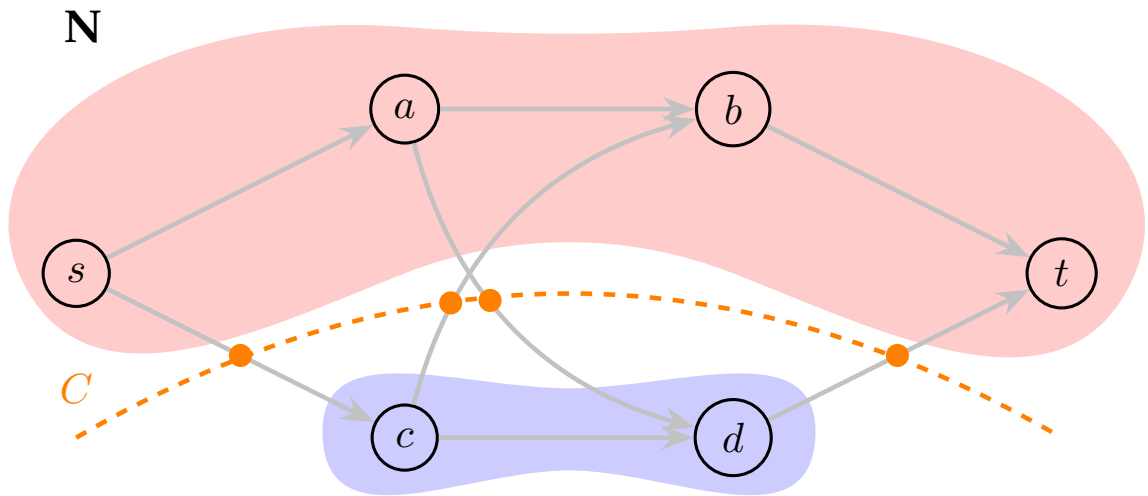


FIGURE 2.7: Network \mathbf{N} with an invalid cut \mathbf{C} . The cut does not partition source node s and sink node t into distinct sets.

Maximal Flow The largest amount of flow that is able to reach the sink from the source is known as the maximal flow. A network with a maximal flow, also known as a *max-flow*, is illustrated in Figure 2.9.

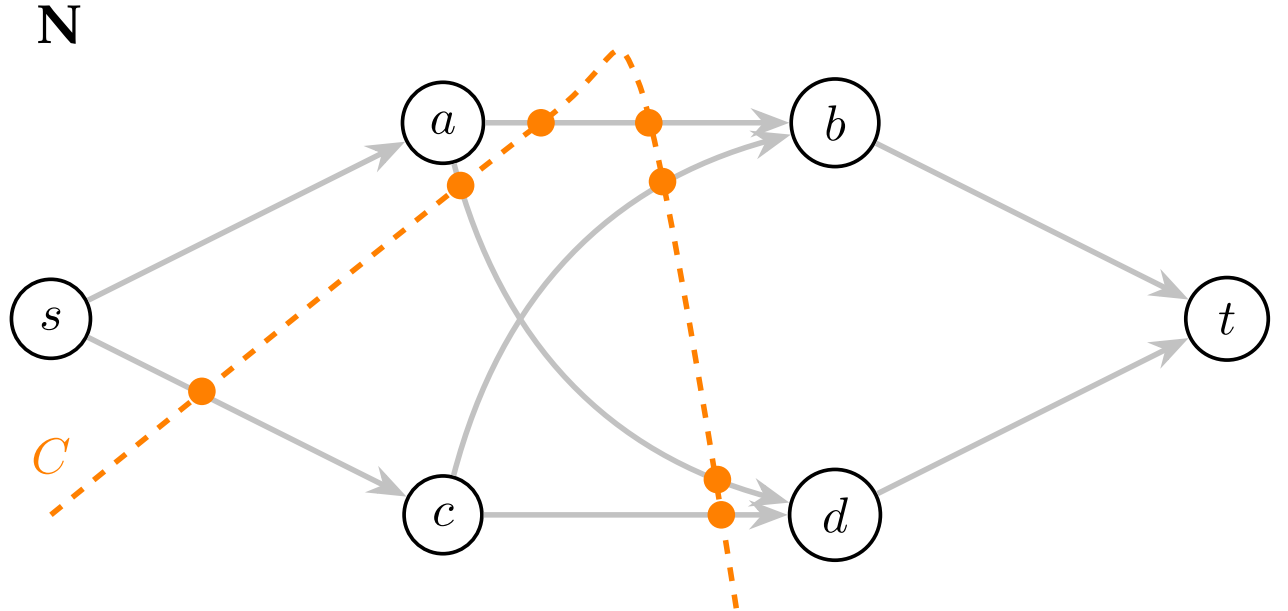


FIGURE 2.8: Network **N** with an invalid cut **C**. The cut partition partitions the graph into more than two sets and the cut intersects the edges ab and ad twice.

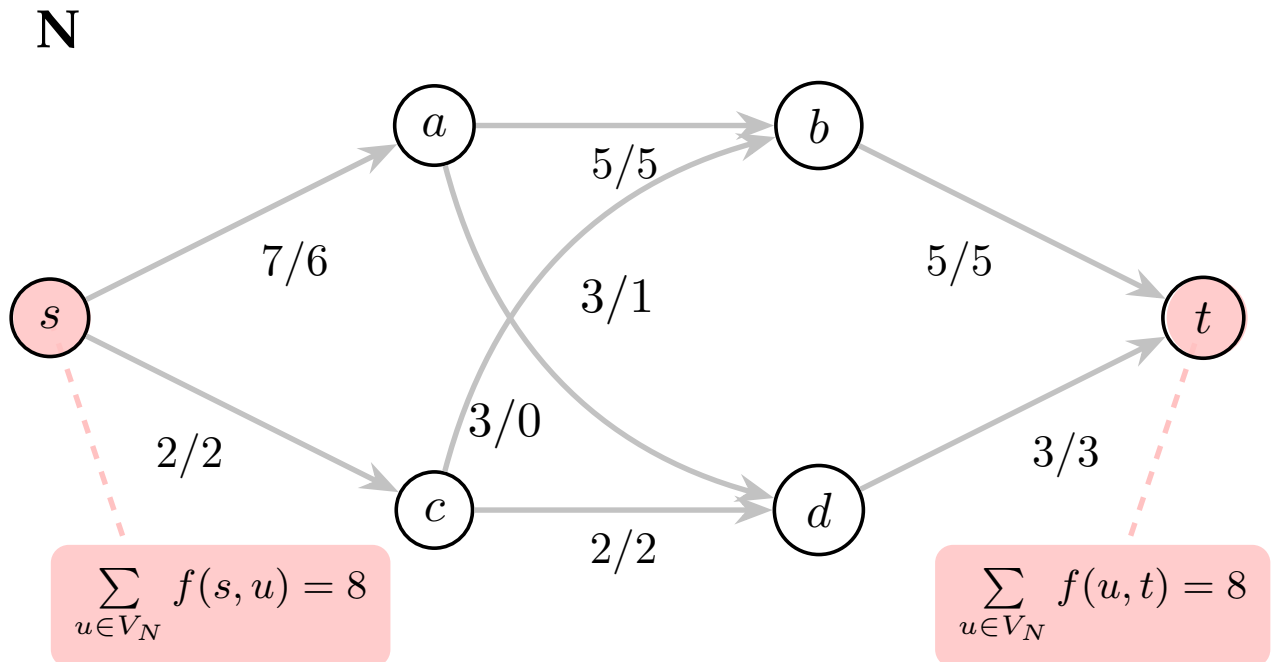


FIGURE 2.9: Network **N** with maximum flow. There is no way to push more flow out of the source into the sink without breaking the rules for the conservation of flow.

Minimal Cut A cut C on a network $\mathbf{N} = (V, E)$ is a minimal cut if there exists no other cut C' where $\kappa(C') < \kappa(C)$. A network with a minimal cut, also known as a *min-cut*, is illustrated in Figure 2.10.

In Figure 2.9 and Figure 2.10 the maximum flow and the minimum cut yield the same answer. This is not a coincidence, in fact the two problems are duals of each other, known as the *max-flow min-cut duality*. This was proven by P. Elias, A. Feinstein, and C.E. Shannon [169] and by Ford and Fulkerson [161] independently in 1956. This duality is immensely helpful in developing machine algorithms to compute the minimum, since it is easier to find a maximum flow. It is important to

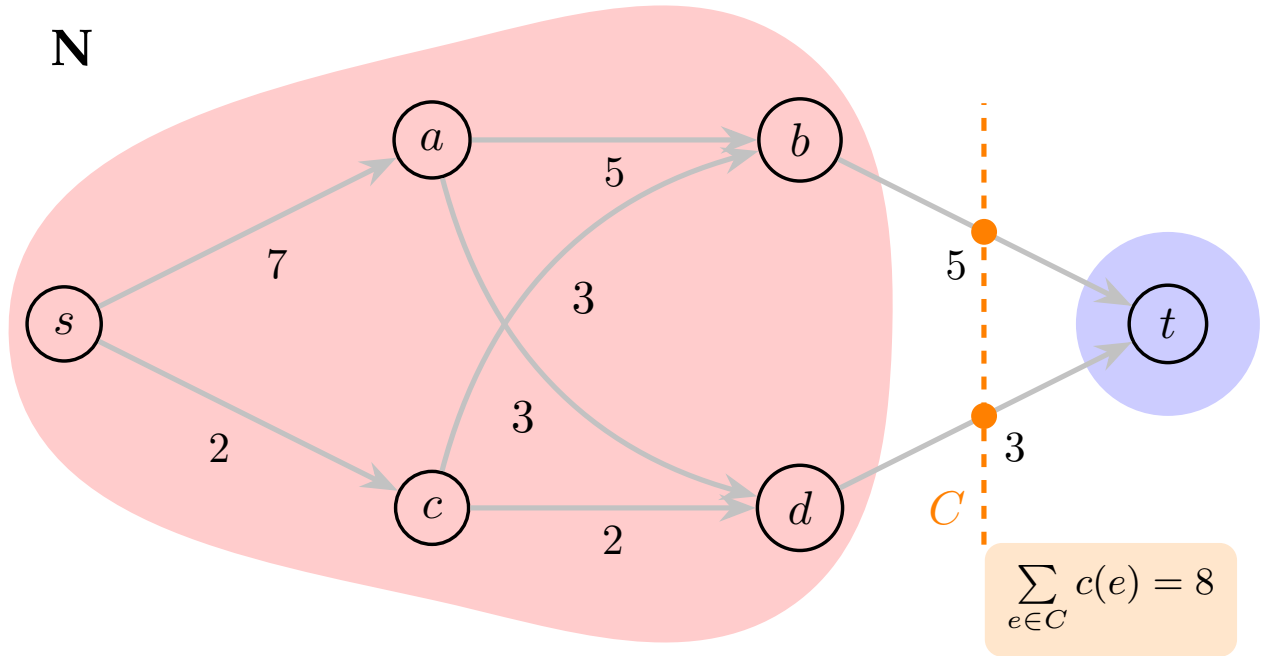


FIGURE 2.10: Network N with minimal cut C . The sum of the capacity of all the edges in the cut set is the minimum of all possible valid cuts on the network N .

realise that there maybe many cuts that can be minimum cut and many flow configurations that can yield the maximum flow, hence the solution is not guaranteed to be unique only an optimum.

2.3.2 Image Segmentation Graph Structure

In graph cut image segmentation the energy function, defined by the image, has to be represented as a graph, specifically a network. We now look at how 2D binary segmentation energy is constructed as a graph. The graph that is constructed uses the MRF, Section 2.2.1, model of the image as its base. Each pixel is a node in the graph. The connections between "pixel nodes" are bi-directional, which is generally decomposed into two uni-directional edges, and are known as *n-links* which is synonymous with *neighbour-links*. Additionally, each label is also represented as a node. Each "pixel node" is attached to all "label nodes". In binary segmentation, there are two labels i.e. object and background. The edges that connect "label nodes" to "pixel nodes" are called *t-links* which is synonymous with *terminal-links*. In keeping with network construction, one label will be the source and the other will be the sink. The t-link weights are generally learned from user input seeds or automatically generated seeds. Seeds mark which type of pixels belong to the object and which belong to the background, an illustration is shown in Figure 2.11(a). With the seed data and the neighbourhood interaction, we can construct a graph representation of the energy to be minimised over the image as illustrated in Figure 2.11(b). Once a graph has been constructed, we then call upon a max-flow/min-cut method which will minimise the energy function by partitioning the graph into two subgraphs, as shown in Figure 2.11(c). All pixels are classified according to which "label node" they're still attached to after the max-flow/min-cut algorithm has run, this is illustrated in Figure 2.11(d).

2.3.3 Submodular Functions

In the previous section we talked about representing the energy function as a graph. However, not all energy functions can be represented as a graph. Moreover, minimising an arbitrary energy function, even if the energy is binary, is NP-hard [170]. There does exist a class of functions which is graph

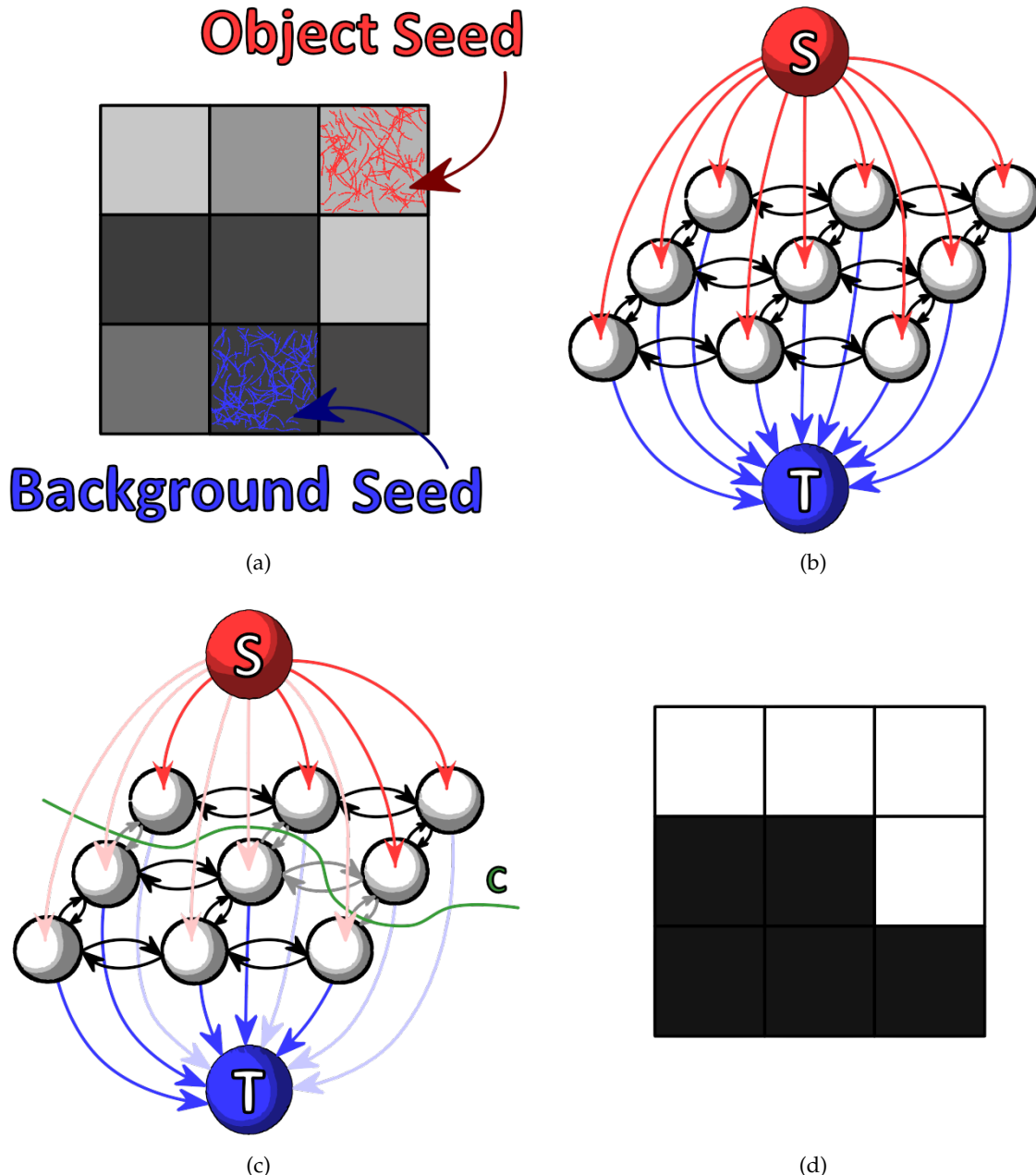


FIGURE 2.11: Overall process of the graph cut image segmentation process. **(a)** Image with object and background seeds. **(b)** Graph representation of the energy function to be minimised over the image. The n-links are represented by black arrows, the t-links from the source are shown in red, and the t-links to the sink are shown in blue. **(c)** Minimised energy function by cut C . The light red, light blue and grey edges are those that belong to the cut set C . **(d)** Segmentation mask after label assignment. In this case, all nodes that are still attached to the source, their corresponding pixel label is shown in white, similarly, nodes that are connected to the sink have their corresponding pixel labels shown in black.

representable and is able to be minimised in polynomial time, i.e. an exact global minimum can be obtained in a single graph cut. These energy functions are known as *submodular functions*. They are sometimes referred to as "discrete analog of convex functions" since they're the easiest to minimise, much like convex functions. For an energy to be submodular, it must satisfy the submodularity constraint:

$$f^p(a, b) + f^p(a+1, b+1) \leq f^p(a, b+l) + f^p(a+1, b), \quad \forall a, b \in \mathcal{L}, \quad (2.17)$$

where \mathcal{L} is an ordered label set. The type of energies we are concerned with are second order binary energies, and enforcing the submodularity constraint means that the energy function must to satisfy:

$$E_{ij}(0, 0) + E_{ij}(1, 1) \leq E_{ij}(0, 1) + E_{ij}(1, 0), \quad \forall \{i, j\} \in \mathcal{N}, \quad (2.18)$$

where $\mathcal{L} = \{0, 1\}$. It is necessary and sufficient for an energy function to satisfy Equation (2.18) to compute the exact global minimum in polynomial time in a single graph cut. This was first characterised by Kolomogorov and Zabih [151].

2.4 Graph Cut Algorithms for Energy Minimisation

Image segmentation via graph cuts can be seen as three main stages. Firstly the problem is modelled and a suitable energy function is designed. Generally, this is a trade-off between accuracy and constraining to the submodularity constraint. Secondly, a graph is constructed which represents the energy function. Thirdly, and finally, the energy function is minimised by using a max-flow/min-cut algorithm. In this section we discuss the last stage. The minimisation algorithms are either general or specific to the energy functions. We briefly discuss some of the most common max-flow algorithms.

2.4.1 Ford-Fulkerson

The Ford-Fulkerson max-flow algorithm [161] is designed to on an arbitrary network with one source and one sink. Ford and Fulkerson proved that the max-flow and min-cut problems are duals of each other, hence solving one means that you've obtained the solution to the other. Augmenting path algorithms iteratively search for open path from the source to the sink. When a path is found, the maximum flow that can be pushed in that path is pushed through that path by incrementing the flow on each edge of that path. The path is said to be *augmented*. If there are no available paths which can be augmented, the solution has been found and the algorithm terminates. The maximum flow is then obtained by the flow leaving the source or the flow entering the sink. A Ford-Fulkerson max-flow algorithm is shown in Algorithm 1. The min-cut, and segmentation, problem can be solved using Algorithm 2. In image segementation we only require the sets \mathcal{V}_S and \mathcal{V}_T , so the last step is not necessary. The Ford-Fulkerson algorithm exhibit very poor performance. The primary cause is that each new augmenting path has to be found from scratch. In [153], they countered this by reusing as much information as possible from the existing path.

2.4.2 Dinic/Edmonds-Karp

The Ford-Fulkerson max-flow algorithm is a very inefficient method to finding the max-flow. In practice the runtime is too high making it unfavourable. An improvement on this augmenting path based algorithm was designed by Dinic[162] in 1970 and independently by Edmonds and Karp[163] in 1972. The improvement is a change in searching for a path which can be augmented. The Edmonds-Karp algorithm finds the shortest path from the source to the sink by defining the lenght of all edges to be one and using a breadth first search form the source. The amount of flow to be augmented into each path is the minimal residual capacity of the edges in the path. This ensure that on each augmentation atleast one path is *saturated*. The edges that become saturated are said to be *critical*. The Edmonds-Karp max-flow algorithm is shown in Algorithm 3. The worst-case complexity is

Algorithm 1 Ford-Fulkerson Max-flow

```

1: procedure MAXFLOW( $G$ )                                ▷ The maximum flow on graph  $G$ 
2:   while  $p = \text{findPath}(s, t)$  do                      ▷ Find an open path  $p$  between  $s$  and  $t$ 
3:     if  $p = \emptyset$  then                                ▷ See if a solution has been found
4:       break
5:     end if

6:      $\text{maxflow}_p = 0$ 
7:     for each edge  $e \in p$  do                          ▷ Find max-flow on path  $p$ 
8:        $\text{maxflow}_p \leftarrow \min(\text{maxflow}_p, c(e) - f(e))$  ▷ Residual capacity on edge  $e$ 
9:     end for

10:    for each  $e \in p$  do                             ▷ Push max-flow on path  $p$ 
11:       $f(e) \leftarrow f(e) + \text{maxflow}_p$            ▷ Augment each path on path  $p$  with flow  $\text{maxflow}_p$ 
12:    end for
13:  end while
14: end procedure

```

Algorithm 2 Min-cut from Max-flow

```

1: Calculate max-flow on  $\mathcal{G}$ 
2: Partition  $\mathcal{V}$  into  $\mathcal{V}_S$  and  $\mathcal{V}_T$ 
3:  $\mathcal{C} = \{(u, v) \in \mathcal{E} \mid u \in \mathcal{V}_S \wedge v \in \mathcal{V}_T\}$ 

```

Algorithm 3 Edmonds-Karp Max-flow

```

1: procedure MAXFLOW( $G$ )                                ▷ The maximum flow on graph  $G$ 
2:   while  $p = \text{BFS}(s, t)$  do                      ▷ Find the shortest and open path  $p$  between  $s$  and  $t$ 
3:     if  $\text{length}(p) = 0$  then                            ▷ See if a solution has been found
4:       break
5:     end if

6:      $\text{minrescap}_p = \infty$ 
7:     for each edge  $e \in p$  do                          ▷ Find augmenting flow to saturate an edge
8:        $\text{minrescap}_p \leftarrow \min(\text{minrescap}_p, c(e) - f(e))$  ▷ Residual capacity on edge  $e$ 
9:     end for

10:    for each  $e \in p$  do                             ▷ Push flow on path  $p$ 
11:       $f(e) \leftarrow f(e) + \text{minrescap}_p$            ▷ Augment each edge with flow  $\text{minrescap}_p$ 
12:    end for
13:  end while
14: end procedure

```

$O(|\mathcal{V}|, |\mathcal{E}|^2)$. Depending on the graph structure other searching strategies may be more efficient, e.g. depth first search (DFS) [171], etc.

2.4.3 Push-Relabel

Originally developed by Andrew V. Goldberg and Robert E. Tarjan [164]. Previous algorithms, such as Ford-Fulkerson, used the concept of residual networks and augmenting paths to determine max-flow. Push-Relabel used the concept of preflow to determine max-flow instead of augmenting paths.

Sometimes referred as the *Preflow-Push Algorithm*. Preflow is a concept originally developed by A.V. Karzanov.

The algorithm works at converting a preflow, f , into a normal flow and then terminates. This flow also turns out to be the maximum flow. Goldberg and Tarjan defined a generic Push-Relabel algorithm which solves the maximum flow problem.

Preflow A preflow is a real-valued function, f , on vertex pairs. The total flow into a vertex can exceed the flow out of a vertex but not vice versa.

A preflow where all $v \in V - \{s, t\}$ has a flow excess of zero, $e_f(v) = 0$, is a normal flow. The preflow function is also referred to as the **s-t preflow**.

Preflow must satisfy:

1. Capacity Constraint

$$\forall u, v \in V, f(u, v) \leq c(u, v)$$

2. Antisymmetry/Skew Symmetry

$$\forall u, v \in V, f(u, v) = -f(v, u)$$

3. Nonnegative Constrain

The flow into $v \in V - \{s\}$ must be greater than or equal to the flow out of v . $\forall u \in V, v \in V - \{s\}, \sum f(u, v) > 0$

Flow Excess Flow excess, $e_f(v)$, is the net flow into v where $v \in V$ for some preflow f .

$$e_f(v) = \begin{cases} \infty & \text{if } v = s \\ \sum_{u \in V} f(u, v) & \text{if } v \in V - \{s\} \end{cases}$$

Active Vertex An active vertex/node is a vertex v which satisfies all of the properties:

1. Not a source or sink, $v \in V - \{s, t\}$

2. Positive flow excess, $e_f(v) > 0$

3. Has a valid label, $d(v) < \infty$

Push-Relabel also uses the concept of a residual graph, $G_f^* = (V, E_f)$.

Residual Capacity The residual capacity of a preflow is defined as $r_f(v, w) = c(v, w) - f(v, w)$.

Residual Edges The residual edges for a preflow f is defined as the set of edges with positive residual capacity. $E_f = \{(v, w)\} | r_f(v, w) > 0$.

Labelling Push-Relabel also use a valid labelling function, d , to determine which vertex pairs should be selected for the push operation.

A valid labelling, d , is a nonnegative integer function applied to all vertices to denote a label. The labelling is often referred as the height or distance from the sink node, t . This function is sometimes compared to the physical intuition that liquids naturally flow downhill.

A valid labelling for a preflow consists of:

1. For $v \in V, 0 \leq d(v) \leq \infty$

2. $d(s) = |V|$ (source condition)

3. $d(t) = 0$ (sink condition)

4. $d(v) = d(w) + 1$ for every residual edge $(v, w) \in E_f$

Algorithm 4 Push Operation

Input: Preflow f , labels d , and (v, w) where $v, w \in V$ **Output:** Preflow f **Applicable:** if $v \in V - \{s, t\}$, $d(v) < \infty$, $e_f(v) > 0$, $r_f(v, w) > 0$ and $d(v) = d(w) + 1$

```

1: procedure PUSH( $G, G^*, v, w$ )
2:    $\delta \leftarrow \min(e_f(v), r_f(v, w))$                                  $\triangleright$  Find the maximum flow can be pushed from  $v$ 
3:    $f_G(v, w) \leftarrow f(v, w) + \delta$                                  $\triangleright$  Push flow and update residual graph
4:    $f_{G^*}(w, v) \leftarrow f(w, v) - \delta$                              $\triangleright$  Update excess on  $G$  and its residual graph  $G^*$ 
5:    $e_G(v) \leftarrow e_f(v) - \delta$ 
6:    $e_{G^*}(w) \leftarrow e_f(w) + \delta$ 
7:   return  $\delta$ 
8: end procedure

```

A labelling d and a preflow f are said to be compatible if d adheres to the properties above.

The algorithm pushes flow excess starting at the source, s , along all vertices towards the sink, t . The algorithm maintains a compatible vertex labelling function, d , to the preflow, f . The labelling is used to determine where to push the flow excess. The algorithm repeatedly performs either a push or a relabel operation so long as there is an active vertex in G_f^* .

Push Operation The push operation is used to move flow from one vertex to another. The transfer of excess can be performed across the vertex pair $(v, w) \in E_f$ if:

1. v is an active vertex
2. the edge has positive residual capacity, $r_f(v, w) > 0$
3. the label distance $d(v) = d(w) + 1$

This allows the algorithm to move δ excess flow: $\delta = \min(e_f(v), r_f(v, w))$ from v to w . A push is considered *saturating* if no more flow can be sent over the edge, $\delta = r_f(v, w)$. A push is considered to be *non-saturating* if all the excess from v the push over the edge and the edge still has some capacity, $\delta = e_f(v)$. The push operation is shown in Algorithm 4.

Relabel Operation The relabel operation is used to increase the label value of a single active vertex so that excess flow can be pushed out of the active vertex. The relabel operation is performed when all the residual edges of the active vertex have positive residual capacity, $r_f(v, w) > 0$. This implies that v 's label is less than or equal to all vertices, $d(v) \leq d(w)$, meaning that no push operation across the edges is possible given the push condition $d(v) = d(w) + 1$.

The relabel operation for some vertex v selects the smallest label for the vertices with positive residual edges, $r_f(v, w) > 0$. The active vertex is then assigned the smallest label value +1 such that $d(v) := \min\{d(v) + 1 | (v, w) \in E_f\}$. This will allow the vertex v to potentially push its excess flow to atleast one of the other vertices during the algorithm's next iteration. The relabel operation is shown in Algorithm 5.

Discharge Operation The coordination of pushing excess flow from and relabelling a vertex is handled in a discharge operation. The idea is to push as much excess flow, from the currently picked active vertex, to its neighbours. If no more flow can be pushed but the node is still active then relabel it. The discharge operation is shown in Algorithm 6.

Algorithm 5 Relabel Operation

Input: Preflow f , labels d , and $v \in V - \{s, t\}$ **Output:** Labels d **Applicable:** if $v \in V - \{s, t\}$, $d(v) < \infty$, $e_f(v) > 0$, and $\forall w \in V, r_f(v, w) > 0$ which implies $d(v) \leq d(w)$

```

1: procedure RELABEL( $v$ )
2:    $d(v) \leftarrow \infty$ 
3:   for each vertex  $w \in \mathcal{N}_v$  do                                 $\triangleright$  Consider all the neighbours of  $v$ 
4:     if  $\{(v, w) \in E_f\} \neq 0$  then                                 $\triangleright$  Is  $w$  reachable from  $v$ 
5:        $d(v) \leftarrow \min(d(v), d(w) + 1)$ 
6:     end if
7:   end for
8:   return  $d$ 
9: end procedure

```

Algorithm 6 Discharge Operation

Input: $v \in V - \{s, t\}$ **Output:** State of node**Applicable:** if $v \in V - \{s, t\}$, $d(v) < \infty$, $e_f(v) > 0$

```

1: procedure DISCHARGE( $v$ )
2:    $i \leftarrow v.current\_neighbour$                                  $\triangleright$  index of the current neighbour under consideration
3:   while  $(e(v) > 0) \wedge (i < \text{size}(v.neighbour))$  do           $\triangleright$   $neighbour$  is the list of neighbours
4:     if  $(d(v) == d(v.neighbour[i]) + 1) \wedge (r_f(v, v.neighbour[i]) > 0)$  then
5:       push( $v, v.neighbour[i]$ )
6:        $i \leftarrow (i + 1)$ 
7:     end if
8:     if  $e(v) > 0$  then
9:       relabel( $v$ )
10:    end if
11:     $v.current\_neighbour \leftarrow i$                                  $\triangleright$  Pick up from this neighbour on the next discharge
12:    return  $e(v) > 0$                                                $\triangleright$  Is node still active
13:   end while
14: end procedure

```

The algorithm also maintains a list of active nodes to discharge. The complete Push-Relabel algorithm is shown in Algorithm 7. The algorithm repeatedly pushes flow between nodes until there are no more active nodes.

There are many variations of the push-relabel algorithm [164, 172]. Most of these are heuristic implementations to reduce execution time. One such heuristic is the *First-in First-out* (FIFO) [164]. With this implementation the theoretical run-time is shown to be $O(|V|^3)$. Cubic complexities are unacceptable in practice, however in practice this heuristic displays a great boost in speed optimisation. Empirical runtime over theoretical runtime is accepted in practice.

Instead of discharging nodes in the order that they entered the *Active_node* list, a better heuristic is to discharge nodes in descending order of node level/height. This heuristic is known as *Highest level first* (HLF). Flow is pushed from higher level nodes to lower level nodes first. This allows a greater dissipation of flow.

Another popular heuristic is *Global relabel*. In this heuristic, all nodes are periodically labelled from the distance of the node to the sink. This can be done by running a BFS from the sink node t in the residual graph G^* . When used in conjunction with the FIFO heuristic, there's a huge performance speedup. The Global relabel heuristic is expensive to perform so it is only run after every $|V|$ relabel

Algorithm 7 Push-Relabel Maxflow Algorithm

Input: $\mathcal{G} = (\mathcal{V}, \mathcal{E})$ **Output:** Maximum flow, f

```

1: procedure MAXFLOW( $\mathcal{G}$ )
2:    $d(s) \leftarrow |\mathcal{V}|$                                  $\triangleright$  Initilise the height of all nodes
3:    $d(t) \leftarrow 0$ 
4:   for  $\forall v \in \mathcal{V} - \{s, t\}$  do
5:      $d(v) \leftarrow 0$ 
6:   end for
7:   for  $\forall v \in \mathcal{N}_s$  do                                 $\triangleright$  Saturate all outgoing edges from the source
8:      $d(v) \leftarrow 1$ 
9:      $f_G(s, v) \leftarrow c(\text{edge}(s, v))$ 
10:     $f_{G^*}(v, s) \leftarrow -c(\text{edge}(s, v))$ 
11:     $e_G(s) \leftarrow -c(\text{edge}(s, v))$ 
12:     $e_G(v) \leftarrow c(\text{edge}(s, v))$ 
13:    Append  $v$  to Active_node                                 $\triangleright$  Build the active node list
14:  end for
15:  while  $\text{size}(\text{Active\_node}) > 0$  do                 $\triangleright$  While there are active nodes, discharge them
16:     $\text{current\_node} \leftarrow \text{pop\_front}(\text{Active\_node})$        $\triangleright$  Get the first active node
17:     $\text{state} \leftarrow \text{discharge}(\text{current\_node})$ 
18:    if  $\text{state} == \text{ACTIVE}$  then           $\triangleright$  If node is still active then put it at the end of the list
19:       $\text{push}(\text{Active\_node}, \text{current\_node})$ 
20:    end if
21:  end while
22:  return  $e(t)$                                  $\triangleright$  Final flow is equal to the flow entering the sink node
23: end procedure

```

operations.

The final heuristic we discuss is known as the *Gap relabel*. This heuristic is based on an important observation, nodes can only push to other nodes that are one level lower. Hence, if there are no nodes of a certain level, d , then it is not possible for higher nodes, at level $d + 1$, to send their flow to the nodes at the next lowest level, $d - 1$, hence this gap in the levels allows us to relabel all nodes that are higher than level d to $|\mathcal{V}|$. These relabelled nodes will no more be considered in further push or relabel operations. When the max-flow is determined, graph partitioning can be easily obtained. All nodes that are equal to or higher than the source are part of the source set, i.e $\mathcal{V}_S = \{v \in \mathcal{V} | d(v) \geq |\mathcal{V}|\}$ and $\mathcal{V}_T = \mathcal{V} - \mathcal{V}_S$.

2.4.4 Move Making Algorithms

Modern move making algorithms based on combinatorial graph cuts outperform previous move making methods, such as simulated annealing and ICM, as well as message passing algorithms because of their increased accuracy and efficiency [173]. Specifically, the α -expansion and $\alpha\beta$ -swap [122] has become very popular and gained a large acceptance in the vision community [174].

In the α -expansion, the algorithm iteratively makes the move to expand the α -label set. The label that provides the largest decrease in energy for all labels is kept. When no further label changes can be made, then the algorithm has reached convergence and terminates. In the $\alpha\beta$ -swap, the algorithm iteratively chooses two pixel sets with labels α and β and swaps the labels of the pixels within these sets. The swap between the pair of labels that results in the largest decrease in energy is chosen. Similarly, when no more swap moves can be made, the algorithm has reached convergence and

terminates. For binary segmentation, both of these algorithms require just one iteration to reach convergence and the optimal move is determined by using graph cuts.

Chapter 3

Pre-Processing and Post-Processing Scheme for Fluorescence Microscopy Images

Fluorescence microscopy has become an indispensable tool [5] in myriad of scientific disciplines such as chemistry, biology, neurobiology and medicine to name a few. It gives scientists visual access to physiological processes and other cellular and sub-cellular activities. Fluorescence microscopy coupled with the tremendous technological advancement of image acquisition has lead to an explosion of raw image data such that the sheer volume of images acquired presents too much of a burden on manual analysis [5]. Consequently, there is a need for highly accurate automated analysis. In such image analysis, image segmentation has established itself as a key process in identifying and extracting objects of interest which can thereafter be used in higher level image analysis. The ever increasing demand on image segmentation is to extract the objects of interest with greater accuracy in a shorter time.

There are many factors that degrade the quality of fluorescence images and these can result in sub-optimal segmentations. These factors have been studied independently to a great deal and have been successfully applied to real-world data. Some of these problems are poor contrast, photo-bleaching, a not black enough background, non-fluorescence of samples, improper excitation, etc.

Literature is rich with techniques that are able to, a high degree, negate the effect of these factors [175–177]. There is, however, a lack of definition of a scheme prior to segmentation that prepares an image such that accurate segmentation can be achieved.

The task of defining a set of criteria an image has to meet for reliable segmentation results is not a trivial one. However, there are some basic notions that an image can be tuned towards which would present a better image for the purpose of segmentation. Image enhancement on the original image can be done to facilitate higher level analysis e.g. contrast enhancement. This paper aims to design a hybrid algorithm that builds on highly successful algorithms to produce better results. The process emphasises

1. Noise reduction
2. Object data enhancement
3. Edge completion and enhancement
4. Reduction of intra-region variance

3.1 Preprocessing Scheme

3.1.1 Denoising

Removing useless channels Many segmentation algorithms are designed to work on gray scale images. If we have a colour image it is first converted to gray scale. Through the advancements in

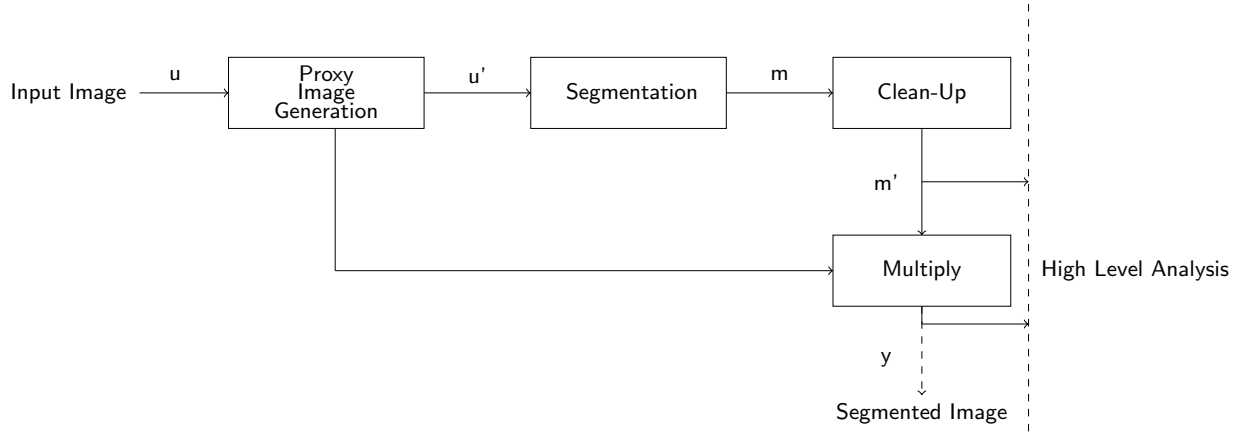


FIGURE 3.1: Segmentation Scheme.

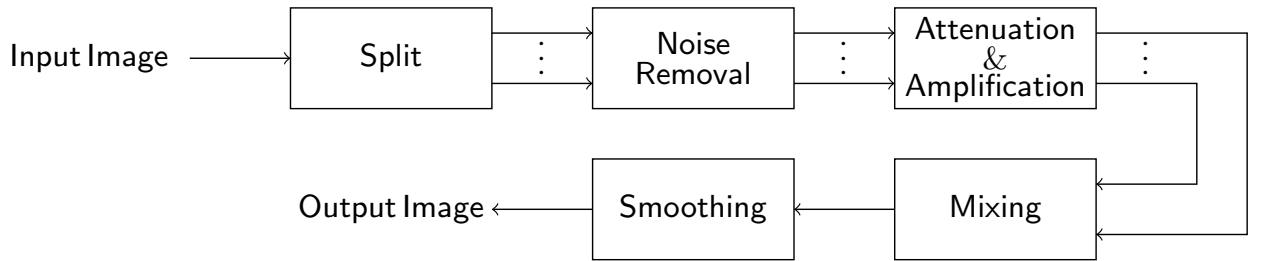


FIGURE 3.2: Proxy image generation.

optical engineering it is now possible for fluorescence images to be obtained in colour, however not all channels add object data to the image. They in fact degrade the image due to the noise in that channel. Often enough, these redundant channels will just be "data-less and noisy", so eliminating this channel will provide a huge improvement for segmentation purposes.

Poisson Noise Reduction In Section 3.1.1 and Section 1.4 we mentioned that the primary form of noise in fluorescent images is Poisson noise. It is important to remove as much noise as possible without dampening the boundary information. To this end we've used the Total-Variation anisotropic denoising (Bregman Split). Although it was developed to remove Gaussian noise, it was shown by Rodriguez *et al.*[178] that it supersedes other state-of-the-art Poisson noise removal methods, e.g. wavelets [179], platelets[180], minimum description length [181], while maintaining signal integrity.

The Poisson distribution, which has equal mean and standard deviation i.e. $\mu = \sigma$, is defined by

$$P(n, \mu) = \frac{e^{-\mu} \mu^n}{n!} \quad (3.1)$$

Let $y = \{y_i : i = 1, \dots, N\}$ and $x = \{x_i : i = 1, \dots, N\}$ be the observed and the true image, respectively. The sample y_i is a Poisson contaminated form of x_i . We desire to recover the signal x from the observed signal y . From Bayes' Law we get

$$P(x|y) = \frac{P(y|x)P(x)}{P(y)} \quad (3.2)$$

Therefore, we wish to find the maximum of $P(y|x)P(x)$. If all samples are affected by Poisson noise we have

$$P(y|x) = P(y, x) = \frac{e^{-x_i} x_i^{y_i}}{y_i!} \quad (3.3)$$

Thus the likelihood of observing y given the true image x is given by

$$P(y|x) = \prod_{i=1}^N \frac{e^{-x_i} x_i^{y_i}}{y_i!} \quad (3.4)$$

In anisotropic TV denoising we wish to recover the original image given the noisy image by minimising the constrained problem

$$\min_u \left\| \frac{du}{dx} \right\|_1 + \left\| \frac{du}{dy} \right\|_1 + \frac{\mu}{2} \|u - f\|_2^2 \quad (3.5)$$

where $\mu > 0$ is the regularisation parameter which affects the balance between noise removal and signal preservation [182], u is the true image and f is the noisy image. We actually solve the unconstrained problem

$$\min_{u,dx,dy} \|dx\|_1 + \|dy\|_1 + \frac{\mu}{2} \|u - f\|_2^2 + \frac{\lambda}{2} \|dx - u_x\|_2^2 + \frac{\lambda}{2} \|dy - u_y\|_2^2 \quad (3.6)$$

This can be solved using the Bregman Split algorithm [183]. The algorithm is run iteratively until the error, $e = \frac{|u' - u|}{|u|}$ where u' is the image obtained after denoising the input image u , is less than a user-defined tolerance factor, ϵ .

3.1.2 Separation under Intensity

The fundamental principle underlying binary image segmentation is to split-up an image into regions, where regions that are labelled l_0 share similar values with regard to the feature under consideration. This also means that there is high dissimilarity with the regions that are labelled l_1 . For grayscale images, such as the type we are concerned with, this feature is generally intensity. With respect to segmentation with regard a feature, an ideal image is one where there isn't an overlap in the feature space between the background and the object, as illustrated in Figure 3.3. In real images (non-synthetic) this is almost never the case as there is no known feature space or it does not exist.

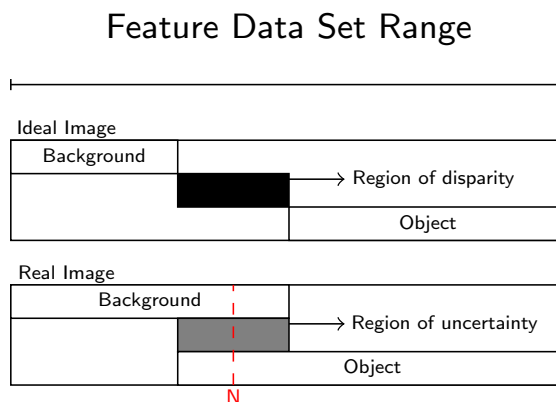


FIGURE 3.3: Feature data set.

Grayscale medical image segmentation typically uses intensity as the dominant feature on which the applied segmentation algorithms are biased. Hence, it is common to precede segmentation by contrast enhancement [184, 185]. The problem here lies with the fact that the aim contrast enhancement is to bring out the details more clearly that are otherwise obscured due to limited dynamic range, non-uniform illumination, etc. In fluorescence image this does not necessarily mean that the enhanced image possesses better segmentation qualities, in terms of intensity.

In this section we present a novel mapping function whose aim is to shrink the "region of uncertainty" by non-linearly widening the gap between background pixels and object pixels. This function is composed of two piecewise sub-functions; one for data attenuation and one for data amplification. We first design the properties the mapping function should have.

Remapping Function Properties The remap function is denoted as $\tilde{x}_i = R(x_i)$, where \tilde{x}_i is the new value which remaps the input pixel, x_i , using the function R . The range on which R works is $[0, L]$, where 0 and L represent the lowest and highest values a pixel can take respectively. For 8-bit gray scale images the highest value is usually $L = 255$. Let the value that represents the greatest classification uncertainty be denoted N , as illustrated in Figure 3.3.

1. *R must be non-decreasing in the interval $[0, L]$*

This is a trivial criterion arising from the context in which our problem is defined. We are specifically focussing on non-inverted fluorescence images therefore the background will ideally be black. Consequently, it is not possible for a lower intensity pixel to have a higher probability of belonging to the object compared to a pixel of a higher gray level intensity.

2. *$\tilde{x}_i = R(x_i = N) = N$*

This value has no bias as to whether it tends more to the background or the object. It is best left unaltered.

3. *Attenuation: $\tilde{x}_i < x_i, \forall x_i < N$*

R must remap gray-level intensities below N , according to $0 \leq \tilde{x}_i \leq x_i$.

4. *Amplification: $\tilde{x}_i > x_i, \forall x_i > N$*

R must remap gray-level intensities above N , according to $x_i \leq \tilde{x}_i \leq L$.

5. *R' must be non-decreasing in the interval $[0, N]$*

Given two pixels, p_1 and p_2 , with values x_1 and x_2 respectively where $x_1 < x_2$. It is more probable for p_2 to belong to the object since it has a higher value. Also, pixels with gray levels intensities closer 0 do not need to be attenuated as much.

6. *R' must be non-increasing in the interval $[N, L]$*

As the pixels values approach L , less amplification is needed since the pixels are already more likely to be classified as belonging to the object.

Function Design Many functions can be designed given the criteria presented. We have decided that one of the better solutions is to make the mapping function a piece-wise quadratic Bezier curve. The motivation for this is its appeal in easy and intuitive tuning of the sub-functions. The two functions are R_{att} , for the attenuation section, and R_{amp} , for the amplification section as shown in Figure 3.4.

There are three anchor points the function must pass through. These are $p_0(0, 0)$, $p_2(N, N)$ and $p_4(L, L)$. If the curve between p_0 and p_2 is a straight line and if the curve between p_2 and p_4 is a straight line then there is no change between the output and input image since the gradient of the line segments are equal and equal to 1. Additional control points are needed to bend the curve. There is a particular class of curves whose shapes are useful for our purpose. This places constraints on the position of the control points. Relative to the straight line, $y = x$, $x \in [0, L]$, the amplification curve would be above the relaxed line, $p_{3y} > p_{3x}$, and similarly the attenuation curve would be below the

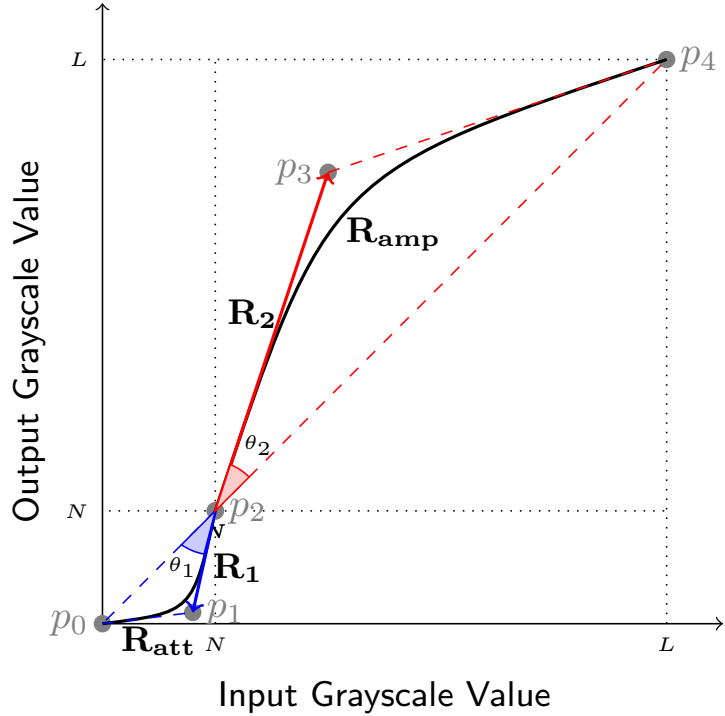


FIGURE 3.4: Plot of remapping function.

line, $p_{1y} < p_{1x}$. Also, given that the function is to be a one-to-one function, the control point for the attenuation function $p_{1x} < N$; similarly the control point for the amplification function $p_{3x} > N$.

The controls points in the Cartesian representation don't say much about the amount of tension in the curve. A more useful representation is to represent the control point implicitly as an angular deviation of the straight line and a magnitude, $p_c(R_c, \theta_c)$. Where $\theta_c \in [0, \frac{\pi}{4}]$ and $R_c \in \mathbb{R}^+$. The angular deviation is the measure off the straight line which is counter-clockwise for the amplification function and clockwise for the attenuation function. The deviation, θ_c , where $c \in 1, 2$, away from the straight line is further implicitly represented as a range $\kappa_c \in [0, 1]$ where $\kappa_c = 0$ implies $\theta_c = 0$ would mean no deviation, and $\kappa_c = 1$ implies $\theta_c = \frac{\pi}{4}$ would mean maximum deviation. The only real advantage in defining the function this way is that the parameters are more geometrically correlated to the curve. As the curve approaches the ends of it domain, less attenuation/amplification occurs, which meets criterions 5 and 6.

The position of the attenuation control point is calculated as

$$p_1 = \left(p_{2x} - R_1 \cos\left[\frac{\pi}{4}(1 + \kappa_1)\right], p_{2y} - R_1 \sin\left[\frac{\pi}{4}(1 + \kappa_1)\right] \right)$$

Similarly, the position of the amplification control point, as shown in Figure 3.5, can be calculated as

$$p_3 = \left(p_{2x} + R_2 \cos\left[\frac{\pi}{4}(1 + \kappa_2)\right], p_{2y} + R_2 \sin\left[\frac{\pi}{4}(1 + \kappa_2)\right] \right)$$

The piecewise functions that define the curve are given by

$$R_{att}(t) = \sum_{i=0}^2 p_i J_i^n \quad (3.7)$$

$$R_{amp}(t) = \sum_{i=2}^4 p_i J_i^n \quad (3.8)$$

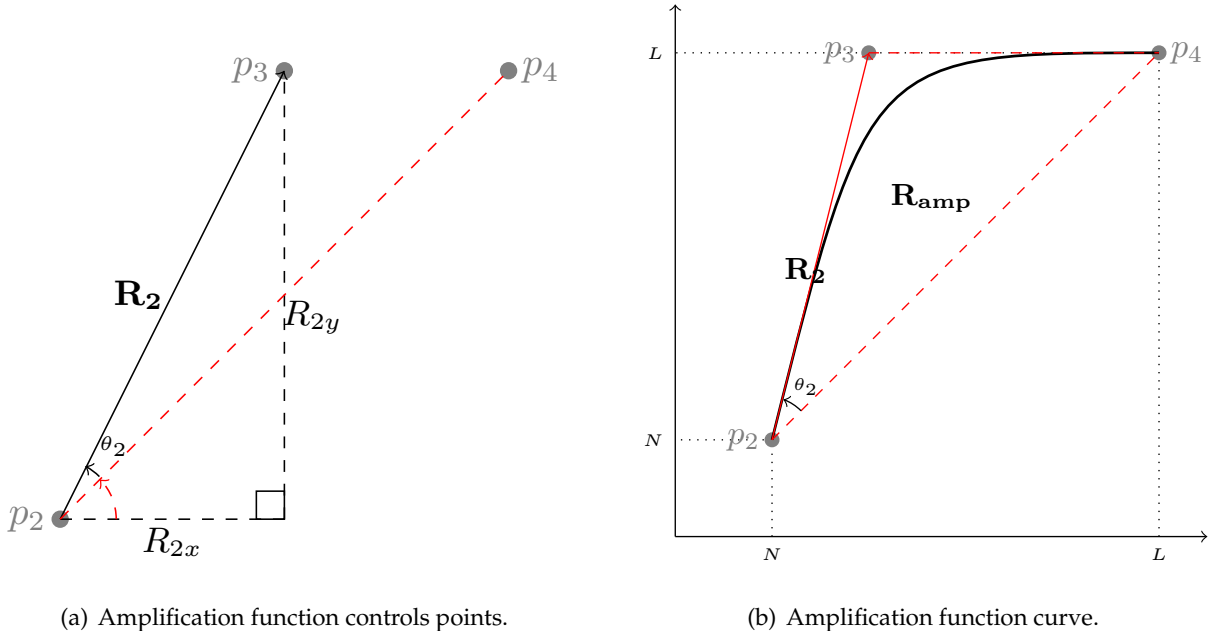


FIGURE 3.5: Amplification function control points and curve.

Where J_i^n is the Bernstein basis function, defined as

$$J_i^n = \binom{n}{i} t^i (1-t)^{n-i}, \quad t \in [0, 1] \quad (3.9)$$

For each input gray level intensity $x \in [0, L]$ we require corresponding output gray level intensity $y \in [0, L]$. The curve is expressed as a parametrisation with respect to t for each of its x and y parameters. For a curve defined by three control points q_0, q_1 and q_2 where $q_0 < q_1 < q_2$, the equation for the curve determined by these points is the quadratic bezier given by

$$R = \sum_{i=0}^2 q_i J_i^n \quad (3.10)$$

For a quadratic bezier curve, this simplifies to

$$\begin{aligned} R &= q_0(1-t)^2 + 2q_1(1-t)t + q_2t^2 \\ 0 &= (q_0 - 2q_1 + q_2)t^2 + (-2q_0 + 2q_1)t + (q_0 - R) \end{aligned}$$

Therefore for the parametric function R_x , we require the set of values of t for which $R_x \in [q_{0x}, q_{2x}]$. The value of t for a given R_x is determined by the solution to the quadratic equation.

Let $a = q_{0x} - 2q_{1x} + q_{2x}$, $b = -2q_{0x} + 2q_{1x}$, and $c = q_{0x} - R_x$.

It is seen that $b > 0$, since $q_{1x} > q_{0x}$, and $c \leq 0$, since $R_x \geq q_{0x}$.

Rewrite a as $a = (q_{0x} - q_{1x}) + (q_{2x} - q_{1x})$. For the case of a , there are two cases.

1. For $q_{1x} \in [q_{0x}, \frac{q_{2x}-q_{0x}}{2}]$, $a > 0$.

In this case $-4ac > 0$ hence $\sqrt{b^2 - 4ac} > b$.

\therefore the only value of t which is positive and must be the solution is given by

$$t = \frac{(q_{1x} - q_{0x}) + \sqrt{R_x(q_{0x} - 2q_{1x} + q_{2x}) + (q_{1x}^2 - q_{0x}q_{2x})}}{q_{0x} - 2q_{1x} + q_{2x}} \quad (3.11)$$

2. For $q_{1x} > \frac{q_{2x} - q_{0x}}{2}$, $a < 0$.

It is known that a real solution exists. This means that

$$\begin{aligned} b^2 - 4ac &\geq 0 \\ b^2 &\geq 4ac \\ \Rightarrow \sqrt{b^2 - 4ac} &< b \end{aligned}$$

\therefore the only value of t which is positive and must be the solution is given by

$$t = \frac{(q_{1x} - q_{0x}) + \sqrt{R_x(q_{0x} - 2q_{1x} + q_{2x}) + (q_{1x}^2 - q_{0x}q_{2x})}}{q_{0x} - 2q_{1x} + q_{2x}} \quad (3.12)$$

In both cases the solution to t can be calculated using the same formula. It is possible for the remapping function to exceed the range, in this case any value that maps to a value higher than the maximum value will be assigned the maximum value i.e. $\tilde{x}_i = \min(R(x_i), L)$, $x_i \in (N, L]$; similarly any value that maps to a value lower than the minimum value will be assigned the minimum value i.e. $\tilde{x}_i = \max(R(x_i), 0)$, $x_i \in [0, N)$.

Function Properties and Constraints This function presents several properties within the constraints defined as follows:

1. The curves obey the convex hull property. The sub-functions will always be contained within the control polygon determined by the control points [186, 187].
2. No attenuation when $\kappa_1 = 0$ and no amplification when $\kappa_2 = 0$.
3. R is continuous in $x_i \in [0, L]$.
4. R , is weakly monotonically increasing in $x_i \in [0, L]$.
5. R'_{att} , is monotonically increasing in $x \in [0, N]$.
6. R'_{amp} , is monotonically decreasing in $x \in [N, L]$.
7. The ends of the curve are coincident with the first and last control points of the control polygon.
8. The direction of the tangent vectors from the end points of the curve are the same as the direction of the vector anchored at the control point and along the line that joins the end point and the centre control point of the control polygon [186, 187].

3.1.3 Channel Mixing

To reconstitute an image from the updated channels we perform channel mixing. In an equi-weighted mixing system, each channel contributes equally to the mixed-down image. This simplistic method of channel mixing does not always produce the best image. A consequence of equi-weighted mixing is that some channels might become very suppressed and may be disregarded by the segmentation algorithm. Hence, it is necessary to assign weights which are channel dependant. These weightings must sum to one, $\sum_{i \in C} w_i = 1$, where C is the set of channels to be mixed-down. The mixed-down image is then calculated as $y = \sum_{i \in C} w_i C_i$, where C_i is channel i . Channels with very low gray level values are given a greater weight.

3.1.4 Intra-Region Smoothing and Edge Completion and Enhancement

One of the criteria which is used in identifying an image is that objects tend to have little intra-region variance. It is common for fluorescence images to be plagued with various degrees of lighting and contrast even within objects. This is primarily due to improper excitation, non-fluorescence of particles and ubiquitous measurement errors during acquisition. In some cases it is easy to visualise the completed edge of the object by joining the disconnected edge components where the extension is along the direction of the edge. We used a coherence enhancing diffusion filter with optimised rotational invariance (CED-ORI) presented in [188–190], which very successfully reduces intra-region variance and joins closely-disconnected edges.

The diffusion works by evolving the image, u , over a time using n discrete time steps, t , called the diffusion time. The evolution equation is defined as:

$$\frac{\partial u}{\partial t} = \nabla \cdot (D \nabla u) \quad (3.13)$$

where $D = \begin{pmatrix} a & b \\ b & c \end{pmatrix}$ is the diffusion tensor which can be adapted to the local image structure measure known as the structure tensor. The structure tensor is given by:

$$J_\rho(\nabla u_\sigma) = G_\rho * (\nabla u_\sigma \nabla u_\sigma^T) \quad (3.14)$$

Where G_ρ is the Gaussian kernel with standard deviation ρ , and $u_\sigma := G_\sigma * u$ where G_σ is the Gaussian kernel with standard deviation σ . The eigenvalues of $J_\rho = \begin{pmatrix} J_{11} & J_{12} \\ J_{12} & J_{22} \end{pmatrix}$ are

$$\mu_1 = \frac{1}{2} \left(J_{11} + J_{22} + \sqrt{(J_{11} - J_{22})^2 + 4J_{12}^2} \right) \quad (3.15)$$

$$\mu_2 = \frac{1}{2} \left(J_{11} + J_{22} - \sqrt{(J_{11} - J_{22})^2 + 4J_{12}^2} \right) \quad (3.16)$$

Where the normalised first eigenvector satisfies

$$\begin{pmatrix} \cos\alpha \\ \sin\alpha \end{pmatrix} \parallel \begin{pmatrix} 2J_{12} \\ J_{22} - J_{11} + \sqrt{(J_{11} - J_{22})^2 + 4J_{12}^2} \end{pmatrix} \quad (3.17)$$

The diffusion tensor's, D , eigenvectors are obtained from the structure tensor eigenvectors using:

$$\lambda_1 = c_1 \quad (3.18)$$

$$\lambda_2 = \begin{cases} c_1 & \text{if } \mu_1 = \mu_2 \\ c_1 + (1 - c_1)e^{\frac{c_2}{(\mu_1 - \mu_2)^2}} & \text{otherwise} \end{cases} \quad (3.19)$$

where $c_1 \in (0, 1)$, $c_2 > 0$. The elements of D are then calculated as:

$$a = \lambda_1 \cos^2 \alpha + \lambda_2 \sin^2 \alpha \quad (3.20)$$

$$b = (\lambda_1 - \lambda_2) \sin \alpha \cos \alpha \quad (3.21)$$

$$c = \lambda_1 \sin^2 \alpha + \lambda_2 \cos^2 \alpha \quad (3.22)$$

Further details on the coherence enhancing diffusion filter with optimised rotational invariance is found in [189]. In [191] and [192] this filter was used primarily for noise removal while preserving edge detail, here we use it for its edge completion and smoothing properties.

3.2 Experimental Results

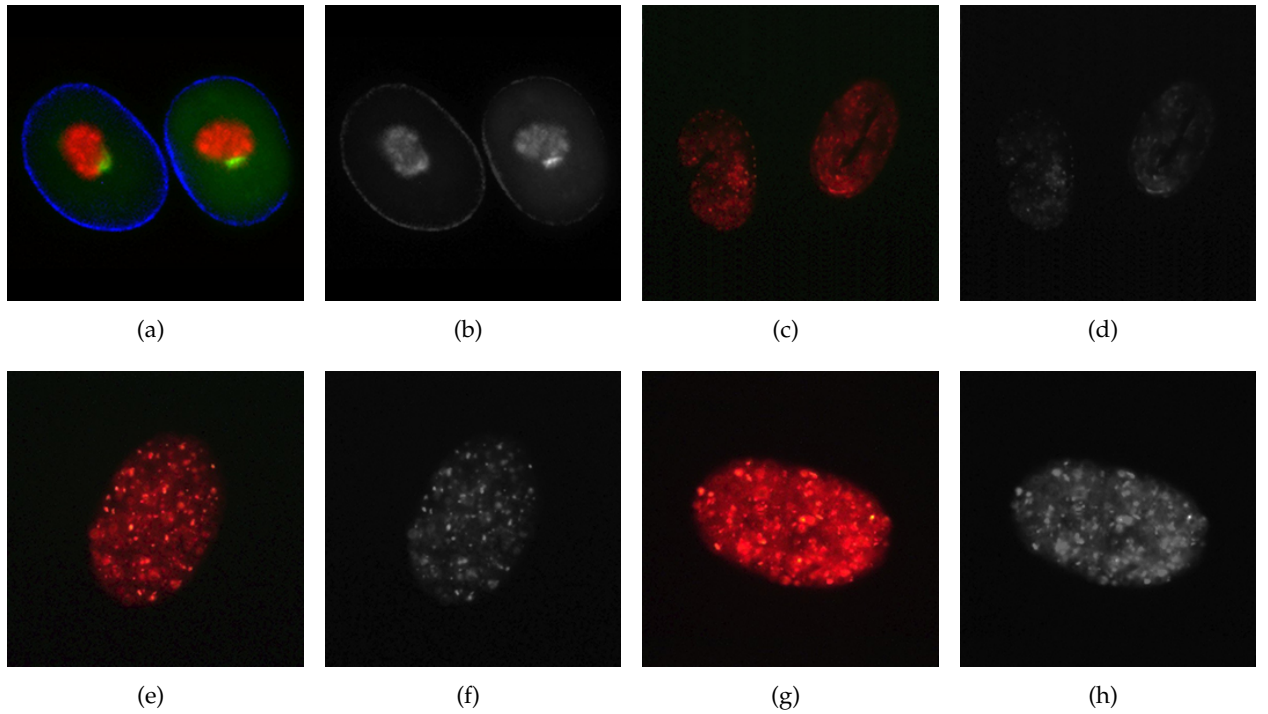


FIGURE 3.6: Original images with direct conversion to grayscale.

Parameter Settings The results of the segmentations are presented in Table 3.1. We compare four pre-processing schemes. In the table, the first scheme is denoted A and represents the results when using the raw gray level image; the second scheme denoted B represents the results of using the coherence enhancing diffusion filter with optimised rotational invariance (CED-ORI) [189], as done in [191] and [192]. The parameters used are: $\sigma = 3.0$, $\rho = 5.0$, $c_1 = 1 \times 10^{-3}$, $c_2 = 1$, $\Delta t = 0.0015$, $n = 20$. The third scheme, denoted C in the table, is the results of having each image denoised using the following parameters: $\lambda = 1$, $\mu = 20$, $\epsilon = 1 \times 10^{-3}$. The fourth scheme, denoted D in the table, is using the proposed scheme. The parameters for the TV denoising and CED-ORI are the same as previously presented. The additional parameters for the third step were set to: $\kappa_1 = 0.17$, $R_1 = 50$, $\kappa_2 = 0.55$, $R_2 = 225$. For the channel mixing step the weights used are shown in Table 3.2.

A numerical comparison of each segmentation, in Table 3.1, shows an increase in the general accuracy of the classification and the segmentation contours are smoother and fit the cell more appropriately.

Execution Time The scheme was implemented in C++ using OpenCV 2.3.4. There were no run-time optimisations performed in the code nor any complexity reduction of algorithms. The Operating System used was Ubuntu 13.10 on a Core 2 Duo 1.3GHz with this 2GB RAM. To get the results, the running times to process 744 images were analysed. The results are shown in Table 3.3. The mean running time versus the image size can be seen in Figure 3.12. As can be seen from Table 3.3, the bulk of the processing time is spent on denoising and intra-region smoothing.

3.3 Discussion

We have presented a scheme that adjusts the properties of an image such that more accurate segmentation can be obtained. Experiments performed on 2D fluorescence microscopy image data show that

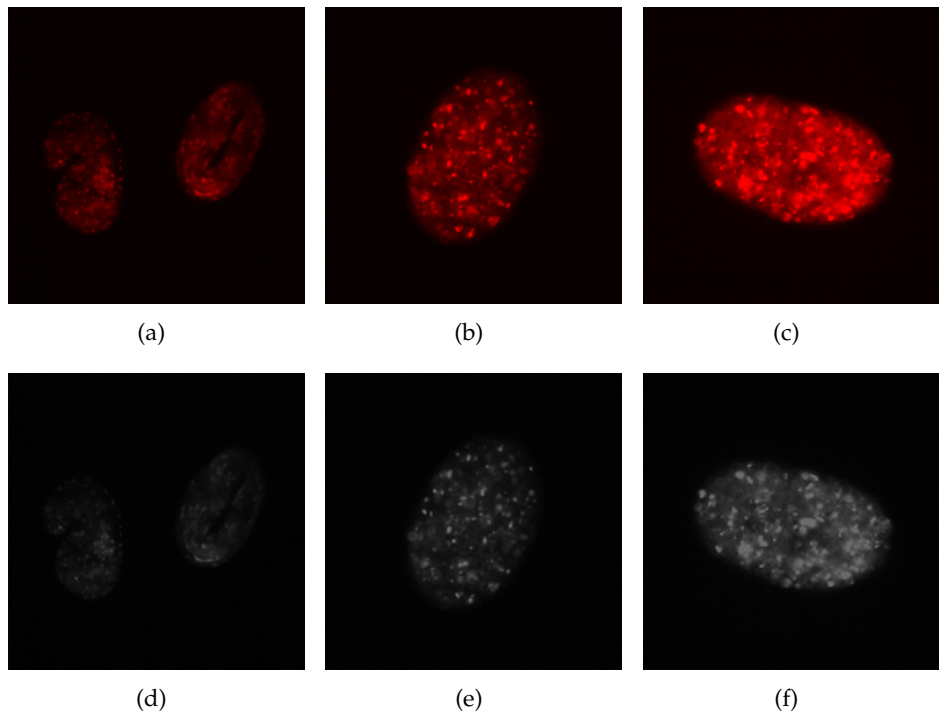


FIGURE 3.7: Removed noisy channels with corresponding grayscale images.

the proposed scheme outperforms the existing techniques. One limitation of the scheme is the tuning of the various parameters. The running time can also be reduced by using parallel computing or by optimizing algorithms used.

TABLE 3.1: Classification Statistics[A - Original gray scale image, B - CED-ORI only, C - Anisotropic TV de-noising only, D - Proposed Preprocessing Scheme]

		Sensitivity	Specificity	F1 score
Image 1	A	0.956157	0.974129	0.975526
	B	0.952542	0.971822	0.974790
	C	0.778485	0.839000	0.874881
	D	0.981447	0.989360	0.987344
Image 2	A	0.967517	0.981730	0.979699
	B	0.972583	0.984701	0.980968
	C	0.932064	0.960116	0.963754
	D	0.973092	0.985008	0.980745
Image 3	A	0.977581	0.997342	0.704079
	B	0.967342	0.993423	0.945607
	C	0.980888	0.996411	0.924565
	D	0.973788	0.994494	0.972452
Image 4	A	0.984491	0.961890	0.964425
	B	0.998658	0.999674	0.972736
	C	0.878951	0.964813	0.934818
	D	0.999495	0.999873	0.989058
Image 5	A	0.999931	0.999980	0.966254
	B	0.997783	0.999318	0.988121
	C	0.982536	0.994460	0.988247
	D	1.000000	1.000000	0.977193

TABLE 3.2: Channel Mixing Weights

	w_R	w_G	w_B
Image 1	0.2	0.6	0.2
Image 2	0.5	0.5	0.0
Image 3	1.0	0.0	0.0
Image 4	1.0	0.0	0.0
Image 5	1.0	0.0	0.0

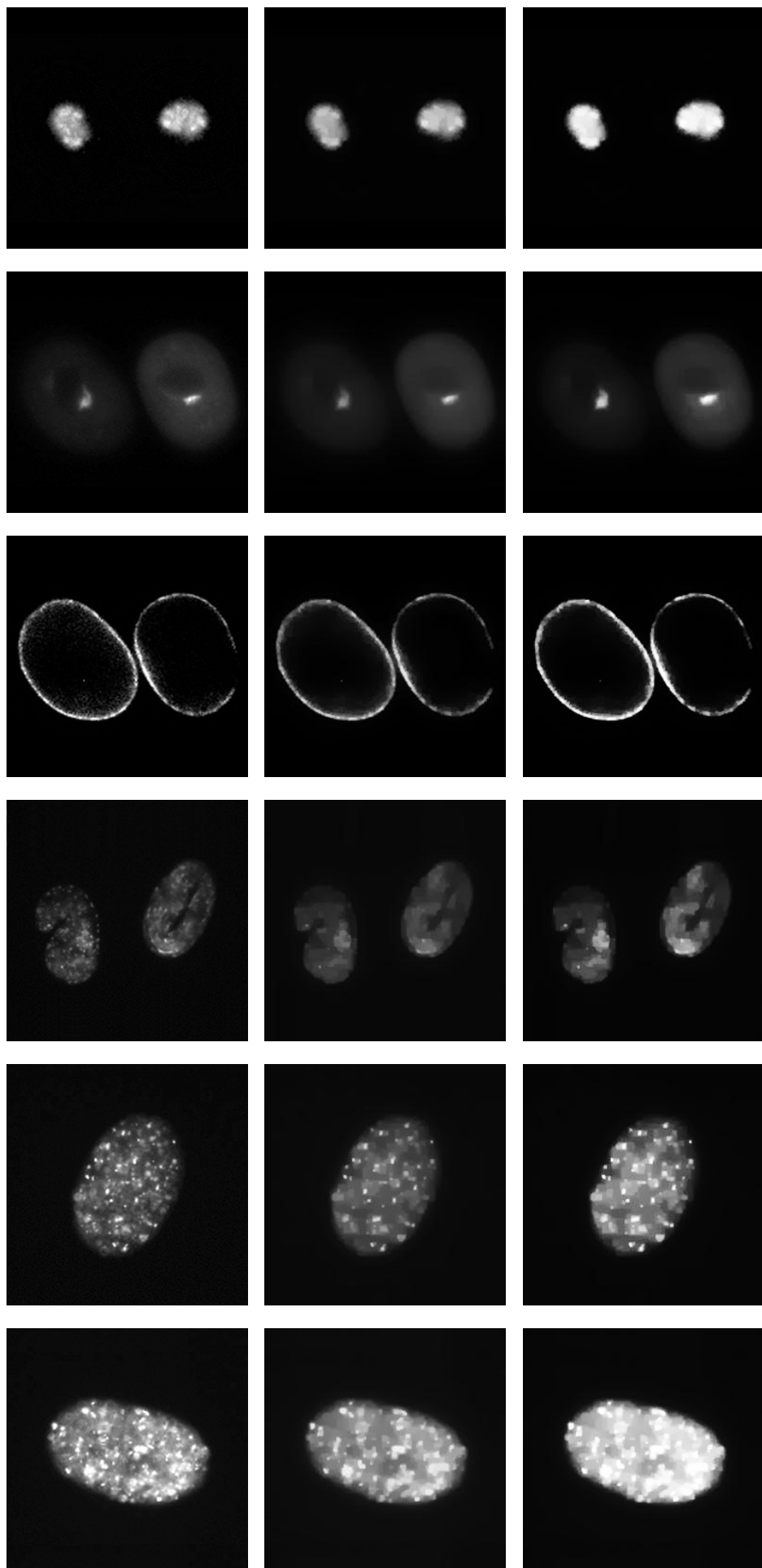


FIGURE 3.8: Original channel, TV denoised and remapped.

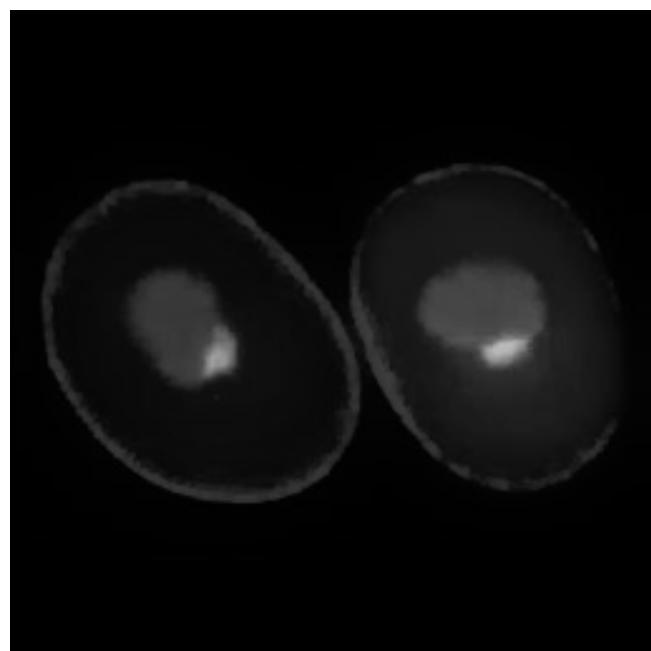


FIGURE 3.9: Mixed.

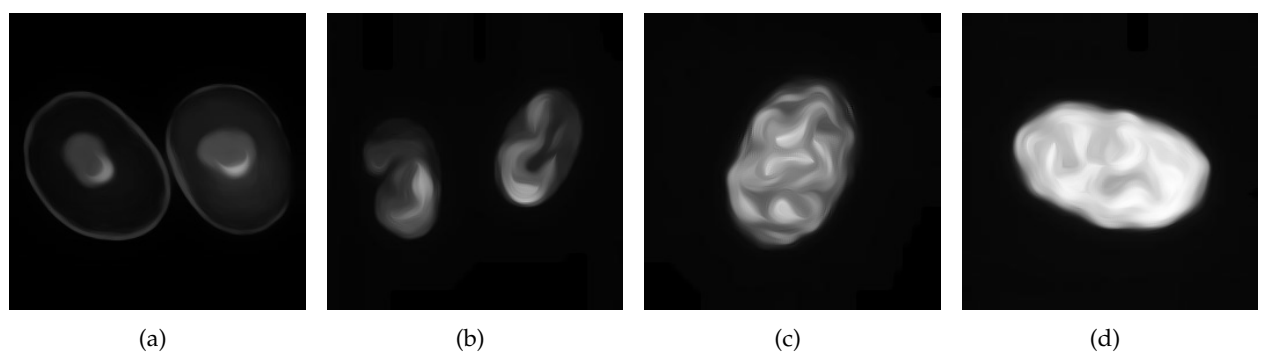


FIGURE 3.10: Final proxy after CED-ORI Filtering.

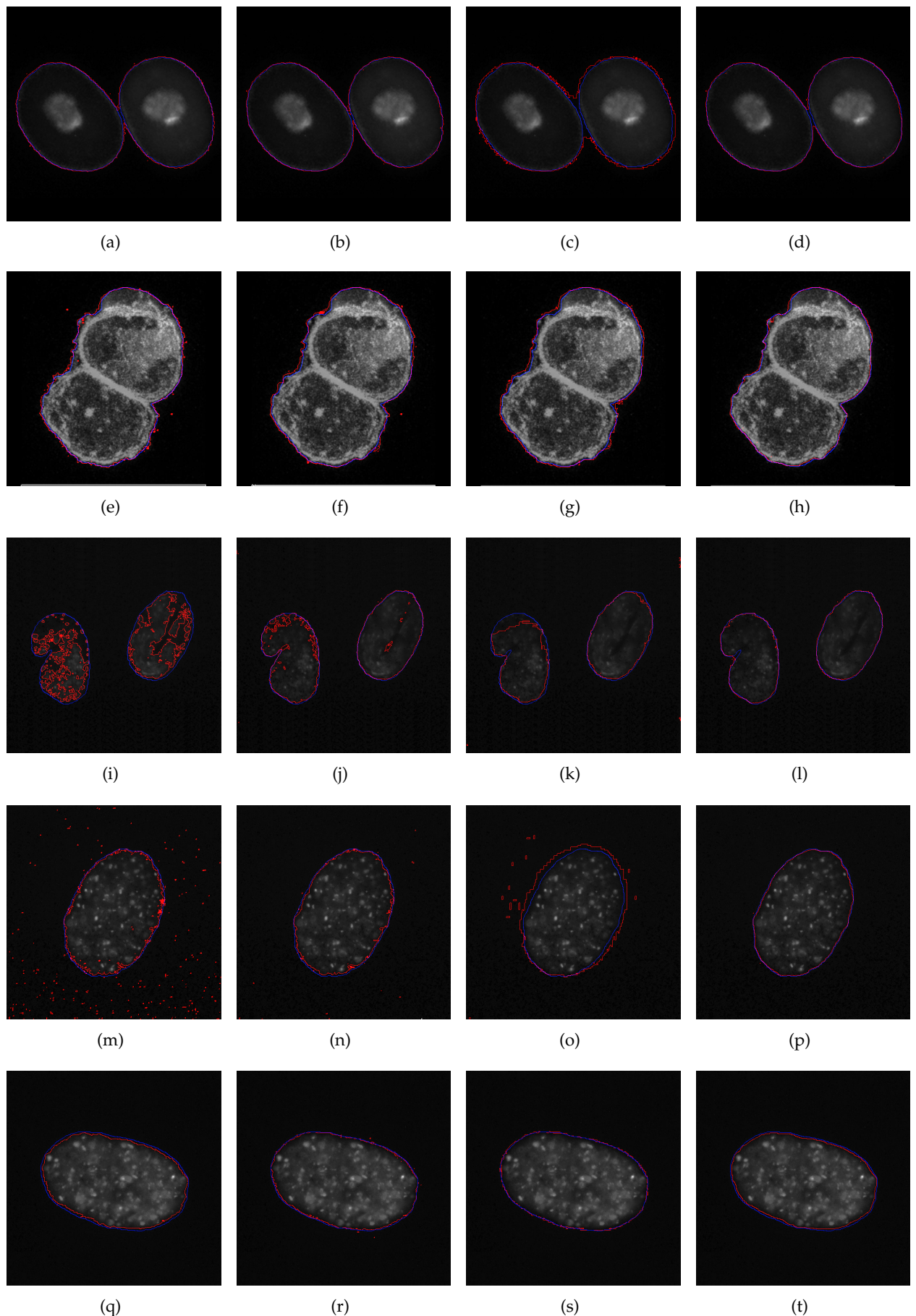


FIGURE 3.11: Segmentation results.

TABLE 3.3: Running Time Results

Chn	Dims	Mean	St. Dev	%TV	%CEDORI
1	64 × 64	4.63	1.02	24.58	74.50
	128 × 128	14.44	4.02	19.12	80.61
	192 × 192	31.73	8.56	22.42	77.44
	256 × 256	58.12	14.40	22.58	77.36
	320 × 320	97.72	24.91	19.86	80.09
	384 × 382	147.96	37.94	18.06	81.91
	448 × 448	188.19	41.16	18.81	81.17
	512 × 512	250.24	52.16	17.68	82.30
Mean				20.39	79.42
St. Dev				2.50	2.72
2	64 × 64	5.77	1.94	39.45	59.78
	128 × 128	17.20	6.86	32.11	67.68
	192 × 6192	38.84	16.02	36.63	63.27
	256 × 256	71.24	26.47	36.84	63.11
	320 × 320	117.12	42.02	33.14	66.83
	384 × 384	174.68	60.64	30.59	69.83
	448 × 448	223.59	69.34	31.66	68.32
	512 × 512	294.50	86.74	30.05	69.93
Mean				33.81	66.04
St. Dev				3.41	3.59
3	64 × 64	6.91	2.85	49.42	49.92
	128 × 128	19.96	9.69	41.50	58.32
	192 × 192	45.96	23.49	46.44	53.47
	256 × 256	84.37	38.54	46.66	53.29
	320 × 320	136.53	59.14	42.64	57.33
	384 × 382	201.40	83.34	39.80	60.18
	448 × 448	258.98	97.52	41.00	58.98
	512 × 512	338.75	121.32	39.19	60.80
Mean				43.33	56.54
St. Dev				3.72	3.87

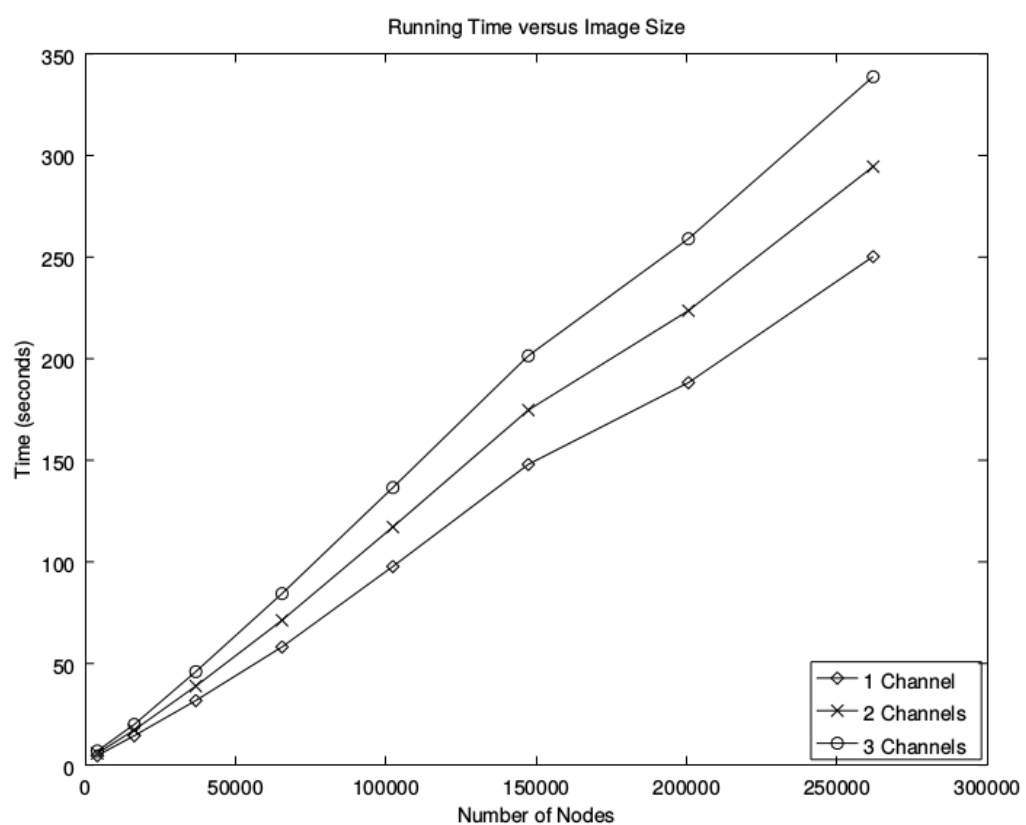


FIGURE 3.12: Running time vs Image size

Chapter 4

Parameter Estimation for ACWE Chan-Vese Segmentation

[Introduction] What is special about the Chan-Vese formulation to the Mumford-Shah evolution energy function. Advantages, disadvantages (parameter estimation). Course of the chapter.

4.1 Graph Cut Model for Chan-Vese Segmentation

In this section we briefly reintroduce the graph cut formulation for the Chan-Vese formulation of the Mumford-Shah evolution energy function for image segmentation. The Mumford-Shah model uses gradient descent techniques to obtain a minimum but as previously discussed, Section 2.2.2, they usually terminate at local minima. By reformulating the energy function in a discrete form that allows for appropriate graph representability, we can use graph cuts, which are able to terminate at a global minimum, to iteratively converge to the optimal solution. For an in-depth exposition into this technique, look to [124, 147, 193].

The level set representation of the Mumford-Shah energy function is

$$\begin{aligned} F(c_1, c_2, \phi) = & \mu \int_{\Omega} \delta(\phi(x, y)) |\nabla \phi(x, y)| dx dy \\ & + \nu \int_{\Omega} H(\phi(x, y)) dx dy \\ & + \lambda_1 \int_{\Omega} |u(x, y) - c_1|^2 H(\phi(x, y)) dx dy \\ & + \lambda_2 \int_{\Omega} |u(x, y) - c_2|^2 (1 - H(\phi(x, y))) dx dy, \end{aligned} \tag{4.1}$$

where $u(x, y)$ is the image, $H(\cdot)$ is the Heaviside step function, $\delta(\cdot)$ is the Dirac delta function, $\phi : \Omega \rightarrow \mathbb{R}$ is the level set function, such that:

$$\begin{aligned} \omega &= \{(x, y) \in \Omega | \Phi(x_p) > 0\} \text{ Inside the boundary} \\ \bar{\omega} &= \{(x, y) \in \Omega | \Phi(x_p) < 0\} \text{ Outside the boundary} \\ C &= \partial \omega = \{(x, y) \in \Omega | \Phi(x_p) = 0\} \text{ Along the boundary}, \end{aligned} \tag{4.2}$$

c_1 and c_2 are the arithmetic means given by:

$$c_1(\phi) = \frac{\int_{\Omega} u(x, y) H(\phi(x, y)) dx dy}{\int_{\Omega} H(\phi(x, y)) dx dy}, \tag{4.3}$$

$$c_2(\phi) = \frac{\int_{\Omega} u(x, y) (1 - H(\phi(x, y))) dx dy}{\int_{\Omega} (1 - H(\phi(x, y))) dx dy}. \tag{4.4}$$

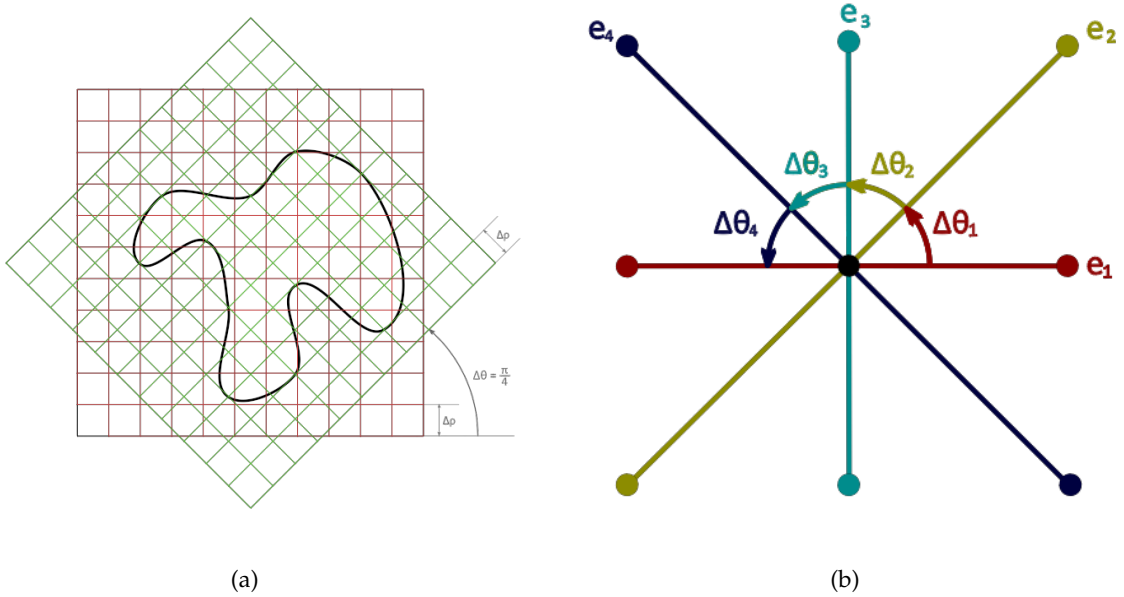


FIGURE 4.1: (a) Cauchy-Crofton length approximation. (b) 8-connected neighbourhood system.

The piecewise smooth approximation of the image is then

$$u(x, y) = c_1 H(\phi(x, y)) + c_2(1 - H(\phi(x, y))). \quad (4.5)$$

Discrete Approximation of Contour Length For the energy function to be represented as a graph, one of the requirements is that it must be in a discrete representation. This means that the length of the contour, the first term in Equation (4.1), must be approximated discretely and be graph representable. This work has already been done by Kolmogorov and Boykov in [194, 195] where they used the Cauchy-Crofton theorem. The theorem states that the length of a curve can be approximated by drawing a large number of straight lines from 0 to 2π and counting the number of intersections between the lines and the contour. The mathematical representation is

$$\int_L n_L dL = \int_0^\pi \int_{-\infty}^\infty n_L d\rho d\theta = 2\|C\|_E, \quad (4.6)$$

where n_L is the number of intersections between the contour C and the line L , $\|C\|_E$ is the Euclidean length of the contour, $0 < \rho < \infty$ and $0 < \theta < 2\pi$. From this the discrete approximation used by Boykov and Zabih is

$$\|C\|_E = \frac{1}{2} \sum_k n_k \frac{\delta^2 \Delta\theta_k}{|e_k|} = \frac{1}{2} \sum_k n_k w_k \quad (4.7)$$

An example of approximating the contour by two grids is illustrated in Figure 4.1(a) using four families of parallel lines which are 45° apart.

Discrete Representation of Mumford-Shah Function With the exception of the second term in Equation (4.1), the remaining terms are represented easily discretely. For each pixel $p \in \Omega$, let x_p be a binary variable such that

$$x_p = \begin{cases} 0 & \phi(p) \leq 0 \\ 1 & \phi(p) > 0 \end{cases} \quad (4.8)$$

The means can now be calculated using

$$c_1 = \frac{\sum_p u(x, y)x_p}{\sum_p x_p}, \quad (4.9)$$

$$c_2 = \frac{\sum_p u(x, y)(1 - x_p)}{\sum_p (1 - x_p)}. \quad (4.10)$$

For simplification, $\nu = 0$. To determine contour length using an 8-neighbourhood system, as illustrated in Figure 4.1(b), we set $\Delta\rho = 1$. The weight w_k is assigned to its corresponding edge e_k . The Euclidean length of the edges is $|e_1| = |e_3| = 1$ and $|e_2| = |e_4| = \sqrt{2}$, therefore the corresponding weights, which are determined using Equation (4.7), is $w_1 = w_3 = \frac{\pi}{8}$ and $w_2 = w_4 = \frac{\pi}{8\sqrt{2}}$. To calculate n_k we need to count the intersections between the lines and the contour. An intersection between two pixels p and q exists if and only if x_p and x_q have different labels.

$$n_k = x_p(1 - x_q) + x_q(1 - x_p); k = (pq) \in \mathcal{N}_p. \quad (4.11)$$

The contour length can now fully be expressed discretely as

$$\|C\|_E = \sum_{p,q \in e_k} w_k(x_p(1 - x_q) + x_q(1 - x_p)). \quad (4.12)$$

The discrete representation of Equation (4.1) is

$$\begin{aligned} F(x_1, \dots, x_n) &= \mu \sum_{p,q \in e_k} w_k(x_p(1 - x_q) + x_q(1 - x_p)) \\ &\quad + \lambda_1 \sum_p |u(x, y) - c_1|^2 x_p \\ &\quad + \lambda_2 \sum_p |u(x, y) - c_2|^2 (1 - x_p) \end{aligned} \quad (4.13)$$

Graph Representation The discrete energy function Equation (4.13) has been shown that it obey the submodularity constraint for graph representability. Therefore the data energy and regularisation energy is

$$E^p(x_p) = \lambda_1 |u(x, y) - c_1|^2 x_p + \lambda_2 |u(x, y) - c_2|^2 (1 - x_p) \quad (4.14)$$

$$E^{pq}(x_p, x_q) = (x_p + x_q - 2x_p x_q) w_{pq} \quad (4.15)$$

The graph for the energy function is constructed as in [151].

4.2 Modified Weighting and Parameter Estimation

In this section we introduce a novel idea to weighting a graph for image segmentation based on the Chan-Vese formulation of the Mumford-Shah evolution function. Previous parameter estimation schemes focused very specifically on a certain image and this resulted in hard-coded. In [193], where this method was first devised, they used the parameter settings $\mu = 0.1 \times 255^2$, $\lambda_1 = \lambda_2 = 1$. This worked very well on their synthetic images proving a strong resilience to noise and initial conditions. However, for fluorescence microscopy images, the results to be a bit too over-segmented for practical use. These parameters were used to segment the images in the sample set, Figure B.1, the segmentation result is shown in Figure 4.2.

In [191], the authors proposed a segmentation and tracking scheme for whole fluorescent cells in a timelapse series. The result was another set of hard-coded parameters which were based on

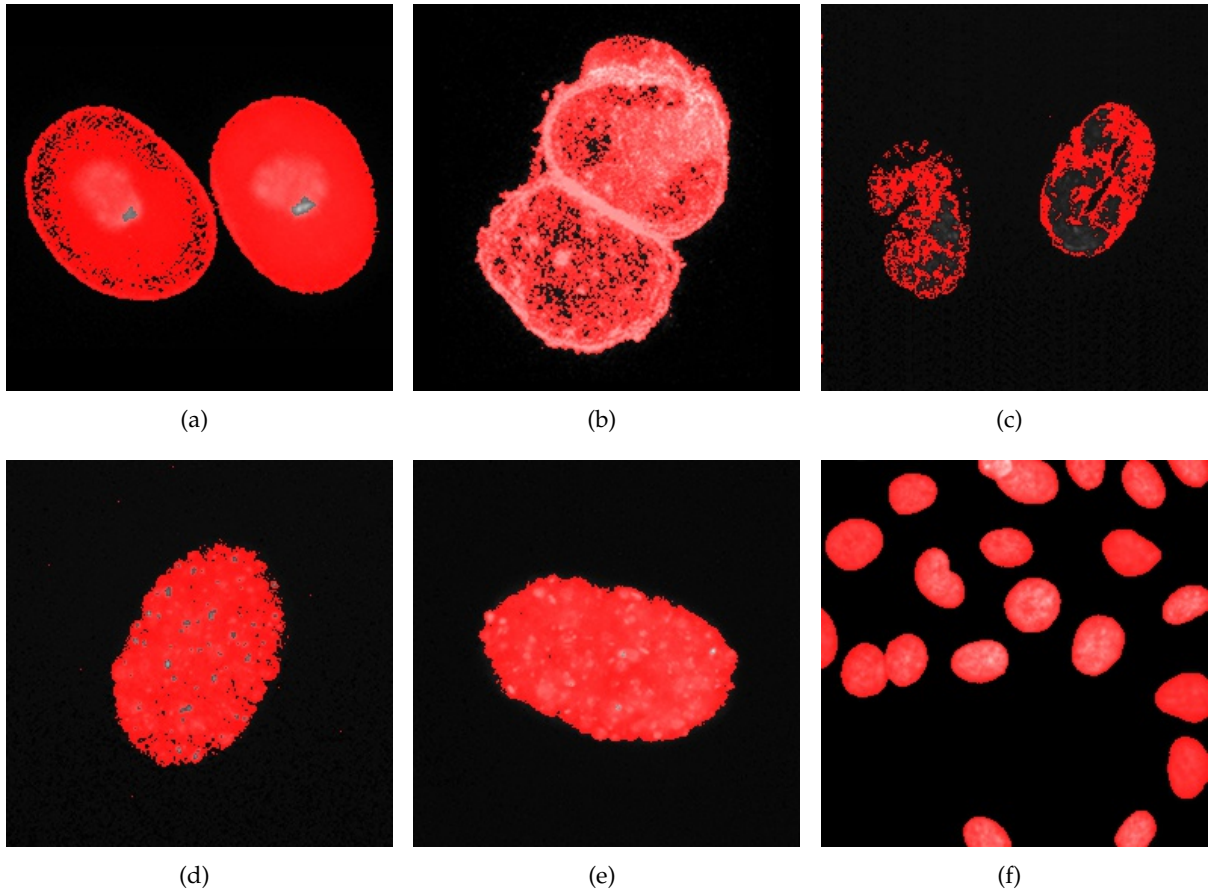


FIGURE 4.2: CAPTION MISSING HERE.

maximising the Jaccard coefficient of the automatically segmented cells in each frame of the timelapse series which was also manually segmented. The optimal parameter settings were $\mu = 0.01$, $\lambda_1 = 1$ and $\lambda_2 = 85$. These parameters were used on the sample set in Figure B.1 and the results proved to be less useful as shown in Figure 4.3. It can be deduced that the parameters were specifically tuned to the image type that was studied.

It can be seen that hard-coded parameter values do not produce very consistent results over a large range of image types as that found in fluorescence microscopy imaging. In the next section, Section 4.2.1 we devise a novel weighting scheme, parameter estimation as well as a new way to think of the parameters involved, in terms of *proxy parameters*. We then specifically focus on tuning these parameter for fluorescence images in Section 4.2.3.

4.2.1 Graph Weighting

The first thing we do is normalise the weighting for both the data and smoothing connections. For the weighting of the neighbourhood connections we use the Euclidean distance between adjacent nodes. This results in neighbourhood connections as illustrated in Figure 4.4. The range of pixel intensities is also normalised i.e. $p \in [0, 1]$. The weight of the connection from the source to the node p is given by $E^i(0)|_{i=p} = \lambda_0|p - c_0|^2$. This is seen as how far away the pixel is from c_0 . Similarly, the weight of the connection from the node to the sink is given by $E^i(1)|_{i=p} = \lambda_1|p - c_1|^2$, i.e. how far away the pixel is from c_1 . The fully connected graph for a single node in the 8-connected neighbourhood system is illustrated in Figure 4.4.

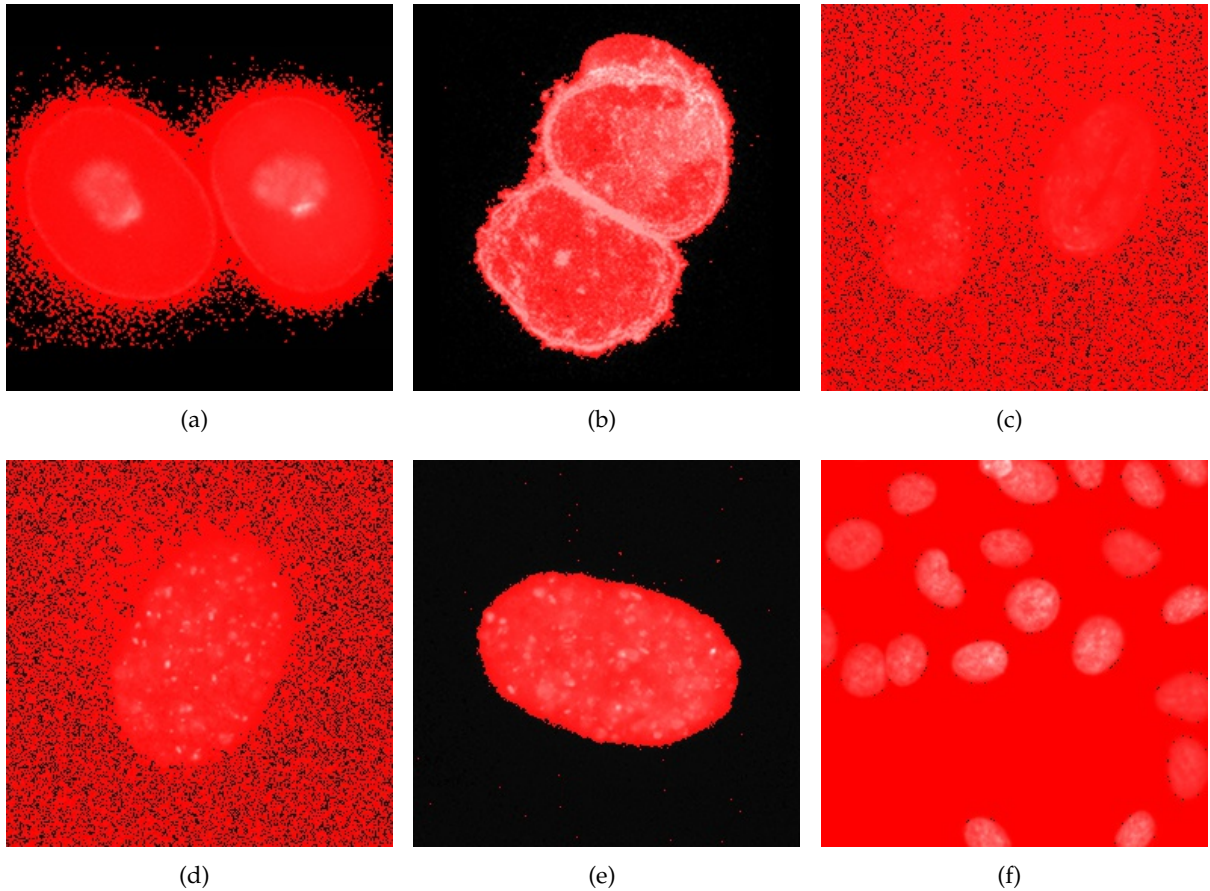


FIGURE 4.3: CAPTION MISSING HERE.

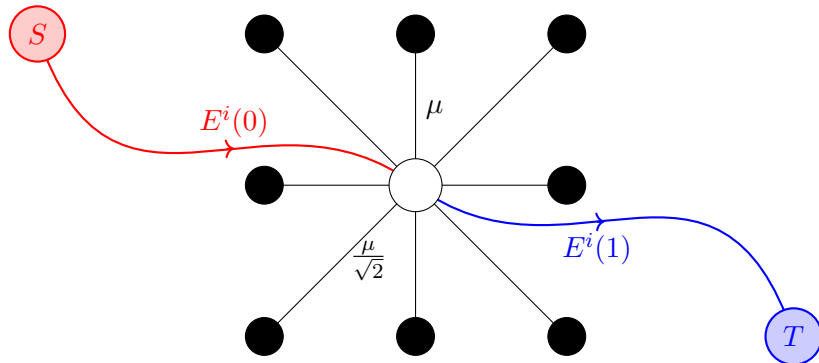


FIGURE 4.4: Fully connected single node.

4.2.2 Analysis of Weighting System and Parameter Relationships

To better understand the relationship between λ_0 and λ_1 and its impact on the final solution we explicitly formalise the dependency and set

$$\lambda_0 = \alpha \lambda_1. \quad (4.16)$$

Forcing this relation between λ_0 and λ_1 makes further analysis simpler and more intuitive. We can immediately see a constraint on α . Since, we require data connections to be positive, i.e. $E^i(0), E^i(1) \geq$

0 (SEE SECTION??), this gives us a lowerbound on α for positive concavity of the energy functions

$$\alpha > 0 \text{ lowerbound on } \alpha \quad (4.17)$$

We will now analyse the flow through a single node. We use Figure 4.4 to facilitate our explanation. From the neighbourhood connections, in an 8-connected neighbourhood construction, the maximum flow into or out of a node to its neighbours is

$$f_{max} = 4\mu + 4\frac{\mu}{\sqrt{2}} = \mu(2\sqrt{2} + 4). \quad (4.18)$$

To guarantee that a node p will be placed in the source set, $p \in S$, we know that the incoming flow from the source must completely saturate all flow outlets, this can be expressed as

$$E^i(0) > E^i(1) + \mu(2\sqrt{2} + 4). \quad (4.19)$$

This can be read as "*The source saturates the sink and all neighbourhood connections*". Similarly to guarantee the node will be in the sink set, $p \in T$

$$E^i(1) > E^i(0) + \mu(2\sqrt{2} + 4). \quad (4.20)$$

This can be read as "*The sink is larger than the source and all neighbourhood connections*". To aid in understanding the energies we use Figure 4.5.

For quadratic energies with $0 < c_0 < c_1 < 1$, there is a point, between c_0 and c_1 , where the incoming flow from the source is completely saturates the sink with no excess remaining. This point, where the energies are equal, we call p_e , i.e. $E_0(p_e) = E_1(p_e)$. This point of zero net flow can be found as follows

$$\begin{aligned} E^{i=p_e}(1) &= E^{i=p_e}(0) \\ \lambda_1(p_e - c_1)^2 &= \lambda_0(p_e - c_0)^2 \\ \frac{(p_e - c_0)^2}{(p_e - c_1)^2} &= \frac{\lambda_1}{\lambda_0} \\ \frac{p_e - c_0}{p_e - c_1} &= \sqrt{\frac{\lambda_1}{\lambda_0}} \quad \text{or} \quad \frac{p_e - c_0}{p_e - c_1} = -\sqrt{\frac{\lambda_1}{\lambda_0}} \end{aligned}$$

We know that

$$\begin{aligned} c_0 &< p_e < c_1 \\ \therefore p_e - c_0 > 0 &\quad \text{and} \quad p_e - c_1 < 0 \end{aligned}$$

It follows directly that

$$\begin{aligned} \frac{p_e - c_1}{p_e - c_0} &= -\sqrt{\frac{\lambda_1}{\lambda_0}} \\ \frac{(p_e - c_0) + (c_0 - c_1)}{p_e - c_0} &= -\sqrt{\frac{\lambda_1}{\lambda_0}} \\ \frac{c_0 - c_1}{p_e - c_0} &= -\left(\sqrt{\frac{\lambda_1}{\lambda_0}} + 1\right) \\ p_e = c_0 + \frac{c_1 - c_0}{\sqrt{\frac{\lambda_1}{\lambda_0}} + 1} \end{aligned}$$

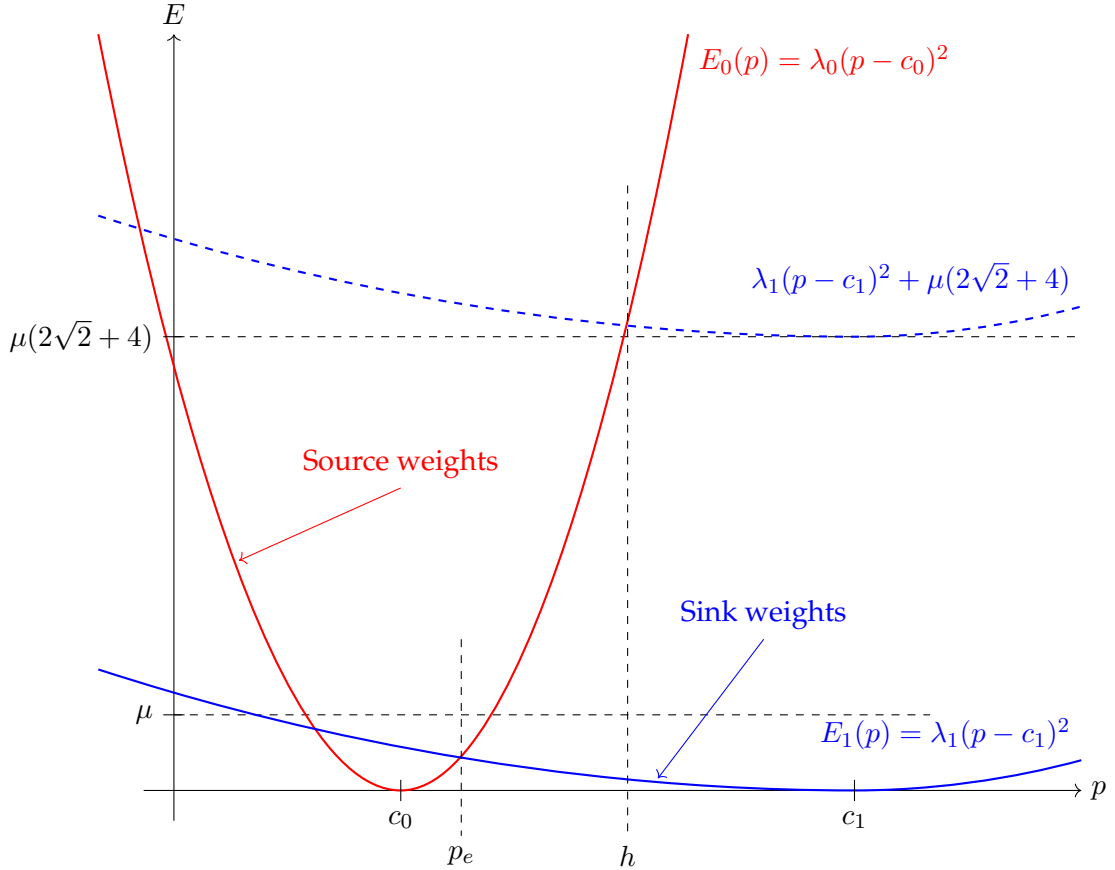


FIGURE 4.5: Data energy functions plot.

After substituting the relation in Equation (4.16) we get

$$p_e = c_0 + \frac{c_1 - c_0}{\sqrt{\alpha} + 1} \quad (4.21)$$

The point where the energies are equal, p_e , is shown in Figure 4.5.

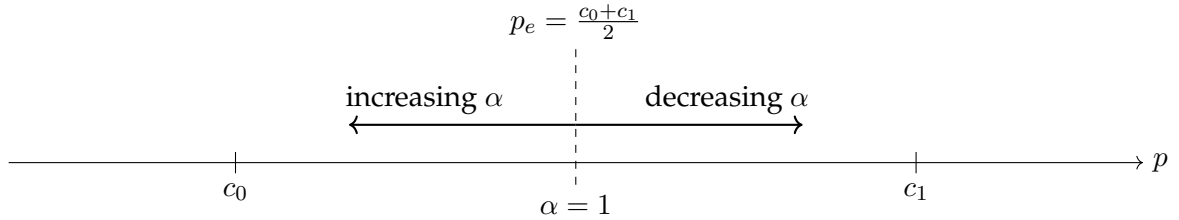
Analysis of the relationship between p_e and α From Equation (4.21) we note that there is one tunable parameter, i.e. α . We can see that p_e and α are inversely related. This is expressed mathematically as

$$\begin{aligned} \text{if } \alpha = 1, p_e &= c_0 + \frac{c_1 - c_0}{1 + \sqrt{1}} = \frac{c_0 + c_1}{2} && \text{(midpoint between } c_0 \text{ and } c_1\text{)} \\ \lim_{\alpha \rightarrow \infty} p_e &= \lim_{\alpha \rightarrow \infty} c_0 + \frac{c_1 - c_0}{1 + \sqrt{\infty}} = c_0 && \text{(maximum } \alpha \text{ yields lowerbound on } p_e\text{)} \\ \lim_{\alpha \rightarrow 0} p_e &= \lim_{\alpha \rightarrow 0} c_0 + \frac{c_1 - c_0}{1 + \sqrt{0}} = c_1 && \text{(minimum } \alpha \text{ yields upperbound on } p_e\text{)} \end{aligned}$$

The relationship between p_e and α is illustrated in Figure 4.6.

Figuring α If we are able to make good estimates on p_e , c_0 and c_1 for the final segmented image, then it is possible to calculate α as follows:

$$\begin{aligned} p_e &= c_0 + \frac{c_1 - c_0}{\sqrt{\alpha} + 1} \\ 1 + \sqrt{\alpha} &= \frac{c_1 - c_0}{p_e - c_0} \end{aligned}$$

FIGURE 4.6: Relationship between α and p_e .

$$\alpha = \left(\frac{c_1 - c_0}{p_e - c_0} - 1 \right)^2 \quad (4.22)$$

Lowerbound on μ When we found the point, p_e , where the energies are equal in Equation (4.21), we ignored the other solution as it was not within the range from c_0 to c_1 . Let this point be p_{e^*} . If this point is positive and $0 < p_{e^*} < c_0$ then we must ensure that at no point within this range that the source flow saturates all the outgoing edges. This force a limit on how low μ can be. This is only of significant concern when $\alpha > 1$. We only need to concern ourselves with the point $p = 0$ as this is the point where the difference $E^i(0) - E^i(1)$ is the largest. The lowerbound on μ can be obtained as follows

$$\begin{aligned} E^i(0)|_{p_i=0} &< E^i(1)|_{p_i=0} + \mu (2\sqrt{2} + 4) \\ \lambda_0 c_0^2 &< \lambda_1 c_1^2 + \mu (2\sqrt{2} + 4) \\ \therefore \mu (2\sqrt{2} + 4) &> \lambda_0 c_0^2 - \lambda_1 c_1^2 \\ \mu &> \frac{\lambda_0 c_0^2 - \lambda_1 c_1^2}{(2\sqrt{2} + 4)} \end{aligned}$$

Taking into account the relation in Equation (4.16) this becomes

$$\mu > \frac{\lambda_1 (\alpha c_0^2 - c_1^2)}{(2\sqrt{2} + 4)} \quad (4.23)$$

Absolutely in the source set From Equation (4.19) we can see that there is a point beyond which all nodes which correspond to pixel value higher than that point will be saturated and have excess flow which means that they will be in the source set. We will call this point the *saturation point* and denote it by h . This is shown in Figure 4.5. This point can be determined as follows:

$$\begin{aligned} \lambda_0 (h - c_0)^2 &> \lambda_1 (h - c_1)^2 + f_{max} \\ \lambda_0 (h - c_0)^2 - \lambda_1 (h - c_1)^2 &> f_{max} \\ (\lambda_0 - \lambda_1) h^2 + (-2\lambda_0 c_0 + 2\lambda_1 c_1) h + (\lambda_0 c_0^2 - \lambda_1 c_1^2 - f_{max}) &> 0 \end{aligned}$$

The solutions to h are

$$h = \frac{(2\lambda_0 c_0 - 2\lambda_1 c_1) \pm \sqrt{(-2\lambda_0 c_0 + 2\lambda_1 c_1)^2 - 4(\lambda_0 - \lambda_1)(\lambda_0 c_0^2 - \lambda_1 c_1^2 - f_{max})}}{2(\lambda_0 - \lambda_1)}$$

Substituting the relation in Equation (4.16)

$$\begin{aligned} h &= \frac{(\alpha c_0 - c_1) \pm \sqrt{(c_1 - \alpha c_0)^2 - (\alpha - 1)(\alpha c_0^2 - c_1^2 - \frac{f_{max}}{\lambda_1})}}{\alpha - 1} \\ &= \frac{(\alpha c_0 - c_1) \pm \sqrt{\alpha(c_0 - c_1)^2 + \frac{f_{max}}{\lambda_1}(\alpha - 1)}}{\alpha - 1} \end{aligned}$$

If the μ is greater than the lowerbound in Equation (4.23) then there is only one solution to h which is of importance. This is the positive solution for h which is

$$h = \frac{(\alpha c_0 - c_1) + \sqrt{\alpha(c_0 - c_1)^2 + \frac{\mu(2\sqrt{2}+4)}{\lambda_1}(\alpha - 1)}}{\alpha - 1} \quad (4.24)$$

This point is marked off in Figure 4.5.

Determining λ_1 Given good approximations for c_0 , c_1 , α , h and μ , we can calculate the appropriate value for λ_1 . We proceed from Equation (4.19) as follows

$$\begin{aligned} \lambda_0(h - c_0)^2 &= \lambda_1(h - c_1)^2 + \mu(2\sqrt{2} + 4) \\ \lambda_1(\alpha(h - c_0)^2 - (h - c_1)^2) &= \mu(2\sqrt{2} + 4) \\ \lambda_1 &= \frac{\mu(2\sqrt{2} + 4)}{\alpha(h - c_0)^2 - (h - c_1)^2} \end{aligned} \quad (4.25)$$

Parameter estimation process The parameter estimation is based on the assumption that sufficiently good approximations for c_0 , c_1 , p_e and h can be obtained. By sufficiently good we are referring to the closeness to the values these parameters would take for an ideal segmentation. From these approximations, we calculate the approximation for α using Equation (4.22). The parameters μ and λ_1 are related and aren't separable, therefore we set choose to set μ . We can then calculate λ_1 using Equation (4.25). For the chosen μ we can calculate the upperbound on λ_1 to ensure that the constraint Equation (4.23) is met. The constraint on λ_1 is calculated as follows

$$\begin{aligned} \mu(2\sqrt{2} + 4) &> \lambda_1(\alpha c_0^2 - c_1^2) \\ \lambda_1 &< \frac{\mu(2\sqrt{2} + 4)}{\alpha c_0^2 - c_1^2} \end{aligned} \quad (4.26)$$

Finally λ_0 can be calculated using Equation (4.16).

4.2.3 Tuning Parameters for Fluorescence Microscopy

The properties of the images obtained in fluorescence microscopy imaging can be used to guide the parameter estimation process. We focus, specifically, on black background images. Due to the fact that the predominant form of noise in the imaging system is Poisson distributed, we can further assume that the darker the background, the less noise that is present therein. The Poisson process also tells us that brighter regions exhibit a greater intensity variation due to the sampling process. Therefore, the curve for $E^i(1)$ is less convex than $E^i(0)$ as in Figure 4.5 and, resultantly, the value for p_e , in Figure 4.6, is shifted to the left. This places a new lowerbound on α for fluorescence images

$$\alpha \geq 1. \quad (4.27)$$

Manual Tuning Before moving further into analysis of the relationships between the parameters, we first perform a manual tuning of parameters and observing the effect on the segmented results. This allows us to understand how strongly correlated the parameter is to the final result. We note that the curves, $E^i(0)$ and $E^i(1)$, can be tuned relative to a fixed value for μ and this wouldn't impact significantly on the range of possible solution sets. Therefore, we set $\mu = 1$ in all our manual parameter tuning. We use a stopping criterion of $\epsilon = 1 \times 10^{-3}$.

We cover a relatively wide range of parameter settings and note the output, i.e. over-segmented, under-segmented, almost ideal, etc. At this point, categorising the segmented output is largely subjective. We also use various initial conditions. Specifically, we use the segmented output from Otsu binarization, K-means ($k = 2$) and Expectation-Maximisation for Gaussian Mixture Modelling (EMGMM) with ($k = 2$). The initial and final means are of significant importance in this study.

For Figure B.1(a), we used show the output for the following combinations of α and λ_1 . $(\alpha, \lambda_1) = \{(30, 150), (40, 50), (40, 100), (40, 150), (40, 200), (45, 150), (50, 150)\}$. The initial segmentation masks are shown in Figure 4.7. The segmented output for the combinations are shown in Figure 4.8.

For Figure B.1(b), we used show the output for the following combinations of α and λ_1 . $(\alpha, \lambda_1) = \{(30, 150), (40, 50), (40, 100), (40, 150), (40, 200), (45, 150), (50, 150)\}$. The initial segmentation masks are shown in Figure 4.9. The segmented output for the combinations are shown in Figure 4.10.

For Figure B.1(c), we used show the output for the following combinations of α and λ_1 . $(\alpha, \lambda_1) = \{(1, 150), (10, 150), (10, 200), (10, 400), (10, 800), (20, 150), (30, 150), (40, 150), (50, 150)\}$. The initial segmentation masks are shown in Figure 4.11. The segmented output for the combinations are shown in Figure 4.12.

For Figure B.1(d), we used show the output for the following combinations of α and λ_1 . $(\alpha, \lambda_1) = \{(30, 50), (30, 100), (30, 150), (40, 100), (40, 150), (50, 150)\}$. The initial segmentation masks are shown in Figure 4.13. The segmented output for the combinations are shown in Figure 4.14.

For Figure B.1(e), we used show the output for the following combinations of α and λ_1 . $(\alpha, \lambda_1) = \{(30, 50), (30, 100), (30, 150), (40, 100), (40, 150), (50, 150)\}$. The initial segmentation masks are shown in Figure 4.15. The segmented output for the combinations are shown in Figure 4.16.

For Figure B.1(f), we used show the output for the following combinations of α and λ_1 . $(\alpha, \lambda_1) = \{(20, 20), (20, 150), (30, 150), (40, 50), (40, 150), (50, 150)\}$. The initial segmentation masks are shown in Figure 4.17. The segmented output for the combinations are shown in Figure 4.18.

The means and standard deviations for the initial masks obtained are shown in Table 4.1.

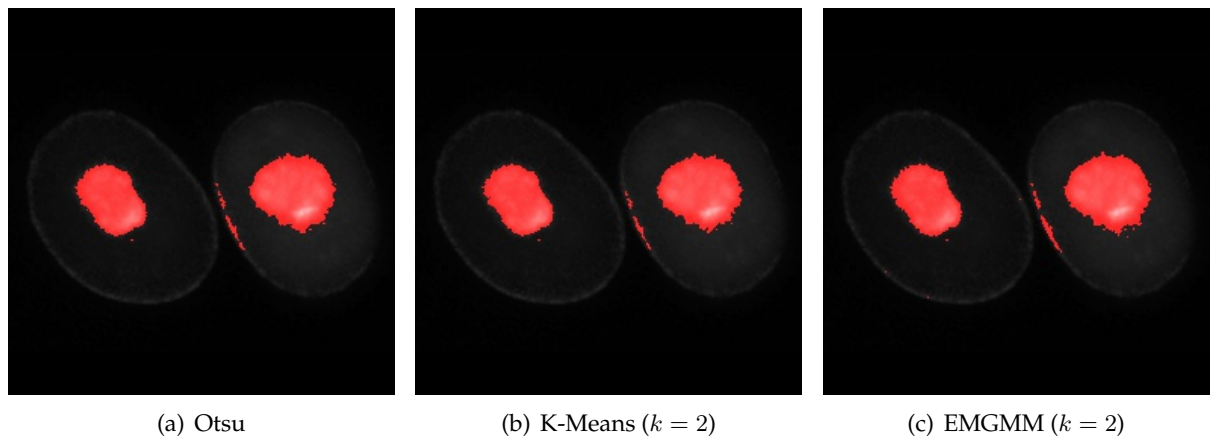
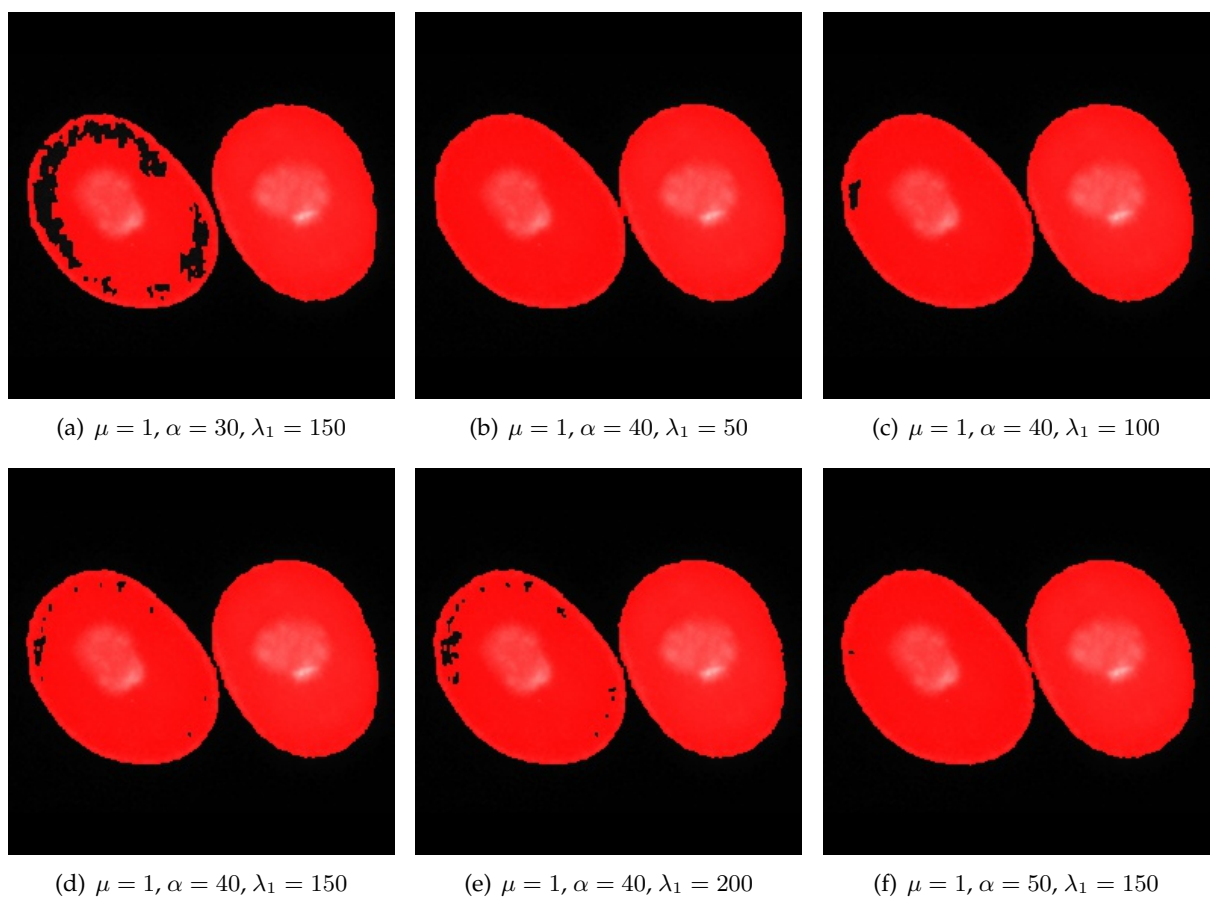


FIGURE 4.7: Image 1 from sample set Figure B.1 initial masks.

FIGURE 4.8: Segmented output for various combination of α and λ_1 for Image 1 in the sample set.

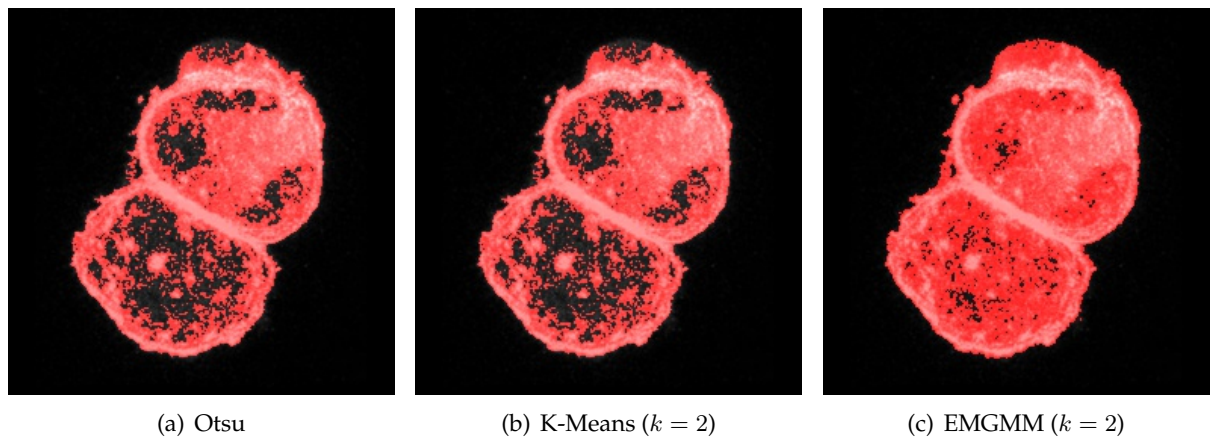
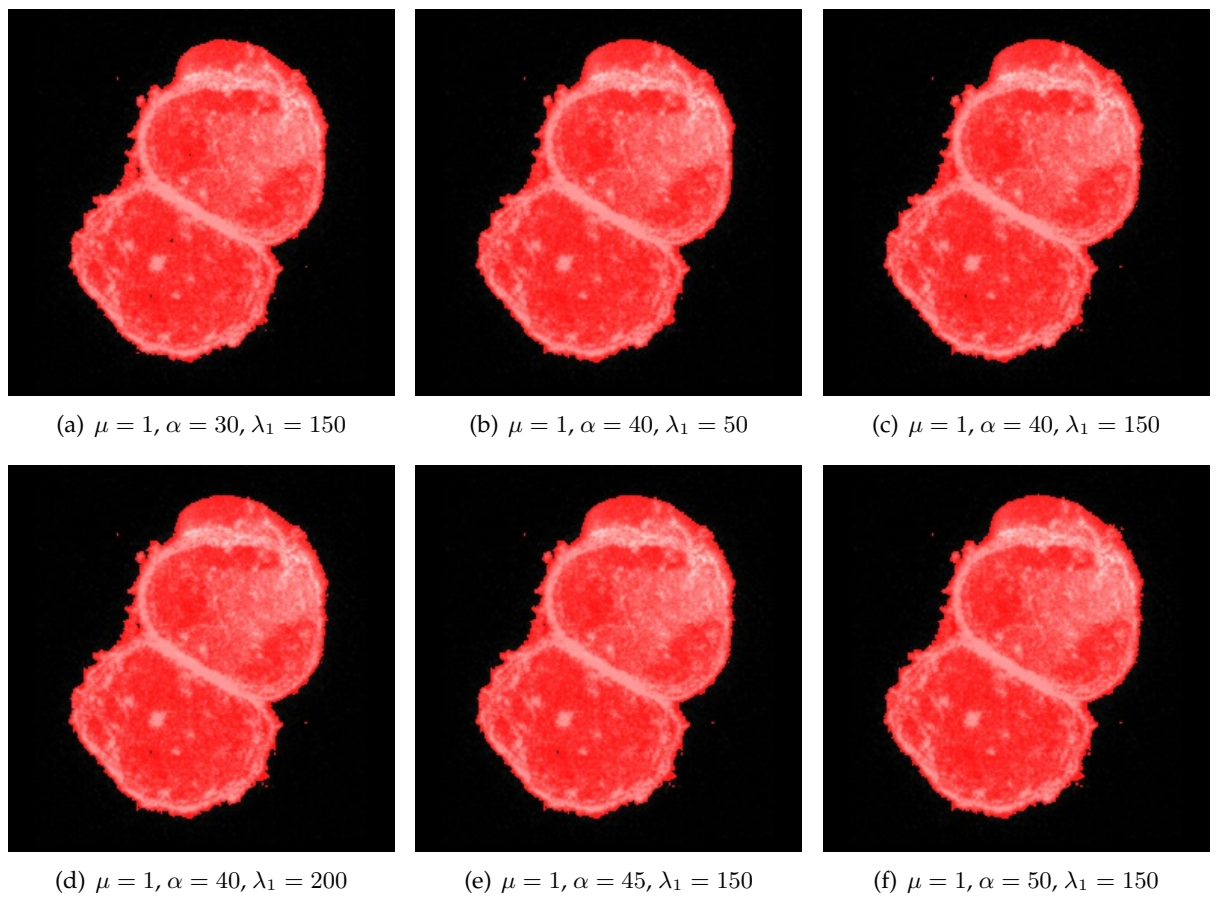


FIGURE 4.9: Image 2 from sample set Figure B.1 initial masks.

FIGURE 4.10: Segmented output for various combination of α and λ_1 for Image 2 in the sample set.

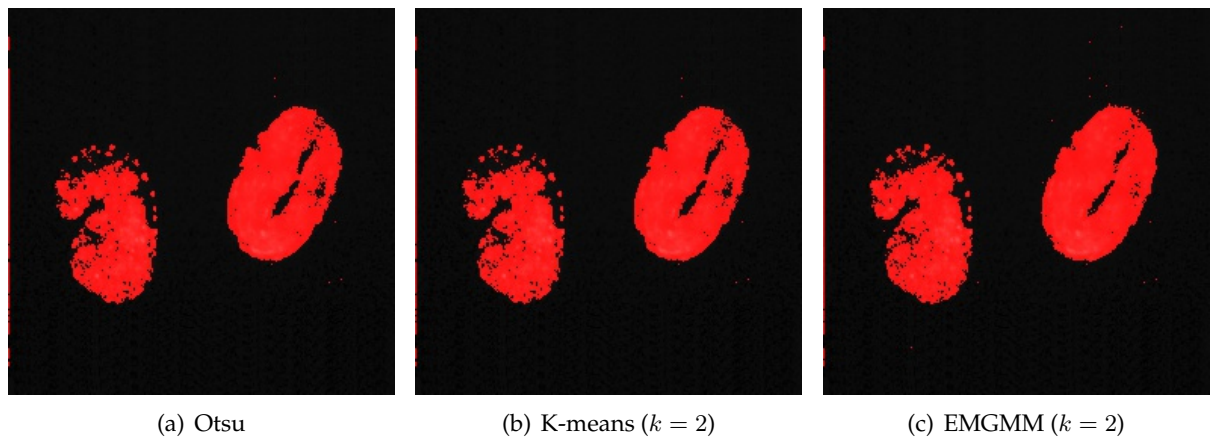
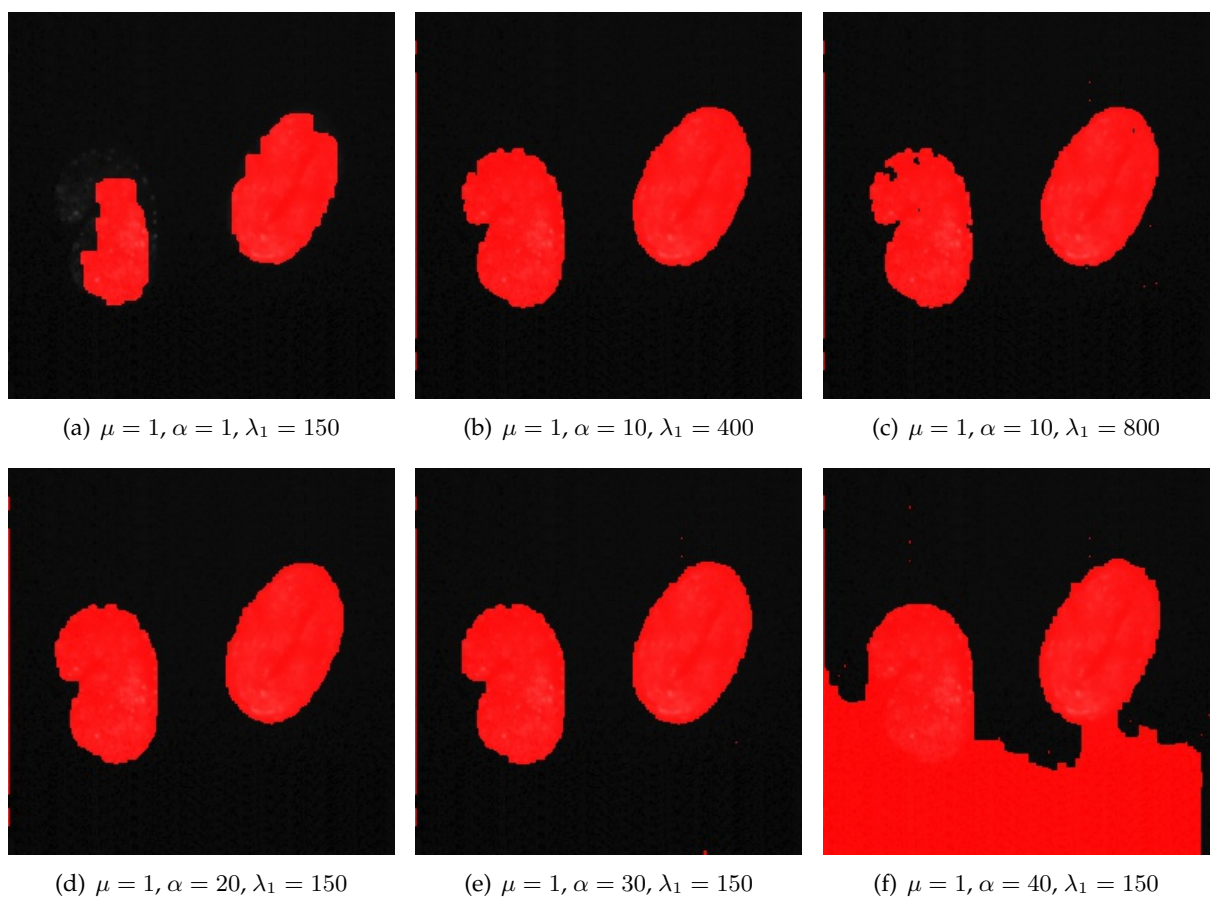


FIGURE 4.11: Image 3 from sample set Figure B.1 initial masks.

FIGURE 4.12: Segmented output for various combination of α and λ_1 for Image 3 in the sample set.

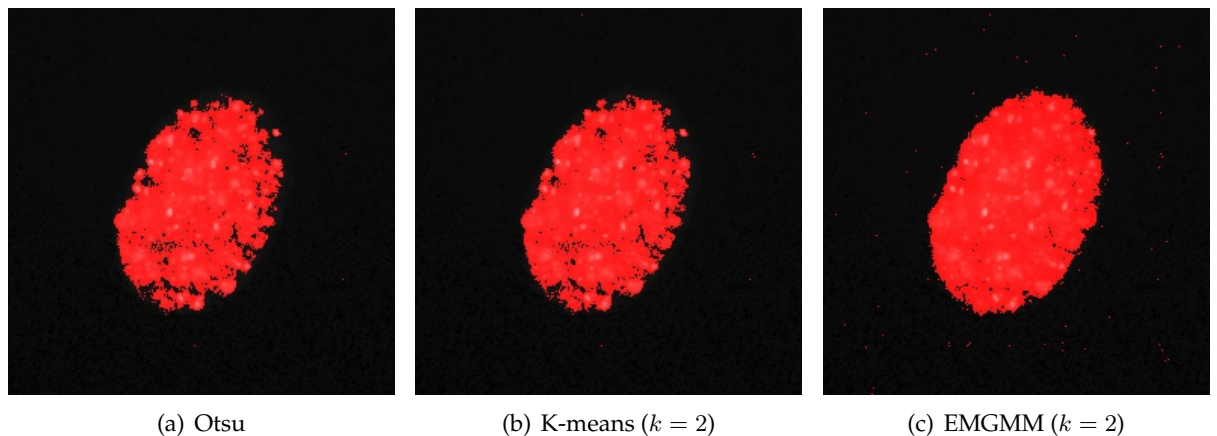
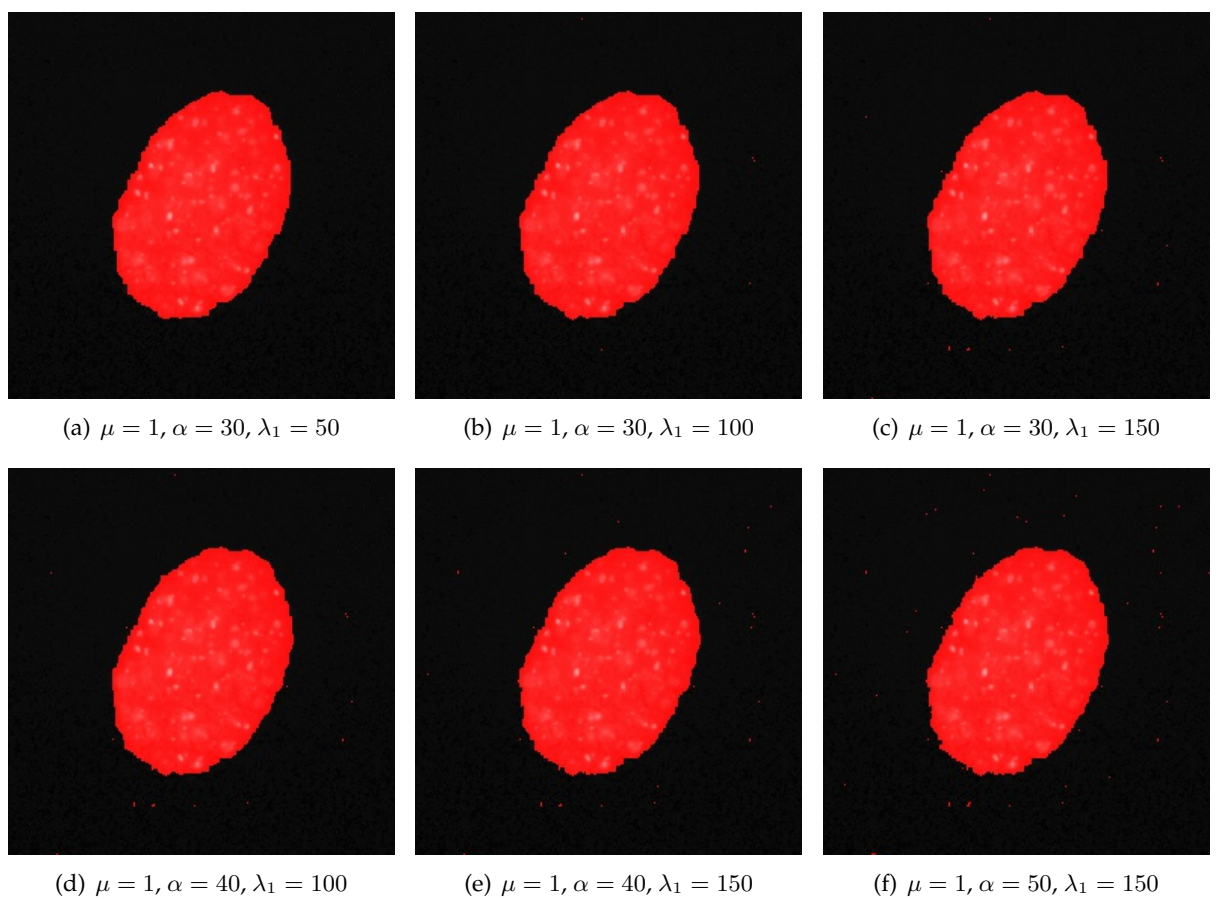


FIGURE 4.13: Image 4 from sample set Figure B.1 initial masks.

FIGURE 4.14: Segmented output for various combination of α and λ_1 for Image 4 in the sample set.

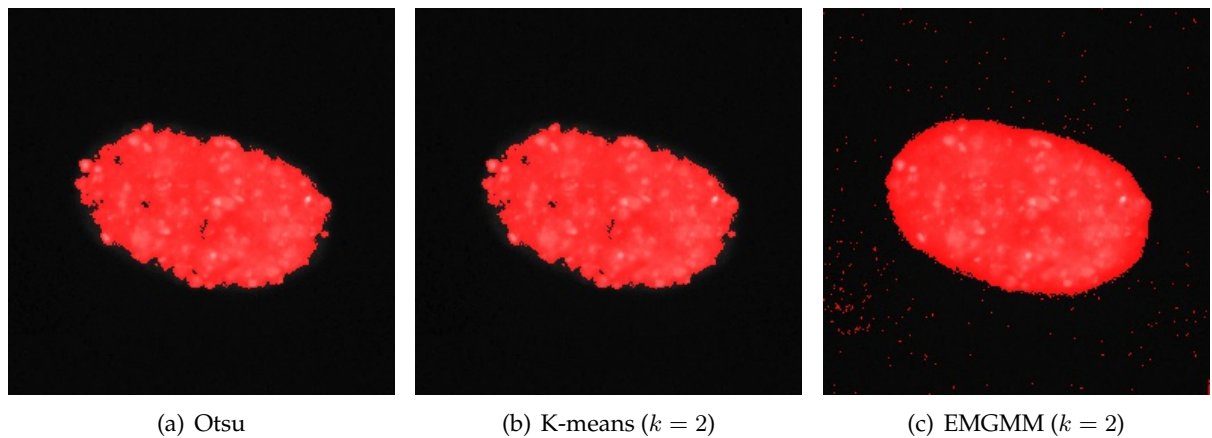


FIGURE 4.15: Image 5 from sample set Figure B.1 initial masks.

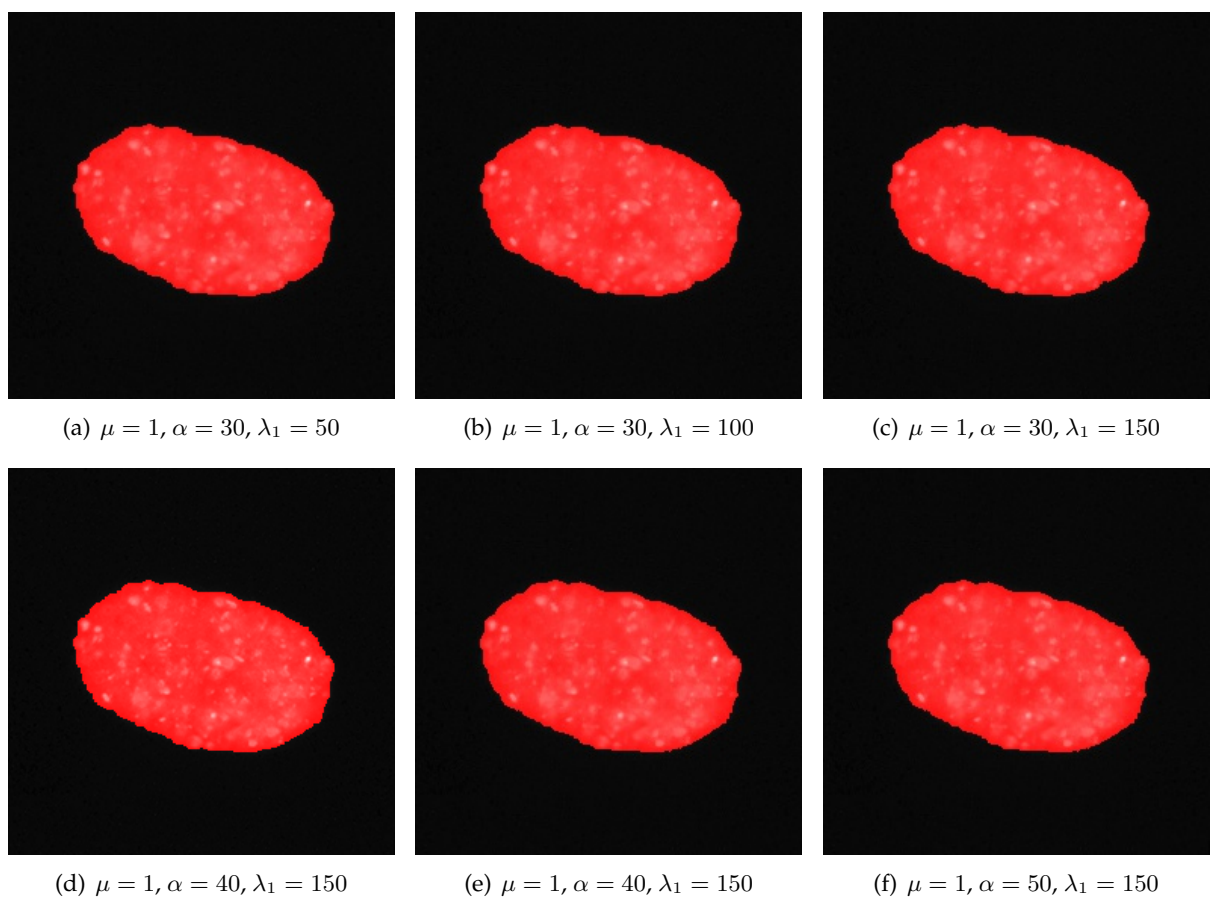


FIGURE 4.16: Segmented output for various combination of α and λ_1 for Image 5 in the sample set.

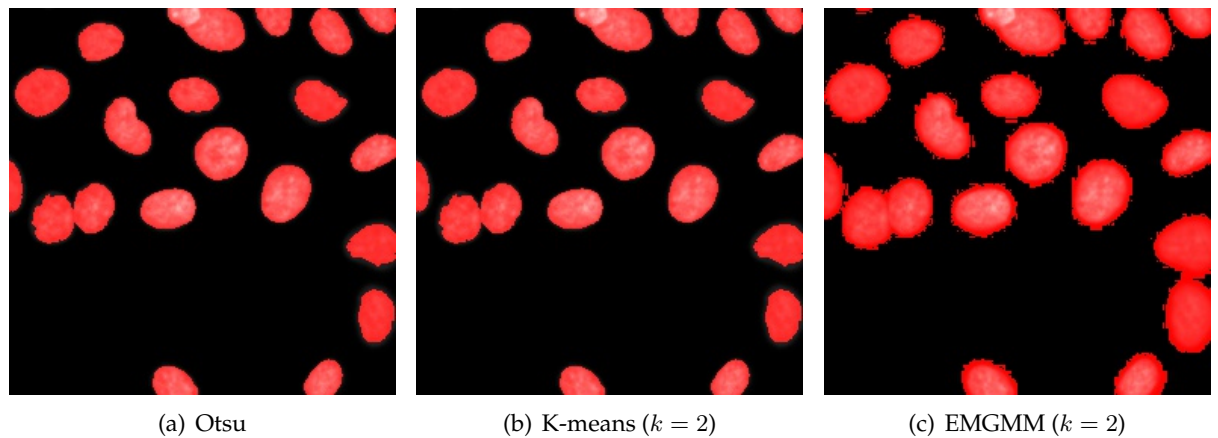


FIGURE 4.17: Image 6 from sample set Figure B.1 initial masks.

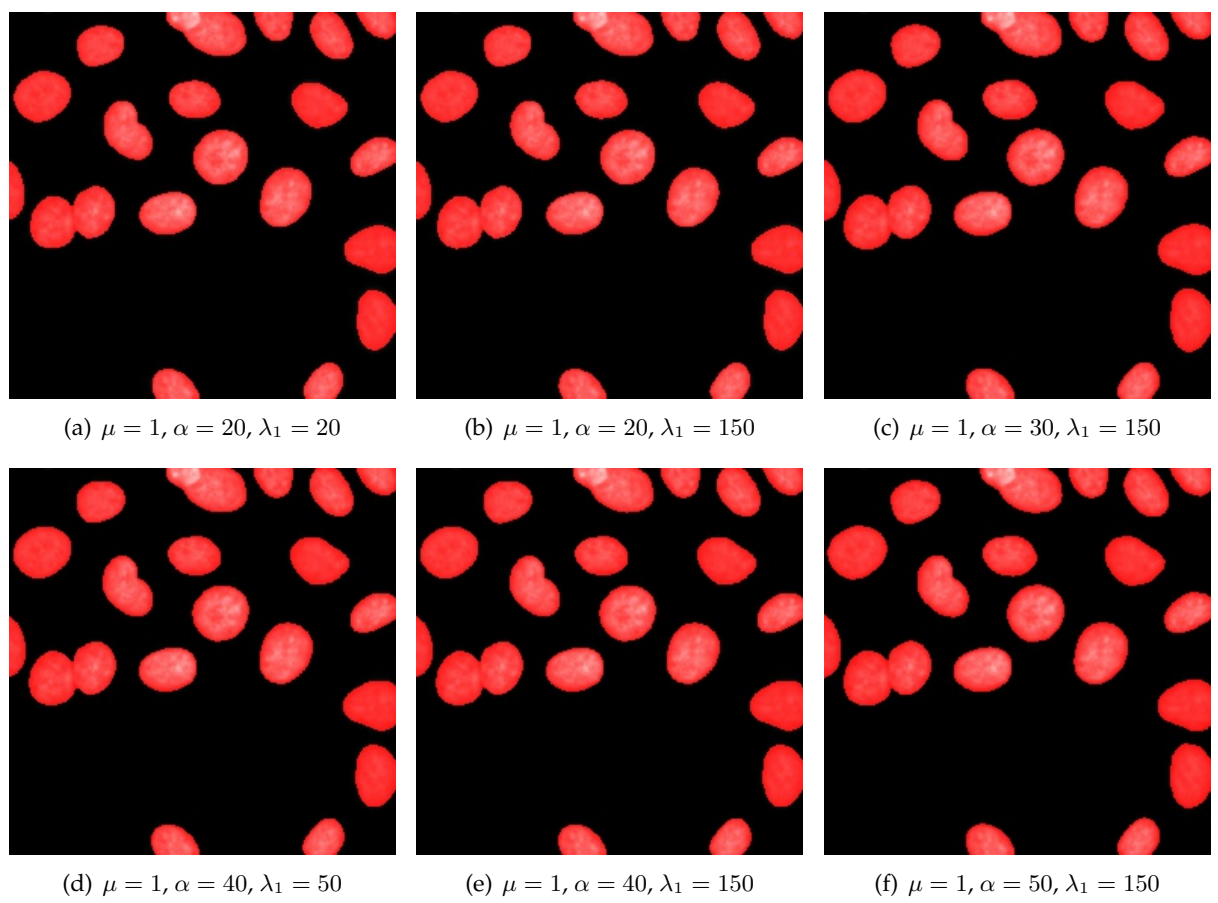
FIGURE 4.18: Segmented output for various combination of α and λ_1 for Image 6 in the sample set.

TABLE 4.1: Initial means and standard deviations for all images in the sample set for Otsu, K-means and EMGMM clustering.

	c_0	c_1	s_0	s_1
Image 1				
Otsu	0.0307515	0.26466	0.0385001	0, 0803506
K-means($k = 2$)	0.0308984	0.267192	0.0387009	0.0793621
EMGMM ($k = 2$)	0.0305648	0.261392	0.0382529	0.081608
Image 2				
Otsu	0.0293218	0.373293	0.054652	0.124376
K-means($k = 2$)	0.0293218	0.373293	0.054652	0.124376
EMGMM ($k = 2$)	0.010789	0.321058	0.0211362	0.140498
Image 3				
Otsu	0.0422978	0.105043	0.0104066	0.0269333
K-means($k = 2$)	0.0422978	0.105043	0.0104066	0.0269333
EMGMM ($k = 2$)	0.042026	0.103124	0.0100784	0.0273395
Image 4				
Otsu	0.0424602	0.147303	0.0133024	0.0513289
K-means($k = 2$)	0.0420671	0.145145	0.0125633	0.0513602
EMGMM ($k = 2$)	0.0407566	0.136167	0.0102742	0.052472
Image 5				
Otsu	0.037086	0.216513	0.0138978	0.0626164
K-means($k = 2$)	—	—	—	—
EMGMM ($k = 2$)	0.0343141	0.190501	0.00456055	0.0782783
Image 6				
Otsu	0.270483	0.00657006	0.0228327	0.0916426
K-means($k = 2$)	0.270483	0.00657006	0.0228327	0.0916426
EMGMM ($k = 2$)	0	0.187883	0	0.133022

The final values for the segmentation results are shown in Table 4.2. The table shows for each image, given the values for the input parameters, whether the degree of acceptance of the output. We take the final results are the means of object and the background. From the final results, we calculate the values for p_e , Equation (4.21), and h , Equation (4.24). The means for each image can vary greatly. To put the values of p_e and h into a relative perspective, they are also shown as a fraction of the distance between c_0 and c_1 . Let $k_p \in (0, 1)$ be the fraction of the distance $p_e - c_0$ and $c_1 - c_0$ as illustrated in Figure 4.19. Let $k_h \in (k_p, 1)$ be the fraction of the distance $h - c_0$ and $c_1 - c_0$ as illustrated in Figure 4.20. The following relation holds $0 < k_p < k_h$.



FIGURE 4.19: p_e as a fraction of the distance between c_0 and c_1 .

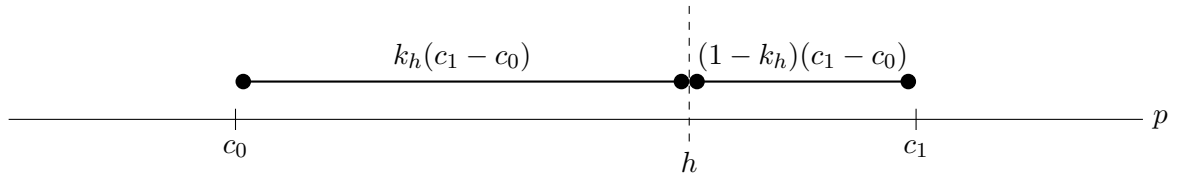
FIGURE 4.20: h as a fraction of the distance between c_0 and c_1 .

TABLE 4.2: Results from manual tuning.

Image	α	λ_1	c_0	c_1	p_e	h	k_p	k_h
1-O	30	100	0.009171	0.117209	0.025851	0.058086	0.154387	0.452755
1-O	40	100	0.006909	0.110953	0.021114	0.049359	0.136527	0.407996
1-O	40	50	0.006803	0.110618	0.020976	0.065665	0.136527	0.566987
1-O	40	150	0.006953	0.111119	0.021175	0.042396	0.136527	0.340248
1-O	40	200	0.007093	0.111541	0.021353	0.038508	0.136527	0.300772
1-O	45	150	0.006832	0.110758	0.020314	0.040326	0.129732	0.322287
1-O	50	150	0.006681	0.110301	0.019519	0.038516	0.123899	0.307235
1-K	30	100	0.009557	0.118306	0.026346	0.058499	0.154387	0.450049
1-K	40	100	0.006928	0.111013	0.021138	0.049379	0.136527	0.407847
1-K	40	50	0.006818	0.110658	0.020995	0.065680	0.136527	0.566856
1-K	40	150	0.007063	0.111430	0.021312	0.042514	0.136527	0.339679
1-K	40	200	0.007176	0.111789	0.021459	0.038600	0.136527	0.300384
1-K	45	150	0.006852	0.110824	0.020340	0.040348	0.129732	0.322165
1-K	50	150	0.006685	0.110311	0.019524	0.038521	0.123899	0.307219
1-E	30	150	0.008876	0.116478	0.025489	0.049694	0.154387	0.379343
1-E	40	100	0.006687	0.110890	0.020913	0.049142	0.136527	0.407426
1-E	40	50	0.006788	0.110583	0.020959	0.065649	0.136527	0.567093
1-E	40	150	0.006944	0.111087	0.021163	0.042385	0.136527	0.340313
1-E	40	200	0.007058	0.111434	0.021308	0.038469	0.136527	0.300940
1-E	45	150	0.006800	0.110654	0.020273	0.040291	0.129732	0.322481
1-E	50	150	0.006676	0.110283	0.019512	0.038510	0.123899	0.307268
2-O	30	150	0.007640	0.309246	0.054204	0.066628	0.154387	0.195579
2-O	40	50	0.007449	0.308057	0.048489	0.076410	0.136527	0.229407
2-O	40	100	0.007428	0.307890	0.048449	0.063950	0.136527	0.188118
2-O	40	150	0.007424	0.307975	0.048457	0.059239	0.136527	0.172400
2-O	40	200	0.007441	0.308094	0.048488	0.056764	0.136527	0.164052
2-O	45	150	0.007423	0.307976	0.046415	0.056577	0.129732	0.163545
2-O	50	150	0.007297	0.307166	0.044450	0.054107	0.123899	0.156103
2-K	30	150	0.007640	0.309246	0.054204	0.066628	0.154387	0.195579
2-K	40	50	0.007449	0.308057	0.048489	0.076410	0.136527	0.229407
2-K	40	100	0.007428	0.307890	0.048449	0.063950	0.136527	0.188118
2-K	40	150	0.007424	0.307975	0.048457	0.059239	0.136527	0.172400

2-K	40	200	0.007441	0.308094	0.048488	0.056764	0.136527	0.164052
2-K	45	150	0.007423	0.307976	0.046415	0.056577	0.129732	0.163545
2-K	50	150	0.007297	0.307166	0.044450	0.054107	0.123899	0.156103
2-E	30	150	0.007556	0.308779	0.054061	0.066498	0.154387	0.195674
2-E	40	50	0.007568	0.308796	0.048694	0.076578	0.136527	0.229095
2-E	40	100	0.007564	0.308815	0.048693	0.064163	0.136527	0.187881
2-E	40	150	0.007566	0.308838	0.048697	0.059458	0.136527	0.172244
2-E	40	200	0.007558	0.308800	0.048686	0.056948	0.136527	0.163952
2-E	45	150	0.007467	0.308260	0.046489	0.056646	0.129732	0.163496
2-E	50	150	0.007343	0.307470	0.044528	0.054178	0.123899	0.156053
3-O	10	150	0.041366	0.096327	0.054571	0.108955	0.240253	1.229755
3-O	10	200	0.041364	0.096323	0.054568	0.099806	0.240253	1.063370
3-O	10	400	0.041359	0.096339	0.054568	0.082894	0.240253	0.755457
3-O	10	800	0.041371	0.096708	0.054666	0.071643	0.240253	0.547049
3-O	20	150	0.041323	0.095848	0.051287	0.089056	0.182743	0.875426
3-O	30	150	0.041267	0.094999	0.049563	0.080313	0.154387	0.726674
3-O	40	150	0.044802	0.057616	0.046551	0.078701	0.136527	2.645434
3-K	10	150	0.041366	0.096327	0.054571	0.108955	0.240253	1.229755
3-K	10	200	0.041364	0.096323	0.054568	0.099806	0.240253	1.063370
3-K	10	400	0.041359	0.096339	0.054568	0.082894	0.240253	0.755457
3-K	10	800	0.041371	0.096708	0.054666	0.071643	0.240253	0.547049
3-K	20	150	0.041323	0.095848	0.051287	0.089056	0.182744	0.875426
3-K	30	150	0.041267	0.094999	0.049563	0.080313	0.154387	0.726674
3-K	40	150	0.044802	0.057616	0.046551	0.078701	0.136527	2.645434
3-E	10	150	0.041362	0.096283	0.054557	0.108952	0.240253	1.230667
3-E	10	200	0.041357	0.096260	0.054548	0.099799	0.240253	1.064463
3-E	10	400	0.041356	0.096309	0.054559	0.082890	0.240253	0.755812
3-E	10	800	0.041367	0.096932	0.054717	0.071656	0.240253	0.545117
3-E	20	150	0.041321	0.095836	0.051284	0.089054	0.182744	0.875599
3-E	30	150	0.041262	0.094923	0.049545	0.080307	0.154387	0.727635
3-E	40	150	0.044849	0.057396	0.046562	0.078753	0.136527	2.702195
4-O	30	50	0.040339	0.131121	0.054355	0.107943	0.154387	0.744683
4-O	30	100	0.040328	0.131038	0.054332	0.088659	0.154387	0.532819
4-O	30	150	0.040319	0.130976	0.054315	0.080354	0.154387	0.441615
4-O	40	100	0.040240	0.129694	0.052453	0.082233	0.136527	0.469438
4-O	40	150	0.040264	0.130244	0.052549	0.075108	0.136527	0.387237
4-O	50	150	0.040232	0.129761	0.051324	0.071509	0.123899	0.349362
4-K	30	50	0.040356	0.131362	0.054406	0.107962	0.154387	0.742875
4-K	30	100	0.040343	0.131304	0.054386	0.088682	0.154387	0.531430
4-K	30	150	0.040339	0.131307	0.054383	0.080387	0.154387	0.440244
4-K	40	100	0.040233	0.129556	0.052428	0.082222	0.136527	0.470084

4-K	40	150	0.040260	0.130177	0.052536	0.075101	0.136527	0.387482
4-K	50	150	0.040223	0.129553	0.051291	0.071494	0.123899	0.350061
4-E	30	50	0.040262	0.129873	0.054097	0.107852	0.154387	0.754261
4-E	30	100	0.040254	0.129884	0.054091	0.088555	0.154387	0.538901
4-E	30	150	0.040237	0.129708	0.054049	0.080225	0.154387	0.446937
4-E	40	100	0.040236	0.129624	0.052439	0.082227	0.136527	0.469763
4-E	40	150	0.040225	0.129532	0.052418	0.075043	0.136527	0.389868
4-E	50	150	0.040201	0.129085	0.051213	0.071456	0.123899	0.351638
5-O	30	50	0.034756	0.201631	0.060519	0.104517	0.154387	0.418045
5-O	30	150	0.034757	0.201659	0.060525	0.079633	0.154387	0.268872
5-O	40	150	0.034675	0.200630	0.057333	0.073912	0.136527	0.236429
5-O	50	150	0.034487	0.197806	0.054722	0.069683	0.123899	0.215506
5-K	30	50	0.034756	0.201631	0.060519	0.104517	0.154387	0.418045
5-K	30	150	0.034757	0.201659	0.060525	0.079633	0.154387	0.268872
5-K	40	150	0.034675	0.200630	0.057333	0.073912	0.136527	0.236429
5-K	50	150	0.034487	0.197806	0.054722	0.069683	0.123899	0.215506
5-E	30	50	0.034683	0.200718	0.060316	0.104407	0.154387	0.419937
5-E	30	150	0.034681	0.200701	0.060313	0.079483	0.154387	0.269859
5-E	40	150	0.034582	0.199297	0.057069	0.073726	0.136527	0.237648
5-E	50	150	0.034580	0.199280	0.054986	0.069870	0.123899	0.214269
6-O	20	20	0.002964	0.251959	0.048466	0.136161	0.182744	0.534939
6-O	20	150	0.002932	0.251781	0.048407	0.066168	0.182744	0.254113
6-O	30	50	0.001533	0.228802	0.036620	0.074639	0.154387	0.321672
6-O	30	150	0.001521	0.238690	0.038137	0.053144	0.154387	0.217666
6-O	40	50	0.001817	0.242106	0.034623	0.066509	0.136527	0.269226
6-O	40	150	0.001815	0.242097	0.034619	0.047477	0.136527	0.190034
6-O	50	50	0.001259	0.235130	0.030236	0.059146	0.123899	0.247513
6-O	50	150	0.001239	0.234857	0.030184	0.041921	0.123899	0.174135
6-K	20	20	0.002964	0.251959	0.048466	0.136161	0.182744	0.534939
6-K	20	150	0.002932	0.251781	0.048407	0.066168	0.182744	0.254113
6-K	30	50	0.001533	0.228802	0.036620	0.074639	0.154387	0.321672
6-K	30	150	0.001521	0.238690	0.038137	0.053144	0.154387	0.217666
6-K	40	50	0.001817	0.242106	0.034623	0.066509	0.136527	0.269226
6-K	40	150	0.001814	0.242097	0.034619	0.047476	0.136527	0.190034
6-K	50	50	0.001259	0.235130	0.030236	0.059146	0.123899	0.247513
6-K	50	150	0.001239	0.234857	0.030185	0.041921	0.123899	0.174135
6-E	20	20	0.002643	0.249529	0.047759	0.135753	0.182744	0.539155
6-E	20	150	0.002584	0.249164	0.047645	0.065530	0.182744	0.255277
6-E	30	50	0.002252	0.246370	0.039940	0.076508	0.154387	0.304183
6-E	30	150	0.002246	0.246324	0.039928	0.054615	0.154387	0.214558
6-E	40	50	0.001527	0.238746	0.033914	0.066025	0.136527	0.271893

TABLE 4.3: Average of final means for good segmentations.

Image	\bar{c}_0	\bar{c}_1
1	0,006824	0,110693
2	0,007468	0,308217
3	0,041334	0,095952
4	0,040282	0,130360
5	0,034656	0,200287
6	0,001926	0,241672

6-E	40	150	0.001519	0.238667	0.033896	0.046879	0.136527	0.191277
6-E	50	50	0.001655	0.240298	0.031222	0.059817	0.123899	0.243720
6-E	50	150	0.001645	0.240193	0.031201	0.042755	0.123899	0.172337

Upon comparing the initial means in Table 4.1 and final means for the acceptable and good segmentation results in Table 4.2, the values of the initial means are larger. This is due to over-segmentation produced by Otsu, K-means and EMGMM clustering. A naïve approach to shifting the initial means closer to the final means is to dilate the initial mask. This pushes the boundaries of the contour for the object to accept the lower intensity neighbouring pixels as well as removes these relatively higher values from the background mask.

To determine the optimal dilation size, we compare the difference of the mean values for each image in Table 4.2, for the good segmentation results only. These values are shown in Table 4.3. We use an elliptical element for dilation. The results of the dilation and the difference from the respective final means is shown in Table 4.4, Table 4.5 and Table 4.6 for the initial masks obtained from Otsu binarization, K-means and EMGMM clustering respectively. The closest values to the average final mean is highlighted in blue. From the tables it can be seen that a dilation size of 3 for a elliptical dilation element results in mean values that are closest to the average final means.

TABLE 4.4: Dilation after Otsu binarization.

Image	Size	c_0	c_1	$ c_0 - \bar{c}_0 $	$ c_1 - \bar{c}_1 $	$\sum_i c_i - \bar{c}_i $
1	3	0.027716	0.205161	0.020892	0.094468	0.115360
1	5	0.026188	0.173038	0.019364	0.062345	0.081709
1	7	0.024682	0.151369	0.017858	0.040676	0.058534
1	9	0.023158	0.136273	0.016334	0.025580	0.041914
1	11	0.021564	0.124931	0.014739	0.014238	0.028978
1	13	0.019981	0.116536	0.013157	0.005843	0.018999
1	15	0.018341	0.109705	0.011517	0.000988	0.012505
2	3	0.007563	0.301761	9.47e-05	0.006456	0.006551
2	5	0.006025	0.286271	0.001443	0.021946	0.023389
2	7	0.005386	0.273472	0.002082	0.034745	0.036827
2	9	0.004936	0.262053	0.002532	0.046164	0.048696
2	11	0.004587	0.250695	0.002881	0.057522	0.060403
2	13	0.004277	0.240651	0.003191	0.067566	0.070757

2	15	0.004041	0.231146	0.003428	0.077071	0.080498
3	3	0.041796	0.090729	0.000462	0.005223	0.005685
3	5	0.041641	0.084544	0.000307	0.011408	0.011715
3	7	0.041535	0.080118	0.000201	0.015834	0.016034
3	9	0.042983	0.076541	0.001649	0.019411	0.021059
3	11	0.041439	0.073293	0.000105	0.022659	0.022764
3	13	0.041397	0.070676	6.27e-05	0.025276	0.025339
3	15	0.041369	0.068354	3.48e-05	0.027599	0.027633
4	3	0.041060	0.133918	0.000778	0.003558	0.004336
4	5	0.040715	0.128101	0.000433	0.002259	0.002692
4	7	0.040534	0.122898	0.000252	0.007462	0.007714
4	9	0.040429	0.118341	0.000147	0.012019	0.012166
4	11	0.040354	0.113853	7.17e-05	0.016507	0.016579
4	13	0.040297	0.109960	1.53e-05	0.020400	0.020415
4	15	0.040235	0.106414	4.70e-05	0.023946	0.023993
5	3	0.035322	0.203137	0.000666	0.002850	0.003516
5	5	0.034726	0.193711	7.02e-05	0.006576	0.006646
5	7	0.034434	0.184644	0.000222	0.015643	0.015865
5	9	0.034281	0.176477	0.000375	0.023810	0.024185
5	11	0.034188	0.168599	0.000468	0.031688	0.032156
5	13	0.034120	0.161732	0.000536	0.038555	0.039091
5	15	0.034056	0.155296	0.000600	0.044991	0.045591
6	3	0.000457	0.209125	0.001469	0.032547	0.034016
6	5	7.29e-05	0.171123	0.001853	0.070549	0.072402
6	7	1.84e-05	0.144280	0.001908	0.097392	0.099299
6	9	1.08e-05	0.125501	0.001915	0.116171	0.118086
6	11	1.15e-05	0.110706	0.001914	0.130966	0.132880
6	13	1.27e-05	0.100486	0.001913	0.141186	0.143099
6	15	1.44e-05	0.092725	0.001912	0.148947	0.150858

TABLE 4.5: Dilation after K-means clustering.

Image	Size	c_0	c_1	$ c_0 - \bar{c}_0 $	$ c_1 - \bar{c}_1 $	$\sum_i c_i - \bar{c}_i $
1	3	0.027716	0.205161	0.020892	0.094468	0.115360
1	5	0.026188	0.173038	0.019364	0.062345	0.081709
1	7	0.024682	0.151369	0.017858	0.040676	0.058534
1	9	0.023158	0.136273	0.016334	0.025580	0.041914
1	11	0.021564	0.124931	0.014739	0.014238	0.028978
1	13	0.019981	0.116536	0.013157	0.005843	0.018999
1	15	0.018341	0.109705	0.011517	0.000988	0.012505
2	3	0.007563	0.301761	9.47e-05	0.006456	0.006551

2	5	0.006025	0.286271	0.001443	0.021946	0.023389
2	7	0.005386	0.273472	0.002082	0.034745	0.036827
2	9	0.004936	0.262053	0.002532	0.046164	0.048696
2	11	0.004587	0.250695	0.002881	0.057522	0.060403
2	13	0.004277	0.240651	0.003191	0.067566	0.070757
2	15	0.004041	0.231146	0.003427	0.077071	0.080499
3	3	0.041796	0.090729	0.000462	0.005223	0.005685
3	5	0.041641	0.084544	0.000307	0.011408	0.011715
3	7	0.041535	0.080118	0.000201	0.015834	0.016034
3	9	0.041480	0.076541	0.000146	0.019411	0.019557
3	11	0.041439	0.073293	0.000105	0.022659	0.022764
3	13	0.041397	0.070676	6.27e-05	0.025276	0.025339
3	15	0.041369	0.068354	3.48e-05	0.027599	0.027633
4	3	0.041060	0.133918	0.000778	0.003558	0.004336
4	5	0.040715	0.128101	0.000433	0.002259	0.002692
4	7	0.040534	0.122898	0.000252	0.007462	0.007714
4	9	0.040429	0.118341	0.000147	0.012019	0.012166
4	11	0.040354	0.113853	7.17e-05	0.016507	0.016579
4	13	0.040297	0.109960	1.53e-05	0.020400	0.020415
4	15	0.040235	0.106414	4.70e-05	0.023946	0.023993
5	3	0.035322	0.203137	0.000666	0.002850	0.003516
5	5	0.034726	0.193711	7.02e-05	0.006576	0.006646
5	7	0.034434	0.184644	0.000222	0.015643	0.015865
5	9	0.034281	0.176477	0.000375	0.023810	0.024185
5	11	0.034188	0.168599	0.000468	0.031688	0.032156
5	13	0.034120	0.161732	0.000536	0.038555	0.039091
5	15	0.034056	0.155296	0.000600	0.044991	0.045591
6	3	0.000457	0.209125	0.001469	0.032547	0.034016
6	5	7.29e-05	0.171123	0.001853	0.070549	0.072402
6	7	1.84e-05	0.144280	0.001908	0.097392	0.099299
6	9	1.08e-05	0.125501	0.001915	0.116171	0.118086
6	11	1.15e-05	0.110706	0.001914	0.130966	0.132880
6	13	1.27e-05	0.100486	0.001913	0.141186	0.143099
6	15	1.44e-05	0.092725	0.001912	0.148947	0.150858

TABLE 4.6: Dilation after EM-GMM clustering.

Image	Size	c_0	c_1	$ c_0 - \bar{c}_0 $	$ c_1 - \bar{c}_1 $	$\sum_i c_i - \bar{c}_i $
1	3	0.027251	0.198511	0.020427	0.087818	0.108245
1	5	0.025597	0.166707	0.018773	0.056014	0.074787
1	7	0.023968	0.146071	0.017144	0.035378	0.052522

1	9	0.022313	0.131983	0.015489	0.021290	0.036779
1	11	0.020595	0.121338	0.013771	0.010645	0.024416
1	13	0.018866	0.113441	0.012042	0.002748	0.014789
1	15	0.017084	0.107025	0.010260	0.003668	0.013928
2	3	0.006516	0.294763	0.000952	0.013454	0.014406
2	5	0.005719	0.280590	0.001748	0.027627	0.029375
2	7	0.005165	0.268079	0.002303	0.040138	0.042441
2	9	0.004774	0.256867	0.002694	0.051350	0.054044
2	11	0.004438	0.245779	0.003030	0.062438	0.065468
2	13	0.004165	0.235995	0.003303	0.072222	0.075525
2	15	0.003947	0.226736	0.003521	0.081481	0.085002
3	3	0.041729	0.089955	0.000395	0.005997	0.006392
3	5	0.041603	0.083968	0.000269	0.011984	0.012252
3	7	0.041502	0.079529	0.000168	0.016423	0.016590
3	9	0.041435	0.075914	0.000101	0.020038	0.020138
3	11	0.041384	0.072717	5.00e-05	0.023236	0.023285
3	13	0.041335	0.070134	1.30e-06	0.025819	0.025819
3	15	0.041299	0.067855	3.52e-05	0.028097	0.028132
4	3	0.040788	0.114645	0.000506	0.015715	0.016221
4	5	0.040886	0.099155	0.000604	0.031205	0.031809
4	7	0.041119	0.087943	0.000838	0.042417	0.043255
4	9	0.041369	0.080176	0.001087	0.050184	0.051271
4	11	0.041665	0.074350	0.001383	0.056010	0.057393
4	13	0.042029	0.070365	0.001747	0.059995	0.061742
4	15	0.042324	0.067586	0.002042	0.062774	0.064816
5	3	0.034368	0.147707	0.000288	0.052580	0.052868
5	5	0.034298	0.119630	0.000358	0.080657	0.081015
5	7	0.034222	0.102563	0.000434	0.097724	0.098158
5	9	0.034181	0.092259	0.000475	0.108028	0.108504
5	11	0.034143	0.085251	0.000513	0.115036	0.115549
5	13	0.034105	0.080911	0.000551	0.119377	0.119928
5	15	0.034075	0.077899	0.000581	0.122388	0.122969
6	3	0.000000	0.136655	0.001926	0.105017	0.106943
6	5	0.000000	0.116893	0.001926	0.124779	0.126705
6	7	0.000000	0.103734	0.001926	0.137938	0.139864
6	9	0.000000	0.094463	0.001926	0.147209	0.149135
6	11	0.000000	0.087325	0.001926	0.154347	0.156273
6	13	0.000000	0.082486	0.001926	0.159186	0.161112
6	15	0.000000	0.079177	0.001926	0.162495	0.164421

When defining the values for p_e and h implicitly and k_p and k_h respectively, we can find the updated equation for determining α following from Equation (4.22)

$$\begin{aligned}\alpha &= \left(\frac{c_1 - c_0}{p_e - c_0} - 1 \right)^2 \\ &= \left(\frac{c_1 - c_0 - p_e + c_0}{p_e - c_0} \right)^2 \\ &= \left(\frac{c_1 - c_0 - c_0 - k_p(c_1 - c_0) + c_0}{c_0 + k_p(c_1 - c_0) - c_0} \right)^2 \\ &= \left(\frac{c_1 - c_0 - k_p(c_1 - c_0)}{k_p(c_1 - c_0)} \right)^2 \\ &= \left(\frac{(1 - k_p)(c_1 - c_0)}{k_p(c_1 - c_0)} \right)^2\end{aligned}$$

Therefore, given k_p , the equation to calculate α is

$$\alpha = \left(\frac{1 - k_p}{k_p} \right)^2 \quad (4.28)$$

$$\alpha - 1 = \frac{1 - 2k_p + k_p^2 - k_p^2}{k_p^2} = \frac{1 - 2k_p}{k_p^2} \quad (4.29)$$

Following from Equation (4.25)...

$$\begin{aligned}h &= c_0 + k_h(c_1 - c_0) = c_1 - (1 - k_h)(c_1 - c_0) \\ \alpha(c_0 + k_h(c_1 - c_0) - c_0)^2 - (c_1 - (1 - k_h)(c_1 - c_0) - c_1)^2 &= \alpha k_h^2(c_1 - c_0)^2 + (k_h - 1)^2(c_1 - c_0)^2 \\ &= \alpha k_h^2(c_1 - c_0)^2 - (k_h - 1)^2(c_1 - c_0)^2 \\ &= (c_1 - c_0)^2(\alpha k_h^2 - (k_h - 1)^2) \\ &= (c_1 - c_0)^2 (\alpha k_h^2 - k_h^2 + 2k_h - 1) \\ &= (c_1 - c_0)^2 (k_h^2(\alpha - 1) + 2k_h - 1) \\ &= (c_1 - c_0)^2 \left(\left(\frac{1 - 2k_p}{k_p^2} \right) k_h^2 + 2k_h - 1 \right) \\ \lambda_1 &= \frac{\mu (2\sqrt{2} + 4)}{(c_1 - c_0)^2 \left(\left(\frac{1 - 2k_p}{k_p^2} \right) k_h^2 + 2k_h - 1 \right)} \quad (4.30)\end{aligned}$$

4.3 Experimental Results

The parameters α and λ_1 , in the proposed parameter estimation method, depend greatly on predicting good final means, c_0 and c_1 , as well as p_e and h for the ideal segmentation. For determining α we find the average of all k_p in Table 4.2 for all good segmentations. This is calculated to be

$$k_p = 0.154494.$$

From this we can calculate the value for α immediately using Equation (4.28). This turns out to be

$$\alpha = 29.9509. \quad (4.31)$$

Similarly, to determine h we find the average of all k_h in Table 4.2 for all good segmentations. This is calculated to be

$$k_h = 0.412737.$$

It is rarely the case where this is known or can be calculated, if ever at all. Instead, we use the results from three popular unsupervised clustering algorithms and compare the final segmented result against a ground truth. The algorithms chosen to generate an initial mask, from which we calculate c_0 and c_1 are: Otsu [196], k-means [197] with $k = 2$ and Expectation Maximisation Gaussian Mixture Modelling (EMGMM) [198] with $k = 2$. From observations we see that these algorithms tend to generate over-segmented results. In light of this, we generate a fourth mask which is an EMGMM output with dilation. For dilation we used an elliptical shape with a radius of $3px$. Once we have the initial mask and have calculated the initial c_0 and c_1 from this initial mask, we calculate λ_1 using Equation (4.30). Now that we have α and λ_1 we calculate λ_0 using Equation (4.16). We set the termination criterion at $\epsilon = 1 \times 10^{-3}$.

We also compare our results to two previously published parameter settings. The first is the parameter settings used in [193], by El Zehiry *et al.*, which is where this technique was first published. Their results showed excellent segmentation output on synthetic images and mammography images with very high robustness against noise. They do not specify the noise type. The second parameter setting which we test against is presented in [191], by Masaka *et al.*. Their parameter setting were based on a timelapse series of fluorescence images. Their scheme is a hybrid of algorithms design to segment whole fluorescent cells, however, we use the parameters settings they've presented for segmentation only. Their parameters were obtained by minimising the Jaccard coefficient over the timelapse series. Their results show a greater area of cell detection and smoother boundaries. Although, the smoother contours are a result of CED-ORI [cite cedor] which is part of the scheme before segmentation.

The initial masks used in subsequent parameter estimation is shown in Figures 4.21, 4.23, 4.25, 4.27, 4.29, 4.31, 4.33, 4.35, 4.37, 4.39, 4.41, 4.43, 4.45, 4.47, 4.49, 4.51, 4.53, 4.55, 4.57, 4.59, 4.61, 4.63, 4.65, 4.67 and 4.69.

The segmented outputs are shown in Figures 4.22, 4.24, 4.26, 4.28, 4.30, 4.32, 4.34, 4.36, 4.38, 4.40, 4.42, 4.44, 4.46, 4.48, 4.50, 4.52, 4.54, 4.56, 4.58, 4.60, 4.62, 4.64, 4.66, 4.68 and 4.70.

The parameter settings and corresponding results are summarised in Table 4.7. The last column, labelled "Diff", is a measure of how far off the final means are from the ideal. It is calculated as

$$Diff = |c_0^{Final} - c_0^{Ideal}| + |c_1^{Final} - c_1^{Ideal}|.$$

In Table 4.7 differentiate between methods on the same image as follows:

[imageno]-[method],

where *imageno* goes from 1 to 25 and *method* is defined as follows:

- n** - using parameter setting presented in [193].
- m** - using parameter setting presented in [191].
- o** - Proposed method with parameters estimated from an initial Otsu segmentation.
- k** - Proposed method with parameters estimated from an initial K-means segmentation with $k = 2$.
- e** - Proposed method with parameters estimated from an initial EMGMM segmentation with $k = 2$.

d - Proposed method with parameters estimated from an initial EMGMM segmentation with $k = 2$ and an elliptical dilation of $3px$.

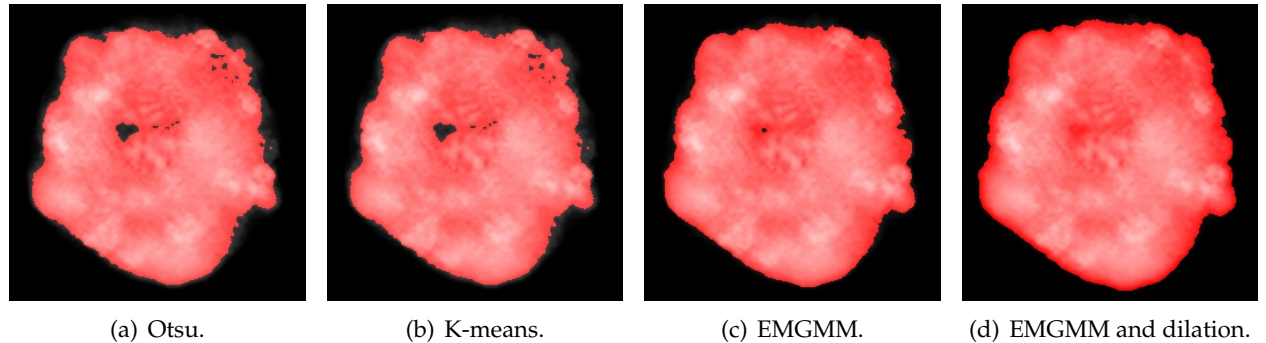


FIGURE 4.21: Image 1 from test set Appendix B initial masks.

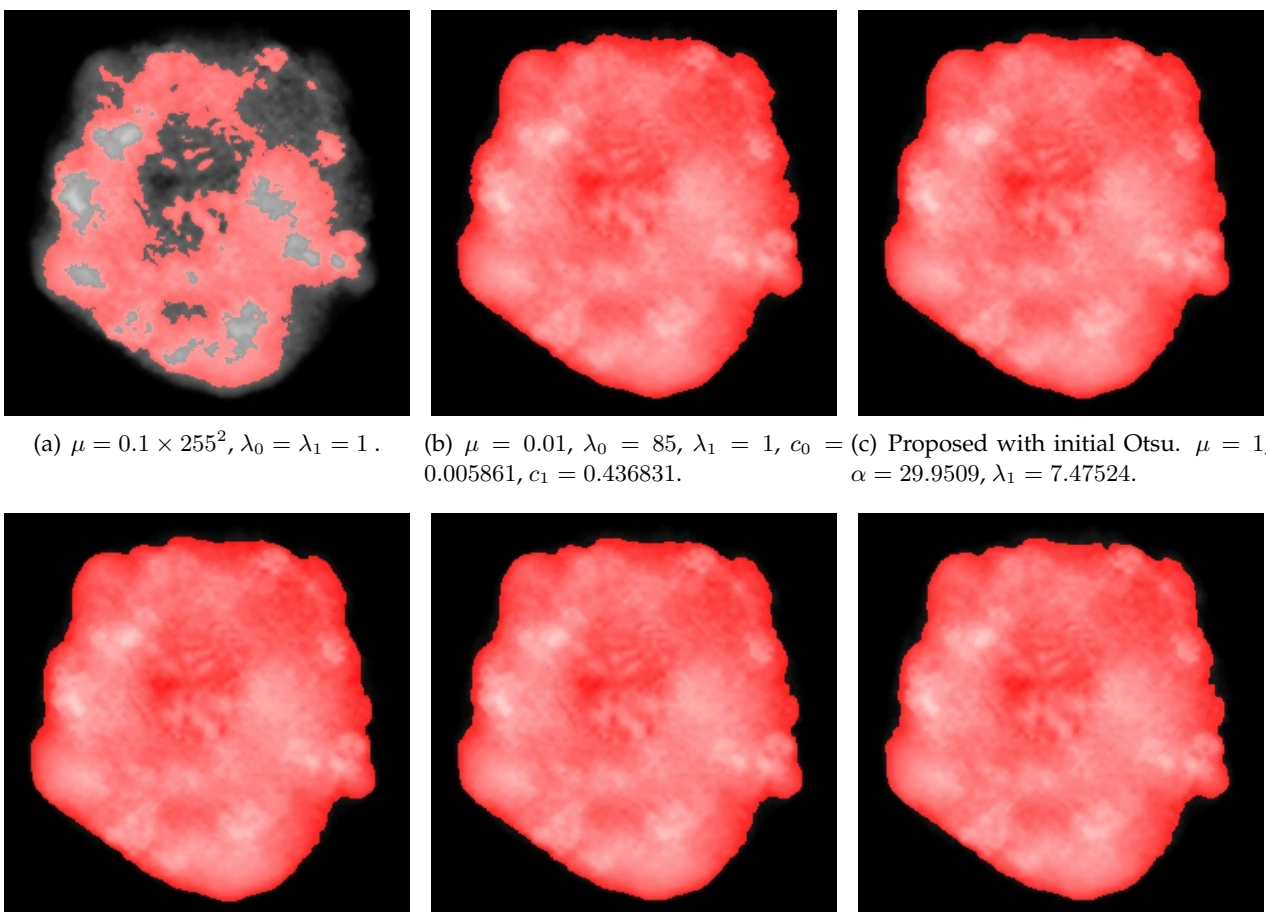


FIGURE 4.22: Image 1 from test set Appendix B segmentation results.

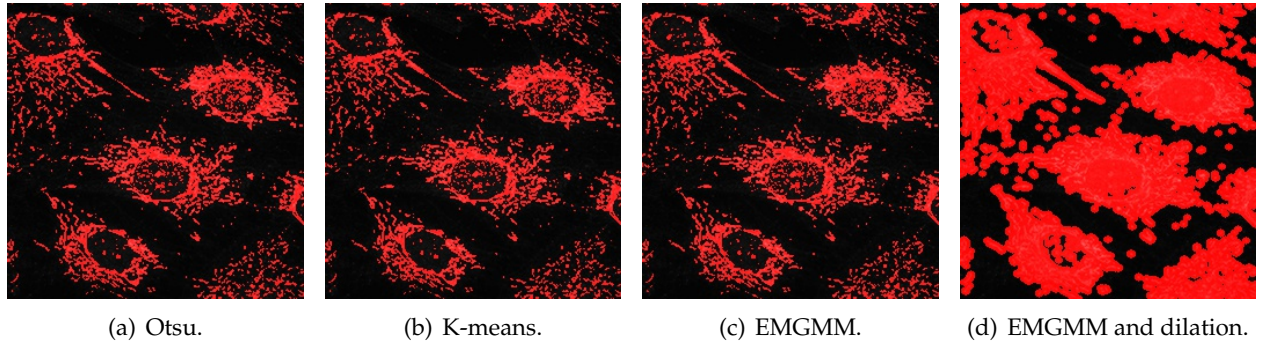


FIGURE 4.23: Image 2 from test set Appendix B initial masks.

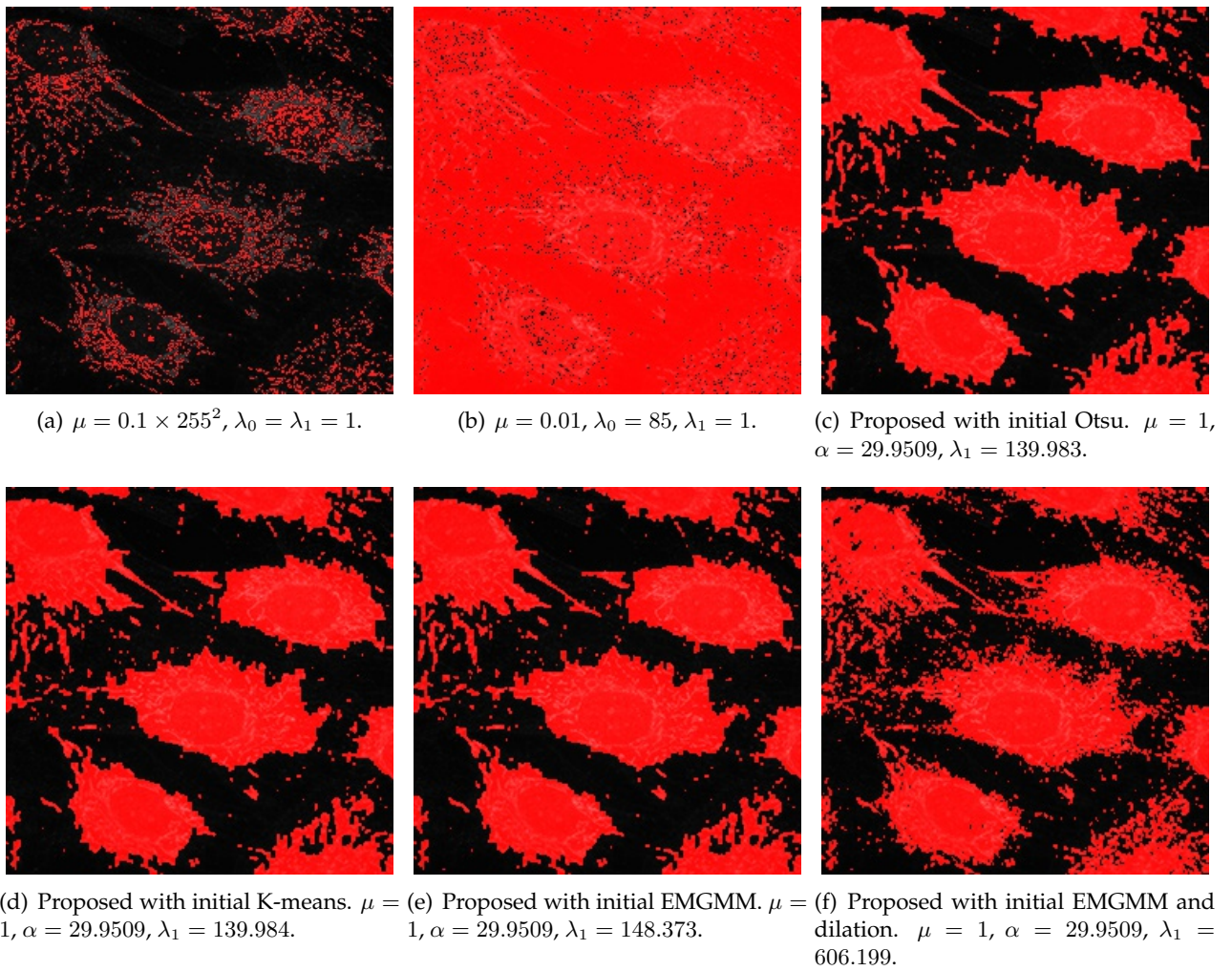


FIGURE 4.24: Image 2 from test set Appendix B segmentation results.

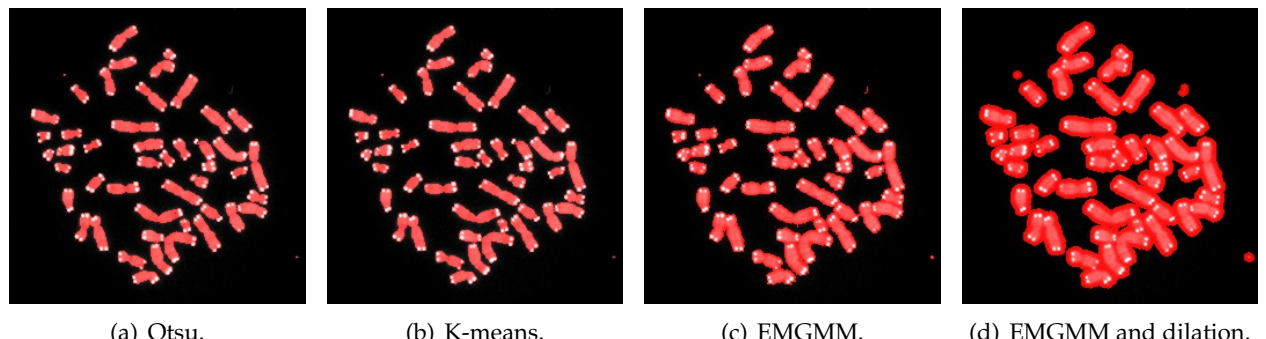


FIGURE 4.25: Image 3 from test set Appendix B initial masks.

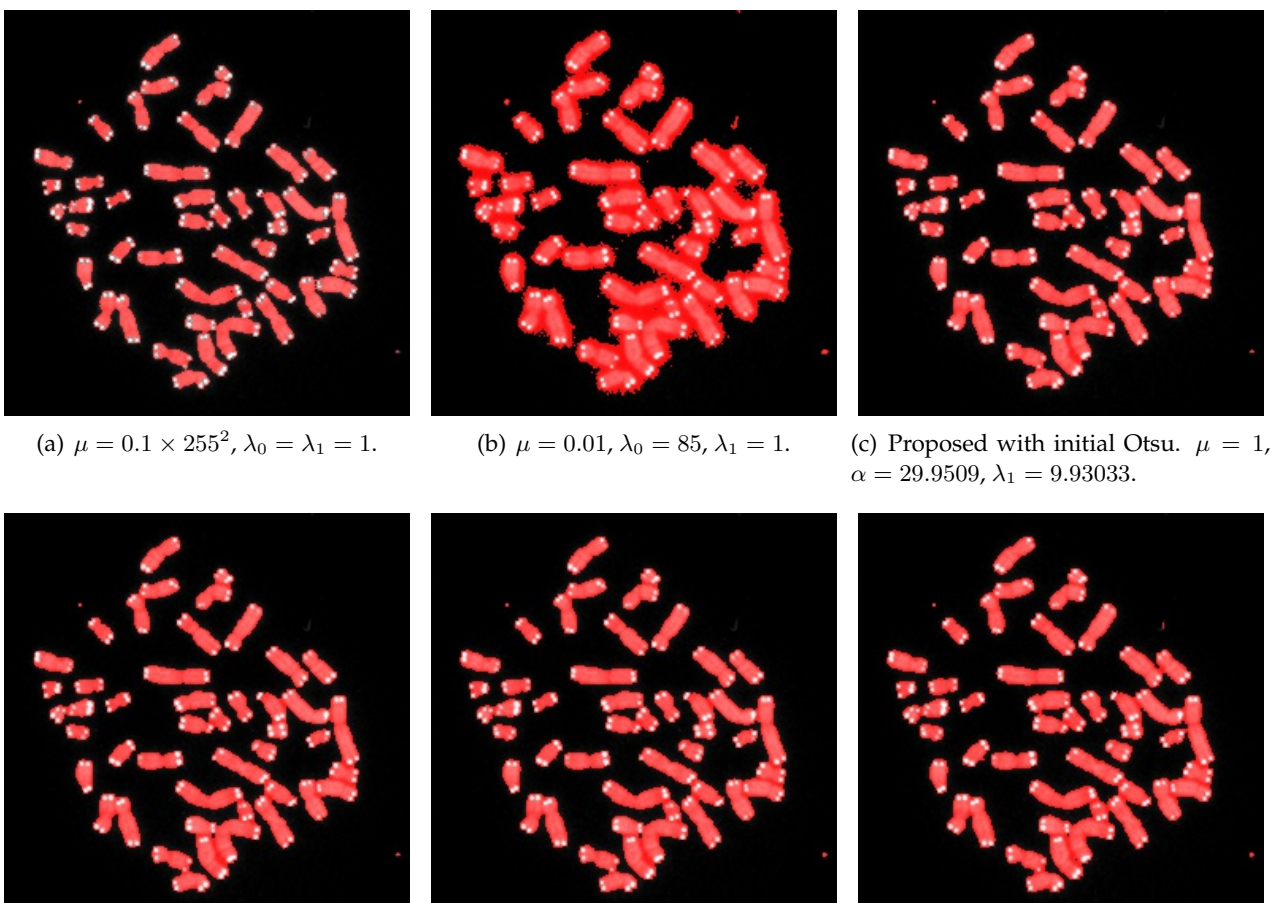


FIGURE 4.26: Image 3 from test set Appendix B segmentation results.

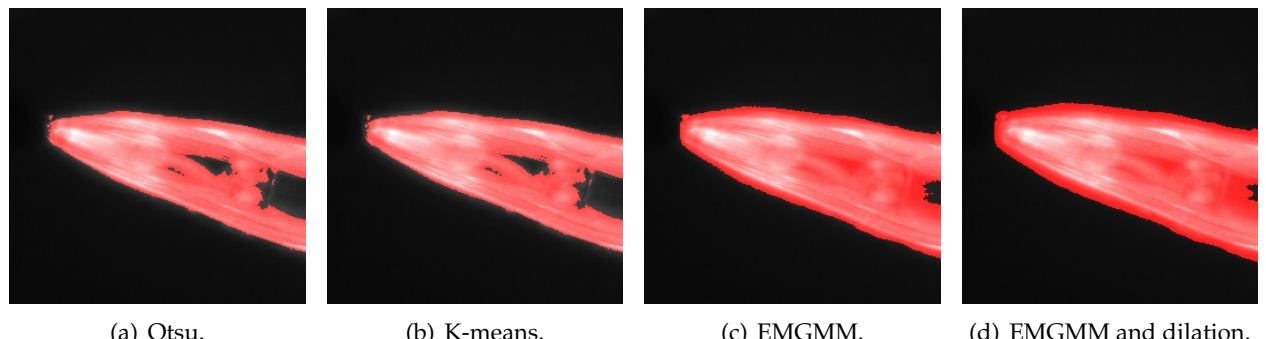


FIGURE 4.27: Image 4 from test set Appendix B initial masks.

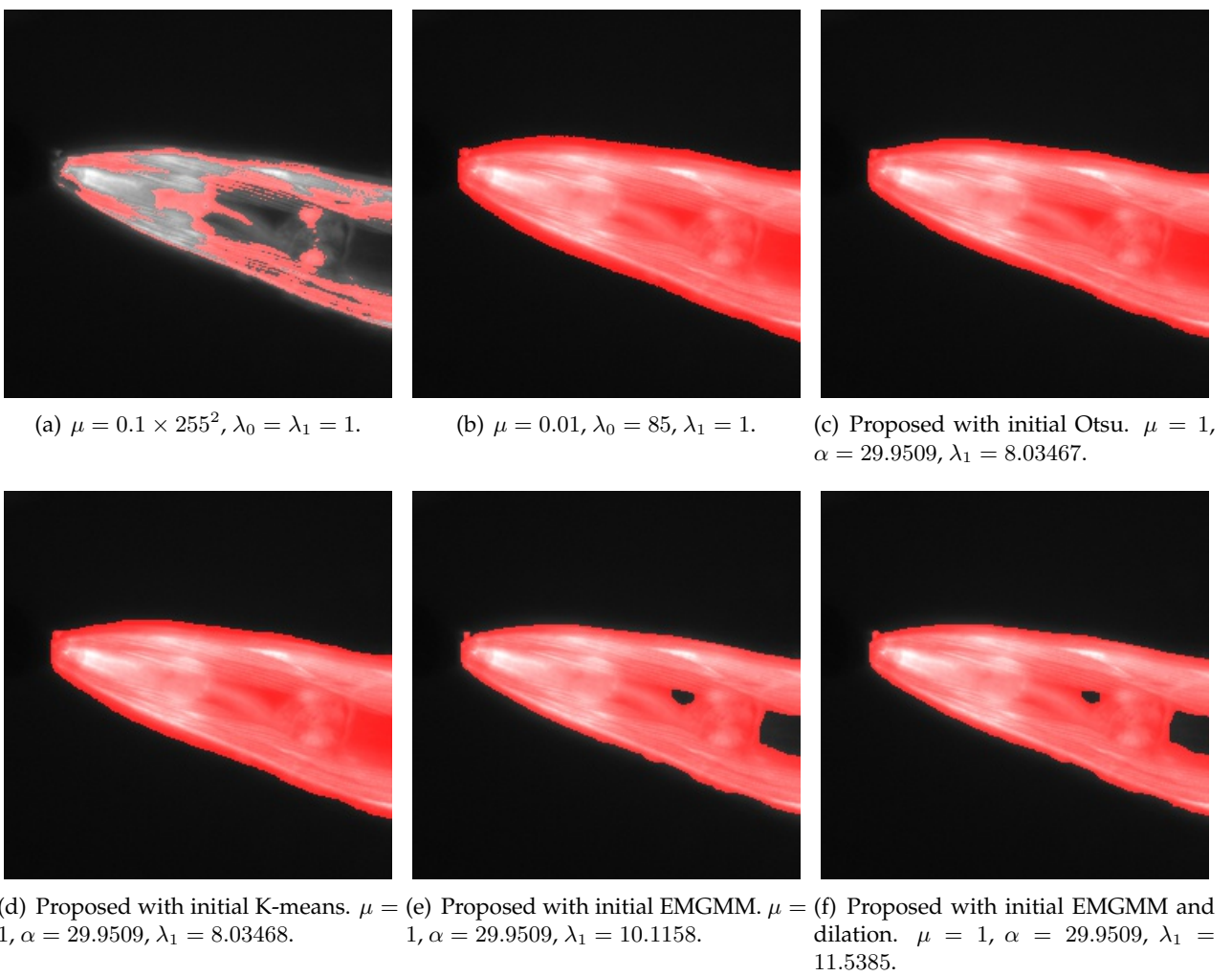


FIGURE 4.28: Image 4 from test set Appendix B segmentation results.

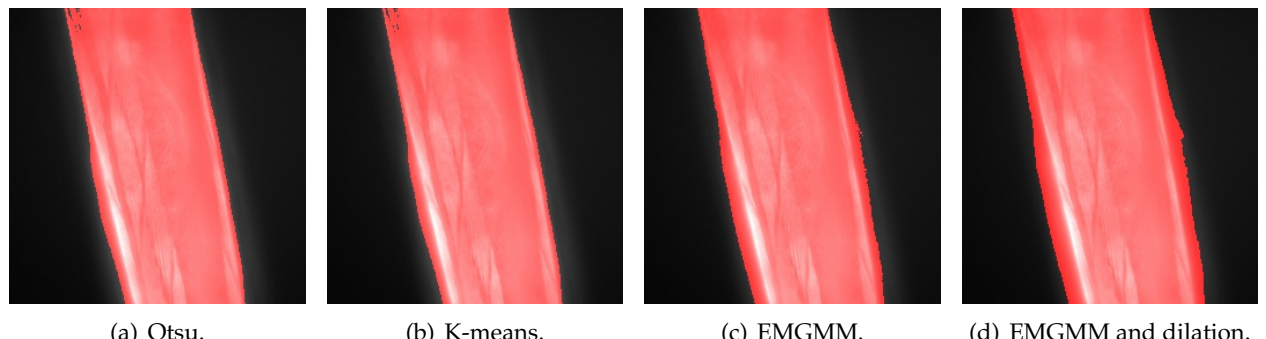


FIGURE 4.29: Image 5 from test set Appendix B initial masks.

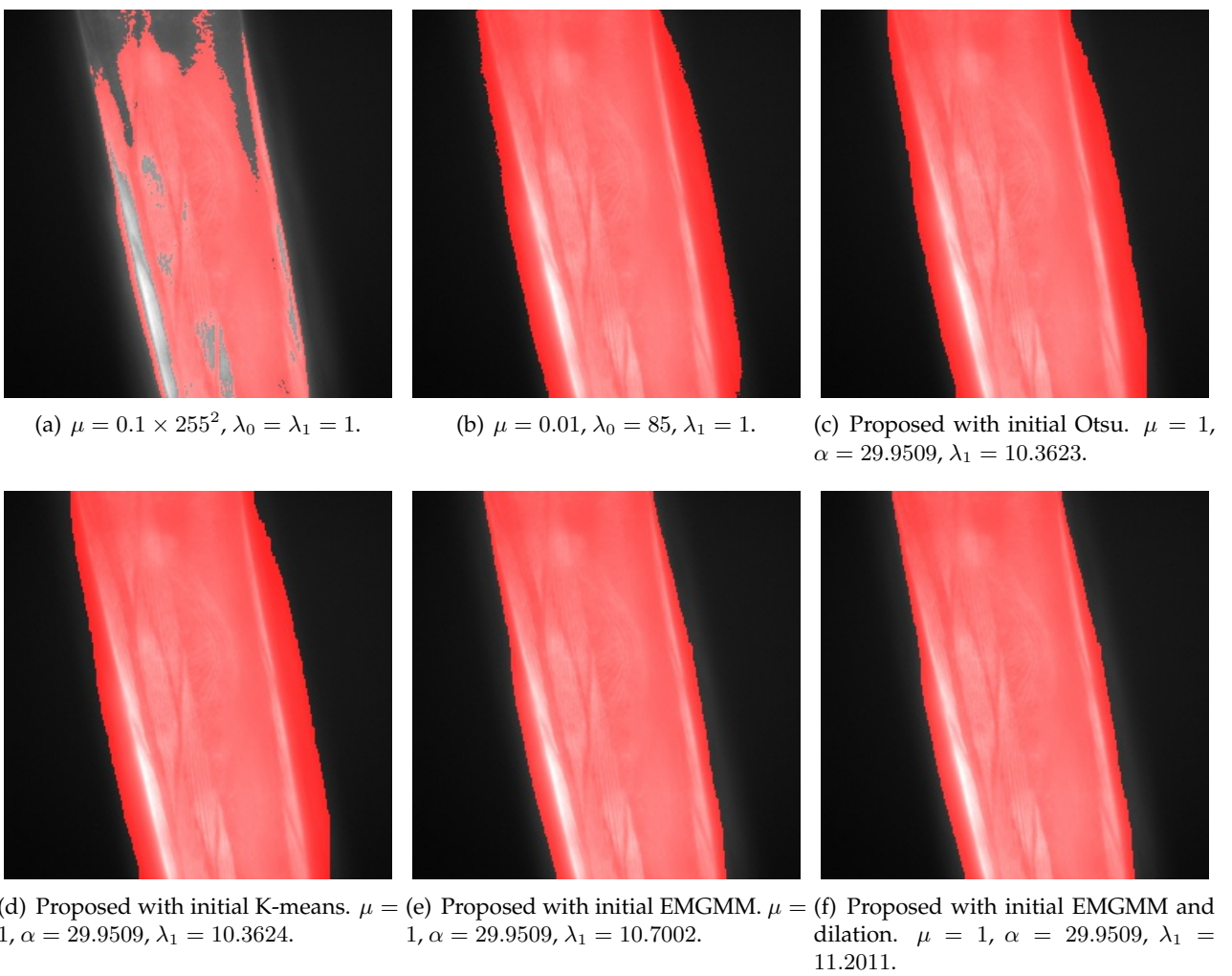


FIGURE 4.30: Image 5 from test set Appendix B segmentation results.

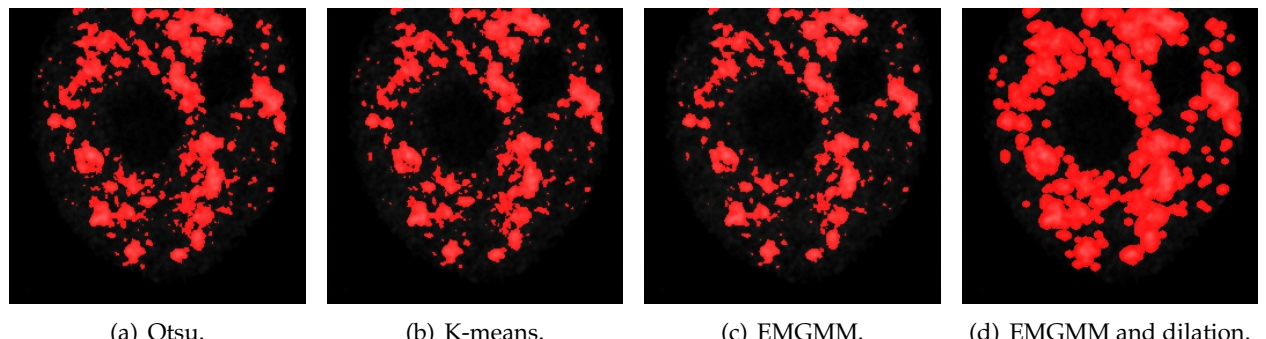


FIGURE 4.31: Image 6 from test set Appendix B initial masks.

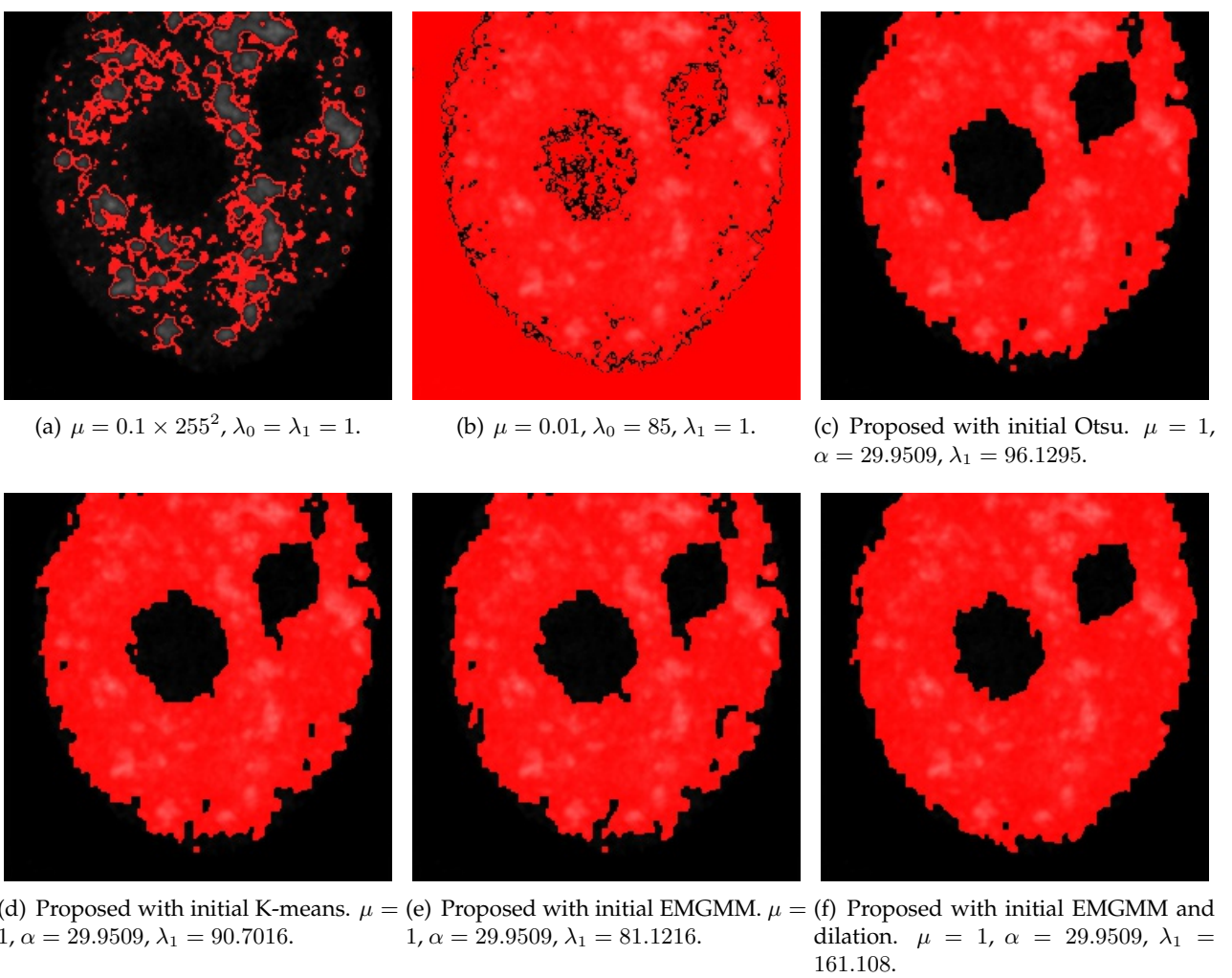


FIGURE 4.32: Image 6 from test set Appendix B segmentation results.

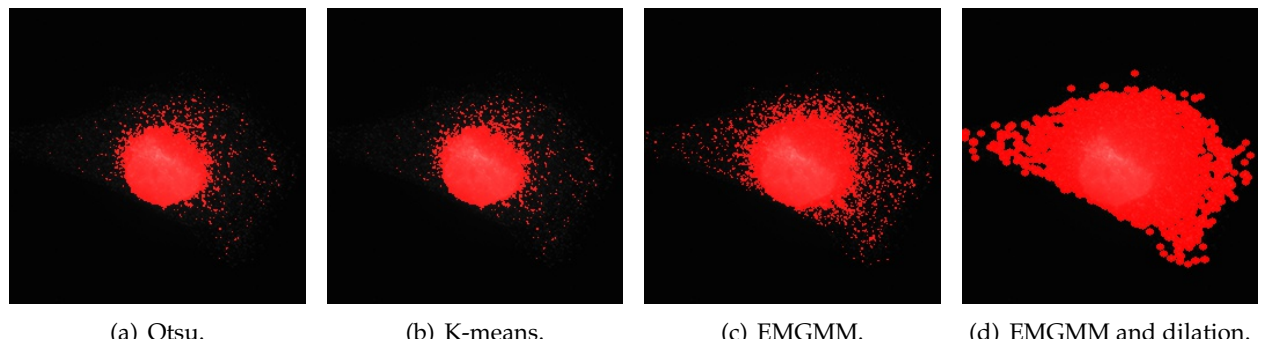


FIGURE 4.33: Image 7 from test set Appendix B initial masks.

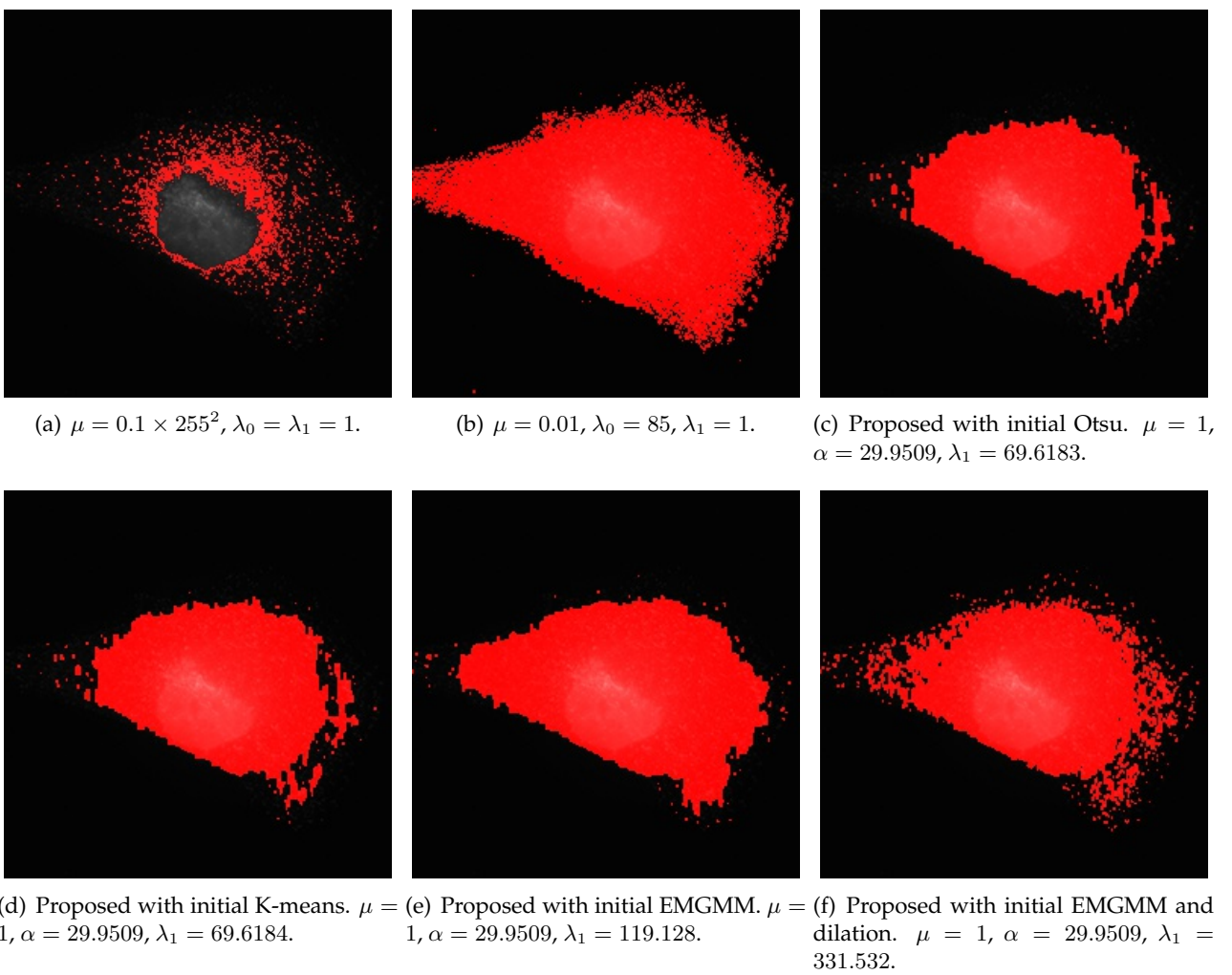


FIGURE 4.34: Image 7 from test set Appendix B segmentation results.

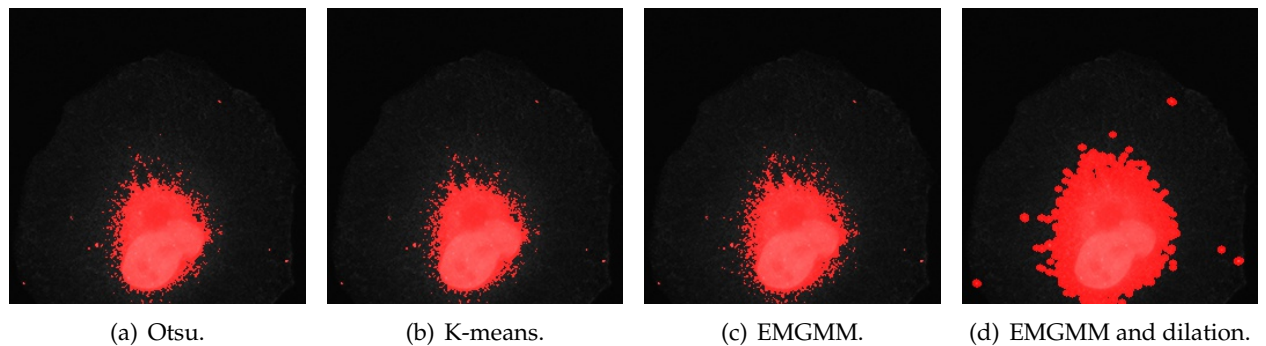


FIGURE 4.35: Image 8 from test set Appendix B initial masks.

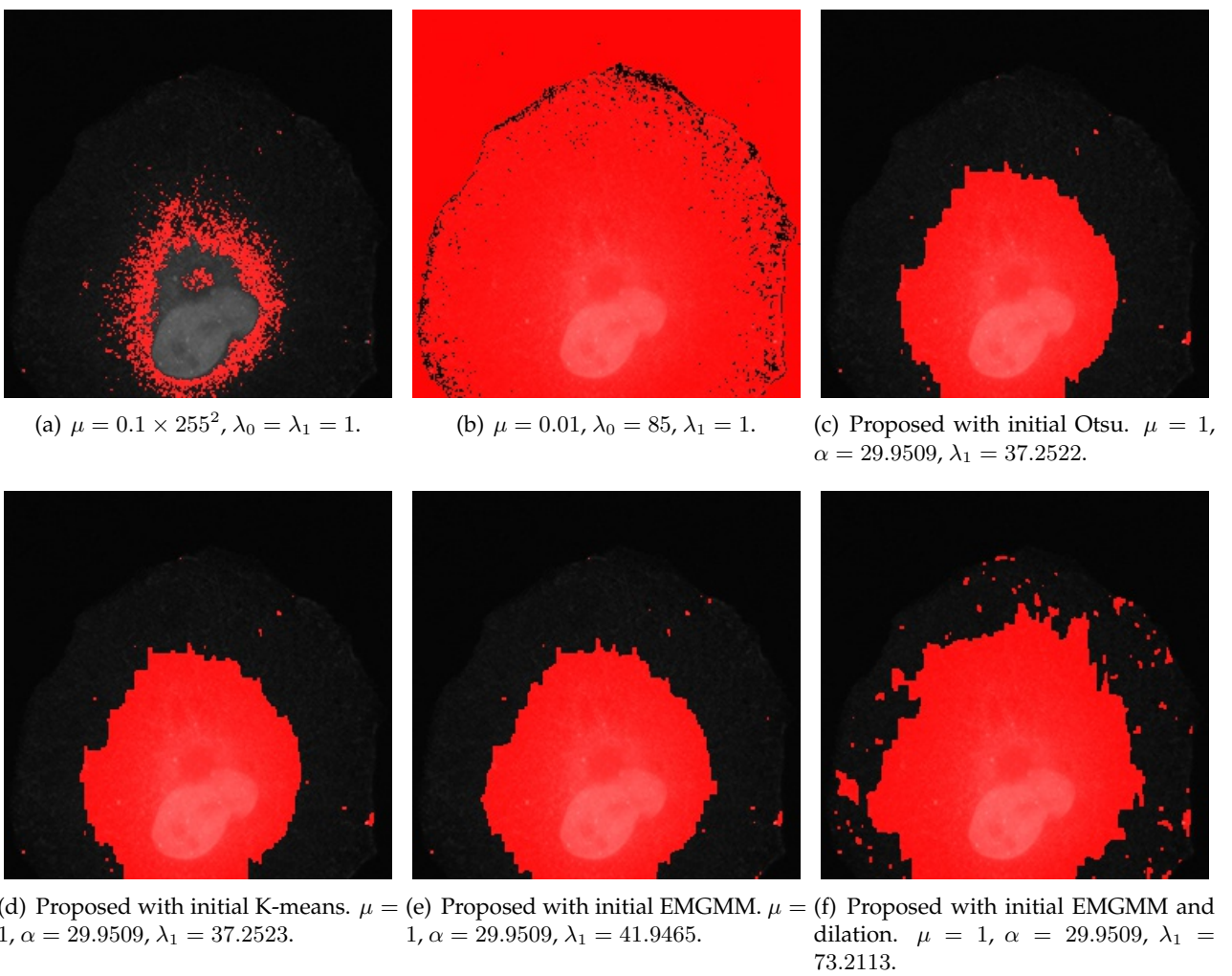


FIGURE 4.36: Image 8 from test set Appendix B segmentation results.

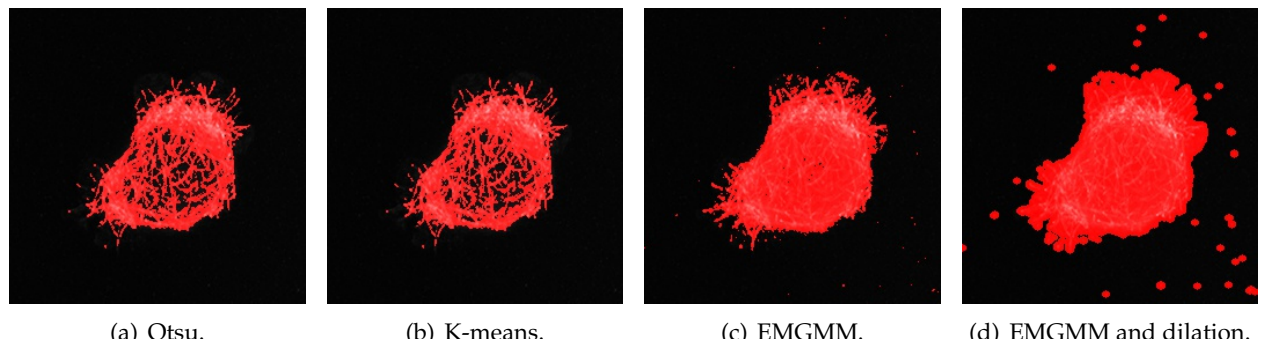


FIGURE 4.37: Image 9 from test set Appendix B initial masks.

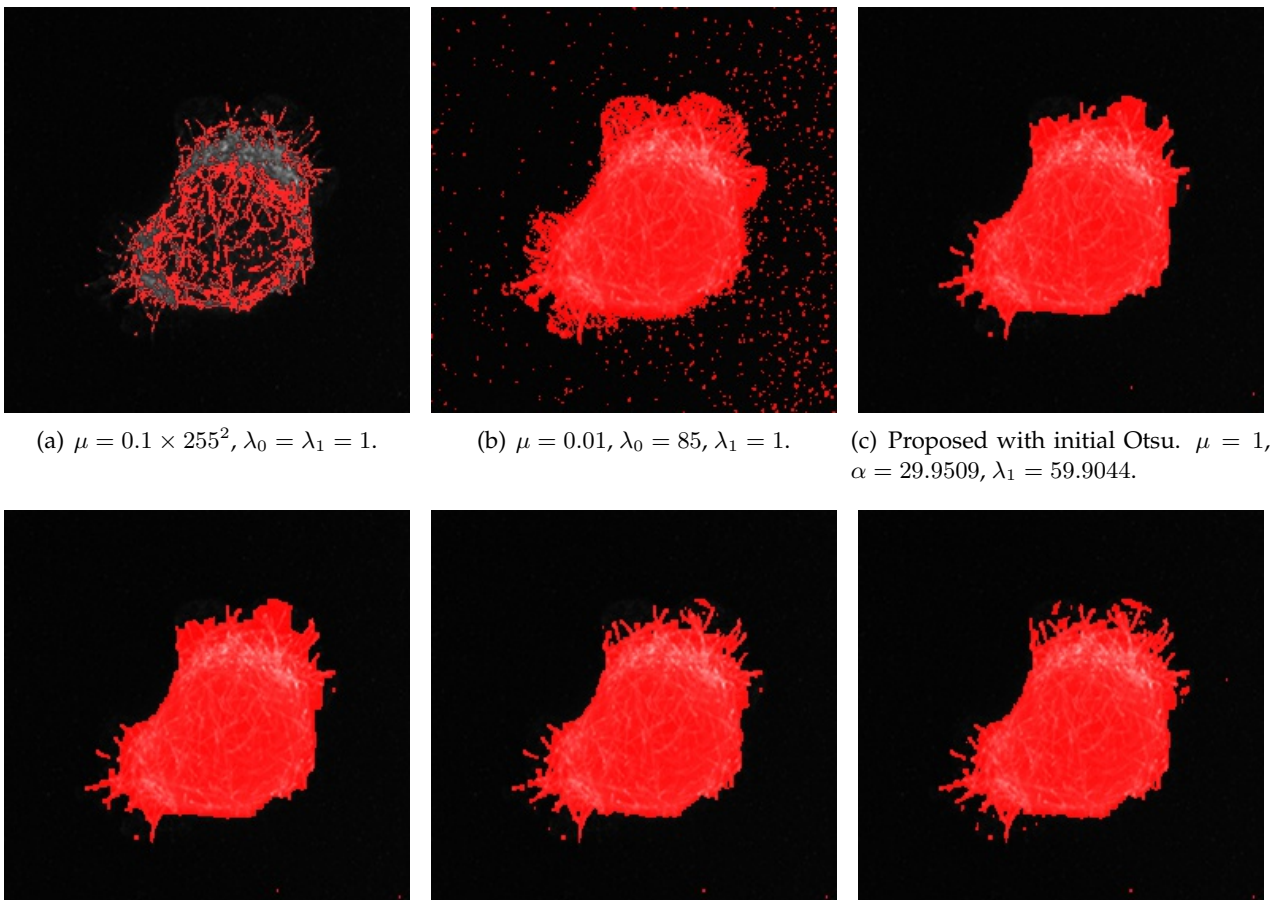


FIGURE 4.38: Image 9 from test set Appendix B segmentation results.

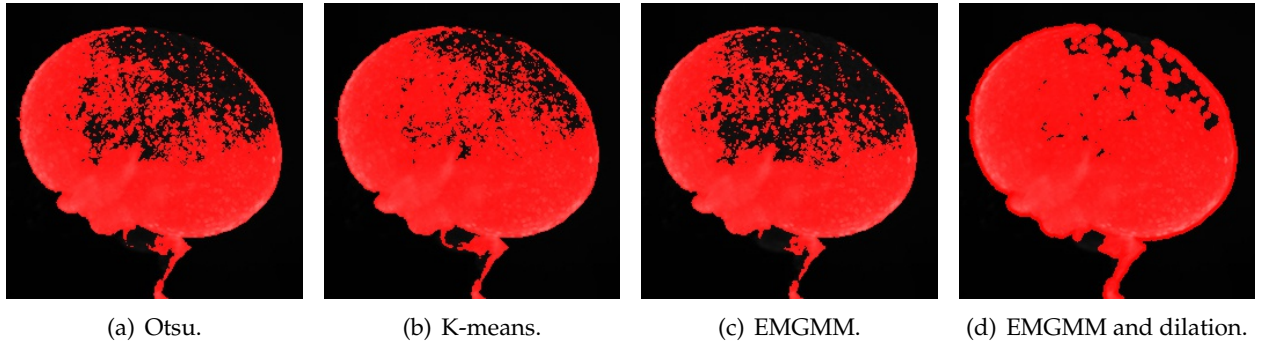


FIGURE 4.39: Image 10 from test set Appendix B initial masks.

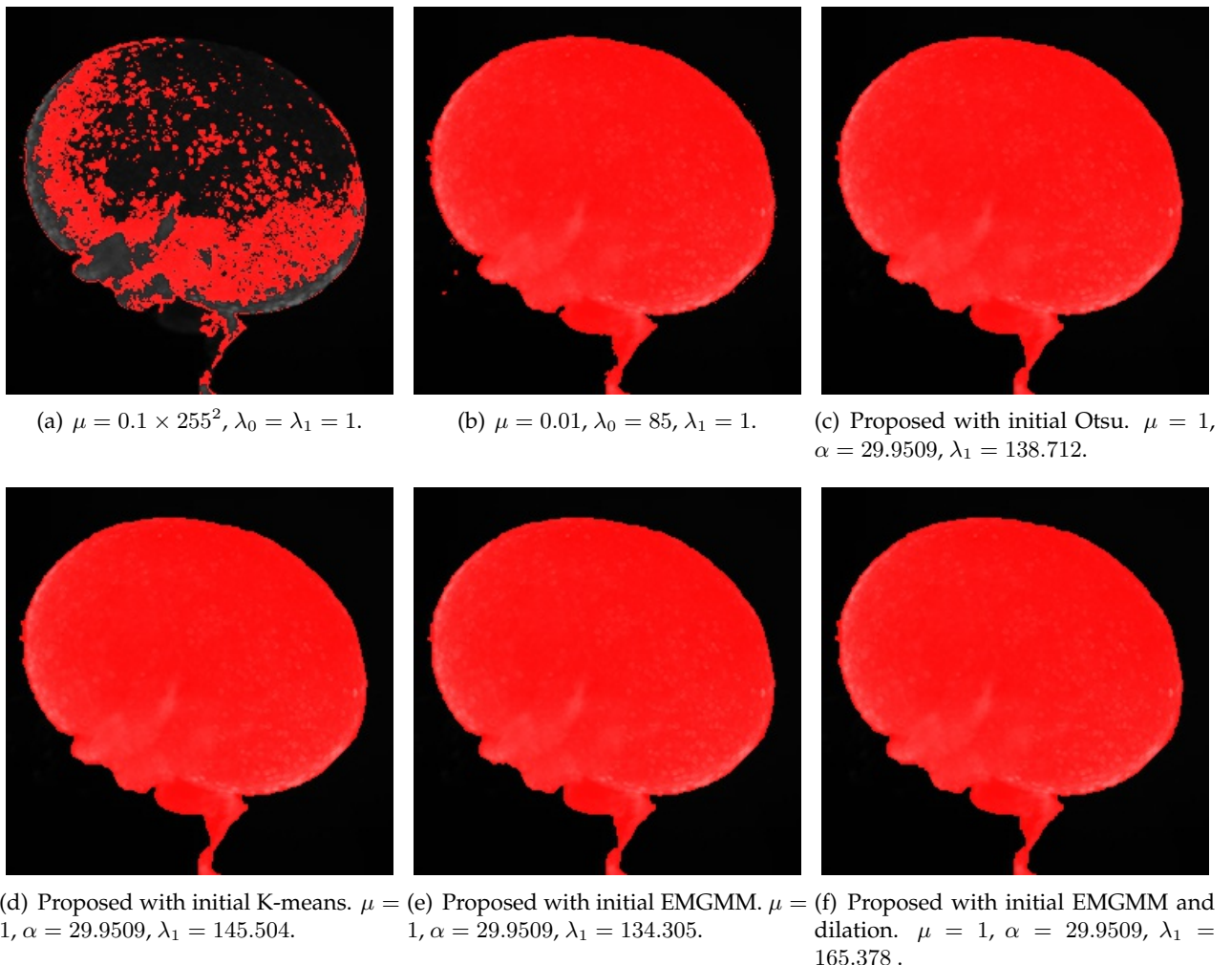


FIGURE 4.40: Image 10 from test set Appendix B segmentation results.

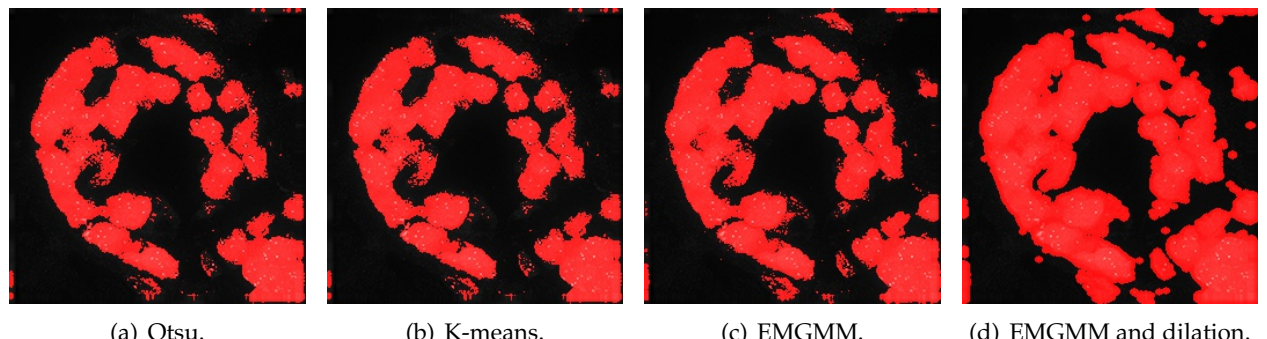


FIGURE 4.41: Image 11 from test set Appendix B initial masks.

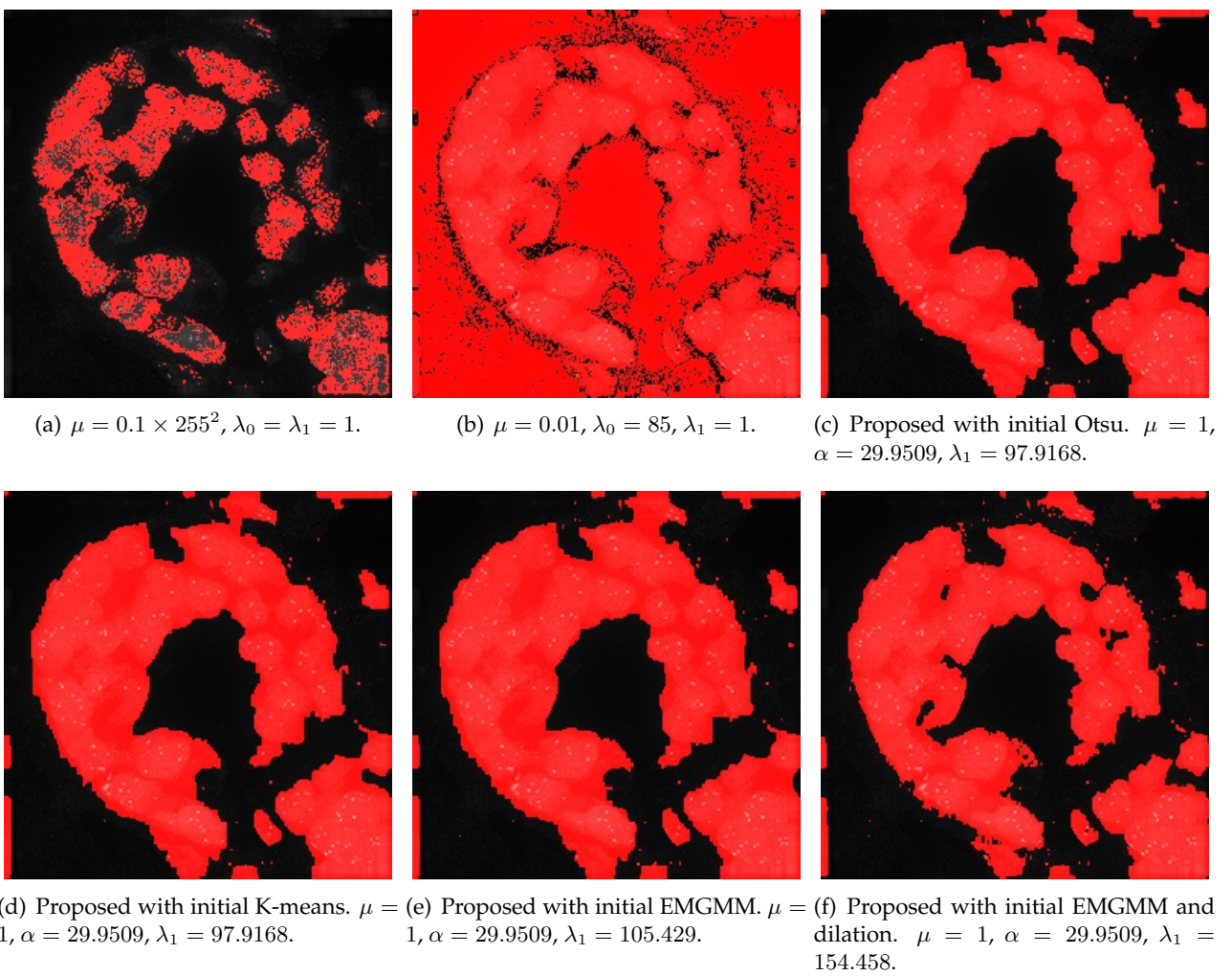


FIGURE 4.42: Image 11 from test set Appendix B segmentation results.

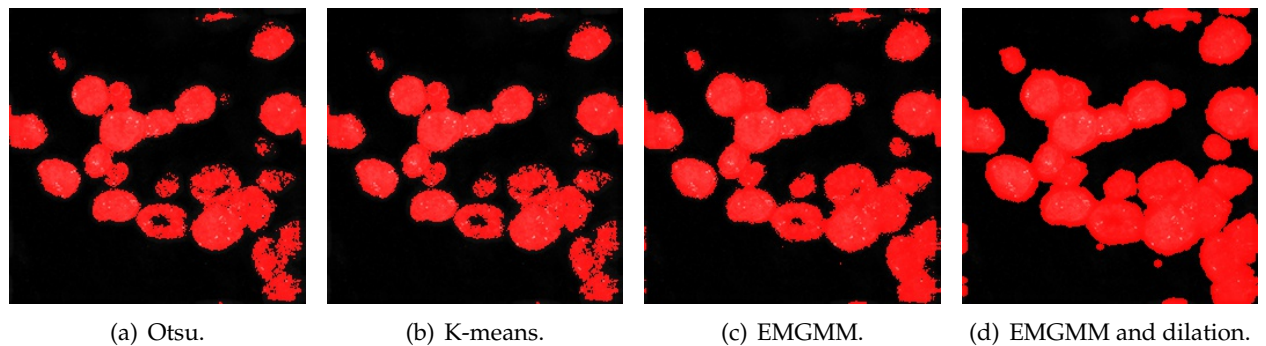


FIGURE 4.43: Image 12 from test set Appendix B initial masks.

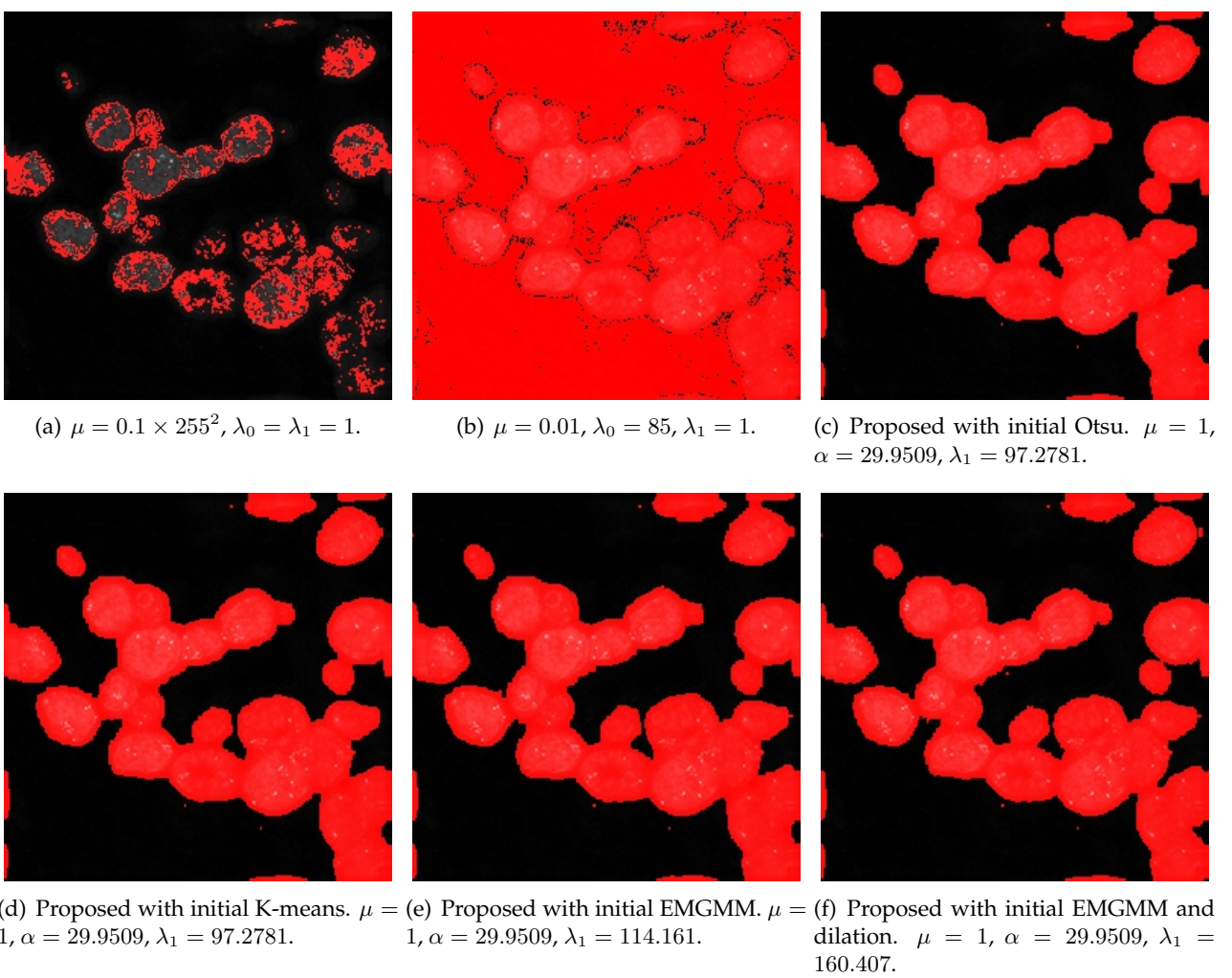


FIGURE 4.44: Image 12 from test set Appendix B segmentation results.

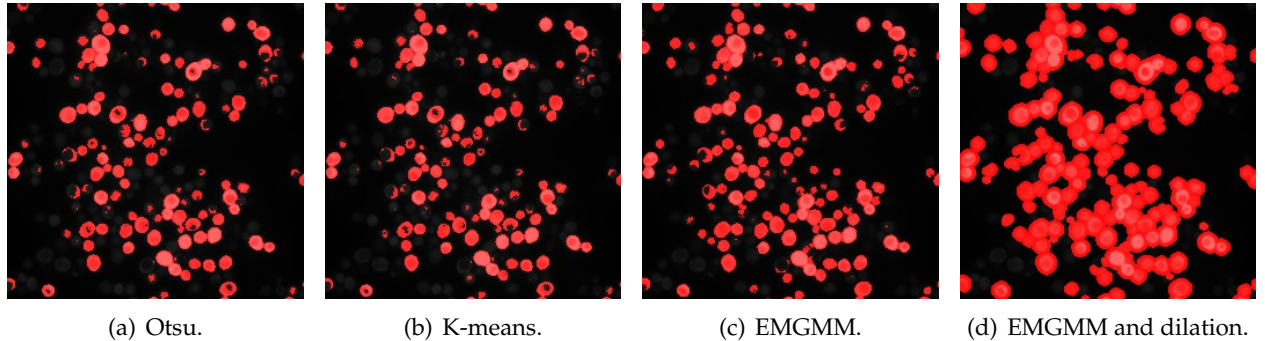


FIGURE 4.45: Image 13 from test set Appendix B initial masks.

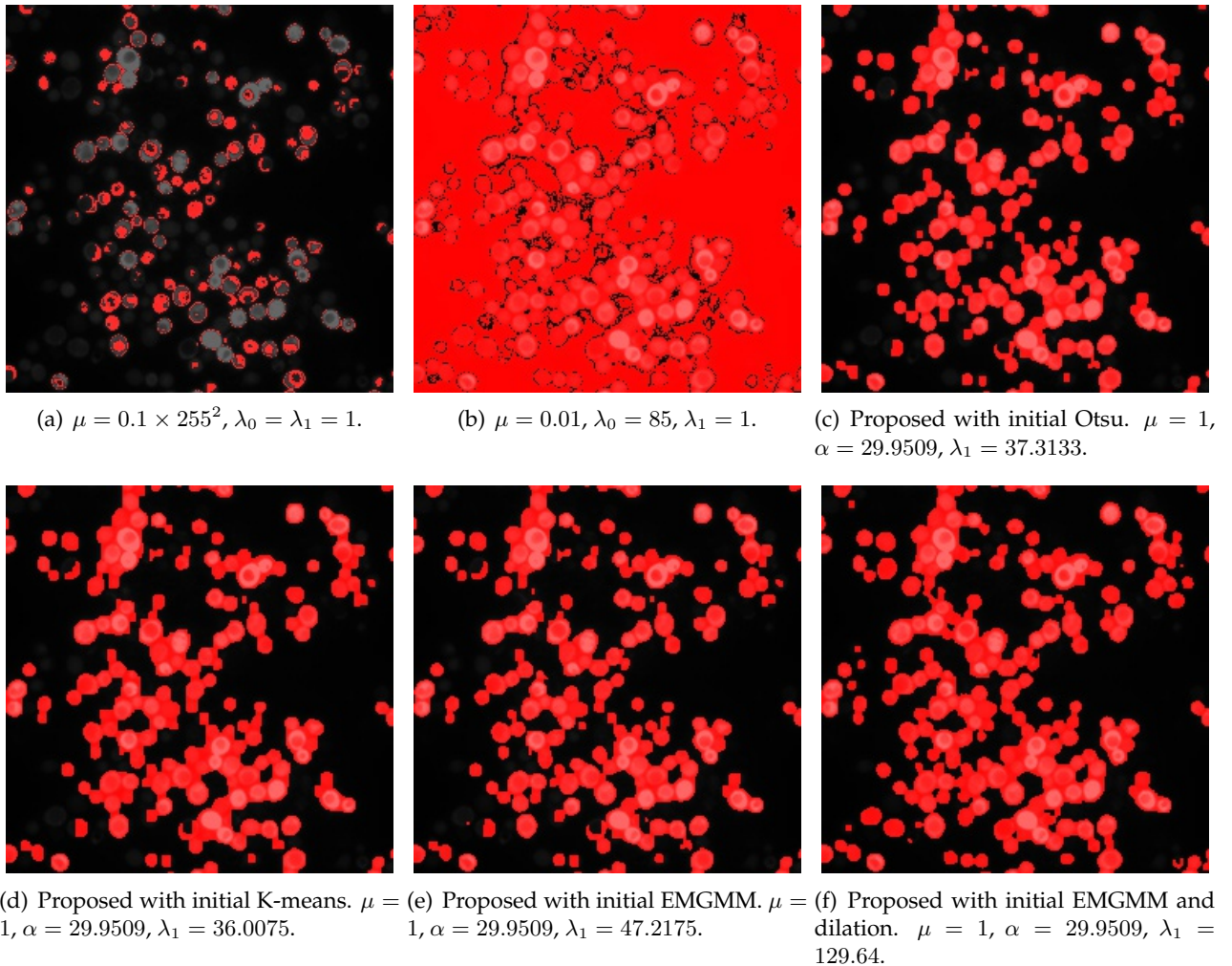


FIGURE 4.46: Image 13 from test set Appendix B segmentation results.

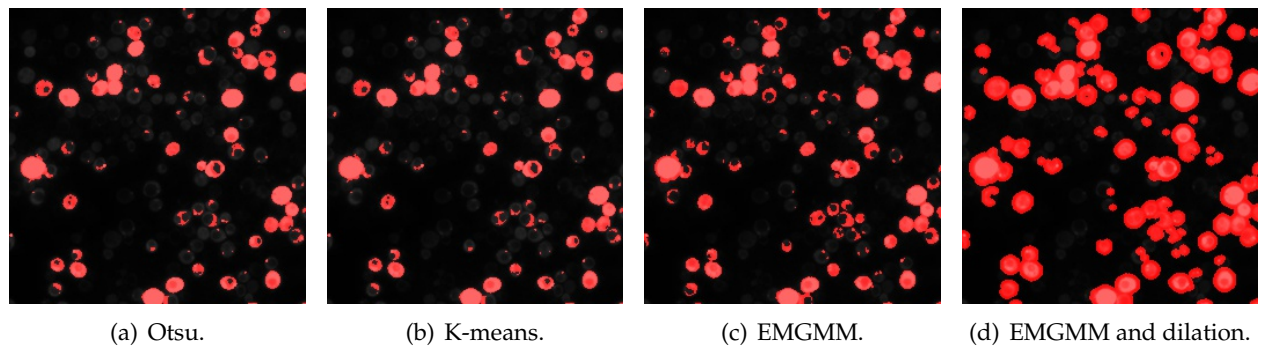


FIGURE 4.47: Image 14 from test set Appendix B initial masks.

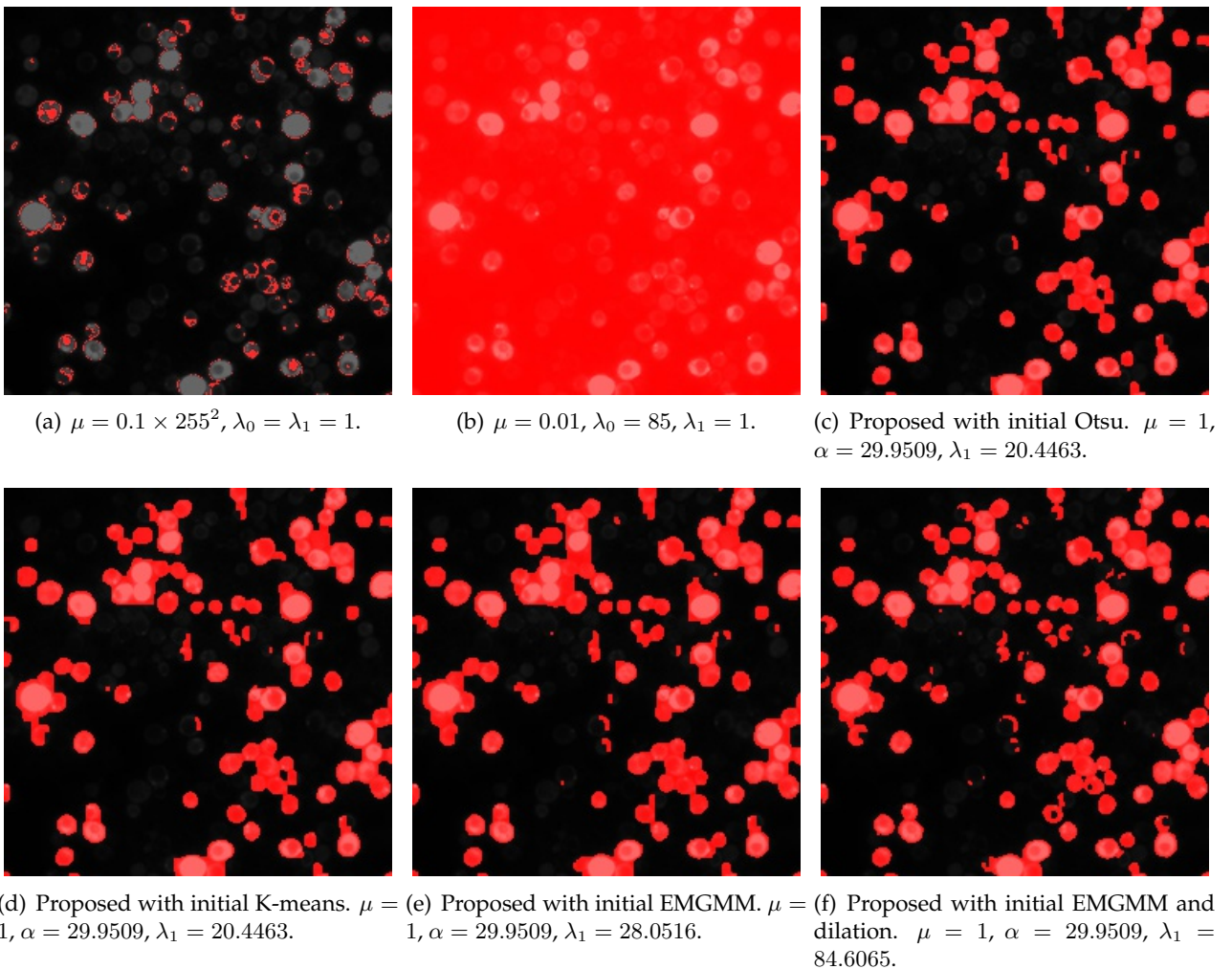


FIGURE 4.48: Image 14 from test set Appendix B segmentation results.

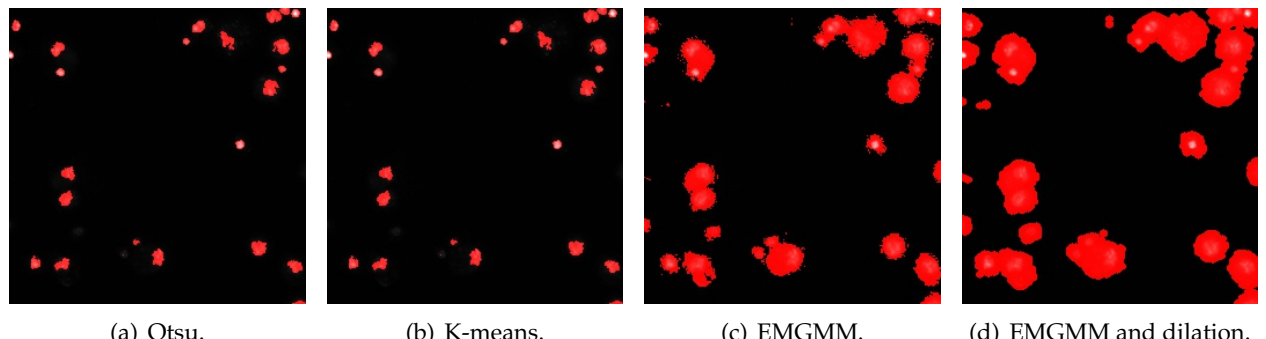


FIGURE 4.49: Image 15 from test set Appendix B initial masks.

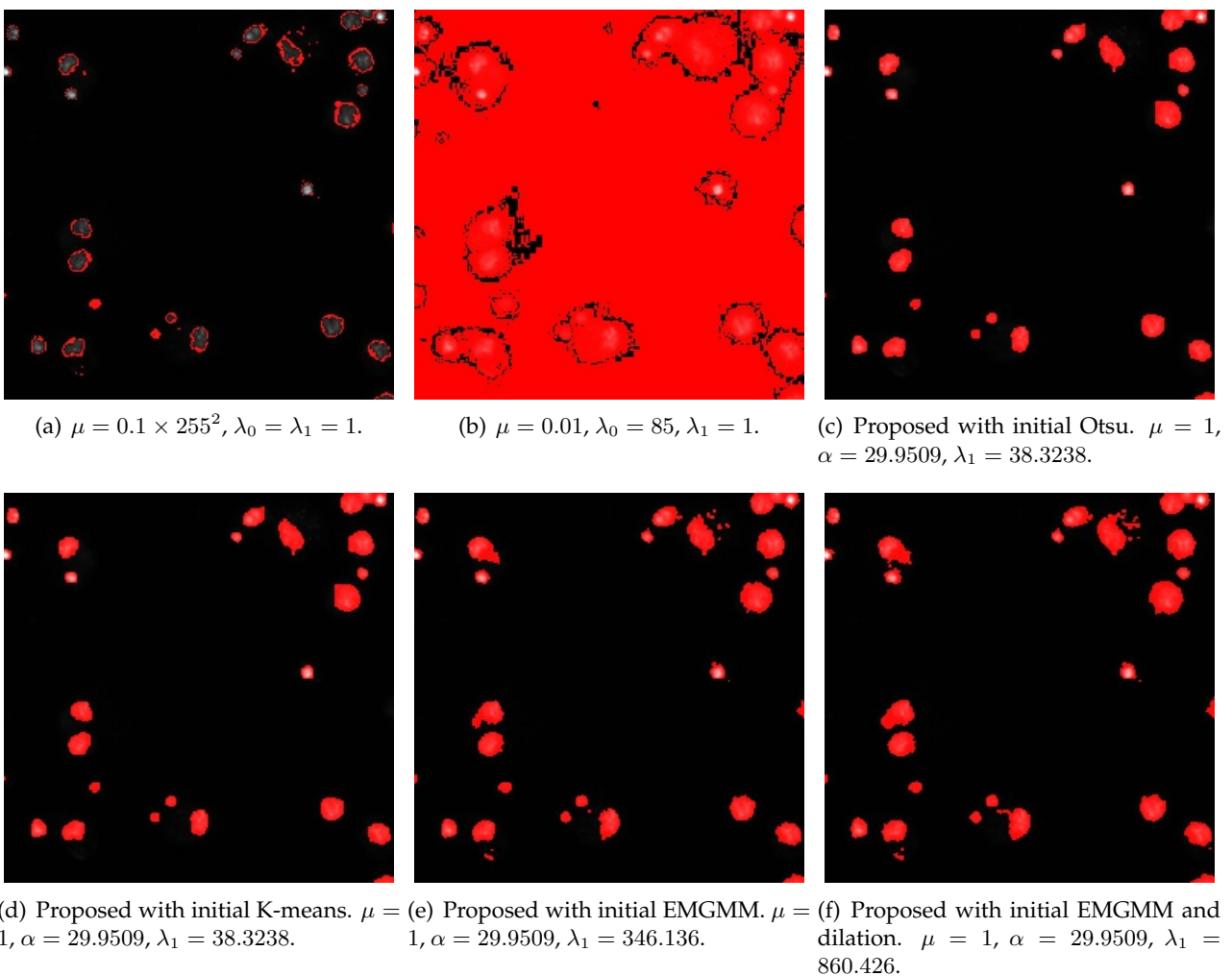


FIGURE 4.50: Image 15 from test set Appendix B segmentation results.

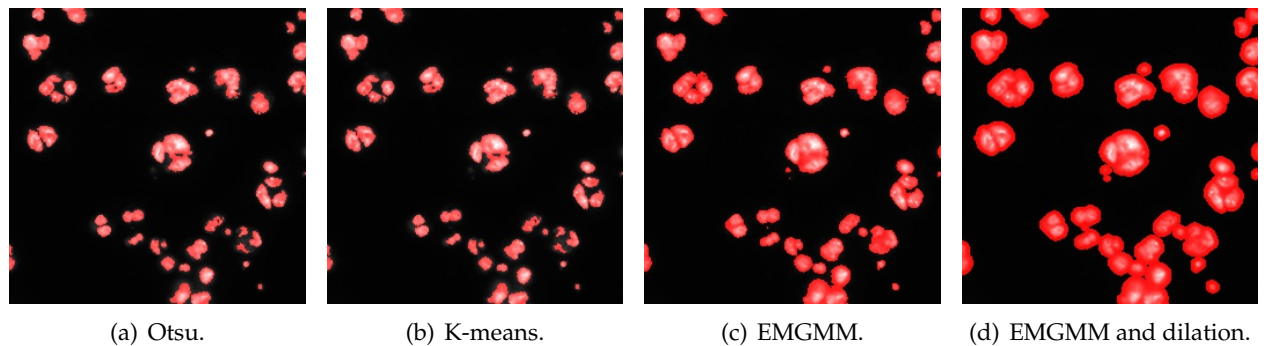


FIGURE 4.51: Image 16 from test set Appendix B initial masks.

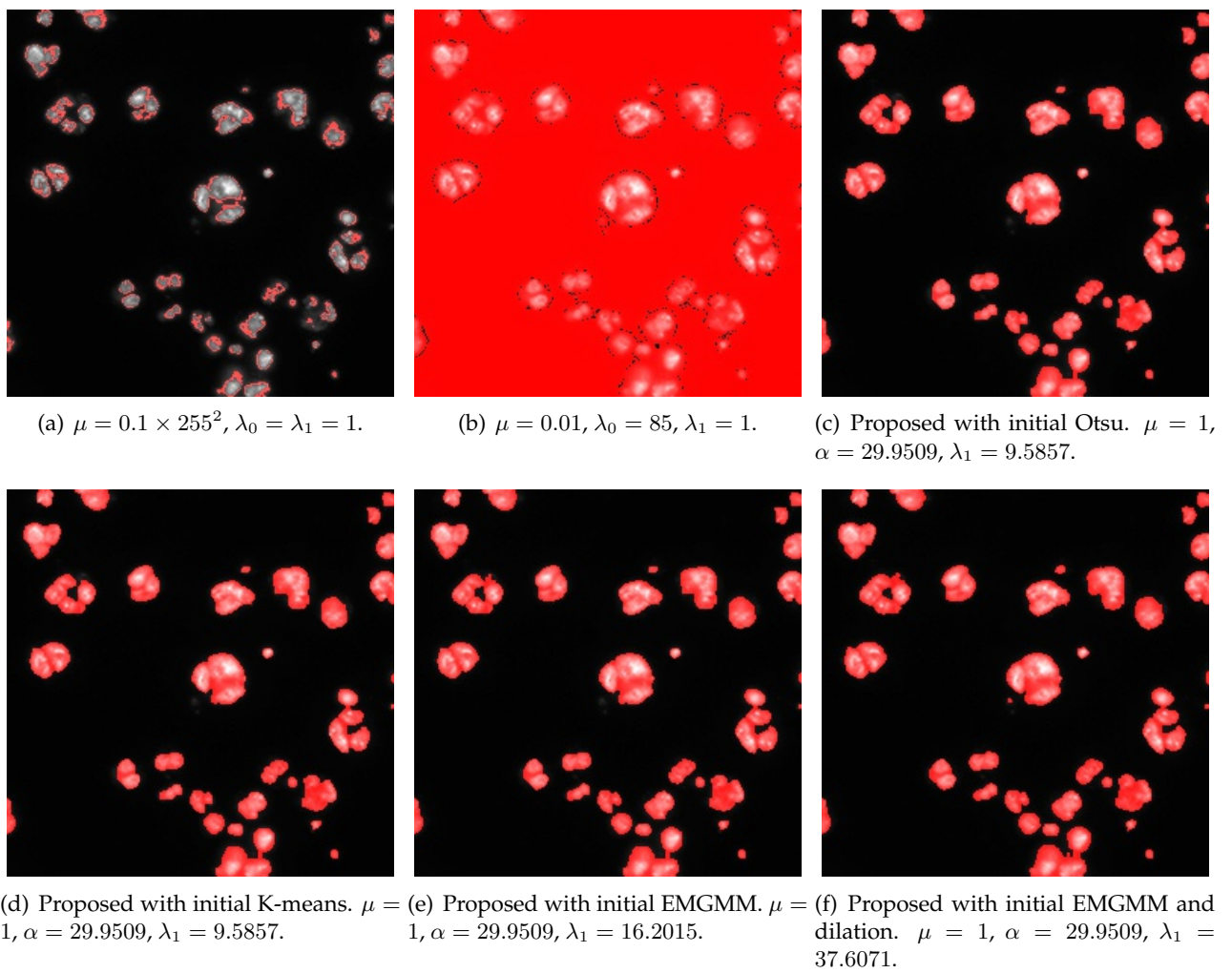


FIGURE 4.52: Image 16 from test set Appendix B segmentation results.

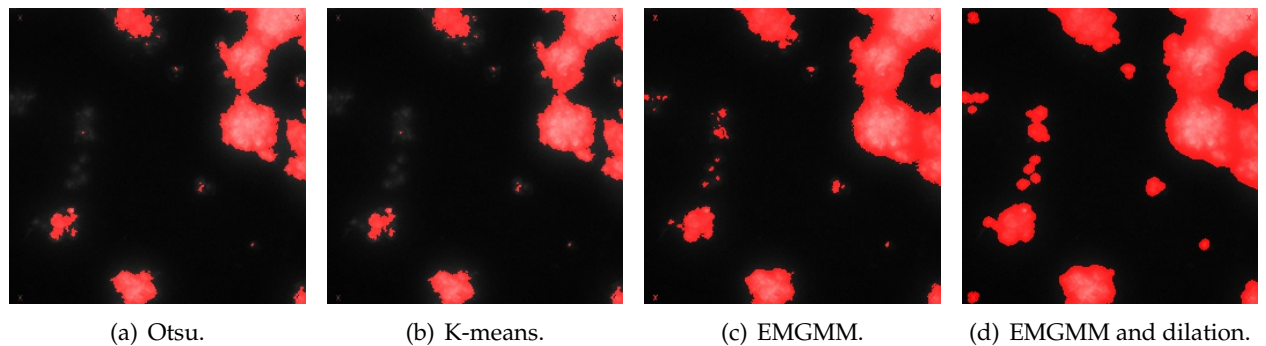


FIGURE 4.53: Image 17 from test set Appendix B initial masks.

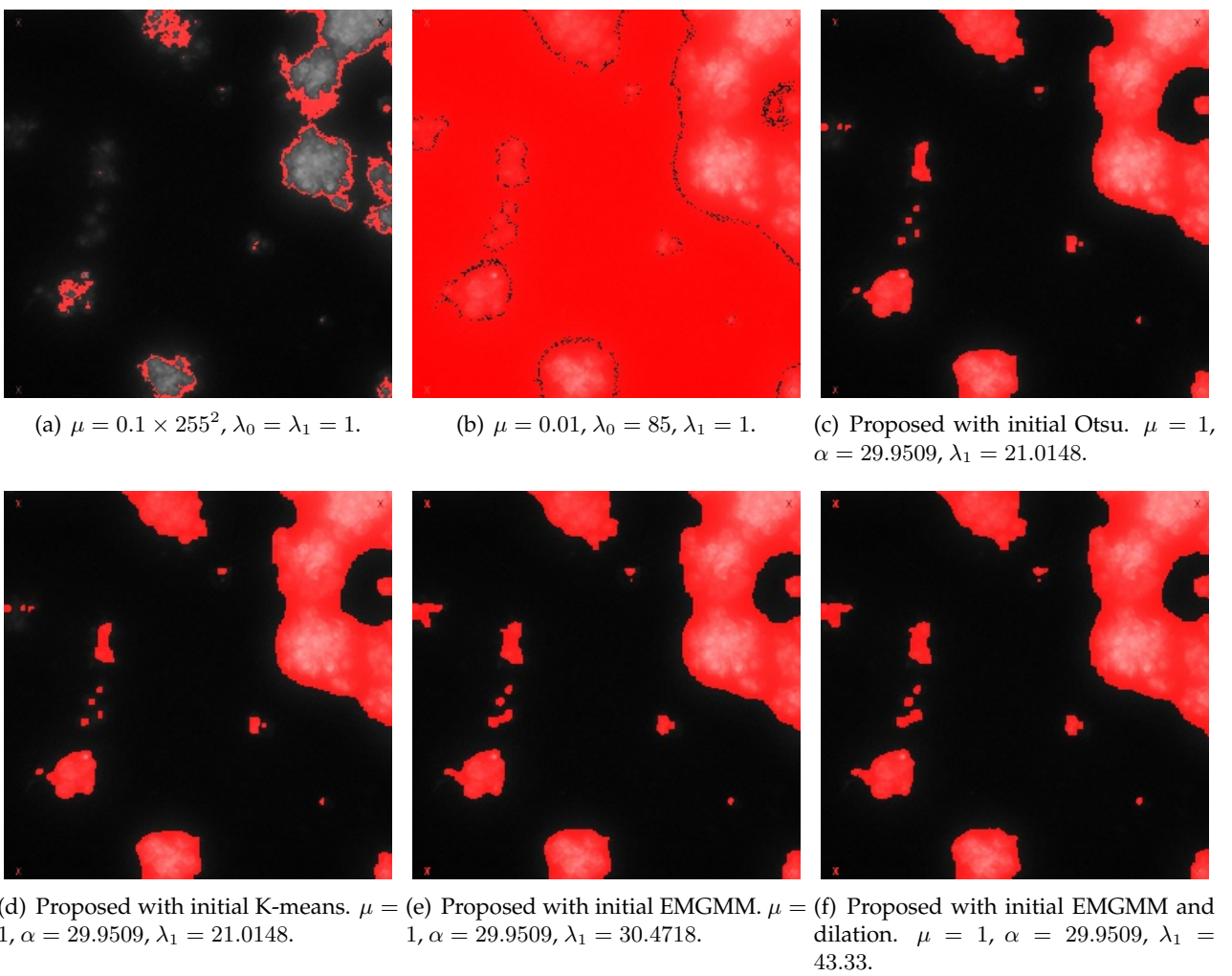


FIGURE 4.54: Image 17 from test set Appendix B segmentation results.

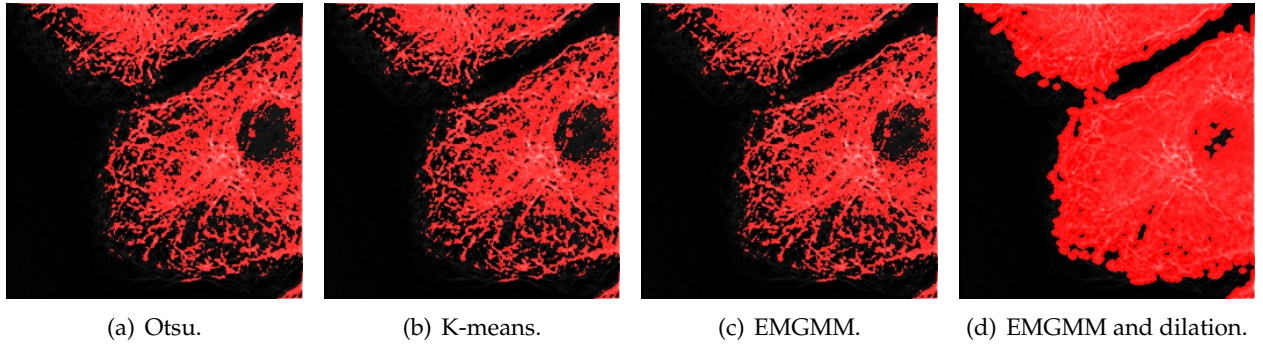


FIGURE 4.55: Image 18 from test set Appendix B initial masks.

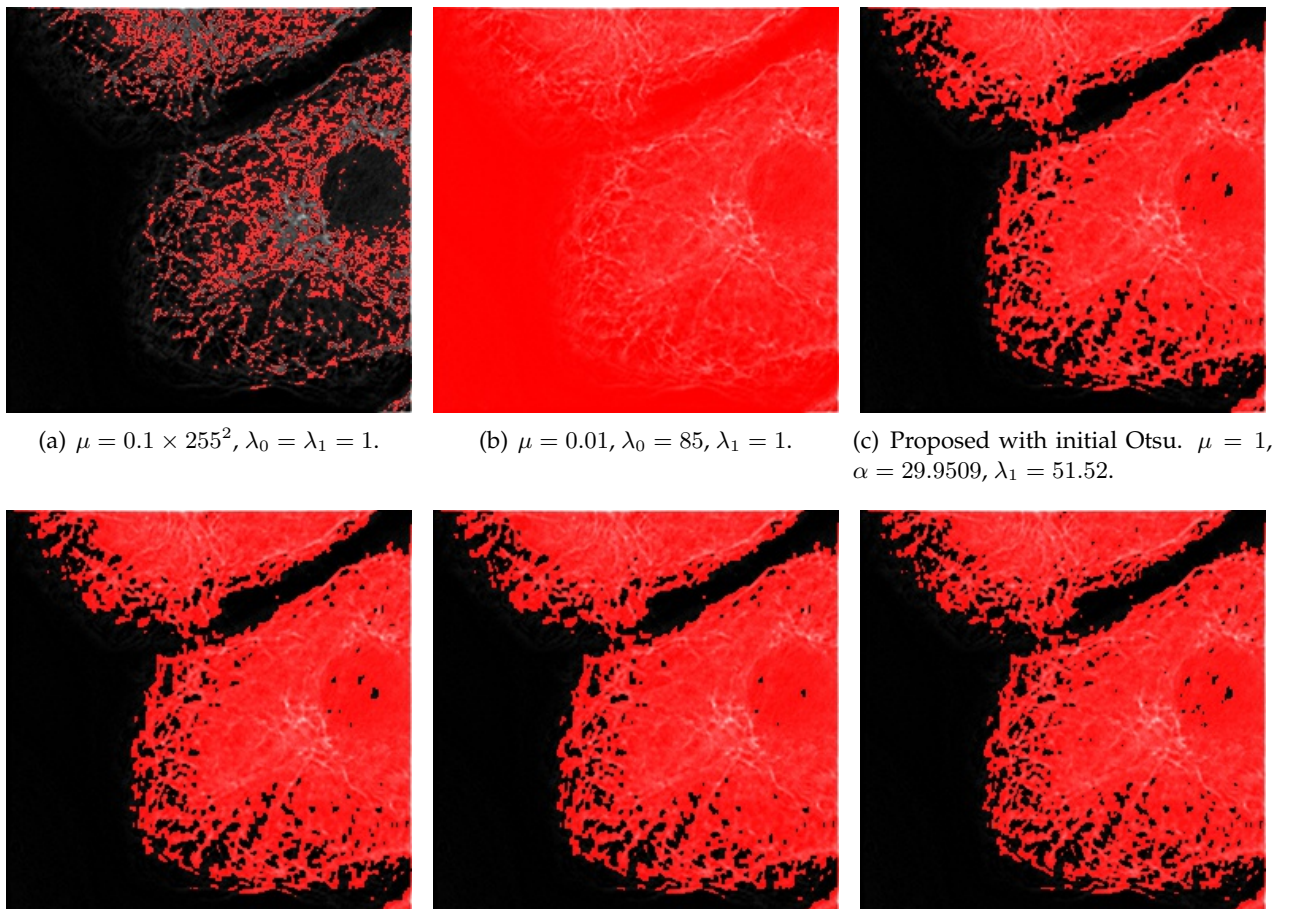


FIGURE 4.56: Image 18 from test set Appendix B segmentation results.

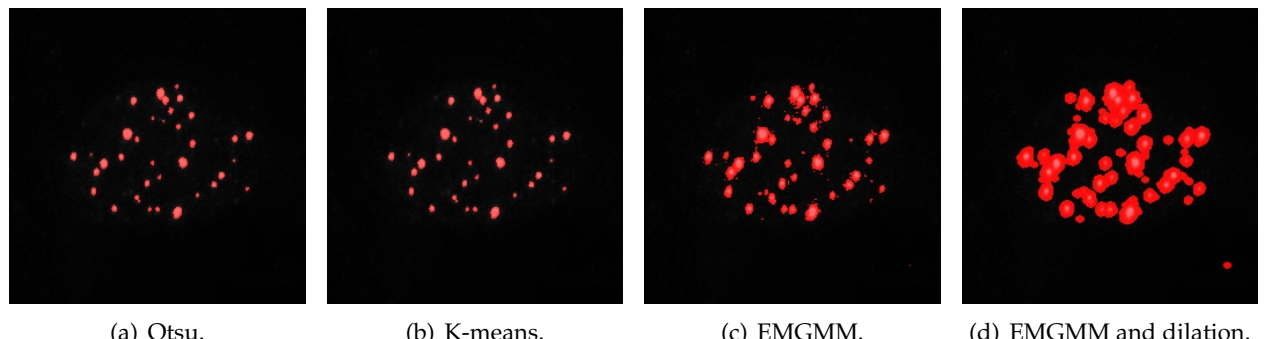


FIGURE 4.57: Image 19 from test set Appendix B initial masks.

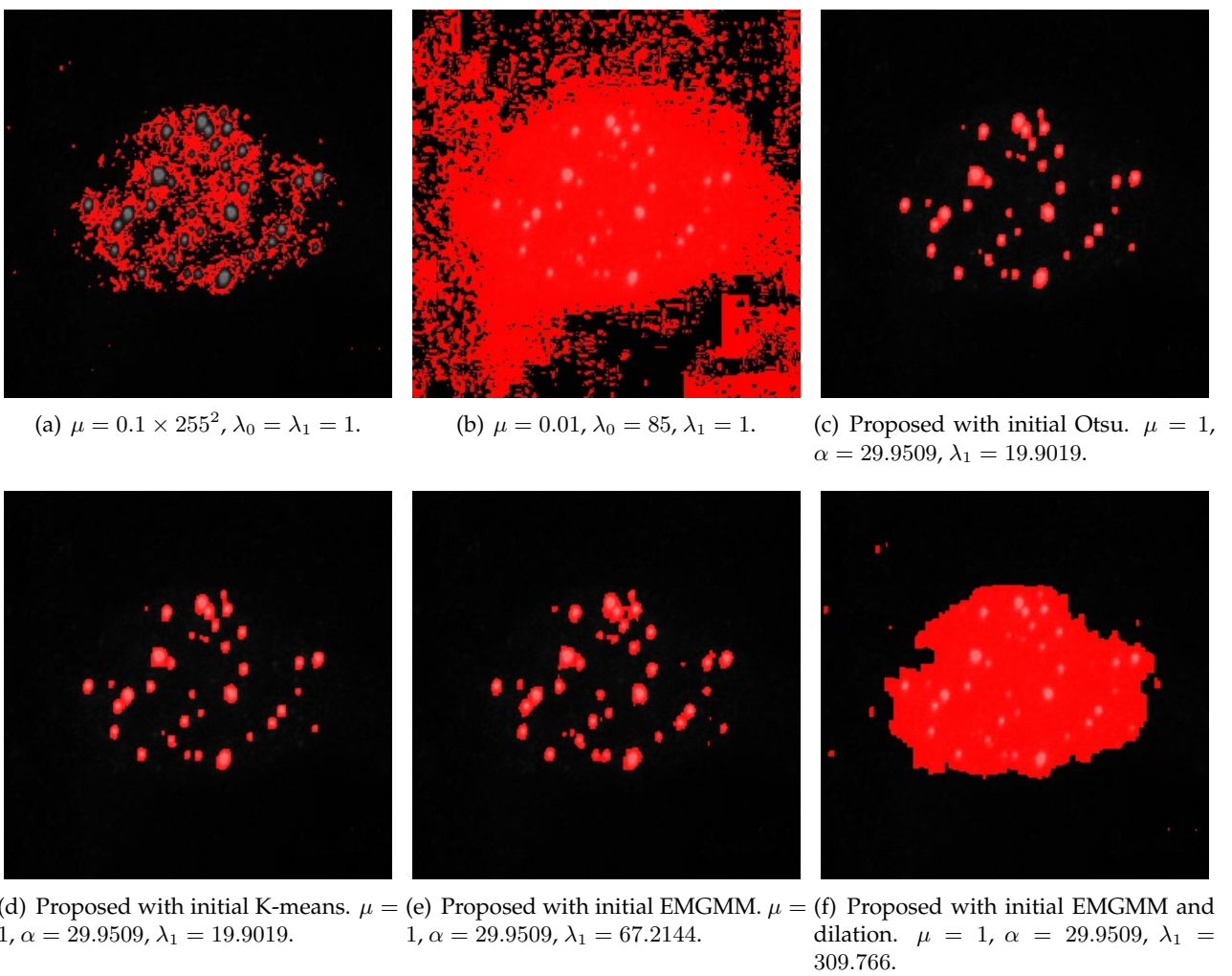


FIGURE 4.58: Image 19 from test set Appendix B segmentation results.

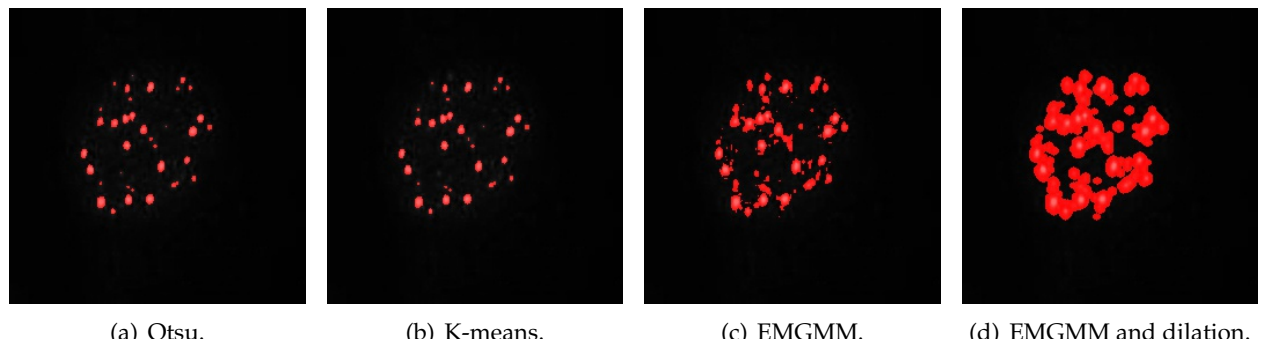


FIGURE 4.59: Image 20 from test set Appendix B initial masks.

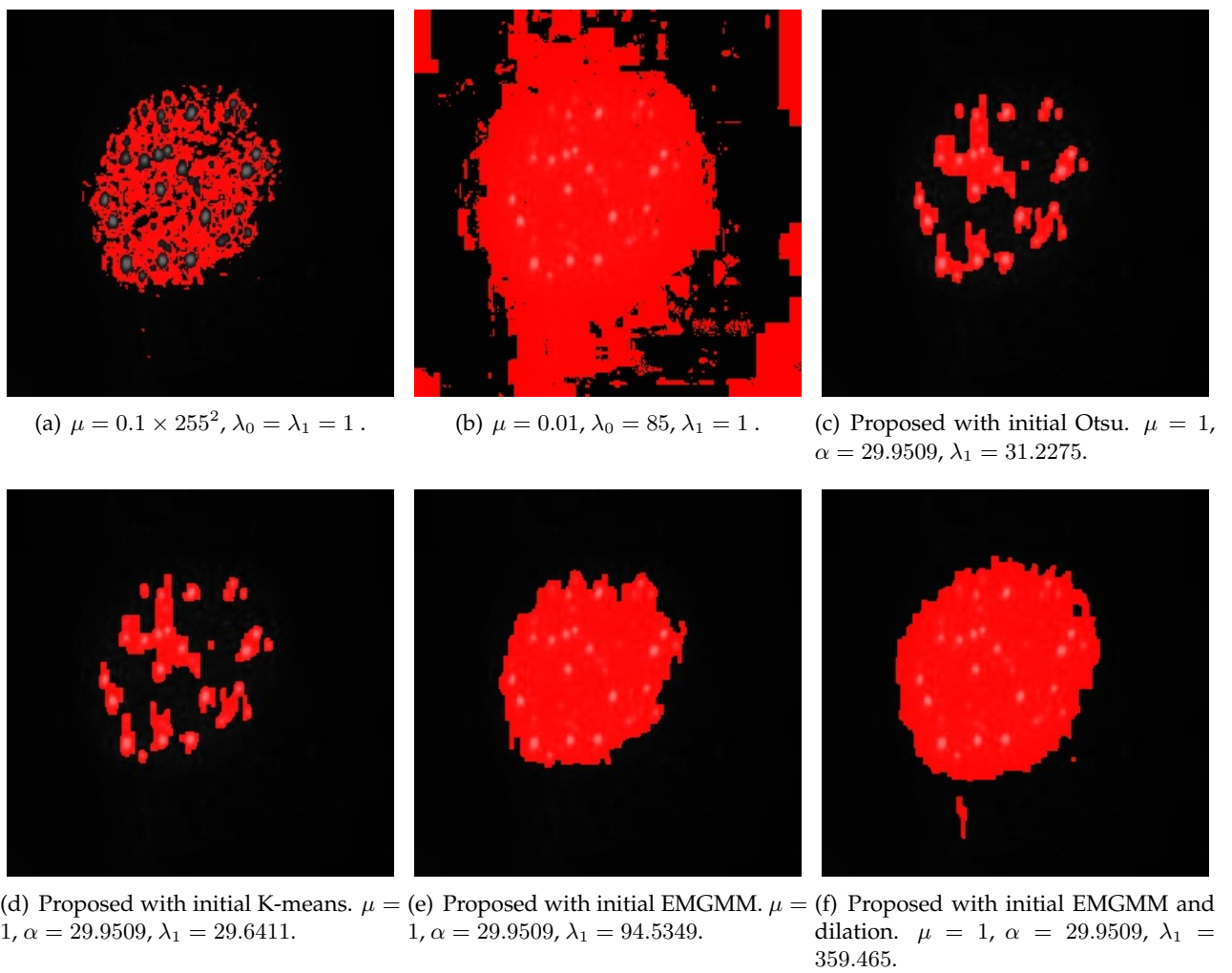


FIGURE 4.60: Image 20 from test set Appendix B segmentation results.

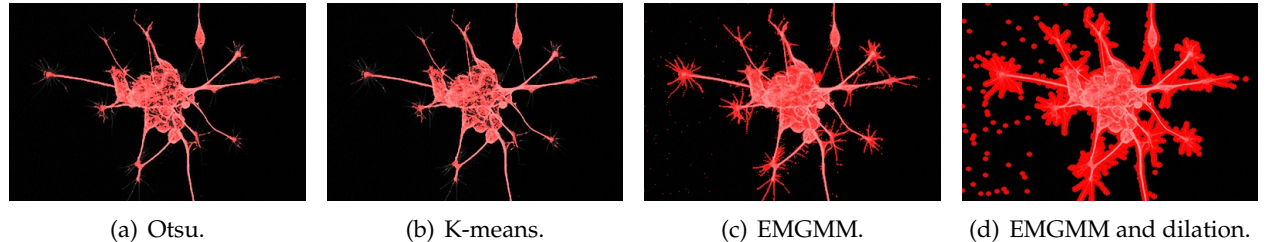


FIGURE 4.61: Image 21 from test set Appendix B initial masks.

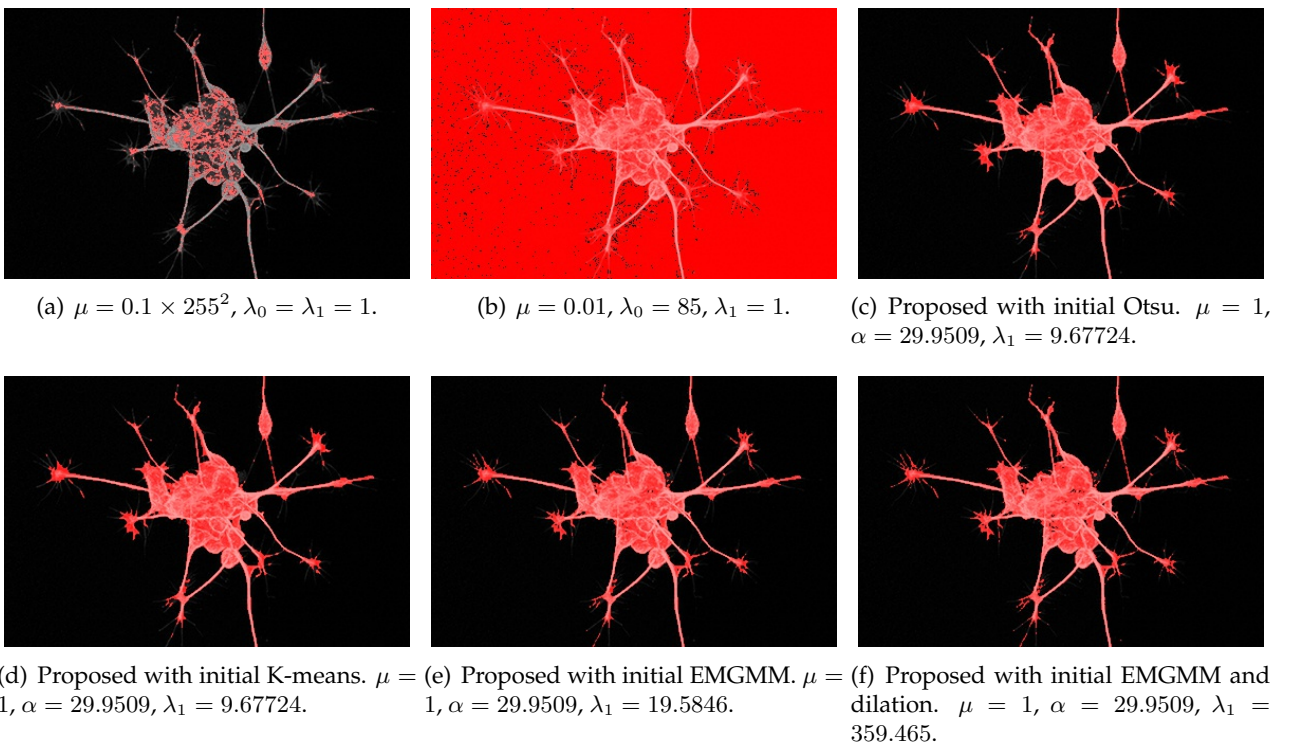


FIGURE 4.62: Image 21 from test set Appendix B segmentation results.

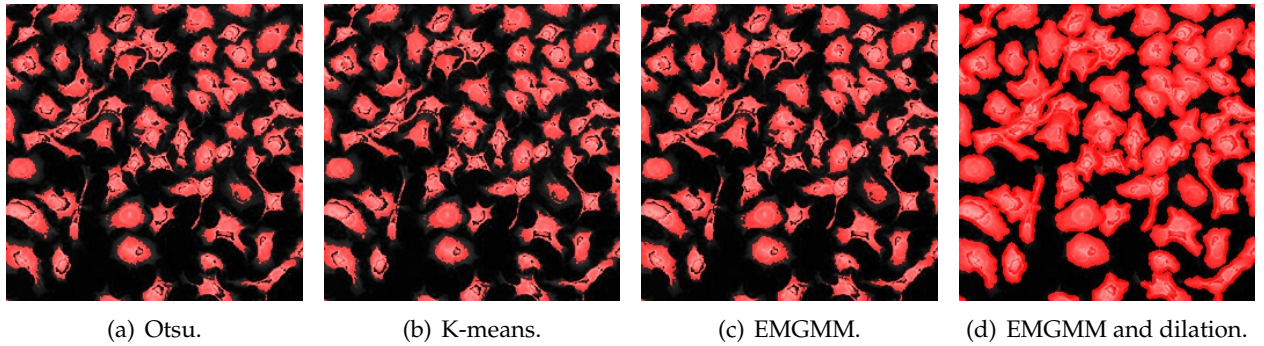


FIGURE 4.63: Image 22 from test set Appendix B initial masks.

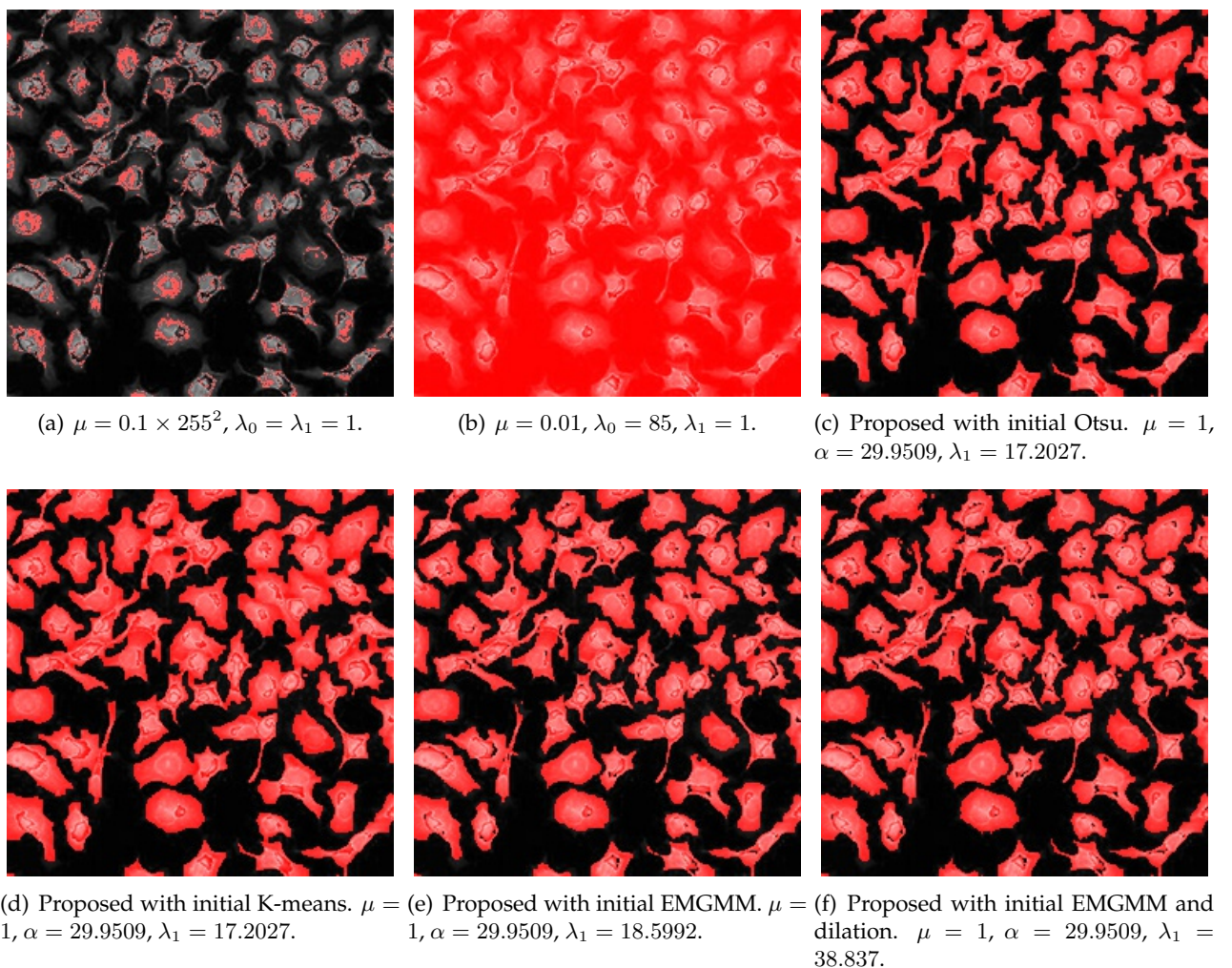


FIGURE 4.64: Image 22 from test set Appendix B segmentation results.

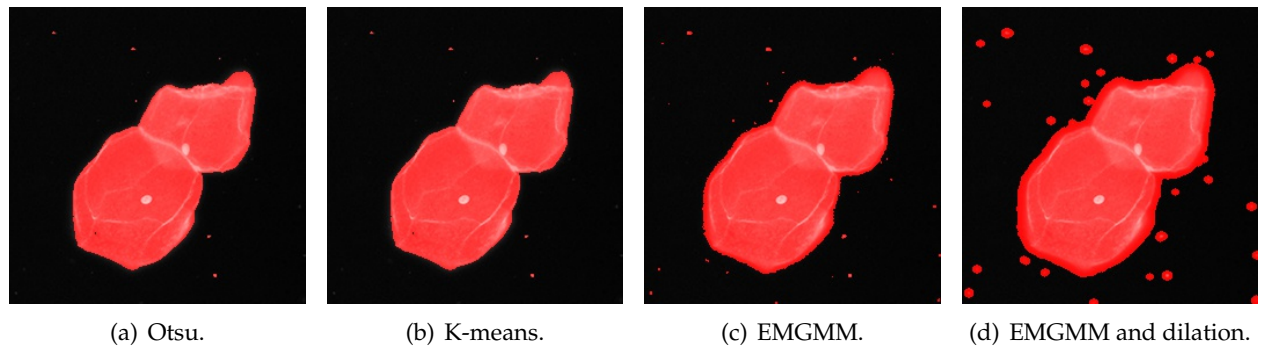


FIGURE 4.65: Image 23 from test set Appendix B initial masks.

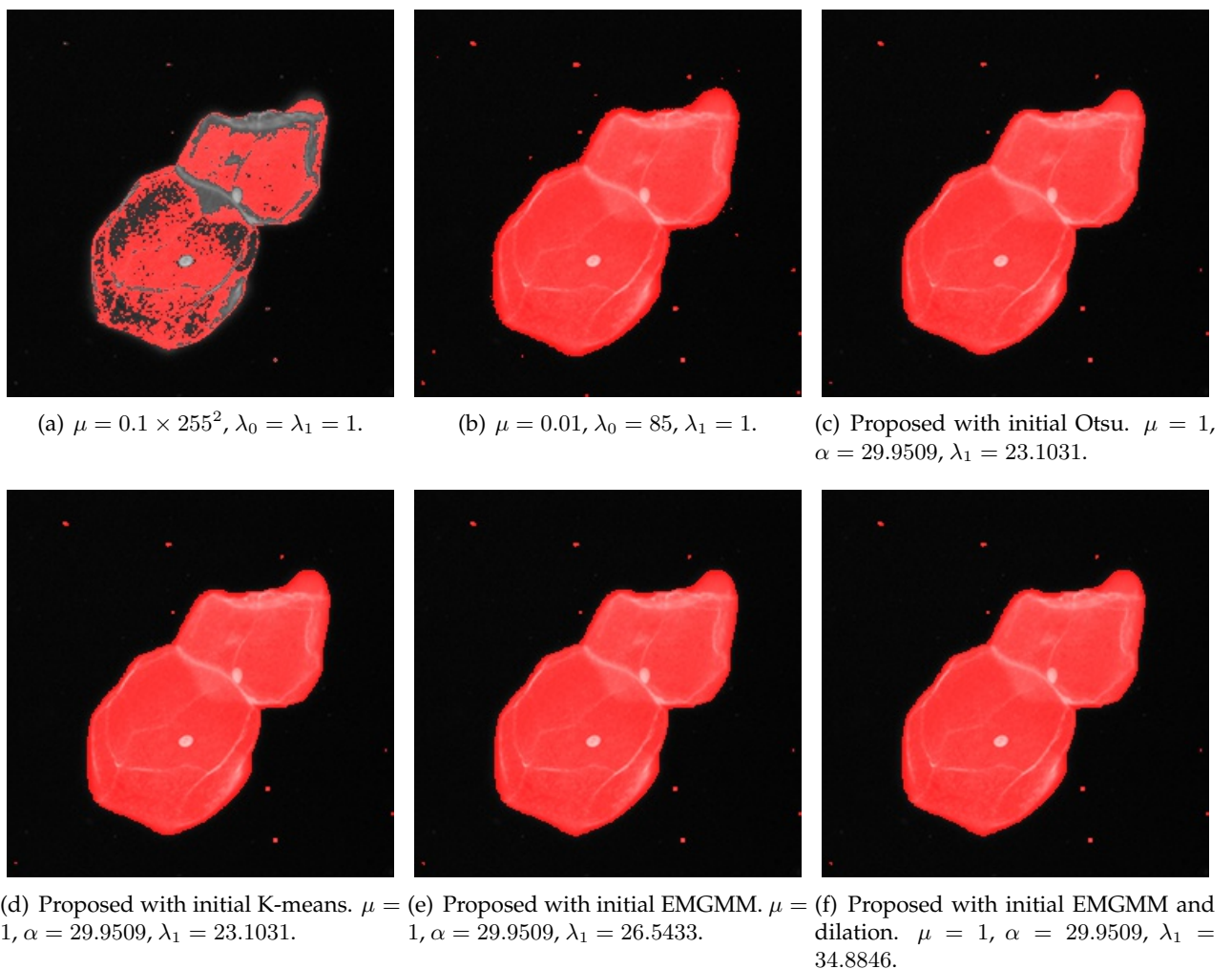


FIGURE 4.66: Image 23 from test set Appendix B segmentation results.

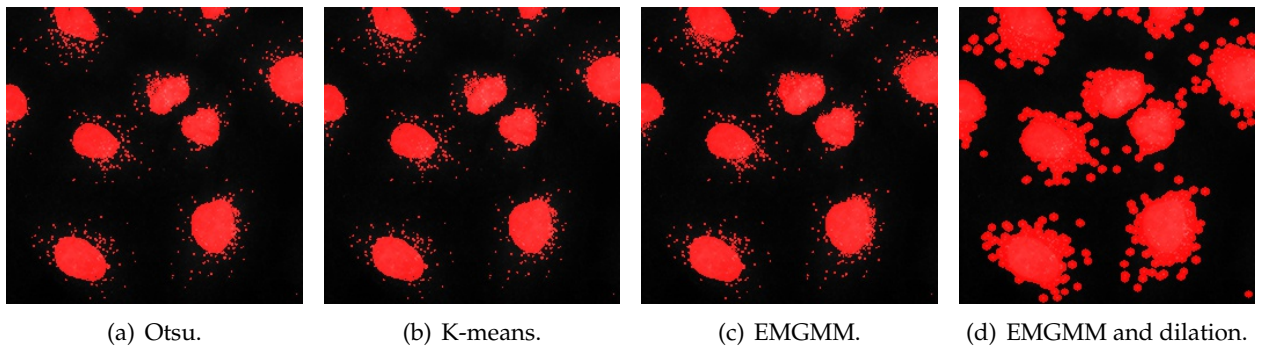


FIGURE 4.67: Image 24 from test set Appendix B initial masks.

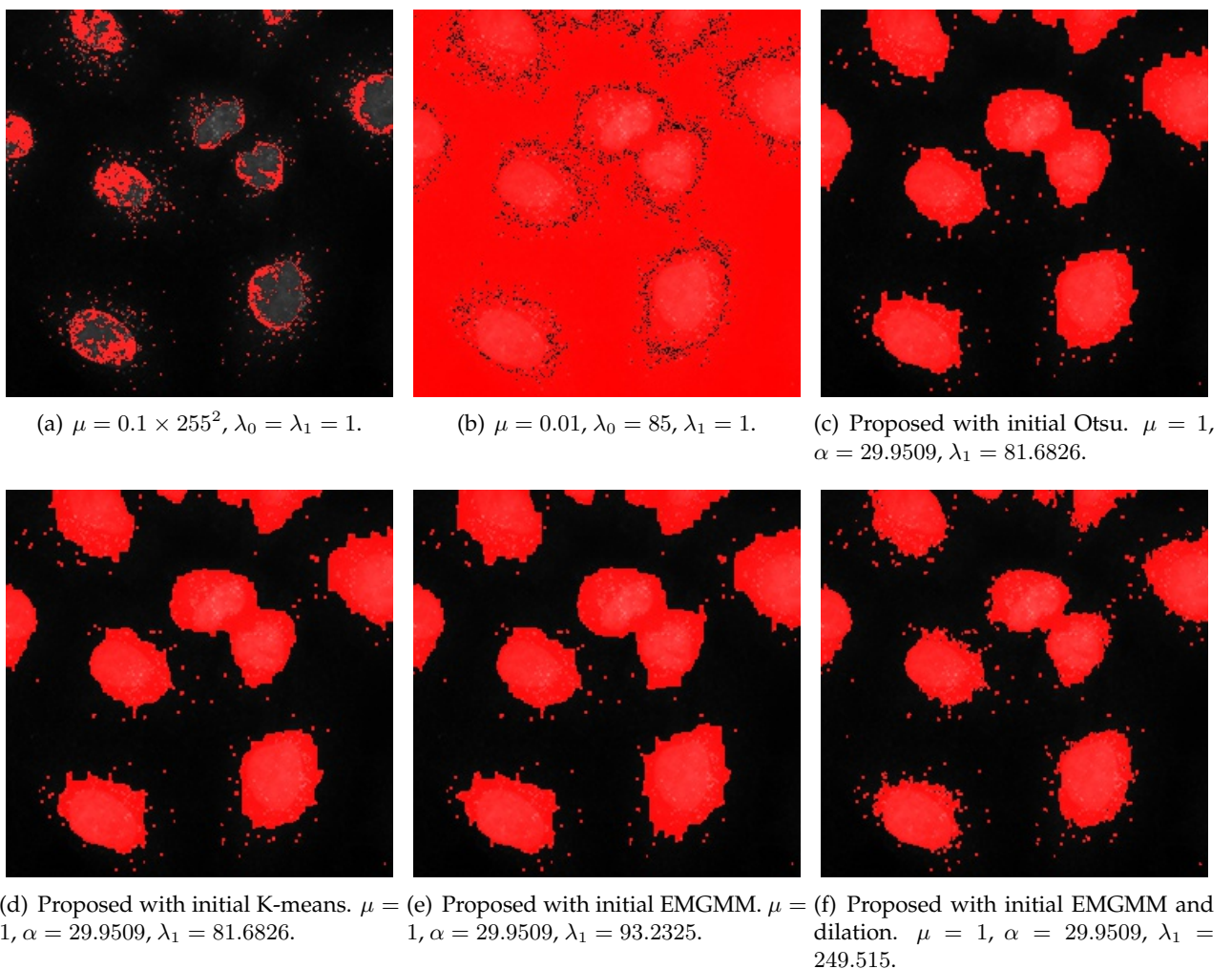


FIGURE 4.68: Image 24 from test set Appendix B segmentation results.

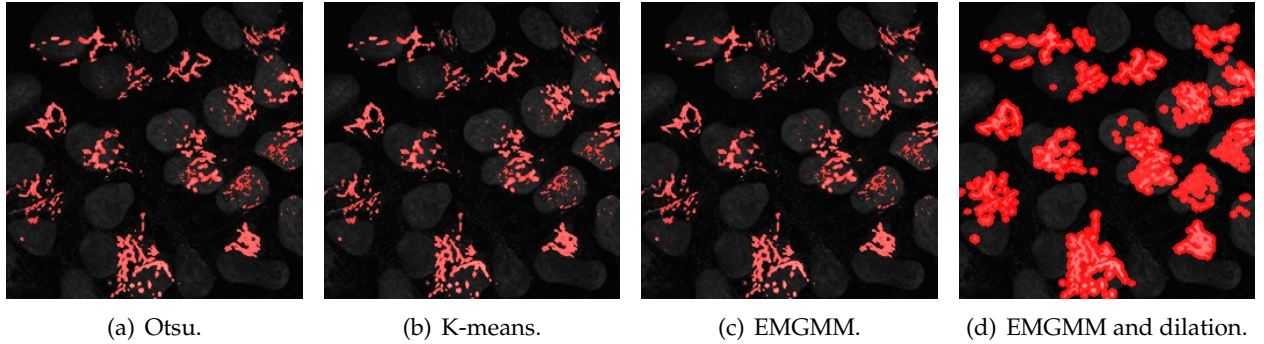


FIGURE 4.69: Image 25 from test set Appendix B initial masks.

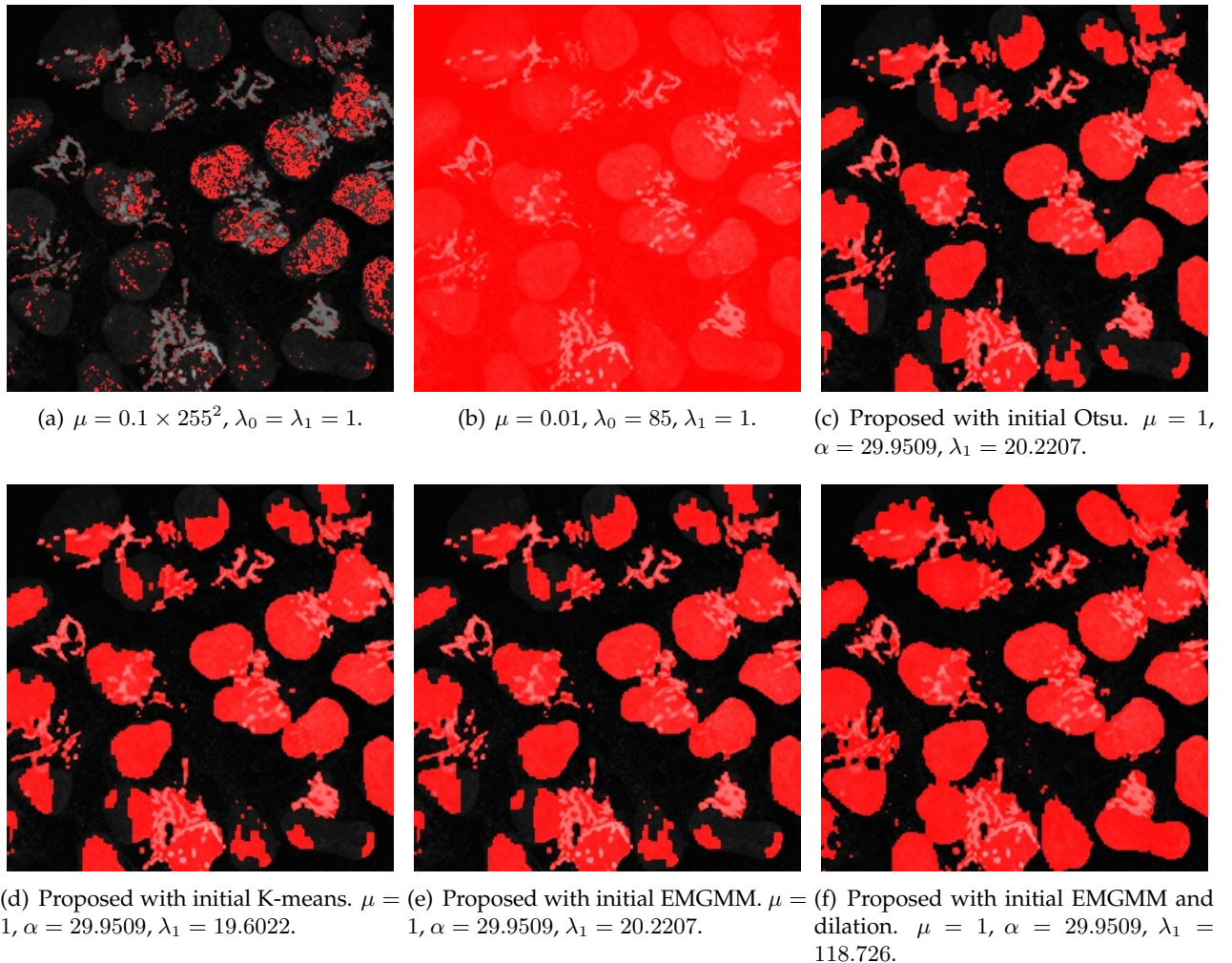


FIGURE 4.70: Image 25 from test set Appendix B segmentation results.

25-e	0.06532	0.33175	0.10640	0.17529	29.9509	20.2207	0.03901	0.16680			0.03806
25-d	0.08493	0.40334	0.07377	0.10217	29.9509	118.726	0.02844	0.14221			0.00289

As can be seen, the parameter settings presented previously in literature are not robust over a large range of image types that commonly occur in fluorescence microscopy whereas the proposed method produces more subjectively consistent and visually accurate segmentations. From the table we can also see that the final means from the proposed method are closer to the ideal means obtained from the groundtruth.

Measuring Segmentation Efficiency We now objectively compare the methods under critique. We use a confusion matrix to quantify the number of correct and incorrect classifications. We relate the classification of each pixel as:

TP (True Positives) An object pixel that is correctly classified as an object.

TN (True Negatives) A background pixel that is correctly classified as a background.

FP (False Positives) A background pixel that is incorrectly classified as an object.

FN (False Negatives) An object pixel that is incorrectly classified as a background.

From these counts we calculate the following binary classification measures:

$$precision = \frac{TP}{TP + FP}$$

$$recall = \frac{TP}{TP + FN}$$

$$accuracy = \frac{TP + TN}{TP + TN + FP + FN}$$

$$MCC = \frac{TP \times TN - FP \times FN}{\sqrt{(TP + FP)(TP + FN)(TN + FP)(TN + FN)}}$$

Accuracy is the fraction of the pixels that are correctly classified from among all pixels. MCC is the *Matthews Correlation Coefficient* and is more accurate measure of accuracy when comparing classes whose sizes differ greatly. Its results is a value between -1 and $+1$, where -1 refers to a complete opposite classification, i.e. all background pixels are classified as object and all object are classified as background, and $+1$ means a perfect classification, 0 is equivalent to a random classification. The results for each image in the test set is tabulated in Table 4.8. The overall efficiency for each method is tabulated in Table 4.9. For each table, rows that are highlighted in blue show the method that performed the best for each image in Table 4.8 and over the test set in Table 4.9.

TABLE 4.8: Segmentation Efficiency.

Image	TP	TN	FP	FN	Precision	Recall	Accuracy	MCC
1-n	24954	25516	0	15066	1.000000	0.623538	0.770111	0.626140
1-m	37875	25506	10	2145	0.999736	0.946402	0.967117	0.934010
1-o	37973	25506	10	2047	0.999737	0.948851	0.968613	0.936880
1-k	37973	25506	10	2047	0.999737	0.948851	0.968613	0.936880
1-e	37736	25510	6	2284	0.999841	0.942929	0.965057	0.930095
1-d	37364	25513	3	2656	0.999920	0.933633	0.959427	0.919468
2-n	5561	43411	179	16385	0.968815	0.253395	0.747253	0.416180
2-m	21864	120	43470	82	0.334650	0.996264	0.335449	-0.008374

2-o	21856	37015	6575	90	0.768738	0.995899	0.898300	0.804725
2-k	21856	37015	6575	90	0.768738	0.995899	0.898300	0.804725
2-e	21878	36617	6973	68	0.758310	0.996901	0.892563	0.795678
2-d	21867	34669	8921	79	0.710244	0.996400	0.862671	0.748686
3-n	9113	55407	24	992	0.997373	0.901831	0.984497	0.939774
3-m	10105	47657	7774	0	0.565188	1.000000	0.881378	0.697081
3-o	10104	54541	890	1	0.919047	0.999901	0.986404	0.950885
3-k	10104	54541	890	1	0.919047	0.999901	0.986404	0.950885
3-e	10105	54277	1154	0	0.897504	1.000000	0.982391	0.937454
3-d	10105	53847	1584	0	0.864488	1.000000	0.975830	0.916397
4-n	10654	49844	99	4939	0.990793	0.683255	0.923126	0.783314
4-m	15593	46825	3118	0	0.833360	1.000000	0.952423	0.883930
4-o	15593	47552	2391	0	0.867048	1.000000	0.963516	0.90859
4-k	15593	47552	2391	0	0.867048	1.000000	0.963516	0.90859
4-e	14839	48771	1172	754	0.926800	0.951645	0.970612	0.919839
4-d	14920	48593	1350	673	0.917025	0.956840	0.969131	0.916491
5-n	21195	38591	2276	3474	0.903029	0.859175	0.912262	0.811918
5-m	24669	31160	9707	0	0.717623	1.000000	0.851883	0.739708
5-o	24669	31482	9385	0	0.724408	1.000000	0.856796	0.747027
5-k	24669	31482	9385	0	0.724408	1.000000	0.856796	0.747027
5-e	24669	35418	5449	0	0.819078	1.000000	0.916855	0.842536
5-d	24669	35427	5440	0	0.819323	1.000000	0.916992	0.842769
6-n	8041	25755	0	31740	1.000000	0.202132	0.515686	0.300907
6-m	38173	1358	24397	1608	0.610085	0.959579	0.603195	0.028915
6-o	35876	25713	42	3905	0.998831	0.901838	0.939774	0.883440
6-k	35096	25729	26	4685	0.999260	0.882230	0.928116	0.863032
6-e	34459	25734	21	5322	0.999391	0.866218	0.918472	0.846506
6-d	37815	25503	252	1966	0.993380	0.950579	0.966156	0.931253
7-n	3213	47332	19	14972	0.994121	0.176684	0.771255	0.364534
7-m	17876	43120	4231	309	0.808613	0.983008	0.930725	0.846322
7-o	13903	47235	116	4282	0.991726	0.764531	0.932892	0.832125
7-k	13903	47235	116	4282	0.991726	0.764531	0.932892	0.832125
7-e	16478	46937	414	1707	0.975491	0.906131	0.967636	0.918642
7-d	14740	46846	505	3445	0.966874	0.810558	0.939728	0.847704
8-n	4494	22158	0	38884	1.000000	0.103601	0.406677	0.193924
8-m	42118	133	22025	1260	0.656627	0.970953	0.644699	-0.075582
8-o	16780	22158	0	26598	1.000000	0.386832	0.594147	0.419288
8-k	16780	22158	0	26598	1.000000	0.386832	0.594147	0.419288
8-e	17641	22158	0	25737	1.000000	0.406681	0.607285	0.433758
8-d	24348	22141	17	19030	0.999302	0.561298	0.709366	0.548682
9-n	4890	53207	3	7436	0.999387	0.396722	0.886490	0.589732

9-m	12325	49186	4024	1	0.753869	0.999919	0.938583	0.834732
9-o	12301	52336	874	25	0.933662	0.997972	0.986282	0.957060
9-k	12301	52336	874	25	0.933662	0.997972	0.986282	0.957060
9-e	12258	52948	262	68	0.979073	0.994483	0.994965	0.983657
9-d	12298	52633	577	28	0.955184	0.997728	0.990768	0.970635
10-n	14187	31146	2	20201	0.999859	0.412557	0.691727	0.500151
10-m	34387	30887	261	1	0.992467	0.999971	0.996002	0.992013
10-o	34373	31109	39	15	0.998867	0.999564	0.999176	0.998348
10-k	34381	31095	53	7	0.998461	0.999796	0.999084	0.998165
10-e	34363	31115	33	25	0.999041	0.999273	0.999115	0.998226
10-d	34384	31013	135	4	0.996089	0.999884	0.997879	0.995755
11-n	14671	40720	132	10013	0.991083	0.594353	0.845200	0.684969
11-m	24500	3572	37280	184	0.396568	0.992546	0.428345	0.166735
11-o	24284	33091	7761	400	0.757809	0.983795	0.875473	0.769468
11-k	24284	33091	7761	400	0.757809	0.983795	0.875473	0.769468
11-e	24347	32248	8604	337	0.738885	0.986347	0.863571	0.751768
11-d	24030	35179	5673	654	0.809009	0.973505	0.903458	0.812402
12-n	7204	45666	295	12371	0.960661	0.368020	0.806732	0.519903
12-m	19530	776	45185	45	0.301785	0.997701	0.309845	0.060018
12-o	19415	39881	6080	160	0.761522	0.991826	0.904785	0.806923
12-k	19415	39881	6080	160	0.761522	0.991826	0.904785	0.806923
12-e	19465	39285	6676	110	0.744616	0.994381	0.896454	0.793664
12-d	19408	39947	6014	167	0.763433	0.991469	0.905685	0.808358
13-n	2608	53651	1298	7979	0.667691	0.246340	0.858444	0.346226
13-m	10541	2533	52416	46	0.167432	0.995655	0.199493	0.079031
13-o	9284	47991	6958	1303	0.571604	0.876925	0.873947	0.639563
13-k	9606	46365	8584	981	0.528092	0.907339	0.854050	0.617332
13-e	9525	47363	7586	1062	0.556659	0.899688	0.868042	0.638175
13-d	10320	44499	10450	267	0.496870	0.974780	0.836472	0.620618
14-n	1461	51387	508	12180	0.742001	0.107104	0.806396	0.231433
14-m	13641	0	51895	0	0.208145	1.000000	0.208145	NaN
14-o	9703	48117	3778	3938	0.719754	0.711311	0.882263	0.641301
14-k	9703	48117	3778	3938	0.719754	0.711311	0.882263	0.641301
14-e	10329	47119	4776	3312	0.683813	0.757203	0.876587	0.641224
14-d	10154	47865	4030	3487	0.715877	0.744374	0.885300	0.657278
15-n	936	62133	33	2434	0.965944	0.277745	0.962357	0.507270
15-m	3370	3061	59105	0	0.053942	1.000000	0.098129	0.051537
15-o	2847	62143	23	523	0.991986	0.844807	0.991669	0.911385
15-k	2847	62143	23	523	0.991986	0.844807	0.991669	0.911385
15-e	3345	61918	248	25	0.930977	0.992582	0.995834	0.959144
15-d	3363	61528	638	7	0.840540	0.997923	0.990158	0.911074

16-n	4543	58089	4	2900	0.999120	0.610372	0.955688	0.762067
16-m	7443	99	57994	0	0.113743	1.000000	0.115082	0.013923
16-o	7434	57377	716	9	0.912147	0.998791	0.988937	0.948497
16-k	7434	57377	716	9	0.912147	0.998791	0.988937	0.948497
16-e	7434	57155	938	9	0.887960	0.998791	0.985550	0.934020
16-d	7437	56680	1413	6	0.840339	0.999194	0.978348	0.905052
17-n	2858	55353	634	6691	0.818442	0.299298	0.888229	0.452365
17-m	9536	298	55689	13	0.146202	0.998639	0.150055	0.020336
17-o	8509	51944	4043	1040	0.677900	0.891088	0.922440	0.734195
17-k	8509	51944	4043	1040	0.677900	0.891088	0.922440	0.734195
17-e	8915	51233	4754	634	0.652206	0.933606	0.917786	0.736986
17-d	9006	50960	5027	543	0.641773	0.943135	0.915009	0.733933
18-n	10662	28372	3	26499	0.999719	0.286914	0.595612	0.384991
18-m	37161	0	28375	0	0.567032	1.000000	0.567032	NaN
18-o	34582	28099	276	2579	0.992082	0.930599	0.956436	0.914421
18-k	34653	28086	289	2508	0.991729	0.932510	0.957321	0.916017
18-e	35373	27881	494	1788	0.986227	0.951885	0.965179	0.930209
18-d	34845	28118	257	2316	0.992678	0.937677	0.960739	0.922580
19-n	6080	49795	190	9471	0.969697	0.390972	0.852585	0.559970
19-m	15551	21811	28174	0	0.355655	1.000000	0.570099	0.393942
19-o	1743	49985	0	13808	1.000000	0.112083	0.789307	0.296349
19-k	1743	49985	0	13808	1.000000	0.112083	0.789307	0.296349
19-e	2340	49985	0	13211	1.000000	0.150473	0.798416	0.344988
19-d	15144	48771	1214	407	0.925786	0.973828	0.975266	0.933388
20-n	7631	52325	94	5486	0.987832	0.581764	0.914856	0.719637
20-m	13112	31433	20986	5	0.384539	0.999619	0.679703	0.479944
20-o	3934	52419	0	9183	1.000000	0.299916	0.859879	0.505181
20-k	3742	52419	0	9375	1.000000	0.285279	0.856949	0.491933
20-e	11467	52403	16	1650	0.998607	0.874209	0.974579	0.919788
20-d	12993	50360	2059	124	0.863208	0.990547	0.966690	0.904878
21-n	5859	54029	0	5648	1.000000	0.509168	0.913818	0.678954
21-m	11504	410	53619	3	0.176650	0.999739	0.181793	0.035231
21-o	9354	54019	10	2153	0.998932	0.812896	0.966995	0.883569
21-k	9354	54019	10	2153	0.998932	0.812896	0.966995	0.883569
21-e	9367	54019	10	2140	0.998934	0.814026	0.967194	0.884286
21-d	9386	54016	13	2121	0.998617	0.815677	0.967438	0.885155
22-n	9992	36090	0	19454	1.000000	0.339333	0.703156	0.469557
22-m	29446	0	36090	0	0.449310	1.000000	0.449310	NaN
22-o	29301	33903	2187	145	0.930545	0.995076	0.964417	0.930373
22-k	29301	33903	2187	145	0.930545	0.995076	0.964417	0.930373
22-e	28465	35927	163	981	0.994306	0.966685	0.982544	0.964943

22-d	29163	35176	914	283	0.969611	0.990389	0.981735	0.963345
23-n	11850	49497	42	4147	0.996468	0.740764	0.936081	0.824684
23-m	15994	48127	1412	3	0.918879	0.999812	0.978409	0.944698
23-o	15978	48676	863	19	0.948756	0.998812	0.986542	0.964737
23-k	15978	48676	863	19	0.948756	0.998812	0.986542	0.964737
23-e	15978	48664	875	19	0.948080	0.998812	0.986359	0.964275
23-d	15978	48665	874	19	0.948137	0.998812	0.986374	0.964313
24-n	3284	57098	577	4577	0.850557	0.417759	0.921356	0.562635
24-m	7861	1055	56620	0	0.121912	1.000000	0.136047	0.047223
24-o	7853	48469	9206	8	0.460344	0.998982	0.859406	0.621496
24-k	7853	48469	9206	8	0.460344	0.998982	0.859406	0.621496
24-e	7858	47094	10581	3	0.426162	0.999618	0.838501	0.589715
24-d	7844	50004	7671	17	0.505575	0.997837	0.882690	0.661018
25-n	5597	32002	27	27910	0.995199	0.167040	0.573715	0.296608
25-m	33507	0	32029	0	0.511276	1.000000	0.511276	NaN
25-o	23435	31813	216	10072	0.990867	0.699406	0.843018	0.720953
25-k	22771	31815	214	10736	0.990690	0.679589	0.832916	0.704884
25-e	23435	31813	216	10072	0.990867	0.699406	0.843018	0.720953
25-d	31767	31142	887	1740	0.972836	0.948071	0.959915	0.920148

From the marked-up rows, we can clearly see that the proposed method supercedes the competitor methods. This is better shown in Table 4.9. From the data in Table 4.8 we plot Precision vs Recall in Figure 4.71. From Figure 4.71 we can see that the parameter settings proposed by Masaka *et al.* tend to have low precision bu a very high recall. We can also see that the parameter settings proposed by El Zehiry *et al.* tend to have very low recall but a high precision. The proposed method, for all initialisation methods, have a relatively high precision and recall. We plot the accuracy over the test set which is shown in Figure 4.72. We can clearly see the the performance of the competitor parameter settings are very erratic. The proposed method is much more stable which is verified by the standard deviation of the accuracy shown in Table 4.9.

TABLE 4.9: Overall Segmentation Efficiency.

Method	Precision		Recall		Accuracy	
	Mean	Std. Dev.	Mean	Std. Dev.	Mean	Std. Dev.
El-Zehiry <i>et al.</i>	0.951912	0.088710	0.421993	0.226299	0.805732	0.151199
Maska <i>et al.</i>	0.485812	0.292765	0.993592	0.014007	0.547369	0.321099
Prop. - Otsu	0.876652	0.153530	0.845668	0.240808	0.911657	0.087720
Prop. - K-means	0.874892	0.157316	0.844808	0.242856	0.909905	0.088468
Prop. - EMGMM	0.875713	0.161034	0.883279	0.202419	0.918983	0.087190
Prop. - EMGMM+Dilate	0.860245	0.149355	0.939366	0.103397	0.935329	0.064493

4.4 Discussion

Discuss the proposed method against the competing methods here.

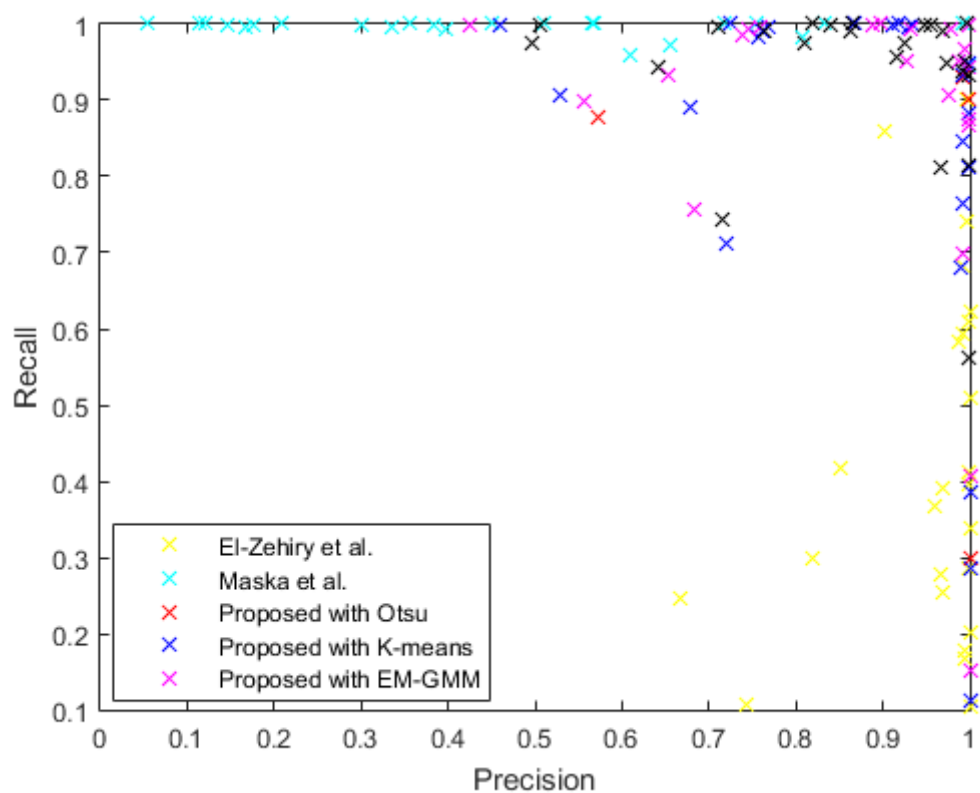


FIGURE 4.71: Precision vs Recall over test set.

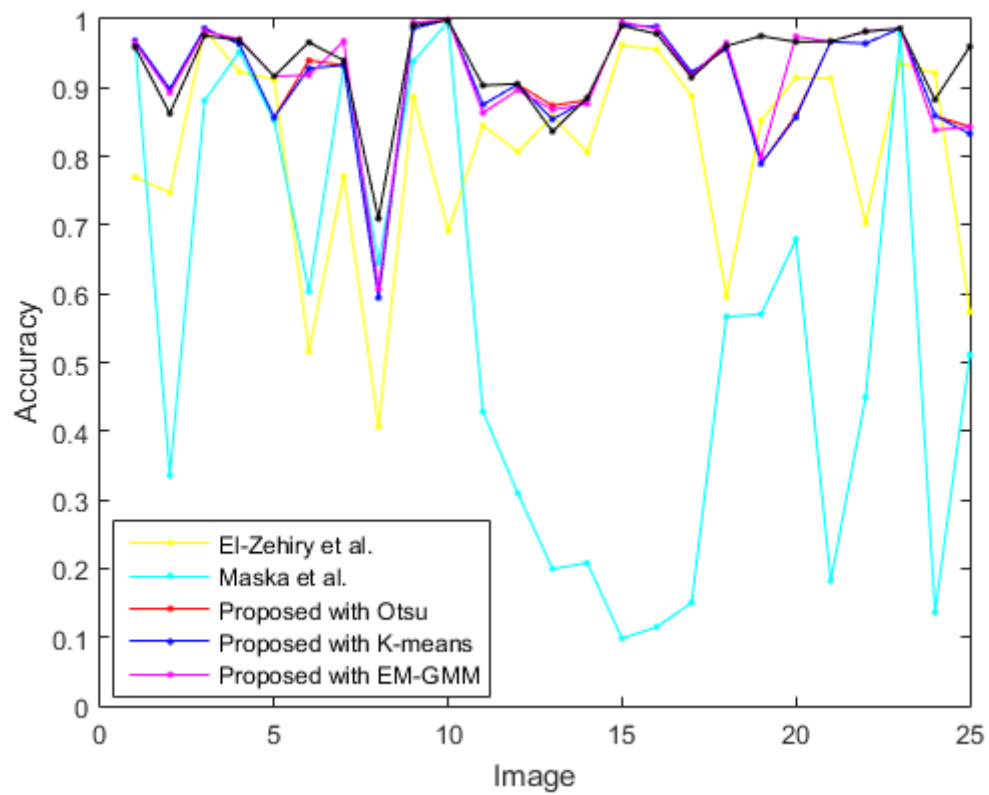


FIGURE 4.72: Accuracy over test set.

Appendix A

Introduction to Graph Theory

Graph A graph G is a pair (V, E) , where V is the set of nodes/vertices and E is the set of edges consisting of pairs (u, v) where $u, v \in V$. The graph is assumed to be finite i.e. $|V| = n$ and $|E| = m$.

In an **undirected graph**, the edge (u, v) and (v, u) are not distinct. That is, they refer to the same edge. However, in a **directed graph**, the two edge are now distinct. In a directed graph with edge (u, v) , u is known as the **tail** and v is known as the **head**. In directed graphs, edges, also known as arcs, are depicted by placing arrowheads at the head of the edge. Given an edge $e = (u, v)$, u and v are said to be **incident** on e . A graph is said to be **simple** if it does not contain any self-loops. A **self-loop** is an edge with both end points being the same vertex.

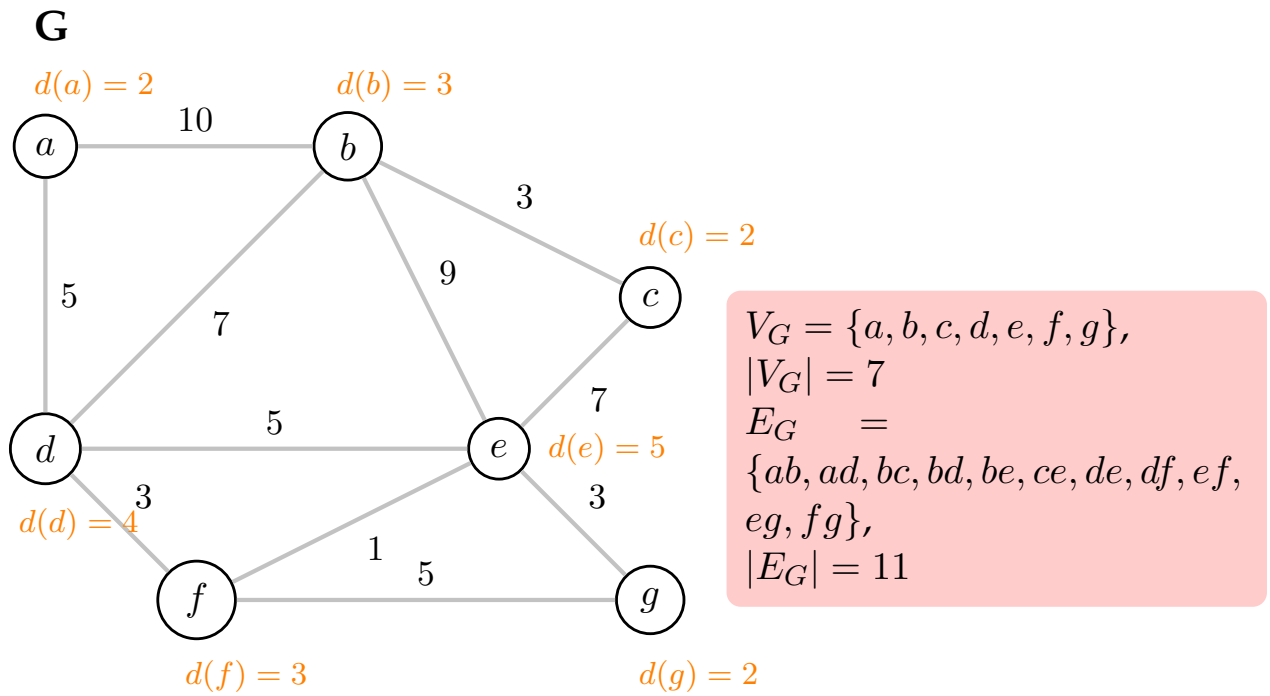


FIGURE A.1: Undirected weighted graph \mathbf{G} . The degree of each node is shown next to the corresponding node. The graph is simple. The red box shows the vertex set, V_G , and edge set, E_G , and their corresponding norm.

Degree The degree of a vertex v is the number of edges incident on it. $deg(v) = |\{(u, v), (v, u) \in E\}|$. A self-loop counts for 2.

If a graph is directed, also known as a **digraph**, then a node v has an **in-degree** $d_{in}(v)$ and an **out-degree** $d_{out}(v)$. A digraph is said to be **balanced** if $d_{in}(v) = d_{out}(v), \forall v \in V$.

Subgraph A graph $G' = (V', E')$ is said to be a sub-graph of $G = (V, E)$, denoted as $G' \subseteq G$, if $V' \subseteq V$ and $E' \subseteq E$.

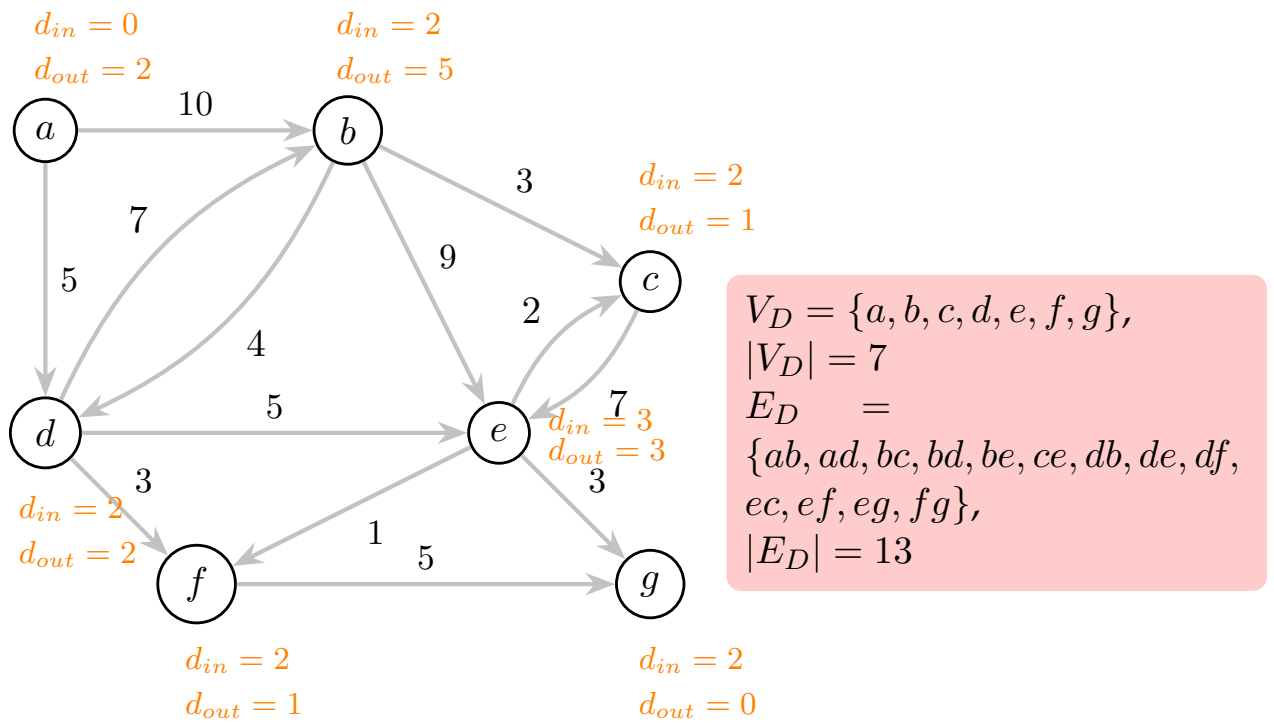
D

FIGURE A.2: Directed weighted graph (Digraph) **D**. The in-degree and out-degree is shown next to each node. The graph is simple and not balanced. The red box shows the vertex set, V_D , and edge set, E_D , and their corresponding norm.

Clique A clique is a maximal subgraph.

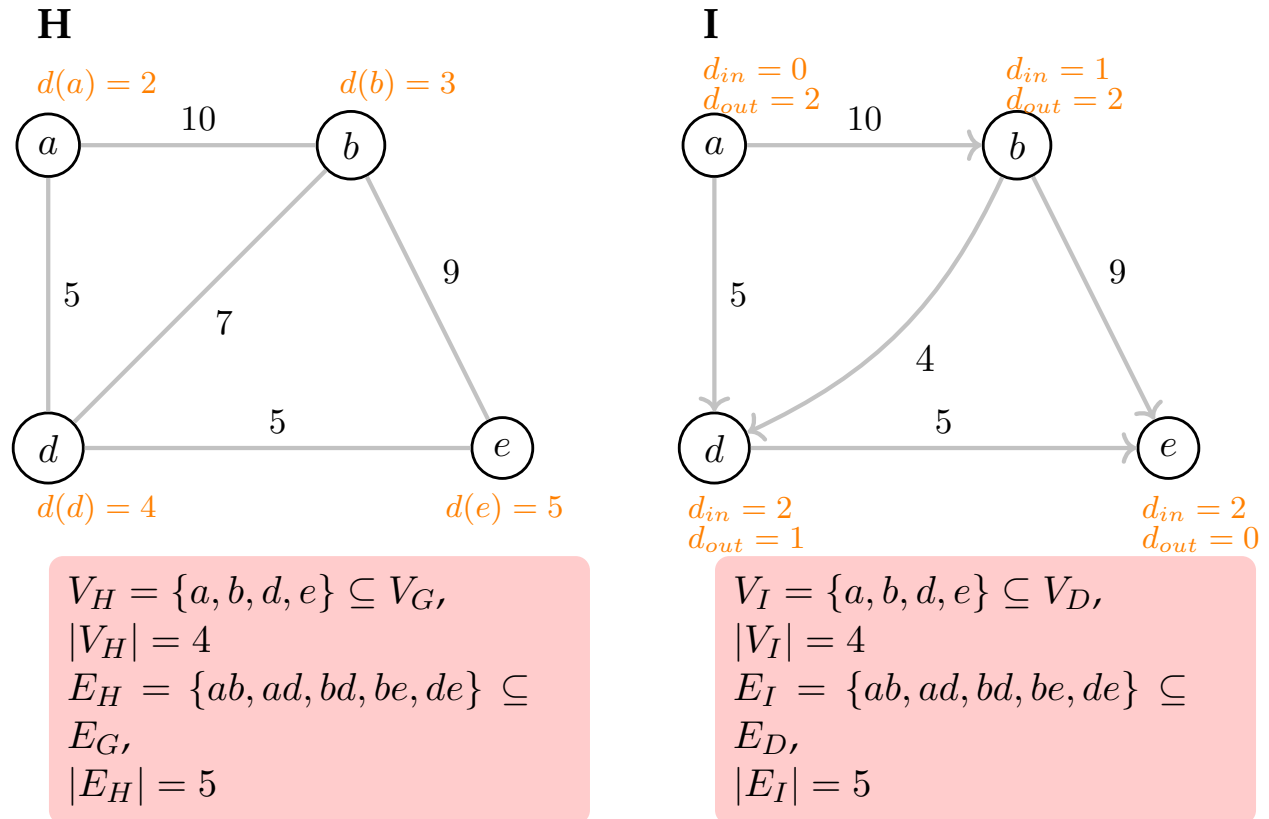


FIGURE A.3: Undirected weighted graph \mathbf{H} is a subgraph of \mathbf{G} in Figure XX, $\mathbf{H} \subseteq \mathbf{G}$. Directed weighted graph \mathbf{I} is a subgraph of \mathbf{D} in Figure XX, $\mathbf{I} \subseteq \mathbf{D}$. The degree of each node is shown next to the corresponding node. The red box shows the vertex set, the edge set and their corresponding norms.

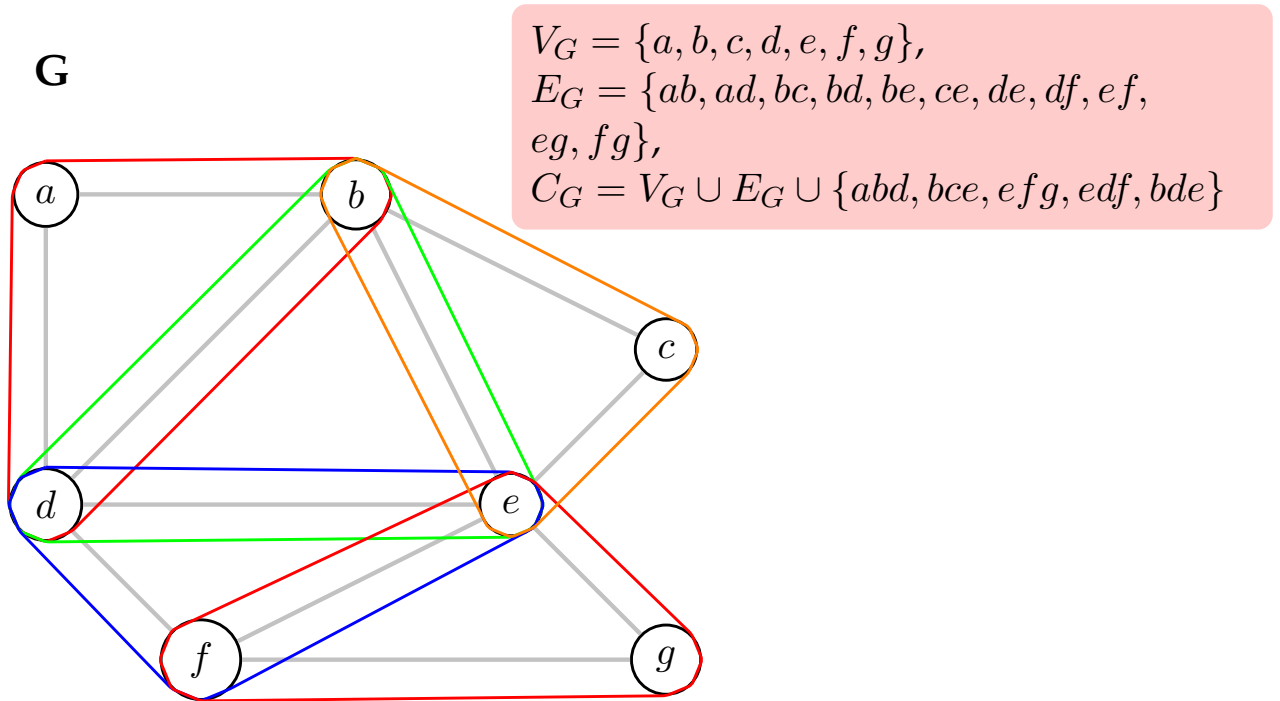


FIGURE A.4: Cliques of the undirected weighted graph \mathbf{G} . The maximal cliques are shown by the hyperedges that encompass the nodes of that clique.

Appendix B

Cell Images Dataset

The dataset is composed of two subsets. One as the sample set and one as the test set. The sample set is used for tuning parameters and testing theories or predictions. This dataset is composed of images that are relatively simple but still try to maintain some of the variation of images obtained in fluorescence microscopy. The other dataset is the test set. This dataset contains more complex images and is used to test the robustness of the segmentation schemes or techniques. We aim for a larger coverage of the types of images that are frequently obtained in fluorescence microscopy.

B.1 Sample Set

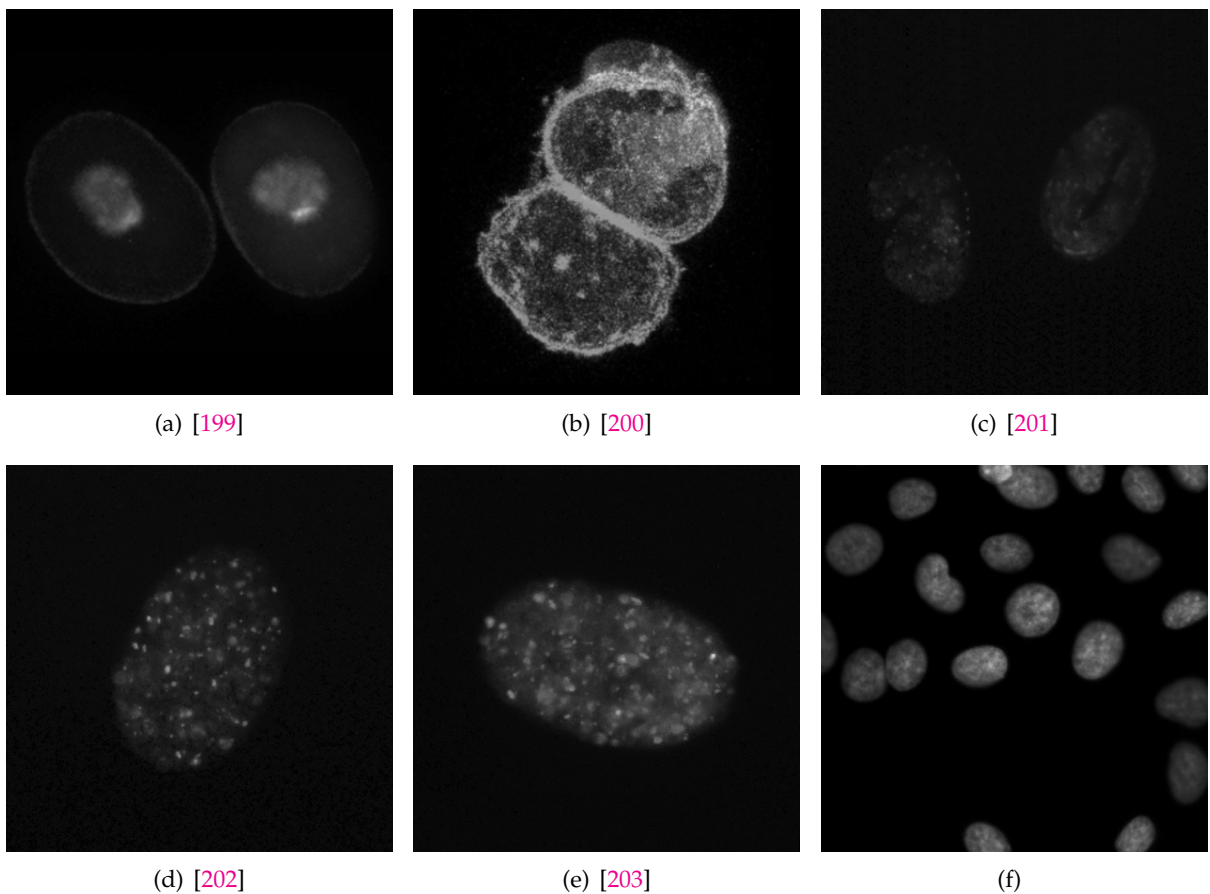
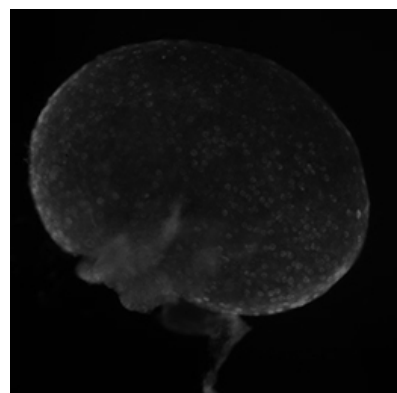


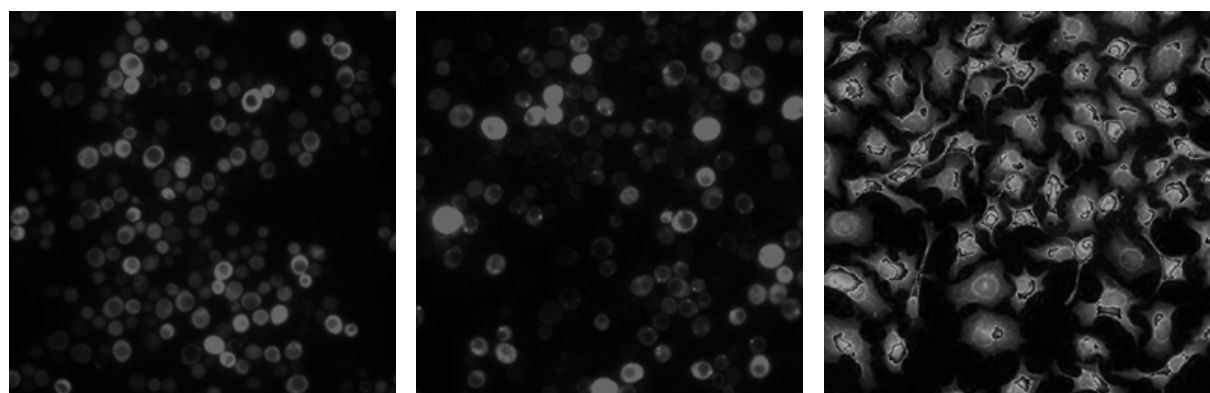
FIGURE B.1: Sample set.

B.2 Test Set



(a) [204]

FIGURE B.2: Uneven Illumination



(a) [205]

(b) [206]

(c) [207]

FIGURE B.3: High cell density

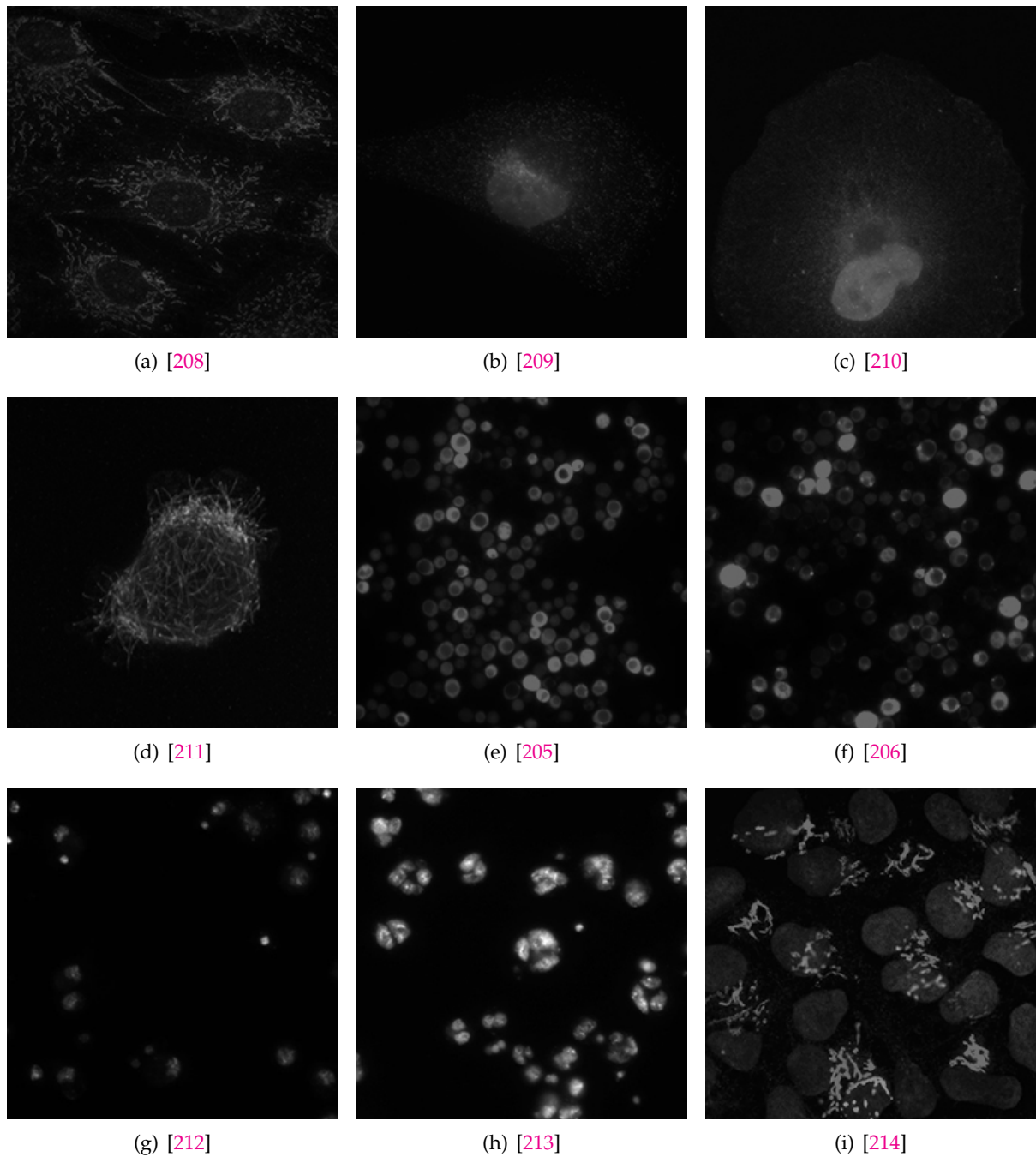


FIGURE B.4: Multi-modal (non-bi-modal)

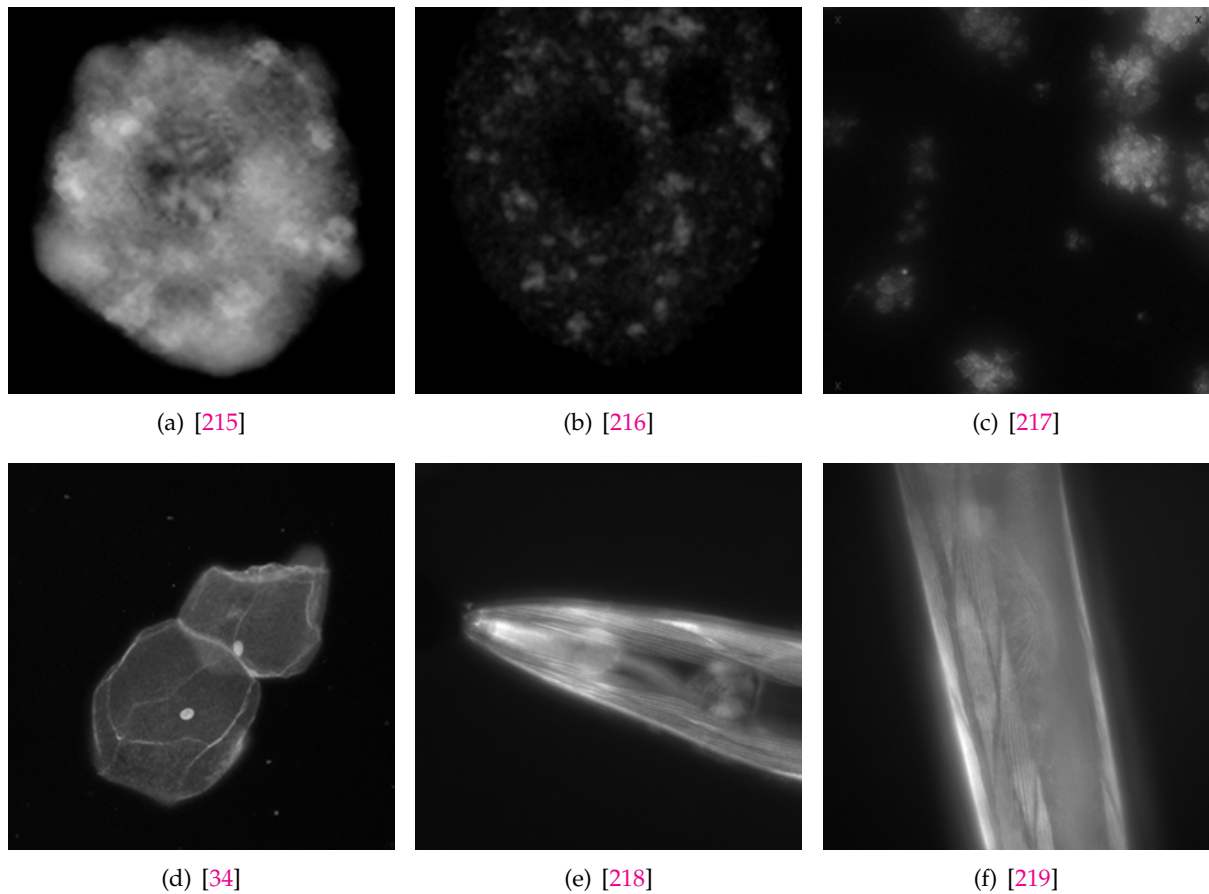


FIGURE B.5: Hazy/Glowing Edges

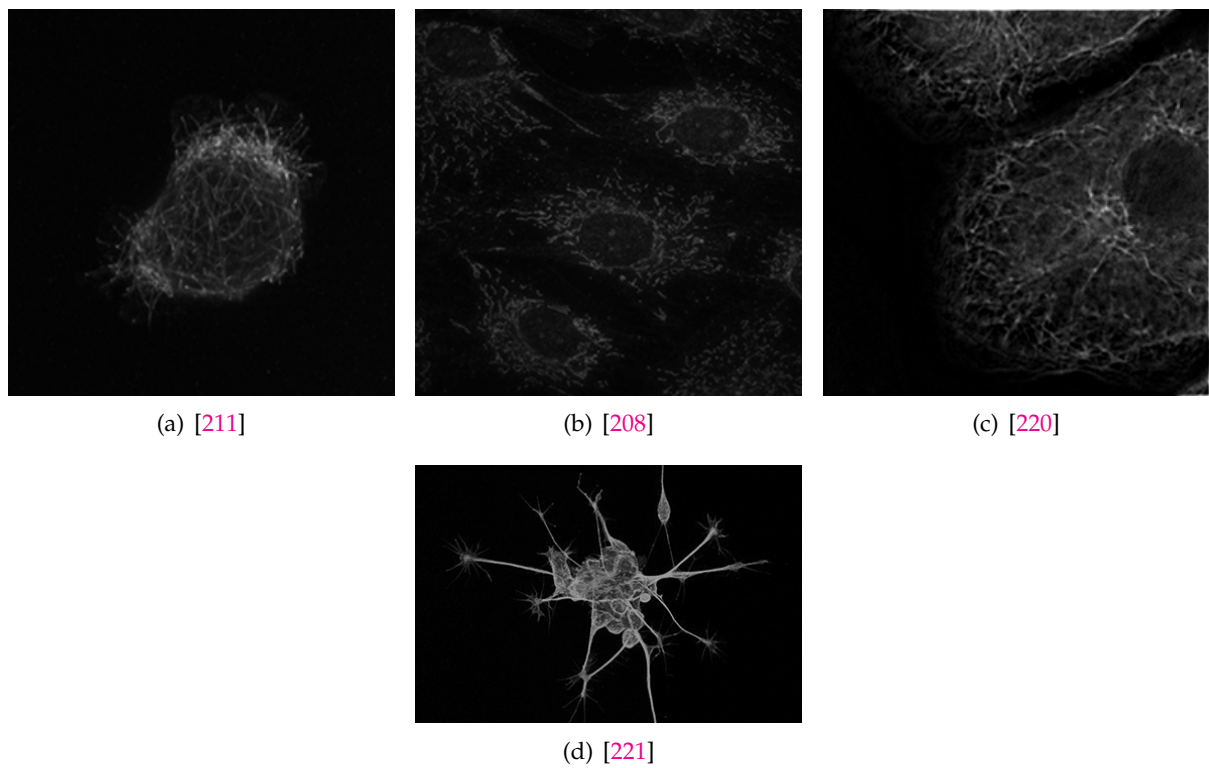


FIGURE B.6: Thin Tentacles

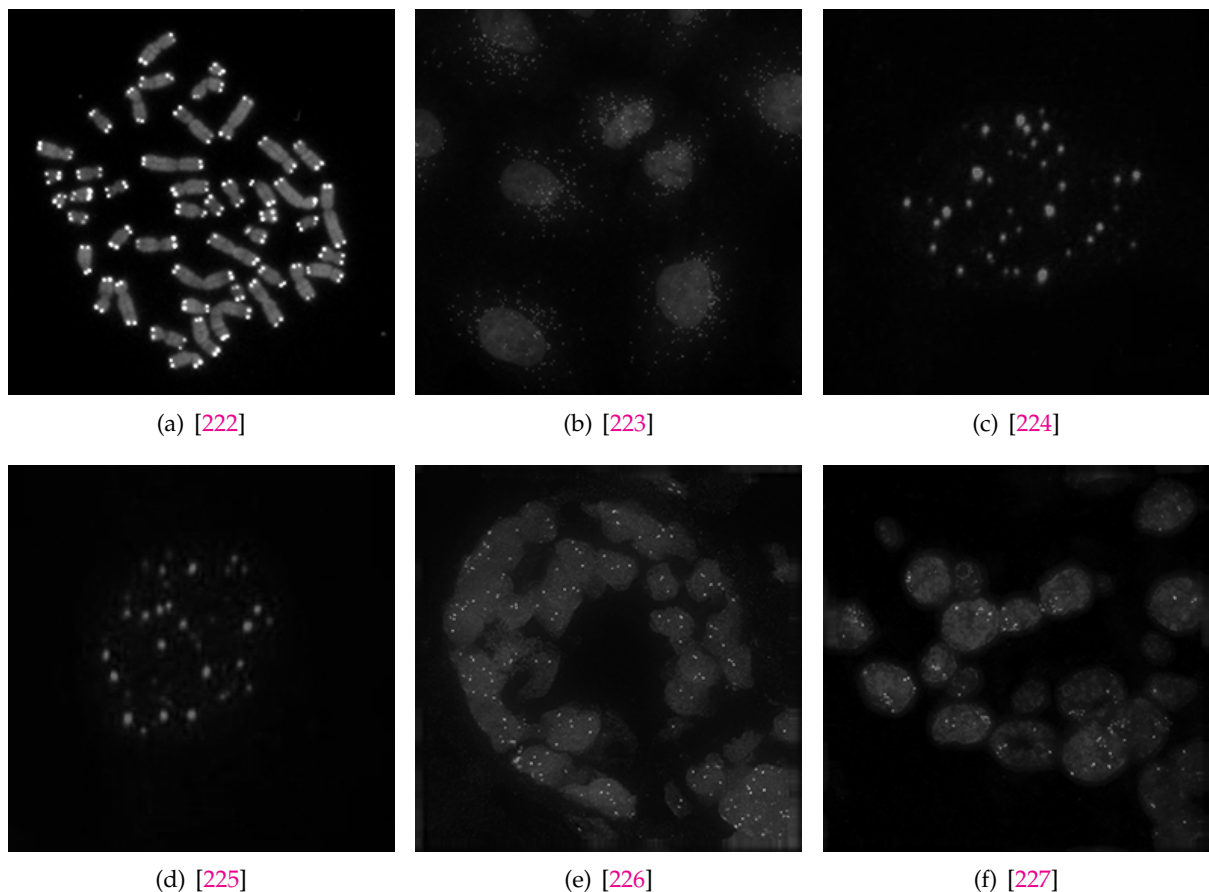


FIGURE B.7: Bright Spots and Speckles

Bibliography

- [1] Kenneth R. Spring. *Encyclopedia of Optical Engineering - Fluorescence Microscopy*. 270 Madison Avenue, New York, New York 10016: Marcel Dekker, Inc., 2003, pp. 548–555. DOI: [10.1081/E-EOE](https://doi.org/10.1081/E-EOE).
- [2] Ondřej Daněk. "Graph Cut Based Image Segmentation in Fluorescence Microscopy [online]". Doctoral theses, Dissertations. Masaryk University, Faculty of Informatics, Brno, 2012 [cit. 2016-09-08]. URL: http://is.muni.cz/th/60931/fi_d/thesis-final.pdf.
- [3] Jan Hubený. "Applications of PDE - Based Image Processing in Fluorescence Microscopy [online]". Doctoral theses, Dissertations. Masaryk University, Faculty of Informatics, Brno, 2008 [cit. 2016-09-07]. URL: http://is.muni.cz/th/4012/fi_d/.
- [4] Fatima A. Merchant and Ammasi Periasamy. "Fluorescence Imaging". In: *Microscope Image Processing*. USA: Elsevier Inc, 2008, pp. 247–271. ISBN: 978-0-12-372578-3.
- [5] Pavel Matula. "Image Processing in Fluorescence Microscopy and its Utilization in Cell Biology Experiments [online]". Doctoral theses, Dissertations. Masaryk University, Faculty of Informatics, Brno, 2012 [cit. 2016-09-09].
- [6] Karl-Friedrich Koch. *Fluorescence Microscopy - Instruments, Methods, Applications*. Lietz Wetzlar, 1972.
- [7] Andrew Vaughan. *Principles of Fluorescence Microscopy*. Document. (accessed September 6, 2016).
- [8] Pinaki Sarder and Arye Nehorai. "Deconvolution Methods for 3-D Fluorescence Microscopy Images". In: *IEEE Signal Processing Magazine* 23.3 (2006), 32—45. DOI: [10.1049/j.1365-2818.2000.00754.x](https://doi.org/10.1049/j.1365-2818.2000.00754.x).
- [9] Mortimer Abramowitz and Michael W. Davidson. *Introduction to Fluorescence*. Website. (accessed September 6, 2016). URL: <http://www.olympusmicro.com/primer/lightandcolor/fluorointroduction.html>.
- [10] Kenneth R. Spring and Michael W. Davidson. *Introduction to Fluorescence Microscopy*. Website. (accessed September 6, 2016). URL: <http://www.microscopyu.com/techniques/fluorescence/introduction-to-fluorescence-microscopy>.
- [11] Jurek W. Dobrucki. "Fluorescence Microscopy". In: *Fluorescence Microscopy: From Principles to Biological Applications*. 1st Edition. Wiley-VCH Verlag GmbH & Co., 2013, pp. 97–142.
- [12] Nobel Media AB. *The Fluorescence Microscopy*. Website. (accessed September 6, 2016). URL: <http://www.nobelprize.org/educational/physics/microscopes/fluorescence/>.
- [13] *Fluorescence SpectraViewer*. Website. (accessed September 18, 2016). URL: <https://www.thermofisher.com/us/en/home/life-science/cell-analysis/labeling-chemistry/fluorescence-spectraviewer.html>.
- [14] Roger Y. Tsien. "The Green Fluorescent Protein". In: *Annual Review of Biochemistry* 67 (1998), pp. 509–544.
- [15] Michal Kozubek. "FISH imaging". In: *Confocal and Two-Photon Microscopy: Foundations, Applications and Advances* (2001), 389—429.
- [16] Z. Theodosiou et al. "Automated Analysis of FISH and immunohistochemistry images: A Review". In: *Cytometry Part A* 71.7 (2007), pp. 439–450.

- [17] Rudolf Amann and Bernhard M. Fuchs. "Single-cell identification in microbial communities by improved fluorescence *in situ* hybridization techniques". In: *Nature Reviews Microbiology* 6.5 (2008), 339—348. DOI: [10.1038/nrmicro1888](https://doi.org/10.1038/nrmicro1888).
- [18] Kelly Cude and Kelly Burke. "Introduction to Fluorescence Microscopy". In: (14 July 2012).
- [19] Kishore Reddy Katikireddy and Finbarr O'Sullivan. "Immunohistochemical and Immunofluorescence Procedures for Protein Analysis". In: *Gene Expression Profiling: Methods and Protocols*. Ed. by Lorraine O'Driscoll. Totowa, NJ: Humana Press, 2011, pp. 155–167. ISBN: 978-1-61779-289-2. DOI: [10.1007/978-1-61779-289-2_11](https://doi.org/10.1007/978-1-61779-289-2_11). URL: http://dx.doi.org/10.1007/978-1-61779-289-2_11.
- [20] Jeff W. Lichtman and José-Angel Conchello. *Nature Methods - Fluorescence microscopy*. Vol. 2. 12. Nature Publishing Group, Decmeber 2005, pp. 910–919. DOI: [10.1038/NMETH817](https://doi.org/10.1038/NMETH817). URL: <http://www.nature.com/naturemethods>.
- [21] Paul D. Andrews, Ian S. Harper, and Jason R. Swedlow. "To 5D and Beyond: Quantitative Fluorescence Microscopy in the Postgenomic Era". In: *Traffic*. Vol. 3. Munksgaard International Publishers, 2002, pp. 29–36.
- [22] George Rice. *Fluorescent Microscopy*. Website. (accessed September 6, 2016). URL: http://serc.carleton.edu/microbelife/research_methods/microscopy/fluromic.html.
- [23] Kavita Aswani, Tushare Jinadasa, and Claire M. Brown. "Fluorescence Microscopy Light Sources". In: *Microscopy Today*. 2012, pp. 22–28. DOI: [10.1017/S1551929512000399](https://doi.org/10.1017/S1551929512000399). URL: www.microscopy-today.com.
- [24] Thermo Fisher Scientific. *Fundamentals of Fluorescence Microscopy*. Website. (accessed September 6, 2016). URL: <https://www.thermofisher.com/us/en/home/life-science/cell-analysis/cell-analysis-learning-center/molecular-probes-school-of-fluorescence/fundamentals-of-fluorescence-microscopy.html>.
- [25] Douglas B. Murphy. *Fundamentals of Light Microscopy and Electronic Imaging*. 2nd Edition. USA: John Wiley & Sons, Inc., 2001. ISBN: 0-471-25391-X.
- [26] Ian T. Young. "Shading Correction: Compensation for Illumination and Sensor Inhomogeneities". In: *Current Protocols in Cytometry*. John Wiley & Sons, Inc., 2001. ISBN: 9780471142959. DOI: [10.1002/0471142956.cy0211s14](https://doi.org/10.1002/0471142956.cy0211s14). URL: <http://dx.doi.org/10.1002/0471142956.cy0211s14>.
- [27] Ghauharali, Hofstraat, and Brakenhoff. "Fluorescence photobleaching-based shading correction for fluorescence microscopy". In: *Journal of Microscopy* 192.2 (1998), pp. 99–113. ISSN: 1365-2818. DOI: [10.1046/j.1365-2818.1998.00412.x](https://doi.org/10.1046/j.1365-2818.1998.00412.x). URL: <http://dx.doi.org/10.1046/j.1365-2818.1998.00412.x>.
- [28] Michael Model. "Intensity Calibration and Flat-Field Correction for Fluorescence Microscopes". In: *Current Protocols in Cytometry*. John Wiley & Sons, Inc., 2001. ISBN: 9780471142959. DOI: [10.1002/0471142956.cy1014s68](https://doi.org/10.1002/0471142956.cy1014s68). URL: <http://dx.doi.org/10.1002/0471142956.cy1014s68>.
- [29] Michael A. Model and Janis K. Burkhardt. "A standard for calibration and shading correction of a fluorescence microscope". In: *Cytometry* 44.4 (2001), pp. 309–316. ISSN: 1097-0320. DOI: [10.1002/1097-0320\(20010801\)44:4<309::AID-CYTO1122>3.0.CO;2-3](https://doi.org/10.1002/1097-0320(20010801)44:4<309::AID-CYTO1122>3.0.CO;2-3). URL: [http://dx.doi.org/10.1002/1097-0320\(20010801\)44:4<309::AID-CYTO1122>3.0.CO;2-3](http://dx.doi.org/10.1002/1097-0320(20010801)44:4<309::AID-CYTO1122>3.0.CO;2-3).
- [30] Anne Carpenter. *CIL 21739*. Picture. (accessed September 9, 2016). URL: <http://www.cellimagelibrary.org/images/21739>.

- [31] Stephen A. Boppart et al. "Optical probes and techniques for molecular contrast enhancement in coherence imaging". In: *Journal of Biomedical Optics* 10.4 (2005), pp. 041208–041208–14. DOI: [10.1117/1.2008974](https://doi.org/10.1117/1.2008974). URL: <http://dx.doi.org/10.1117/1.2008974>.
- [32] Molecular Expressions. *Photobleaching*. Picture. (accessed September 9, 2016). URL: <http://micro.magnet.fsu.edu/primer/java/fluorescence/photobleaching/>.
- [33] Margret Keuper. "Segmentation of Cells and Sub-cellular Structures from Microscopic Recordings [online]". Doctoral theses, Dissertations. Albert-Ludwigs-Universität, 2012 [cit. 2016-09-12]. URL: http://lmb.informatik.uni-freiburg.de/Publications/2012/Keu12/Dissertation_Keuper.pdf.
- [34] Arjan Tibbe. *CIL 40968*. Picture. (accessed September 9, 2016). URL: <http://www.cellimagelibrary.org/images/40968>.
- [35] Eran A. Mukamel, Hazen Babcock, and Xiaowei Zhuang. "Statistical Deconvolution for Superresolution Fluorescence Microscopy". In: *Biophysical Journal* 102.10 (2012), pp. 2391–2400. DOI: [10.1038/srep09894](https://doi.org/10.1038/srep09894). URL: <http://dx.doi.org/10.1016/j.bpj.2012.03.070>.
- [36] Peter J Verveer et al. "High-resolution three-dimensional imaging of large specimens with light sheet-based microscopy". In: *Nature Methods* 4 (2007), pp. 311–313. DOI: [10.1038/nmeth1017](https://doi.org/10.1038/nmeth1017). URL: <http://www.nature.com/nmeth/journal/v4/n4/abs/nmeth1017.html>.
- [37] Ammassi Periasamy, Paul Skoglundand Colten Noakes, and Raymond Keller. "An Evaluation of Two-Photon Excitation Versus Confocal and Digital Deconvolution Fluorescence Microscopy Imaging in Xenopus Morphogenesis". In: *Microscopy Research and Technique* 4 (2007), pp. 311–313. DOI: [10.1038/nmeth1017](https://doi.org/10.1038/nmeth1017). URL: <http://www.nature.com/nmeth/journal/v4/n4/abs/nmeth1017.html>.
- [38] Jason R. Swedlow. "Quantitative Fluorescence Microscopy and Image Deconvolution". In: *Digital Microscopy, 3rd Edition*. Vol. 81. Methods in Cell Biology. Academic Press, 2007, pp. 447–465. DOI: [http://dx.doi.org/10.1016/S0091-679X\(06\)81021-6](https://doi.org/10.1016/S0091-679X(06)81021-6). URL: <http://www.sciencedirect.com/science/article/pii/S0091679X06810216>.
- [39] Johan J. de Rooij, Cyril Ruckebusch, and Paul H. C. Eilers. "Sparse Deconvolution in One and Two Dimensions: Applications in Endocrinology and Single-Molecule Fluorescence Imaging". In: *Analytical Chemistry* 86.13 (2014). PMID: 24893114, pp. 6291–6298. DOI: [10.1021/ac500260h](https://doi.org/10.1021/ac500260h). eprint: [http://dx.doi.org/10.1021/ac500260h](https://doi.org/10.1021/ac500260h). URL: <http://dx.doi.org/10.1021/ac500260h>.
- [40] Alexander Wong, Xiao Yu Wang, and Maud Gorbet. "Bayesian-based deconvolution fluorescence microscopy using dynamically updated nonstationary expectation estimates". In: *Scientific Reports* 5.10849 (2015), pp. 1–9. DOI: [10.1038/srep10849](https://doi.org/10.1038/srep10849). URL: <http://dx.doi.org/10.1038/srep10849>.
- [41] Boyoung Kim and Takeshi Naemura. "Blind Depth-variant Deconvolution of 3D Data in Wide-field Fluorescence Microscopy". In: *Scientific Reports* 5.9894 (2015), pp. 1–9. DOI: [10.1038/srep09894](https://doi.org/10.1038/srep09894). URL: <http://dx.doi.org/10.1038/srep09894>.
- [42] Jing Qin et al. "Detail-preserving Fluorescence Microscopy Image Deconvolution". In: *Conference on Lasers and Electro-Optics*. Optical Society of America, 2016, STh4G.7. DOI: [10.1364/CLEO_SI.2016.STh4G.7](https://doi.org/10.1364/CLEO_SI.2016.STh4G.7). URL: http://www.osapublishing.org/abstract.cfm?URI=CLEO_SI-2016-STh4G.7.
- [43] Ryan Naidoo and Jules-Raymond Tapamo. "A Preprocessing Scheme for Fluorescence Microscopy Image Segmentation". In: *International Journal of Imaging and Robotics* 16.4 (2016), pp. 1–23. ISSN: ISSN 2231–525X.

- [44] Gijsbert Michiel Peter Van Kempen. "Image Restoration in Fluorescence Microscopy [online]". Doctoral theses, Dissertations. Technische Universiteit Delft, 1999 [cit. 2016-09-08]. URL: http://www.tnw.tudelft.nl/fileadmin/Faculteit/TNW/Over_de_faculteit/Afdelingen/Imaging_Science_and_Technology/Research/Research_Groups/Quantitative_Imaging/Publications>List_Publications/doc/thesis_kempen.pdf.
- [45] Erik Meijering. "Cell Segmentation: 50 Years Down the Road [Life Sciences]". In: *IEEE Signal Processing Magazine* 29.5 (2012), pp. 140–145. ISSN: 1053-5888. DOI: [10.1109/MSP.2012.2204190](https://doi.org/10.1109/MSP.2012.2204190).
- [46] Bruce Alberts et al. *Molecular Biology of the Cell*. 5th Edition. New York, NY, USA: Garland Science, 2007. ISBN: 9780815341055.
- [47] Cédrik Vonesch et al. "The Colored Revolution of Bioimaging [An introduction to fluorescence microscopy]". In: *IEEE Signal Processing Magazine* 29.5 (2006), pp. 20–31.
- [48] Ewert Bengtsson, Carolina Wählby, and Joakim Lindblad. "Robust cell image segmentation methods". In: *Pattern Recognition and Image Analysis: Advances in Mathematical Theory and Applications* 14.52 (2004), pp. 157–167. ISSN: 1054-6618.
- [49] W.E. Tolles. "Section of Biology: The Cytoanalyzer—An Example of Physics in Medical Research*". In: *Transactions of the New York Academy of Sciences* 17.3 Series II (1955), pp. 250–256. ISSN: 2164-0947. DOI: [10.1111/j.2164-0947.1955.tb01204.x](https://doi.org/10.1111/j.2164-0947.1955.tb01204.x). URL: <http://dx.doi.org/10.1111/j.2164-0947.1955.tb01204.x>.
- [50] Judith M. S. Prewitt and Mortimer L. Mendelsohn. "The Analysis of Cell Images*". In: *Annals of the New York Academy of Sciences* 128.3 (1966), pp. 1035–1053. ISSN: 1749-6632. DOI: [10.1111/j.1749-6632.1965.tb11715.x](https://doi.org/10.1111/j.1749-6632.1965.tb11715.x). URL: <http://dx.doi.org/10.1111/j.1749-6632.1965.tb11715.x>.
- [51] Metin N. Gurcan et al. "Histopathological image analysis: A review". In: *IEEE Reviews in Biomedical Engineering* (2009), pp. 147–171.
- [52] Alden A. Dima et al. "Comparison of segmentation algorithms for fluorescence microscopy images of cells". In: *Cytometry Part A* 79A.7 (2011), pp. 545–559. ISSN: 1552-4930. DOI: [10.1002/cyto.a.21079](https://doi.org/10.1002/cyto.a.21079). URL: <http://dx.doi.org/10.1002/cyto.a.21079>.
- [53] Z. Pincus and J.A. Theriot. "Comparison of quantitative methods for cell-shape analysis". In: *Journal of Microscopy* 227.2 (2007), pp. 140–156. ISSN: 1365-2818. DOI: [10.1111/j.1365-2818.2007.01799.x](https://doi.org/10.1111/j.1365-2818.2007.01799.x). URL: <http://dx.doi.org/10.1111/j.1365-2818.2007.01799.x>.
- [54] Luís Pedro Coelho, Aabid Shariff, and Robert F. Murphy. "Nuclear Segmentation in Microscope Cell Images: A Hand-Segmented Dataset and Comparison of Algorithms". In: *Proc IEEE Int Symp Biomed Imaging* 5.193098E6.2 (2009), pp. 518–521. ISSN: 1365-2818. DOI: [10.1111/j.1365-2818.2007.01799.x](https://doi.org/10.1111/j.1365-2818.2007.01799.x). URL: <http://www.ncbi.nlm.nih.gov/pmc/articles/PMC2901896/>.
- [55] Qiang Wu, Fatima A. Merchant, and Kenneth R. Castleman. *Encyclopedia of Optical Engineering - Fluorescence Microscopy*. 1st Edition. Elsevier Inc., 2008. ISBN: 978-0-12-372578-3.
- [56] E. Meijering et al. "Design and validation of a tool for neurite tracing and analysis in fluorescence microscopy images". In: *Cytometry Part A* 58A.2 (2004), pp. 167–176. ISSN: 1552-4930. DOI: [10.1002/cyto.a.20022](https://doi.org/10.1002/cyto.a.20022). URL: <http://dx.doi.org/10.1002/cyto.a.20022>.
- [57] Quanli Wang et al. "Image segmentation and dynamic lineage analysis in single-cell fluorescence microscopy". In: *Cytometry Part A* 77A.1 (2010), pp. 101–110. ISSN: 1552-4930. DOI: [10.1002/cyto.a.20812](https://doi.org/10.1002/cyto.a.20812). URL: <http://dx.doi.org/10.1002/cyto.a.20812>.

- [58] Rafael C. Gonzalez and Richard E. Woods. *Digital Image Processing*. 3rd Edition. New Jersey, USA: Prentice Hall, Inc., 2002.
- [59] L.B. Dorini, R. Minetto, and N. J. Leite. "White blood cell segmentation using morphological operators and scale-space analysis". In: *Computer Graphics and Image Processing, 2007. SIBGRAPI 2007. XX Brazilian Symposium on*. 2007, pp. 294–304. DOI: [10.1109/SIBGRAPI.2007.33](https://doi.org/10.1109/SIBGRAPI.2007.33).
- [60] D. Anoraganingrum. "Cell segmentation with median filter and mathematical morphology operation". In: *Image Analysis and Processing, 1999. Proceedings. International Conference on*. 1999, pp. 1043–1046. DOI: [10.1109/ICIAP.1999.797734](https://doi.org/10.1109/ICIAP.1999.797734).
- [61] B.R. Kumar, D.K. Joseph, and T.V. Sreenivas. "Teager energy based blood cell segmentation". In: *Digital Signal Processing, 2002. DSP 2002. 2002 14th International Conference on*. Vol. 2. 2002, pp. 619–622. DOI: [10.1109/ICDSP.2002.1028167](https://doi.org/10.1109/ICDSP.2002.1028167).
- [62] Kan Jiang, Qing-Min Liao, and Sheng-Yang Dai. "A novel white blood cell segmentation scheme using scale-space filtering and watershed clustering". In: *Machine Learning and Cybernetics, 2003 International Conference on*. Vol. 5. 2003, pp. 2820–2825. DOI: [10.1109/ICMLC.2003.1260033](https://doi.org/10.1109/ICMLC.2003.1260033).
- [63] Gang Lin et al. "A hybrid 3D watershed algorithm incorporating gradient cues and object models for automatic segmentation of nuclei in confocal image stacks". In: *Cytometry Part A* 56A.1 (2003), pp. 23–36. ISSN: 1552-4930. DOI: [10.1002/cyto.a.10079](https://doi.org/10.1002/cyto.a.10079). URL: <http://dx.doi.org/10.1002/cyto.a.10079>.
- [64] Michael Kass, Andrew Witkin, and Demetri Terzopoulos. "Snakes: Active contour models". In: *International Journal of Computer Vision* 1.4 (1988), pp. 321–331.
- [65] Vicent Caselles, Ron Kimmel, and Guillermo Sapiro. "Geodesic Active Contours". In: *International Journal of Computer Vision* 22.1 (1997), pp. 61–79. ISSN: 0920-5691. DOI: [10.1023/A:1007979827043](https://doi.org/10.1023/A:1007979827043). URL: <http://dx.doi.org/10.1023/A:1007979827043>.
- [66] Hongsheng Li et al. "Automated actin filament segmentation, tracking and tip elongation measurements based on open active contour models". In: *2009 IEEE International Symposium on Biomedical Imaging: From Nano to Macro*. 2009, pp. 1302–1305. DOI: [10.1109/ISBI.2009.5193303](https://doi.org/10.1109/ISBI.2009.5193303).
- [67] J. Cheng and J. C. Rajapakse^{ast}. "Segmentation of Clustered Nuclei With Shape Markers and Marking Function". In: *IEEE Transactions on Biomedical Engineering* 56.3 (2009), pp. 741–748. ISSN: 0018-9294. DOI: [10.1109/TBME.2008.2008635](https://doi.org/10.1109/TBME.2008.2008635).
- [68] Stanley Osher and Ronald P. Fedkiw. *Level set methods and dynamic implicit surfaces*. Applied mathematical science. New York, N.Y.: Springer, 2003. ISBN: 0-387-95482-1. URL: <http://opac.inria.fr/record=b1099358>.
- [69] O. Dzyubachyk, W. Niessen, and E. Meijering. "Advanced level-set based multiple-cell segmentation and tracking in time-lapse fluorescence microscopy images". In: *2008 5th IEEE International Symposium on Biomedical Imaging: From Nano to Macro*. 2008, pp. 185–188. DOI: [10.1109/ISBI.2008.4540963](https://doi.org/10.1109/ISBI.2008.4540963).
- [70] C. Ortiz de Solórzano et al. "Segmentation of nuclei and cells using membrane related protein markers". In: *Journal of Microscopy* 201 (2001), pp. 404–415.
- [71] Alexandre Dufour et al. "Segmenting and tracking fluorescent cells in dynamic 3-D microscopy with coupled active surfaces." In: *IEEE Transactions on Image Processing* 14.9 (2005), pp. 1396–410. URL: <https://hal.archives-ouvertes.fr/hal-00014483>.
- [72] Oleh Dzyubachyk et al. "Advanced Level-Set-Based Cell Tracking in Time-Lapse Fluorescence Microscopy." In: *IEEE Trans. Med. Imaging* 29.3 (2010), pp. 852–867. URL: <http://dblp.uni-trier.de/db/journals/tmi/tmi29.html#DzyubachykCENM10>.

- [73] Fatima Boukari and Sokratis Makrogiannis. "Spatio-temporal Level-Set Based Cell Segmentation in Time-Lapse Image Sequences". In: *Advances in Visual Computing: 10th International Symposium, ISVC 2014, Las Vegas, NV, USA, December 8-10, 2014, Proceedings, Part II*. Ed. by George Bebis et al. Cham: Springer International Publishing, 2014, pp. 41–50. ISBN: 978-3-319-14364-4. DOI: [10.1007/978-3-319-14364-4_5](https://doi.org/10.1007/978-3-319-14364-4_5). URL: http://dx.doi.org/10.1007/978-3-319-14364-4_5.
- [74] Martin Maška et al. "A Comparison of Fast Level Set-Like Algorithms for Image Segmentation in Fluorescence Microscopy". In: *Advances in Visual Computing: Third International Symposium, ISVC 2007, Lake Tahoe, NV, USA, November 26-28, 2007, Proceedings, Part II*. Ed. by George Bebis et al. Berlin, Heidelberg: Springer Berlin Heidelberg, 2007, pp. 571–581. ISBN: 978-3-540-76856-2. DOI: [10.1007/978-3-540-76856-2_56](https://doi.org/10.1007/978-3-540-76856-2_56). URL: http://dx.doi.org/10.1007/978-3-540-76856-2_56.
- [75] Ondřej Daněk et al. "Segmentation of Touching Cell Nuclei Using a Two-Stage Graph Cut Model". In: *Image Analysis: 16th Scandinavian Conference, SCIA 2009, Oslo, Norway, June 15-18, 2009. Proceedings*. Ed. by Arnt-Børre Salberg, Jon Yngve Hardeberg, and Robert Jenssen. Berlin, Heidelberg: Springer Berlin Heidelberg, 2009, pp. 410–419. ISBN: 978-3-642-02230-2. DOI: [10.1007/978-3-642-02230-2_42](https://doi.org/10.1007/978-3-642-02230-2_42). URL: http://dx.doi.org/10.1007/978-3-642-02230-2_42.
- [76] C. Chen et al. "Constraint factor graph cut-based active contour method for automated cellular image segmentation in RNAi screening". In: *Journal of Microscopy* 230.2 (2008), pp. 177–191. ISSN: 1365-2818. DOI: [10.1111/j.1365-2818.2008.01974.x](https://doi.org/10.1111/j.1365-2818.2008.01974.x). URL: <http://dx.doi.org/10.1111/j.1365-2818.2008.01974.x>.
- [77] Y. Al-Kofahi et al. "Improved Automatic Detection and Segmentation of Cell Nuclei in Histopathology Images". In: *IEEE Transactions on Biomedical Engineering* 57.4 (2010), pp. 841–852. ISSN: 0018-9294. DOI: [10.1109/TBME.2009.2035102](https://doi.org/10.1109/TBME.2009.2035102).
- [78] H. Kong, M. Gurcan, and K. Belkacem-Boussaid. "Partitioning Histopathological Images: An Integrated Framework for Supervised Color-Texture Segmentation and Cell Splitting". In: *IEEE Transactions on Medical Imaging* 30.9 (2011), pp. 1661–1677. ISSN: 0278-0062. DOI: [10.1109/TMI.2011.2141674](https://doi.org/10.1109/TMI.2011.2141674).
- [79] Huei-Fang Yang and Yoonsuck Choe. "Cell tracking and segmentation in electron microscopy images using graph cuts". In: *2009 IEEE International Symposium on Biomedical Imaging: From Nano to Macro*. 2009, pp. 306–309. DOI: [10.1109/ISBI.2009.5193045](https://doi.org/10.1109/ISBI.2009.5193045).
- [80] L. Zhang et al. "Automated segmentation of abnormal cervical cells using global and local graph cuts". In: *2014 IEEE 11th International Symposium on Biomedical Imaging (ISBI)*. 2014, pp. 485–488. DOI: [10.1109/ISBI.2014.6867914](https://doi.org/10.1109/ISBI.2014.6867914).
- [81] Lu Liu et al. "Interactive Separation of Segmented Bones in CT Volumes Using Graph Cut". In: *Medical Image Computing and Computer-Assisted Intervention – MICCAI 2008: 11th International Conference, New York, NY, USA, September 6-10, 2008, Proceedings, Part I*. Ed. by Dimitris Metaxas et al. Berlin, Heidelberg: Springer Berlin Heidelberg, 2008, pp. 296–304. ISBN: 978-3-540-85988-8. DOI: [10.1007/978-3-540-85988-8_36](https://doi.org/10.1007/978-3-540-85988-8_36). URL: http://dx.doi.org/10.1007/978-3-540-85988-8_36.
- [82] Nhat Vu and B.S. Manjunath. "Graph cut segmentation of neuronal structures from transmission electron micrographs". In: *IEEE International Conference on Image Processing* (2008).
- [83] H. P. Ng et al. "Medical Image Segmentation Using K-Means Clustering and Improved Watershed Algorithm". In: *2006 IEEE Southwest Symposium on Image Analysis and Interpretation*. 2006, pp. 61–65. DOI: [10.1109/SSIAI.2006.1633722](https://doi.org/10.1109/SSIAI.2006.1633722).

- [84] Kalpana Shrivastava, Neelesh Gupta, and Neetu Sharma. "Medical Image Segmentation using Modified K Means Clustering". In: *International Journal of Computer Applications* 103.16 (2014), pp. 12–16. ISSN: 0975-8887. DOI: [10.1109/TMI.2011.2141674](https://doi.org/10.1109/TMI.2011.2141674).
- [85] Nameirakpam Dhanachandra, Khumanthem Manglem, and Yambem Jina Chanu. "Image Segmentation Using K -means Clustering Algorithm and Subtractive Clustering Algorithm". In: *Procedia Computer Science* 54 (2015), pp. 764–771. ISSN: 1877-0509. DOI: <http://dx.doi.org/10.1016/j.procs.2015.06.090>. URL: <http://www.sciencedirect.com/science/article/pii/S1877050915014143>.
- [86] Xiaowei Chen, Xiaobo Zhou, and S.T.C. Wong. "Automated segmentation, classification, and tracking of cancer cell nuclei in time-lapse microscopy". In: *IEEE Transactions on Biomedical Engineering* 53.4 (2006), pp. 762–766. ISSN: 0018-9294. DOI: [10.1109/TBME.2006.870201](https://doi.org/10.1109/TBME.2006.870201).
- [87] Jihong Liu, Weina Ma, and Soo-Young Lee. "A Segmentation Method Based on Dynamic Programming for Breast Mass in MRI Images". In: *Medical Biometrics: First International Conference, ICMB 2008, Hong Kong, China, January 4-5, 2008. Proceedings*. Ed. by David Zhang. Berlin, Heidelberg: Springer Berlin Heidelberg, 2007, pp. 307–313. ISBN: 978-3-540-77413-6. DOI: [10.1007/978-3-540-77413-6_39](https://doi.org/10.1007/978-3-540-77413-6_39). URL: http://dx.doi.org/10.1007/978-3-540-77413-6_39.
- [88] Y. Zhang, B. J. Matuszewski, and L. K. Shark. "A Novel Medical Image Segmentation Method using Dynamic Programming". In: *Medical Information Visualisation - BioMedical Visualisation, 2007. MediVis 2007. International Conference on*. 2007, pp. 69–74.
- [89] R. Cardenes et al. "K-Voronoi diagrams computing in arbitrary domains". In: *Image Processing, 2003. ICIP 2003. Proceedings. 2003 International Conference on*. Vol. 2. 2003, pp. 941–944. DOI: [10.1109/ICIP.2003.1246838](https://doi.org/10.1109/ICIP.2003.1246838).
- [90] Chunyan Jiang, Xinhua Zhang, and Christoph Meinel. "Hybrid Framework for Medical Image Segmentation". In: *Computer Analysis of Images and Patterns: 11th International Conference, CAIP 2005, Versailles, France, September 5-8, 2005. Proceedings*. Ed. by André Gagalowicz and Wilfried Philips. Berlin, Heidelberg: Springer Berlin Heidelberg, 2005, pp. 264–271. ISBN: 978-3-540-32011-1. DOI: [10.1007/11556121_33](https://doi.org/10.1007/11556121_33). URL: http://dx.doi.org/10.1007/11556121_33.
- [91] G. Li et al. "Segmentation of Touching Cells Using Gradient Flow Tracking". In: *2007 4th IEEE International Symposium on Biomedical Imaging: From Nano to Macro*. 2007, pp. 77–80. DOI: [10.1109/ISBI.2007.356792](https://doi.org/10.1109/ISBI.2007.356792).
- [92] Fatima A. Merchant, Shishir K. Shah, and Kenneth R. Castleman. "Object Measurement". In: *Microscope Image Processing*. USA: Elsevier Inc, 2008, pp. 195–219. ISBN: 978-0-12-372578-3.
- [93] Charlotte Giesen et al. "Highly multiplexed imaging of tumor tissues with subcellular resolution by mass cytometry". In: *Nature Methods* 11.4 (2014), pp. 417–422. DOI: [10.1038/nmeth.2869](https://doi.org/10.1038/nmeth.2869). URL: <http://dx.doi.org/10.1038/nmeth.2869>.
- [94] Xaosong Yuan et al. "MDL Constrained 3-D Grayscale Skeletonization Algorithm for Automated Extraction of Dendrites and Spines from Fluorescence Confocal Images". In: *Neuroinformatics* 7.4 (2009), pp. 213–232. ISSN: 1559-0089. DOI: [10.1007/s12021-009-9057-y](https://doi.org/10.1007/s12021-009-9057-y). URL: <http://dx.doi.org/10.1007/s12021-009-9057-y>.
- [95] Michal Kozubek and Pavel Matula. "An efficient algorithm for measurement and correction of chromatic aberrations in fluorescence microscopy". In: *Journal of Microscopy* 200.3 (2000), pp. 206–217. ISSN: 1365-2818. DOI: [10.1046/j.1365-2818.2000.00754.x](https://doi.org/10.1046/j.1365-2818.2000.00754.x). URL: <http://dx.doi.org/10.1046/j.1365-2818.2000.00754.x>.

- [96] Dominique Attali and Annick Montanvert. "Computing and Simplifying 2D and 3D Continuous Skeletons". In: *Elsevier Computer Vision and Image Understanding* 67.3 (1997), pp. 261–273. ISSN: 1365-2818. DOI: [10.1046/j.1365-2818.2000.00754.x](https://doi.org/10.1046/j.1365-2818.2000.00754.x). URL: <http://dx.doi.org/10.1046/j.1365-2818.2000.00754.x>.
- [97] Andrew P. French et al. "Colocalization of fluorescent markers in confocal microscope images of plant cells". In: *Nat. Protocols* 3 (4 2008), pp. 619–628. ISSN: 1754-2189. DOI: [10.1038/nprot.2008.31](https://doi.org/10.1038/nprot.2008.31). URL: <http://dx.doi.org/10.1038/nprot.2008.31>.
- [98] Vadim Zinchuk, Olga Zinchuk, and Teruhiko Okada. "Quantitative Colocalization Analysis of Multicolor Confocal Immunofluorescence Microscopy Images: Pushing Pixels to Explore Biological Phenomena". In: *ACTA HISTOCHEMICA ET CYTOCHEMICA* 40.4 (2007), pp. 101–111. DOI: [10.1267/ahc.07002](https://doi.org/10.1267/ahc.07002).
- [99] D. Pinkel, T. Straume, and J.W. Gray. "Cytogenetic analysis using quantitative, high-sensitivity, fluorescence hybridization". In: *Proceedings of the National Academy of Sciences* 83.9 (1986), pp. 2934–2938. eprint: <http://www.pnas.org/content/83/9/2934.full.pdf>. URL: <http://www.pnas.org/content/83/9/2934.abstract>.
- [100] M. Loferer-Krößbacher, J. Klima, and R. Psenner. "Determination of Bacterial Cell Dry Mass by Transmission Electron Microscopy and Densitometric Image Analysis". In: *Appl. Environ. Microbiol.* 64 (2 1998), pp. 688–694. DOI: [10.1038/nmeth929](https://doi.org/10.1038/nmeth929). URL: <http://dx.doi.org/10.1038/nmeth929>.
- [101] N. Watanabe et al. "Motility of bile canaliculi in the living animal: implications for bile flow." In: *The Journal of Cell Biology* 113.5 (1991), pp. 1069–1080. DOI: [10.1083/jcb.113.5.1069](https://doi.org/10.1083/jcb.113.5.1069). eprint: <http://jcb.rupress.org/content/113/5/1069.full.pdf+html>. URL: <http://jcb.rupress.org/content/113/5/1069.abstract>.
- [102] Michael J. Rust, Mark Bates, and Xiaowei Zhuang. "Sub-diffraction-limit imaging by stochastic optical reconstruction microscopy (STORM)". In: *Nat Meth* 3 (10 2006), pp. 793–796. DOI: [10.1038/nmeth929](https://doi.org/10.1038/nmeth929). URL: <http://dx.doi.org/10.1038/nmeth929>.
- [103] Michael V. Boland and Robert F. Murphy. "A neural network classifier capable of recognizing the patterns of all major subcellular structures in fluorescence microscope images of HeLa cells". In: *Bioinformatics* 17.12 (2001), pp. 1213–1223. DOI: [10.1093/bioinformatics/17.12.1213](https://doi.org/10.1093/bioinformatics/17.12.1213). eprint: <http://bioinformatics.oxfordjournals.org/content/17/12/1213.full.pdf+html>. URL: <http://bioinformatics.oxfordjournals.org/content/17/12/1213.abstract>.
- [104] R.O. Duda, P.E. Hart, and D.G. Stork. *Pattern Classification*. John Wiley & Sons, 2001.
- [105] V. Atlamazoglou et al. "Texture analysis of fluorescence microscopic images of colonic tissue sections". In: *Medical and Biological Engineering and Computing* 39.2 (2001), pp. 145–151. ISSN: 1741-0444. DOI: [10.1007/BF02344796](https://doi.org/10.1007/BF02344796). URL: <http://dx.doi.org/10.1007/BF02344796>.
- [106] Riccardo Cicchi et al. "Scoring of collagen organization in healthy and diseased human dermis by multiphoton microscopy". In: *Journal of Biophotonics* 3.1-2 (2010), pp. 34–43. ISSN: 1864-0648. DOI: [10.1002/jbio.200910062](https://doi.org/10.1002/jbio.200910062). URL: <http://dx.doi.org/10.1002/jbio.200910062>.
- [107] Erik J. Sánchez, Lukas Novotny, and Xie Sunney. "Near-Field Fluorescence Microscopy Based on Two-Photon Excitation with Metal Tips". In: *Phys. Rev. Lett.* 82 (20 1999), pp. 4014–4017. DOI: [10.1103/PhysRevLett.82.4014](https://doi.org/10.1103/PhysRevLett.82.4014). URL: <http://link.aps.org/doi/10.1103/PhysRevLett.82.4014>.

- [108] C. Xu et al. "Multiphoton fluorescence excitation: new spectral windows for biological non-linear microscopy". In: *Proceedings of the National Academy of Sciences* 93.20 (1996), pp. 10763–10768. eprint: <http://www.pnas.org/content/93/20/10763.full.pdf>. URL: <http://www.pnas.org/content/93/20/10763.abstract>.
- [109] Rajesh Babu Sekar and Ammasi Periasamy. "Fluorescence resonance energy transfer (FRET) microscopy imaging of live cell protein localizations". In: *Journal of Cellular Biology* 160 (5 2004), pp. 629–633. DOI: [10.1083/jcb.200210140](https://doi.org/10.1083/jcb.200210140).
- [110] Mark J. Miller et al. "Two-Photon Imaging of Lymphocyte Motility and Antigen Response in Intact Lymph Node". In: *Science* 296.5574 (2002), pp. 1869–1873. ISSN: 0036-8075. DOI: [10.1126/science.1070051](https://doi.org/10.1126/science.1070051). eprint: <http://science.sciencemag.org/content/296/5574/1869.full.pdf>. URL: <http://science.sciencemag.org/content/296/5574/1869>.
- [111] Anshu Bagga Mathur, George A. Truskey, and W. Monty Reichert. "Atomic Force and Total Internal Reflection Fluorescence Microscopy for the Study of Force Transmission in Endothelial Cells". In: *Biophysical Journal* 78 (4 2000), pp. 1725–1735. DOI: [10.1016/S0006-3495\(00\)76724-5](https://doi.org/10.1016/S0006-3495(00)76724-5). URL: [http://dx.doi.org/10.1016/S0006-3495\(00\)76724-5](http://dx.doi.org/10.1016/S0006-3495(00)76724-5).
- [112] Tomaso Poggio, Vincent Torre, and Christof Koch. "Computational vision and regularization theory". In: *Nature* 317.6035 (1985), pp. 314–319. DOI: [10.1038/317314a0](https://doi.org/10.1038/317314a0). URL: <http://dx.doi.org/10.1038/317314a0>.
- [113] D. Terzopoulos. "Regularization of Inverse Visual Problems Involving Discontinuities". In: *IEEE Transactions on Pattern Analysis and Machine Intelligence* PAMI-8.4 (1986), pp. 413–424. ISSN: 0162-8828. DOI: [10.1109/TPAMI.1986.4767807](https://doi.org/10.1109/TPAMI.1986.4767807).
- [114] S.I. Kabanikhin. "Definitions and examples of inverse and ill-posed problems". In: *J. Inv. Ill-Posed Problems* 16 (2008), pp. 317–357. ISSN: 0162-8828. DOI: [10.1515/JIIP.2008.069](https://doi.org/10.1515/JIIP.2008.069).
- [115] Albert Tarantola. *Inverse Problem Theory and Methods and Models for Parameter Estimation*. Philadelphia, PA, USA: Society for Industrial and Applied Mathematics, 2005, pp. 1–37. ISBN: 0-89871-572-5.
- [116] Mario Bertero and Patrizia Boccacci. *Introduction to Inverse Problems in Imaging*. Bath, UK: IOP Publishing Ltd, 1998, pp. 1–37. ISBN: 0 7503 0439 1.
- [117] M. Bertero and M. Piana. "Inverse problems in biomedical imaging: modeling and methods of solution". In: *Complex Systems in Biomedicine*. Ed. by Alfio Quarteroni, Luca Formaggia, and Alessandro Veneziani. Milano: Springer Milan, 2006, pp. 1–33. ISBN: 978-88-470-0396-5. DOI: [10.1007/88-470-0396-2_1](https://doi.org/10.1007/88-470-0396-2_1). URL: http://dx.doi.org/10.1007/88-470-0396-2_1.
- [118] Andrew Thomas Delong. "Advances in Graph-Cut Optimization: Multi-Surface Models, Label Costs, and Hierarchical Costs [online]". Doctoral theses, Dissertations. The University of Western Ontario, London Ontario, Canada, 2011 [cit. 2016-09-19]. URL: <http://www.psi.toronto.edu/~andrew/papers/thesis.pdf>.
- [119] David Waltz. "Understanding Line Drawings of Scenes with Shadows". In: *The Psychology of Computer Vision*. McGraw-Hill, 1975, pp. 19–91.
- [120] Azriel Rosenfeld, Robert A. Hummel, and Steven W. Zucker. "Definitions and examples of inverse and ill-posed problems". In: *IEEE Transactions on Systems, MAN, and Cybernetics* 6.6 (1976), pp. 420–433.
- [121] Katsuhiko Sakaue, Akira Amano, and Naokazu Yokoya. "Optimization Approaches in Computer Vision and Image Processing". In: *IEECE Trans. Inf. & Syst.* E82.3 (1999), pp. 534–547.

- [122] Yuri Boykov, Olga Veksler, and Ramin Zabih. "Fast Approximate Energy Minimization via Graph Cuts". In: *IEEE Trans. Pattern Anal. Mach. Intell.* 23.11 (2001), pp. 1222–1239. ISSN: 0162-8828. DOI: [10.1109/34.969114](https://doi.org/10.1109/34.969114). URL: <http://dx.doi.org/10.1109/34.969114>.
- [123] Vladimir Kolmogorov. "Convergent Tree-Reweighted Message Passing for Energy Minimization". In: *Proc. Int'l Workshop Artificial Intelligence and Statistics*. 2005.
- [124] David Mumford. "Optimal approximation by piecewise smooth functions and associated variational problems". In: *Commun. Pure Applied Mathematics* (1989), pp. 577–685.
- [125] Jianbo Shi and Jitendra Malik. "Normalized Cuts and Image Segmentation". In: *IEEE Transactions on Pattern Analysis and Machine Intelligence* 22 (1997), pp. 888–905.
- [126] T. Athanasiadis et al. "Semantic Image Segmentation and Object Labeling". In: *IEEE Transactions on Circuits and Systems for Video Technology* 17.3 (2007), pp. 298–312. ISSN: 1051-8215. DOI: [10.1109/TCSVT.2007.890636](https://doi.org/10.1109/TCSVT.2007.890636).
- [127] Robert J. Adler and Jonathan E. Taylor. *Random fields and geometry*. Springer monographs in mathematics. New York: Springer, 2007. ISBN: 978-0-387-48112-8. URL: <http://opac.inria.fr/record=b1123290>.
- [128] Anatoly V. Skorokhod Iosif I. Gikhman. *Introduction to the Theory of Random Processes*. Dover Books on Mathematics. Dover Publications, 1996. ISBN: 0486693872.
- [129] Matthew Brett, Will Penny, and Stefan Kiebel. *An Introduction to Random Field Theory*. MRC Cognition and Brain Sciences Unit, Cambridge UK, 2003.
- [130] Richard L. Smith. "Introduction to Besag (1974) Spatial Interaction and the Statistical Analysis of Lattice Systems". In: *Breakthroughs in Statistics*. Ed. by Samuel Kotz and Norman L. Johnson. New York, NY: Springer New York, 1997, pp. 285–323. ISBN: 978-1-4612-0667-5. DOI: [10.1007/978-1-4612-0667-5_13](https://doi.org/10.1007/978-1-4612-0667-5_13). URL: http://dx.doi.org/10.1007/978-1-4612-0667-5_13.
- [131] Stuart Geman and Donald Geman. "Stochastic Relaxation, Gibbs Distributions, and the Bayesian Restoration of Images". In: *IEEE Trans. Pattern Anal. Mach. Intell.* 6.6 (1984), pp. 721–741. ISSN: 0162-8828. DOI: [10.1109/TPAMI.1984.4767596](https://doi.org/10.1109/TPAMI.1984.4767596). URL: <http://dx.doi.org/10.1109/TPAMI.1984.4767596>.
- [132] Julian Besag. "On the statistical analysis of dirty pictures". In: *Journal of the Royal Statistical Society B* 48.3 (1986), pp. 48–259.
- [133] John Lafferty. "Conditional random fields: Probabilistic models for segmenting and labeling sequence data". In: Morgan Kaufmann, 2001, pp. 282–289.
- [134] J. M. Hammersley and P. E. Clifford. "Markov random fields on finite graphs and lattices". In: Unpublished manuscript (1971).
- [135] Gerhard Winkler. *Image Analysis, Random Fields and Markov Chain Monte Carlo Methods: A Mathematical Introduction (Stochastic Modelling and Applied Probability)*. Secaucus, NJ, USA: Springer-Verlag New York, Inc., 2006. ISBN: 3540442138.
- [136] Cyril Cassisa. "Local Vs Global Energy Minimization Methods: Application to Stereo Matching". In: *IEEE* (2010), pp. 678–683. ISSN: 978-1-4244-6789-1.
- [137] Olga Veksler. "Efficient Graph-based Energy Minimisation Methods in Computer Vision [online]". Doctoral theses, Dissertations. Cornell University, 1999 [cit. 2016-09-20]. URL: <http://www.csd.uwo.ca/faculty/olga/Papers/thesis.pdf>.
- [138] V. Černý. "Thermodynamical approach to the traveling salesman problem: An efficient simulation algorithm". In: *Journal of Optimization Theory and Applications* 45.1 (1985), pp. 41–51. ISSN: 1573-2878. DOI: [10.1007/BF00940812](https://doi.org/10.1007/BF00940812). URL: <http://dx.doi.org/10.1007/BF00940812>.

- [139] S. Kirkpatrick, C. D. Gelatt, and M. P. Vecchi. "Optimization by simulated annealing". In: *SCIENCE* 220.4598 (1983), pp. 671–680.
- [140] L. A. MacEachern and T. Manku. "Genetic algorithms for active contour optimization". In: *Circuits and Systems, 1998. ISCAS '98. Proceedings of the 1998 IEEE International Symposium on*. Vol. 4. 1998, pp. 229–232. DOI: [10.1109/ISCAS.1998.698801](https://doi.org/10.1109/ISCAS.1998.698801).
- [141] Lucia Ballerini. "Genetic Snakes for Medical Images Segmentation". In: *Evolutionary Image Analysis, Signal Processing and Telecommunications: First European Workshops, EvoIASP'99 and EuroEcTel'99, Göteborg, Sweden, May 26–27, 1999. Proceedings*. Ed. by Riccardo Poli et al. Berlin, Heidelberg: Springer Berlin Heidelberg, 1999, pp. 59–73. ISBN: 978-3-540-48917-7. DOI: [10.1007/10704703_5](https://doi.org/10.1007/10704703_5). URL: http://dx.doi.org/10.1007/10704703_5.
- [142] Lucia Ballerini. "Genetic Snakes for Color Images Segmentation". In: *Applications of Evolutionary Computing: EvoWorkshops 2001: EvoCOP, EvoFlight, EvoIASP, EvoLearn, and EvoSTIM Como, Italy, April 18–20, 2001 Proceedings*. Ed. by Egbert J. W. Boers. Berlin, Heidelberg: Springer Berlin Heidelberg, 2001, pp. 268–277. ISBN: 978-3-540-45365-9. DOI: [10.1007/3-540-45365-2_28](https://doi.org/10.1007/3-540-45365-2_28). URL: http://dx.doi.org/10.1007/3-540-45365-2_28.
- [143] Reinhard Möller and Rene Zeipelt. "Automatic Segmentation of 3D-MRI Data Using a Genetic Algorithm". In: *Medical Imaging and Augmented Reality: First International Workshop, MIAR 2001, Hong Kong, China, June 10–12, 2001. Proceedings*. 2001, pp. 278–281. DOI: [10.1109/MIAR.2001.930303](https://doi.org/10.1109/MIAR.2001.930303). URL: <http://dx.doi.org/10.1109/MIAR.2001.930303>.
- [144] O. Ibáñez et al. "Genetic approaches for topological active nets optimization". In: *Pattern Recognition* 42.5 (2009), pp. 907–917. ISSN: 0031-3203. DOI: <http://dx.doi.org/10.1016/j.patcog.2008.09.005>. URL: <http://www.sciencedirect.com/science/article/pii/S0031320308003762>.
- [145] Chris McIntosh and Ghassan Hamarneh. "Medical Image Segmentation: Energy Minimization and Deformable Models (Chapter 23)". In: *Medical Imaging: Technology and Applications* (2013). Ed. by T. Farncombe and K. Iniewski, pp. 661–692. URL: <http://www.cs.sfu.ca/~hamarneh/ecopy/crc2013a.pdf>.
- [146] D. Terzopoulos. "On matching deformable models to images". In: *Optical Society of America, Topical Meeting on Machine Vision*. Provided by the SAO/NASA Astrophysics Data System. 1987. URL: <http://adsabs.harvard.edu/abs/1980osa..meet..160T>.
- [147] T. F. Chan and L. A. Vese. "Active Contours Without Edges". In: *Trans. Img. Proc.* 10.2 (2001), pp. 266–277. ISSN: 1057-7149. DOI: [10.1109/83.902291](https://doi.org/10.1109/83.902291). URL: <http://dx.doi.org/10.1109/83.902291>.
- [148] Judea Pearl. *Probabilistic Reasoning in Intelligent Systems: Networks of Plausible Inference*. San Francisco, CA, USA: Morgan Kaufmann Publishers Inc., 1988. ISBN: 0-934613-73-7.
- [149] Brendan Frey and David MacKay. "A Revolution: Belief Propagation in Graphs With Cycles". In: *In Neural Information Processing Systems*. MIT Press, 1998, pp. 479–485.
- [150] William T. Freeman, Egon C. Pasztor, and Owen T. Carmichael. "Learning Low-Level Vision". In: *Int. J. Comput. Vision* 40.1 (2000), pp. 25–47. ISSN: 0920-5691. DOI: [10.1023/A:1026501619075](https://doi.org/10.1023/A:1026501619075). URL: <http://dx.doi.org/10.1023/A:1026501619075>.
- [151] Vladimir Kolmogorov and Ramin Zabih. "What energy functions can be minimized via graph cuts?" In: *IEEE Transactions on Pattern Analysis and Machine Intelligence* 26.2 (2004), pp. 65–81.
- [152] Y. Boykov and M.P. Jolly. "Interactive graph cuts for optimal boundary and region segmentation of objects in N-D images". In: *Proc. IEEE Int'l Conf. on Computer Vision* 1 (2001), pp. 105–112.

- [153] Yuri Boykov and Vladimir Kolmogorov. "An Experimental Comparison of Min-Cut/Max-Flow Algorithms for Energy Minimization in Vision". In: *IEEE Transactions on Pattern Analysis and Machine Intelligence* 26 (2001), pp. 359–374.
- [154] Vladimir Kolmogorov et al. "A Comparative Study of Energy Minimization Methods for Markov Random Fields with Smoothness-Based Priors". In: *IEEE Transactions on Pattern Analysis & Machine Intelligence* 30. undefined (2007), pp. 1068–1080. ISSN: 0162-8828. DOI: doi.ieeecomputersociety.org/10.1109/TPAMI.2007.70844.
- [155] P. Kohli, M. Pawan Kumar, and P. H. S. Torr. "P³ & Beyond: Move Making Algorithms for Solving Higher Order Functions". In: *IEEE Transactions on Pattern Analysis and Machine Intelligence* 31.9 (2009), pp. 1645–1656. ISSN: 0162-8828. DOI: [10.1109/TPAMI.2008.217](https://doi.ieeecomputersociety.org/10.1109/TPAMI.2008.217).
- [156] Nikos Komodakis, Georgios Tziritas, and Nikos Paragios. "Fast, Approximately Optimal Solutions for Single and Dynamic MRFs". In: *CVPR*. IEEE Computer Society, 2007. ISBN: 1-4244-1179-3. URL: <http://dblp.uni-trier.de/db/conf/cvpr/cvpr2007.html#KomodakisTP07>.
- [157] M. Pawan Kumar and Daphne Koller. "MAP Estimation of Semi-metric MRFs via Hierarchical Graph Cuts". In: *Proceedings of the Twenty-Fifth Conference on Uncertainty in Artificial Intelligence*. UAI '09. Arlington, Virginia, United States: AUAI Press, 2009, pp. 313–320. ISBN: 978-0-9749039-5-8. URL: <http://dl.acm.org/citation.cfm?id=1795114.1795151>.
- [158] D. M. Greig, B. T. Porteous, and A. H. Seheult. "Exact Maximum A Posteriori Estimation for Binary Images". In: *Journal of the Royal Statistical Society. Series B (Methodological)* 51.2 (1989), pp. 271–279. ISSN: 00359246. URL: <http://www.jstor.org/stable/2345609>.
- [159] Sébastien Roy and Ingemar Johansson Cox. "A maximum-flow formulation of the n-camera stereo correspondence problem". In: *Computer Vision, 1998. Sixth International Conference on*. 1998, pp. 492–499.
- [160] Yuri Boykov, Olga Veksler, and Ramin Zabih. "Markov Random Fields with Efficient Approximations." In: *CVPR*. IEEE Computer Society, 1998, pp. 648–655. ISBN: 0-8186-8497-6. URL: <http://dblp.uni-trier.de/db/conf/cvpr/cvpr1998.html#BoykovVZ98>.
- [161] L. R. Ford and D. R. Fulkerson. "Maximal Flow through a Network". In: *Canadian Journal of Mathematics* 8 (1956), pp. 399–404. URL: <http://www.rand.org/pubs/papers/P605/>.
- [162] E.A. Dinic. "Algorithm for solution of a problem of maximum flow in a network with power estimation". In: *Soviet Math* 11 (1970), pp. 1277–1280.
- [163] Jack Edmonds and Richard M. Karp. "Theoretical Improvements in Algorithmic Efficiency for Network Flow Problems". In: *J. ACM* 19.2 (1972), pp. 248–264. ISSN: 0004-5411. DOI: [10.1145/321694.321699](https://doi.acm.org/10.1145/321694.321699). URL: <http://doi.acm.org/10.1145/321694.321699>.
- [164] Andrew V. Goldberg and Robert E. Tarjan. "A New Approach to the Maximum-flow Problem". In: *J. ACM* 35.4 (1988), pp. 921–940. ISSN: 0004-5411. DOI: [10.1145/48014.61051](https://doi.acm.org/10.1145/48014.61051). URL: <http://doi.acm.org/10.1145/48014.61051>.
- [165] Narsingh Deo. *Graph Theory with Applications to Engineering and Computer Science (Prentice Hall Series in Automatic Computation)*. Upper Saddle River, NJ, USA: Prentice-Hall, Inc., 1974. ISBN: 0133634736.
- [166] John Adrian Bondy. *Graph Theory With Applications*. Oxford, UK, UK: Elsevier Science Ltd., 1976. ISBN: 0444194517.
- [167] Maarten van Steen. *Graph theory and complex networks : An introduction*. Lexington: Maarten van Steen, 2010. ISBN: 978-90-815406-1-2. URL: <http://opac.inria.fr/record=b1130915>.
- [168] Mark Newman. *Networks: An Introduction*. 1st edition. Oxford University Press, 2010. ISBN: 0199206651.

- [169] Eugene Lawler. "4.5. Combinatorial Implications of Max-Flow Min-Cut Theorem, 4.6. Linear Programming Interpretation of Max-Flow Min-Cut Theorem". In: *Combinatorial Optimization: Networks and Matroids*. Ed. by Eugene Lawler. Dover, 2001, pp. 117–120. ISBN: 0-486-41453-1.
- [170] Solomon Eyal Shimony. "Finding MAPs for belief networks is NP-hard". In: *Artificial Intelligence* 68.2 (1994), pp. 399–410. ISSN: 0004-3702. DOI: [http://dx.doi.org/10.1016/0004-3702\(94\)90072-8](http://dx.doi.org/10.1016/0004-3702(94)90072-8). URL: <http://www.sciencedirect.com/science/article/pii/0004370294900728>.
- [171] Thomas H. Cormen et al. *Introduction to Algorithms, Third Edition*. 3rd. The MIT Press, 2009. ISBN: 0262033844, 9780262033848.
- [172] V. B. Cherkassky and V. A. Goldberg. "On Implementing the Push—Relabel Method for the Maximum Flow Problem". In: *Algorithmica* 19.4 (19), pp. 390–410. ISSN: 1432-0541. DOI: [10.1007/PL00009180](https://doi.org/10.1007/PL00009180). URL: <http://dx.doi.org/10.1007/PL00009180>.
- [173] R. Szeliski et al. "A Comparative Study of Energy Minimization Methods for Markov Random Fields with Smoothness-Based Priors". In: *IEEE Transactions on Pattern Analysis and Machine Intelligence* 30.6 (2008), pp. 1068–1080. ISSN: 0162-8828. DOI: [10.1109/TPAMI.2007.70844](https://doi.org/10.1109/TPAMI.2007.70844).
- [174] Nhat Bao Sinh Vu. "Image Segmentation with Semantic Priors: A Graph Cut Approach [online]". Doctoral theses, Dissertations. University of California, Santa Barbara, 2008 [cit. 2016-10-03]. URL: <https://vision.ece.ucsb.edu/sites/vision.ece.ucsb.edu/files/publications/NhatsThesis.pdf>.
- [175] M. Lysaker, A. Lundervold, and Xue-Cheng Tai. "Noise removal using fourth-order partial differential equation with applications to medical magnetic resonance images in space and time". In: *Image Processing, IEEE Transactions* 12.12 (2004), pp. 1579–1590.
- [176] Qian Wang, Liya Chen, and Dinggang Shen. "Fast histogram equalization for medical image enhancement". In: *Engineering in Medicine and Biology Society, 2008. EMBS 2008. 30th Annual International Conference of the IEEE* (2008), pp. 2217–2220.
- [177] Feng Zhou et al. "Medical image enhancement based on NSCT". In: *Smart and Sustainable City 2013 (ICSSC 2013), IET International Conference* (2013), pp. 166–16.
- [178] Isabel Rodrigues, Joao Sanches, and Jose Bioucas-Dias. "Denoising of medical images corrupted by Poisson noise". In: *Image Processing, 2008. ICIP 2008. 15th IEEE International Conference* 4669 (2008), pp. 1756–1759.
- [179] K.E. Timmermann and R.D. Nowak. "Multiscale modeling and estimation of Poisson processes with application to photon-limited imaging". In: *Information Theory, IEEE Transactions* 45.3 (1999), pp. 846–862.
- [180] R.M. Willett and R.D. Nowak. "Fast multiresolution photon-limited image reconstruction". In: *Biomedical Imaging: Nano to Macro, 2004. IEEE International Symposium* 2 (2004), pp. 1192–1195.
- [181] R.D. Nowak and M.A.T. Figueirido. "Unsupervised progressive parsing of Poisson fields using minimum description length criteria". In: *Image Processing, 1999. ICIP 99. Proceedings. 1999 International Conference* 2 (1999), pp. 26–30.
- [182] Pascal Getreuer. "Rudin-Osher-Fatemi Total Variation Denoising using Split Bregman". In: *Image Processing On Line* (2012), pp. 74–95.
- [183] Weibo Wei et al. "Split Bregman Algorithm of TV-L1 Model for Image Diffusion". In: *Pattern Recognition (CCPR), 2010 Chinese Conference* (2010), pp. 1–5.
- [184] Junwhan Kim and Ramin Zabih. "A segmentation algorithm for contrast-enhanced images". In: *Computer Vision, 2003. Proceedings. Ninth IEEE International Conference* (2003), pp. 502–509.
- [185] Kartic Subr, Aditi Majumder, and Sandy Irani. "Greedy algorithm for local contrast enhancement of images". In: *Lecture Notes in Computer Science* 3617 (2005), pp. 171–179.

- [186] John Vince. *Mathematics for Computer Graphics*. 2nd ed. London, England: Springer, 2006.
- [187] Duncan Marsh. *Applied Geometry for Computer Graphics and CAD*. 2nd ed. London, England: Springer, 2005.
- [188] Joachim Weickert. "Coherence-Enhancing Diffusion Filtering". In: *International Journal of Computer Vision* 31.2/3 (1999), pp. 111–127.
- [189] Joachim Weickert and Hanno Scharr. "A scheme for Coherence Enhancing Diffusion Filtering with Optimized Rotational Invariance". In: *Journal of Visual Communication and Image Representation* 13.1/2 (2002), pp. 103–118.
- [190] Joachim Weickert. "Coherence-enhancing shock filters". In: *Pattern Recognition*. Vol. 2781. Springer, 2003, pp. 1–8.
- [191] Martin Maska et al. "Segmentation and Shape Tracking of Whole Fluorescent Cells Based on the Chan-Vese Model". In: *IEEE Trans. Medical Imaging* 32.6 (2013), pp. 995–1006.
- [192] D. Kroon and C.H. Slump. "Coherence filtering to enhance the mandibular canal in cone-beam CT data". In: *IEEE-EMBS Benelux Chapter Symposium* (2009).
- [193] Noha El Zehiry et al. "Graph Cut Optimization for the Mumford-Shah Model". In: *The Seventh IASTED International Conference on Visualization, Imaging and Image Processing*. VIIP '07. Palma de Mallorca, Spain: ACTA Press, 2007, pp. 182–187. ISBN: 978-0-88986-692-8. URL: <http://dl.acm.org/citation.cfm?id=1659167.1659203>.
- [194] Vladimir Kolmogorov and Yuri Boykov. "What Metrics Can Be Approximated by Geo-Cuts, Or Global Optimization of Length/Area and Flux." In: *ICCV*. IEEE Computer Society, 2005, pp. 564–571. ISBN: 0-7695-2334-X. URL: <http://dblp.uni-trier.de/db/conf/iccv/iccv2005-1.html#KolmogorovB05>.
- [195] Yuri Boykov. "Computing geodesics and minimal surfaces via graph cuts". In: *in International Conference on Computer Vision*. 2003, pp. 26–33.
- [196] Nobuyuki Otsu. "A Threshold Selection Method from Gray-Level Histograms". In: *IEEE Transactions on Systems, Man and Cybernetics* 9.1 (1979), pp. 62–66. DOI: [10.1109/TSMC.1979.4310076](https://doi.org/10.1109/TSMC.1979.4310076). URL: <http://dx.doi.org/10.1109/TSMC.1979.4310076>.
- [197] Tapas Kanungo et al. "An Efficient k-Means Clustering Algorithm: Analysis and Implementation". In: *IEEE Trans. Pattern Anal. Mach. Intell.* 24.7 (2002), pp. 881–892. ISSN: 0162-8828. DOI: [10.1109/TPAMI.2002.1017616](https://doi.org/10.1109/TPAMI.2002.1017616). URL: <http://dx.doi.org/10.1109/TPAMI.2002.1017616>.
- [198] M. A. T. Figueiredo and R. Nowak. "Image restoration under wavelet-domain priors: An expectation-maximization approach". In: *IEEE International Conf. on Image Processing - ICIP*. Vol. 1. 2002, pp. 337–340.
- [199] S. Huang et al. *CIL* 9233. Picture. (accessed July 6, 2015). URL: <http://www.cellimage-library.org/images/9233>.
- [200] R. Mejia. *CIL* 11996. Picture. <http://www.cellimagelibrary.org/images/11996>. (accessed July 6, 2015).
- [201] E. Morselli. *CIL* 13902. Picture. <http://www.cellimagelibrary.org/images/13902>. (accessed July 6, 2015).
- [202] E. Morselli. *CIL* 13903. Picture. <http://www.cellimagelibrary.org/images/13903>. (accessed July 6, 2015).
- [203] E. Morselli. *CIL* 13904. Picture. <http://www.cellimagelibrary.org/images/13904>. (accessed July 6, 2015).
- [204] Prue Talbot. *CIL* 12627. Picture. (accessed October 21, 2016). URL: <http://www.cellimagelibrary.org/images/12627>.

- [205] Eugenia Morselli et al. *CIL* 13899. Picture. (accessed October 21, 2016). URL: <http://www.cellimagelibrary.org/images/13899>.
- [206] Eugenia Morselli et al. *CIL* 13901. Picture. (accessed October 21, 2016). URL: <http://www.cellimagelibrary.org/images/13901>.
- [207] Weimiao Yu et al. *CIL* 40217. Picture. (accessed October 21, 2016). URL: <http://www.cellimagelibrary.org/images/40217>.
- [208] Linda Parysek. *CIL* 195. Picture. (accessed October 21, 2016). URL: <http://www.cellimagelibrary.org/images/195>.
- [209] Allen Liu and Sandra L. Schmid. *CIL* 10102. Picture. (accessed October 21, 2016). URL: <http://www.cellimagelibrary.org/images/10102>.
- [210] Allen Liu and Sandra L. Schmid. *CIL* 10104. Picture. (accessed October 21, 2016). URL: <http://www.cellimagelibrary.org/images/10104>.
- [211] Azusa Hotta et al. *CIL* 12294. Picture. (accessed October 21, 2016). URL: <http://www.cellimagelibrary.org/images/12294>.
- [212] Anne Carpenter. *CIL* 21749. Picture. (accessed October 21, 2016). URL: <http://www.cellimagelibrary.org/images/21749>.
- [213] Anne Carpenter. *CIL* 21759. Picture. (accessed October 21, 2016). URL: <http://www.cellimagelibrary.org/images/21759>.
- [214] M. Deshmukh et al. *CIL* 41066. Picture. (accessed October 21, 2016). URL: <http://www.cellimagelibrary.org/images/41066>.
- [215] Olga Pontes and Craig Pikaard. *CIL* 188. Picture. (accessed October 21, 2016). URL: <http://www.cellimagelibrary.org/images/188>.
- [216] R.I. Kumaran, Z. Lazar, and David L. Spector. *CIL* 10093. Picture. (accessed October 21, 2016). URL: <http://www.cellimagelibrary.org/images/10093>.
- [217] Anne Carpenter. *CIL* 32140. Picture. (accessed October 21, 2016). URL: <http://www.cellimagelibrary.org/images/32140>.
- [218] Nikita Orlov, Wendy Iser, and Cathy Wolkow. *CIL* 1057. Picture. (accessed October 21, 2016). URL: <http://www.cellimagelibrary.org/images/1057>.
- [219] Nikita Orlov, Wendy Iser, and Cathy Wolkow. *CIL* 1265. Picture. (accessed October 21, 2016). URL: <http://www.cellimagelibrary.org/images/1265>.
- [220] Michael Cammer and Phyllis Novikoff. *CIL* 35278. Picture. (accessed October 21, 2016). URL: <http://www.cellimagelibrary.org/images/35278>.
- [221] Kate Nobes and Mark Shipman. *CIL* 38974. Picture. (accessed October 21, 2016). URL: <http://www.cellimagelibrary.org/images/38974>.
- [222] Hesed Padilla-Nash and Thomas Ried. *CIL* 228. Picture. (accessed October 21, 2016). URL: <http://www.cellimagelibrary.org/images/228>.
- [223] Jr. Arturo Orjalo, Sally Coassini, and Hans Johansson. *CIL* 41066. Picture. (accessed October 21, 2016). URL: <http://www.cellimagelibrary.org/images/41066>.
- [224] Yi-Chun Maria Chen. *CIL* 37338. Picture. (accessed October 21, 2016). URL: <http://www.cellimagelibrary.org/images/37338>.
- [225] Yi-Chun Maria Chen. *CIL* 37339. Picture. (accessed October 21, 2016). URL: <http://www.cellimagelibrary.org/images/37339>.
- [226] Karen Meaburnn et al. *CIL* 13432. Picture. (accessed October 21, 2016). URL: <http://www.cellimagelibrary.org/images/13432>.

- [227] Karen Meaburn et al. *CIL 13438*. Picture. (accessed October 21, 2016). URL: <http://www.cellimagelibrary.org/images/13438>.